Mediators of Inflammation

Metabolism of the Host and Microbes to Modulate Immunocytes 2021

Lead Guest Editor: Shuai Chen
Guest Editors: Deguang Song, Miaomiao Wu, Mingliang Jin, Xiaolu Jin, and Peng Bin

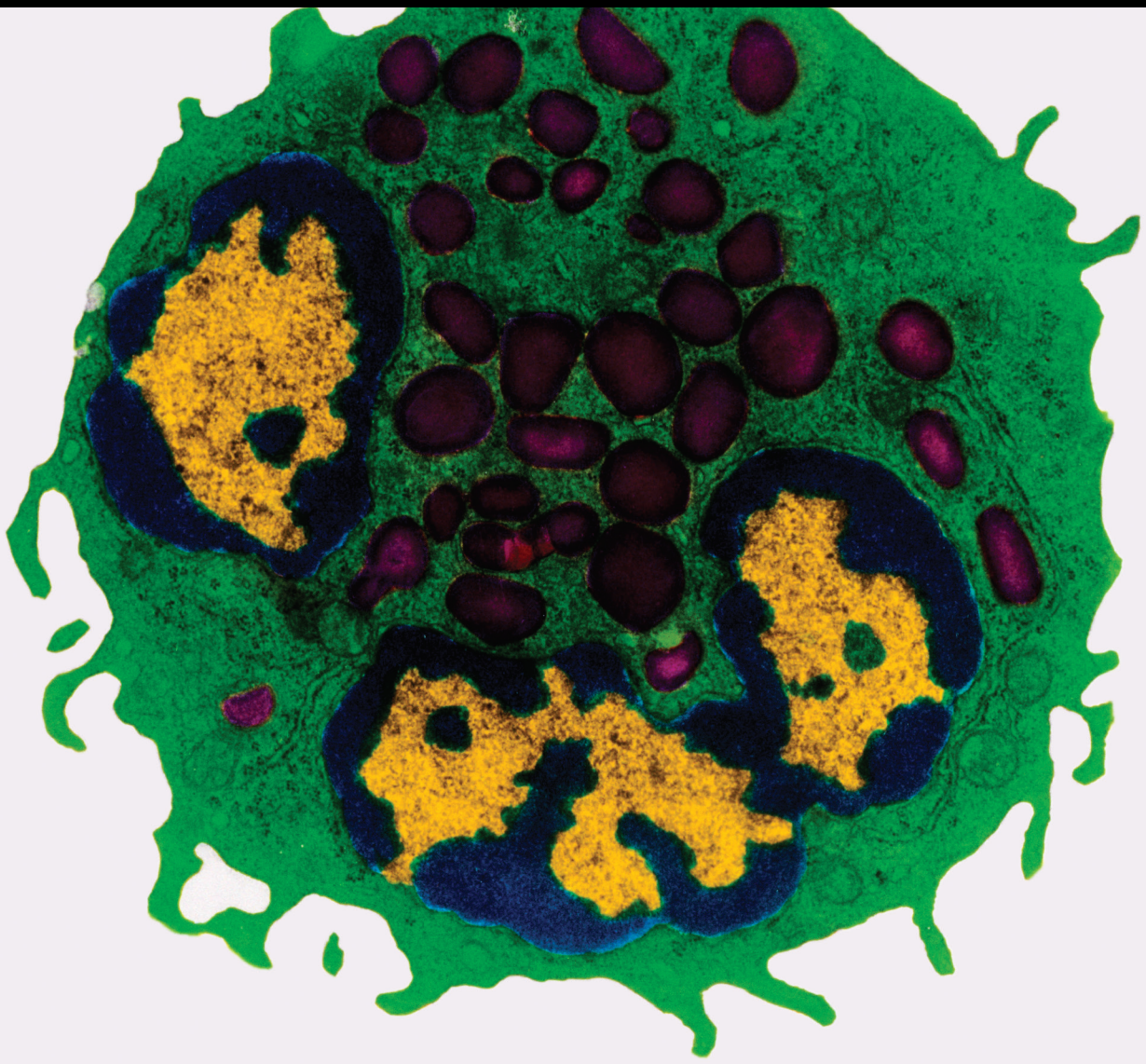

Metabolism of the Host and Microbes to Modulate Immunocytes 2021

Mediators of Inflammation

Metabolism of the Host and Microbes to Modulate Immunocytes 2021

Lead Guest Editor: Shuai Chen
Guest Editors: Deguang Song, Miaomiao Wu, Mingliang Jin, Xiaolu Jin, and Peng Bin

Contents

Hindawi
Mediators of Inflammation
Volume 2022, Article ID 8011988, 14 pages
https://doi.org/10.1155/2022/8011988

Research Article

Quercetin Alleviates the Progression of Breast Cancer-Related Depression via Inhibiting the Pyroptosis and Promoting the Immune Response

Qing Zhu,[1] Lei Yang,[2] Hui Yang,[2] Yuanshan Han,[2] Yun Chen,[1] and Ying He[3]

[1]*Pharmacy Department of Hunan Cancer Hospital/the Affiliated Cancer Hospital of Xiangya School of Medicine, Central South University, Changsha, 410013 Hunan, China*
[2]*Department of Pharmacy, The First Hospital of Hunan university of Chinese Medicine, Changsha, 410007 Hunan, China*
[3]*The Second Department of Breast Surgery, Hunan Cancer Hospital/the Affiliated Cancer Hospital of Xiangya School of Medicine, Central South University, Changsha, 410013 Hunan, China*

Correspondence should be addressed to Ying He; heying@hnca.org.cn

Received 30 September 2021; Revised 17 December 2021; Accepted 26 January 2022; Published 3 March 2022

Academic Editor: Shuai CHEN

Background. Breast cancer-related depression (BCRD) seriously inhibits the life quality of patients with breast cancer. The Xiaoyao Kangai Jieyu Formula is known to inhibit the progression of depression. However, the detailed function of the Xiaoyao Kangai Jieyu Formula in BCRD remains unclear. *Methods*. Network pharmacology was constructed to assess the downstream target of the Xiaoyao Kangai Jieyu Formula in BCRD. In addition, the tail suspension test, sucrose preference test, and forced swimming test were used to test the symptom of depression in mice. Fluoro-Jade B staining was performed to observe the structure of neurons. RT-qPCR and western blot were applied to evaluate mRNA and protein levels. Besides, ELISA was performed to test the inflammatory responses and the immune response-related cytokines. *Results*. Quercetin was identified as the key component of the Xiaoyao Kangai Jieyu Formula. Quercetin significantly inhibited BCRD-induced neuron pyroptosis via downregulation of PYD and card domain containing (ASC), NLR family pyrin domain containing 3 (NLRP3), and caspase-1, and quercetin could reverse BCRD-caused inhibition of neuron viability. Quercetin significantly attenuated the symptom of BCRD in mice, and it could reverse the contents of 5-hydroxytryptamine (5-HT), dopamine (DA), and neutrophil elastase (NE) in mice. Moreover, quercetin could promote the immune responses in xenograft mice via upregulation of interleukin-(IL-) 2, interferon-γ (IFN-γ), and IL-10. *Conclusion*. Quercetin, the active ingredient of the Xiaoyao Kangai Jieyu Formula, effectively mitigated the progression of BCRD by inhibiting pyroptosis, promoting immune response, and improving serum metabolism.

1. Introduction

Patients with breast cancer often exhibit significant emotional instability, especially depression, and the probability of being accompanied by depression has been reached at 40% [1, 2]. Meanwhile, depression is known to affect the life quality of patients seriously and even decrease the survival time of patients with breast cancer by 10%-20% [3]. Therefore, it is of great significance to study the pathogenesis of BCRD for the prevention and treatment of BCRD. At present, the main method of clinical treatment of BCRD is to give adjuvant antidepressant treatment after diagnosis [4]. However, the outcomes remain still limited as the mechanism by which breast cancer develops into BCRD remains largely unknown.

Traditional Chinese medicine is based on dialectical treatment, which has a significant therapeutic effect on the progression of breast cancer and drug resistance [5, 6]. Moreover, traditional Chinese medicine usually has unique advantages in the treatment of depression [7, 8]. The Xiaoyao Kangai Jieyu Formula is a traditional Chinese herbal compound that we have previously found to be highly effective in the

treatment of BCRD [9]. Therefore, formulating prescriptions and formulating drugs (starting from traditional Chinese medicine) based on the etiology and pathogenesis of BCRD have a broader prospect and application value.

Previous studies suggested that the pathogenesis of BCRD mainly focused on autonomic neuroimmunity, neuroendocrine immunity, and oxidative stress injury, which are related to inflammation [10, 11]. In addition, cell pyroptosis is a novel form of cell death (programmed) discovered in recent years, and it is considered to be the most closely related form of cell damage to inflammation [12]. It has been documented that the classical cleavage pathway is mediated by aspartate-specific caspase-1 (aka caspase-1), which can be induced to be upregulated by inflammatory vesicles [13]. Our preliminary data revealed that inflammatory vesicles (NLRP3) are frequently activated during the progression of neurons in BCRD mice. Hence, it is hypothesized that the hippocampal neuron pyroptosis might participate in the occurrence and development of BCRD.

Based on the above background, our study was aimed at investigating the function of the Xiaoyao Kangai Jieyu Formula in inflammatory responses during the progression of BCRD. We hope that this work will exert novel insights into discovering the new methods against BCRD.

2. Material and Methods

2.1. Data Sources of Network Pharmacology. The active constituents of the Xiaoyao Kangai Jieyu Formula were obtained in 3 steps as previously described [14].

The target protein was predicted using the TCMSP database and DrugBank (https://www.drugbank.ca/) and TCMSP database. Other active components (the target proteins were not able to be predicted in these two databases) were analyzed by using SwissTargetPrediction, and the top targets predicted were selected according to the results. Each active constituent and the Xiaoyao Kangai Jieyu Formula active constituent-target protein network were coded by applying Cytoscape (v3.7.1) software for exploring the association between active constituents and target proteins. Additionally, Network Analyzer (a Cytoscape plugin) was applied to investigate the betweenness centrality of the network and the degree.

2.2. Potential Active Target Proteins (PATPs). The intersection between the targets of the Xiaoyao Kangai Jieyu Formula and proteins (related to BCRD) was taken as the PATPs for the following analysis.

2.3. Protein-Protein Interaction (PPI) Investigation. In order to clarify the associations between PATPs, the STRING database was applied to establish the network of PPI. Moreover, the species were only adaptive to Homo sapiens, and a confidence score of 0.95 (<0.4 was considered low confidence, ≤0.7 regarded as medium, and >0.7 considered high) was selected in this analysis. Further experiments used the PPI data. Then, CytoNCA (a Cytoscape plugin) was applied to assess the network of PPI, and the network was established by top proteins ($n = 150$).

2.4. Gene Ontology (GO) Analysis. The molecular mechanisms of the Xiaoyao Kangai Jieyu Formula were determined using GO analysis. MCODE (a Cytoscape plugin) was applied in GO biological process analysis. In detail, the data of PPI were filtered in Cytoscape applying MCODE in this procedure. 0.05 was considered the significance level.

2.5. Kyoto Encyclopedia of Genes and Genomes (KEGG). KEGG analysis was applied to explore potential pathways and biological functions in this work. In addition, KEGG analysis was applied with the ClusterProfiler package of the R language. 0.05 was considered the significance level.

2.6. Untargeted Metabolomics. Samples were placed on dry ice and weighed. A freeze tissue grinder was applied to homogenize the tissue. Tissue homogenate (200 μL) was moved and mixed with 800 μL of methanol/acetonitrile (1 : 1, v/v). The samples were vortexed for 30 s and centrifuged (14,500 rpm, 15 min, 4°C). The supernatant was evaporated to dryness by nitrogen blowing and then reconstituted with 100 μL acetonitrile/water (1 : 1, v/v). Finally, the solution was filtered with a 0.22 μm membrane and analyzed by UHPLC-QTOF-MS (Agilent 1290 UHPLC 6545 MS). The reaction conditions were as follows: a Waters HSS T3 column was applied to separate the sample solution (2 μL) at 40°C with 0.1% formic acid (eluent A) and acetonitrile (eluent B) (the flow rate was 0.3 mL/min). A total 20-minute gradient program was set as follows: 0.01 min, 1% B; 1.5 min, 1% B; 13 min, 99% B; 16.5 min, 99% B; and equilibration time of 16.6 min at 1%.

2.7. Cell Culture. Breast cancer cells (4T1) were purchased from the Chinese Academy of Sciences. Nashed et al. showed that 4T1 facilitates the induction of depression-like states in mice [15]; therefore, 4T1 cells were selected for the study of breast cancer-related depression in this study. In addition, primary neurons originated from Invitrogen (item number: A15585, Waltham, MA, USA). Cells were maintained in DMEM (Invitrogen) with 10% FBS (Gibco) and penicillin (100 U/mL) in the condition of 37°C and 5% CO_2.

2.8. Drug. The Xiaoyao Kangai Jieyu Formula was obtained from Changdu Zhenxing Lo. Ctd. (Hunan, China). The Xiaoyao Kangai Jieyu Formula consists of Bupleurum, Angelica, white peony, poria, Atractylodes, Prunella vulgaris, ginseng, turmeric, Hypericum perforatum, and roasted licorice.

2.9. Cell Treatment. 4T1 cells were exposed to LPS (Sigma, 10 μg/mL) for 6 h. Then, cells were centrifuged, and the supernatants were collected. The cell supernatants were added to primary neurons for 6 h. For the CORD group, primary neurons were exposed to 200 μM CORT for 6 h. 4T1 cells were exposed to LPS (Sigma, 10 μg/mL) for 6 h to simulate BCRD in vitro. Then, cells were centrifuged, and the supernatants were collected. The cell supernatants and 200 μM CORT were added to primary neurons for 6 h [16].

2.10. In Vivo Model. Nude mice (BALB/c, $n = 40$; aged 6-8 weeks) originated from Beijing Vital River. The mice were

Table 1

Gene	Primer sequence	Gene ID	Length
NLRP3	FCCTCTTTGGCCTTGTAAACCAG RTGGCTTTCACTTCAATCCACT	216799	113 bp
ASC(PYCARD)	FCAGAGTACAGCCAGAACAGGACACT RAAGCATCCAGCACTCCGTCCAC	66824	91 bp
Caspase-1	FACAAGGCACGGGACCTATG RTCCCAGTCAGTCCTGGAAATG	12362	237 bp
β-Actin	FACATCCGTAAAGACCTCTATGCC RTACTCCTGCTTGCTGATCCAC	1146	223 bp

placed in the condition of SPF. 4T1 cells (10^7/mL) were injected into mice (subcutaneously). The tumor volume was measured weekly. Then, mice (except the control group) were injected with 30 mg/kg CORT suspension subcutaneously.

Mice in the BCRD+Pac group were injected intraperitoneally with paclitaxel liposomes (20 mg/kg) weekly. Mice in the BCRD+Flu group were administered with fluoxetine hydrochloride (7.8 mg/kg) every day. Mice in the quercetin group were injected intraperitoneally with quercetin at an equivalent daily dose. In addition, mice in the control, depression, BCRD, and breast cancer group were administered with the same amount of distilled water. After 3 weeks of treatment, each group of mice was analyzed according to multiple indicators [16].

The Institutional Animal Care and Use Committees of the Affiliated Cancer Hospital of Xiangya School of Medicine, Central South University, approved the protocol of this work (number 2021-056). The treatment of animals during the experiment conforms to the standards of "Guiding Opinions on Being Kind to Experimental Animals" issued by the Ministry of Science and Technology in 2006.

2.11. Sucrose Preference Test. Decreasing sucrose preference is considered homologous anhedonia, inability to experience pleasure, which mimics depression. The water bottles ($n = 2$) were put in each cage for the purpose of evaluating animal habit influence. Mice were deprived of water and fasted for one day before the experiments. Briefly, sucrose solution (2%) and the drinking water were put in a cage for 6 hours. Finally, measure the liquid content and use the following formula to calculate the sucrose preference as previously described [17].

2.12. Forced Swimming Test. The forced swimming test (FST) is used to measure changes in depressive behavior. The mice received FST, which was in line with the recent work [18]. Put the animal in a glass bottle with a height of 21 cm and a diameter of 16.5 cm. The bottle was added with water (13 cm deep) for 6 minutes. Force the mice to swim for 6 minutes, and observe how long they were motionless in the last 4 minutes. When heads of mice were out of the water and there was no significant movement of the limbs, the mice were defined as static. The result of the resting time was recorded.

2.13. Tail Suspension Test. The mice were individually suspended with tap and separated from each other. Then, the tape was placed 1 cm from the tail tip. The status of the mice was observed for 6 minutes, and the result was recorded.

2.14. CCK8 assay. Cells (5×10^3 per well) were treated for 28 h. Then, cells were treated with CCK8 reagents (10 μL, Beyotime) at 37°C for 2 h. After that, the absorbance (450 nm) was detected by using a microplate reader.

2.15. EthD-III staining. In brief, EthD-III (2 μM) was applied to incubate the cells for 45 min and DAPI was applied to stain the cells. Confocal microscopy (LSM710, Carl Zeiss, Germany) was applied to visualize cells (522/593 nm).

2.16. RT-qPCR. TRIzol (Takara, Tokyo, Japan) was applied to isolate tissues or cells from total RNAs. The PrimeScript RT reagent Kit (Takara) was applied to synthesize cDNAs. The ABI7500 system was performed in RT-qPCR performing SYBR Green. RT-qPCR was applied as follows: 94°C for 2 min, followed by 35 cycles (94°C for 30 s and 55°C for 45 s). The primers originated from GenePharma (Shanghai, China). The $2^{-\triangle\triangle CT}$ method was applied in quantification. β-Actin was considered to be the reference control. The sequences are shown in Table 1.

2.17. Western blot. RIPA buffer was applied to isolate protein from tissues or cell lysates. BCA (Invitrogen) was applied in protein quantification. Subsequently, SDS-PAGE (10%) was applied to separate the proteins (40 μg/lane), and the proteins were then transferred onto PVDF (Invitrogen). Primary antibodies were applied to incubate the membranes overnight after membranes were blocked with skim milk (3%) for 1 h. Afterward, a secondary antibody (anti-rabbit, Abcam; 1 : 5000) was applied to incubate the membranes for 1 h. The Odyssey Imaging System was applied to scan the membranes, and Odyssey v2.0 software (LICOR Biosciences, USA) was applied to analyze the blots. The primary antibodies were as follows: anti-NLRP3 (1 : 1000), anti-ASC (1 : 1000), anti-caspase-1 (1 : 1000), and anti-β-actin (1 : 1000). All antibodies originated from Abcam (USA). β-Actin was applied for quantification.

2.18. ELISA. The ELISA kit originated from Jiancheng, Nanjing (China). The levels of 5-HT (item number: H104-1-1), DA (item number: H170), NE (item number: H344-1), IL-2 (item number: H003), IFN-γ (item number: H025), and IL-10 (item number: H009-1) in the hippocampal/tumor homogenate of mice were determined.

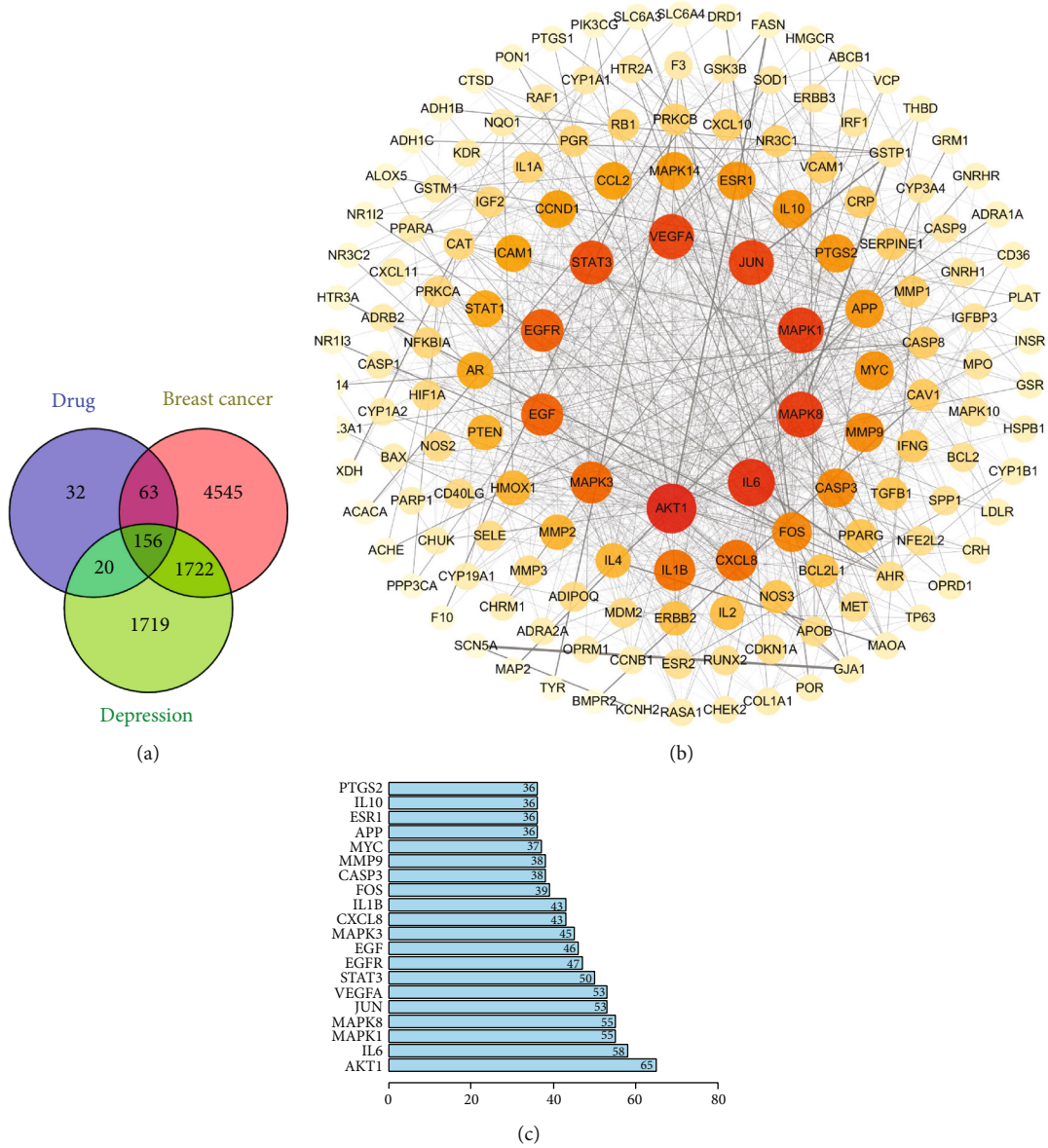

Figure 1: Active targets and PPI network. (a) The overlapped potential active target proteins were presented. (b) The network of PPI containing the active targets was presented. The redder the color, the greater the degree value. The line from thick to thin indicates that the edge betweenness is from big to small. (c) Prediction of the top 20 key targets. The horizontal coordinate is the degree value of each target.

2.19. Flow Cytometry. The tumors were dissociated and suspended. CD8-APC and CD4-FITC were subsequently applied to stain the cells for 15 minutes at 4°C. Afterward, cells were permeabilized for Foxp3-PE (eBiosciences) staining. Flow cytometry (BD FACSAria, USA) was applied to analyze the cells after cells. FlowJo (BD) was applied to quantify the data.

2.20. Histological Examination. KCl (10%) was applied to arrest the tissues, and a Canon camera (Tokyo) was applied to capture the images of tissues. Hematoxylin and eosin (H&E) were applied to stain the sections (4 μm). The cross section was measured at the nucleus level in sectioned myocytes (longitudinally). A microscope (Olympus, Japan) was used to obtain the images. Image-Pro (Plus 6.0, NIH, USA) was applied to analyze the data.

2.21. Statistical Analysis. Data analysis was applied by using SPSS v18.0 (USA). Means ± SEM was applied to express the data. ANOVA (followed by the Tukey–Kramer post hoc test) was applied to compare the differences among experimental groups. $p < 0.05$ indicated significant changes.

3. Results

3.1. The Active Ingredient-BCRD-Target Network. A total of 156 targets were obtained through a comprehensive analysis of the active ingredients of the Xiaoyao Kangai Jieyu Formula, breast cancer, and depression (Figure 1(a)). We constructed

Table 2: Cluster analysis based on Molecular Complex Detection.

Cluster	Network	Nodes	Edges	Node IDs
1	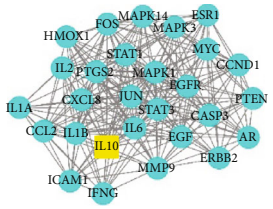	28	254	FOS, STAT1, CXCL8, STAT3, ICAM1, IL1A, IL1B, MYC, AR, CCL2, HMOX1, ERBB2, IFNG, MAPK3, EGF, MMP9, PTEN, JUN, MAPK14, CCND1, IL2, MAPK1, EGFR, IL10, ESR1, IL6, CASP3, PTGS2
2	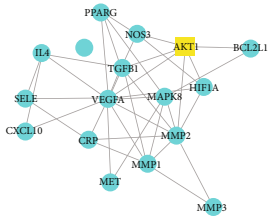	16	39	SELE, MET, PPARG, BCL2L1, CXCL10, IL4, NOS3, VEGFA, CRP, TGFB1, HIF1A, MAPK8, MMP2, MMP1, MMP3, AKT1
3	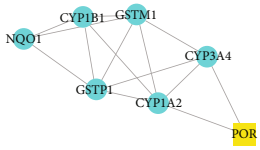	7	14	GSTP1, CYP3A4, CYP1B1, CYP1A2, NQO1, POR, GSTM1
4	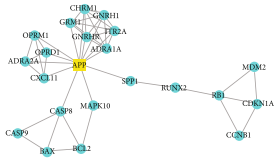	22	47	RUNX2, APP, CXCL11, OPRD1, BAX, ADRA2A, HTR2A, GRM1, CHRM1, RB1, CASP8, GNRH1, CDKN1A, MAPK10, GNRHR, BCL2, ADRA1A, CASP9, SPP1, MDM2, CCNB1, OPRM1

PPI networks for these 156 target genes (Figure 1(b)). Genes with a degree score greater than the average score were selected as key targets, and a total of 53 key targets were screened out. The top 20 targets are shown in Figure 1(c).

Core genes were screened by MCODE analysis. Four gene clusters and four core genes were obtained: APP, AKT1, IL10 and POR, respectively (Table 2).

Based on the included active ingredients, BCRD, and targets, the active ingredient-disease-target network was constructed (Supplementary Figure 1).

3.2. GO and KEGG Enrichment Analysis. Next, GO analysis showed that the active components of the compound were mainly involved in response to lipopolysaccharide, response to drug, and response to molecule of bacterial origin (Figure 2(a)). In addition, KEGG analysis showed that the active components of the compound were related to the following pathways: AGE-RAGE signaling pathway in diabetic complication, lipid and atherosclerosis, and fluid shear stress and atherosclerosis (Figure 2(b)). We constructed a PPI network based on the potential targets and pathways of the Xiaoyao Kangai Jieyu Formula's active components in BCRD (Figure 2(c)). Furthermore, according to the degree of the active ingredient, we found that quercetin is the most important ingredient in the Xiaoyao Kangai Jieyu Formula (Supplementary Table 2).

3.3. The Occurrence of BCRD Induced the Pyroptosis of Neurons. To mimic BCRD *in vitro*, neurons were exposed to the supernatants of LPS-treated 4T1 cells. In Figures 3(a) and 3(b), the number of pyroptotic cells was markedly elevated in BCRD. Meanwhile, the levels of ASC, NLRP3, and caspase-1 in neurons were obviously upregulated in BCRD (Figures 3(c)–3(f)).

3.4. Quercetin Significantly Reversed BCRD-Induced Cell Pyroptosis. Since quercetin was identified as the key constituent of the Xiaoyao Kangai Jieyu Formula, the following analysis was applied to analyze the impact of quercetin on BCRD progression. The data confirmed that the viability of neurons was significantly decreased by the supernatants of LPS-treated 4T1 cells, which was significantly reversed by Pac+Flu or quercetin (Figure 4(a)). Consistently, the supernatants of LPS-treated 4T1 cells markedly upregulated ASC, NLRP3, and caspase-1 levels in neurons, while this phenomenon was partially restored by Pac+Flu or quercetin (Figures 4(b)–4(e)). Meanwhile, Pac+Flu or quercetin obviously reversed the effect of supernatants of LPS-treated 4T1 cells on cell pyroptosis (Figure 4(f)).

3.5. Quercetin Alleviated Neuron Injury and Depressive Behavior in BCRD Mice. To assess the function of quercetin in BCRD *in vivo*, an *in vivo* model of BCRD was constructed. As demonstrated in Figures 5(a)–5(c), the symptom of depression in mice was significantly decreased in BCRD and depression, which was markedly reversed by quercetin or Pac+Flu. In addition, BCRD and depression notably upregulated ASC, NLRP3, and caspase-1 levels in mice,

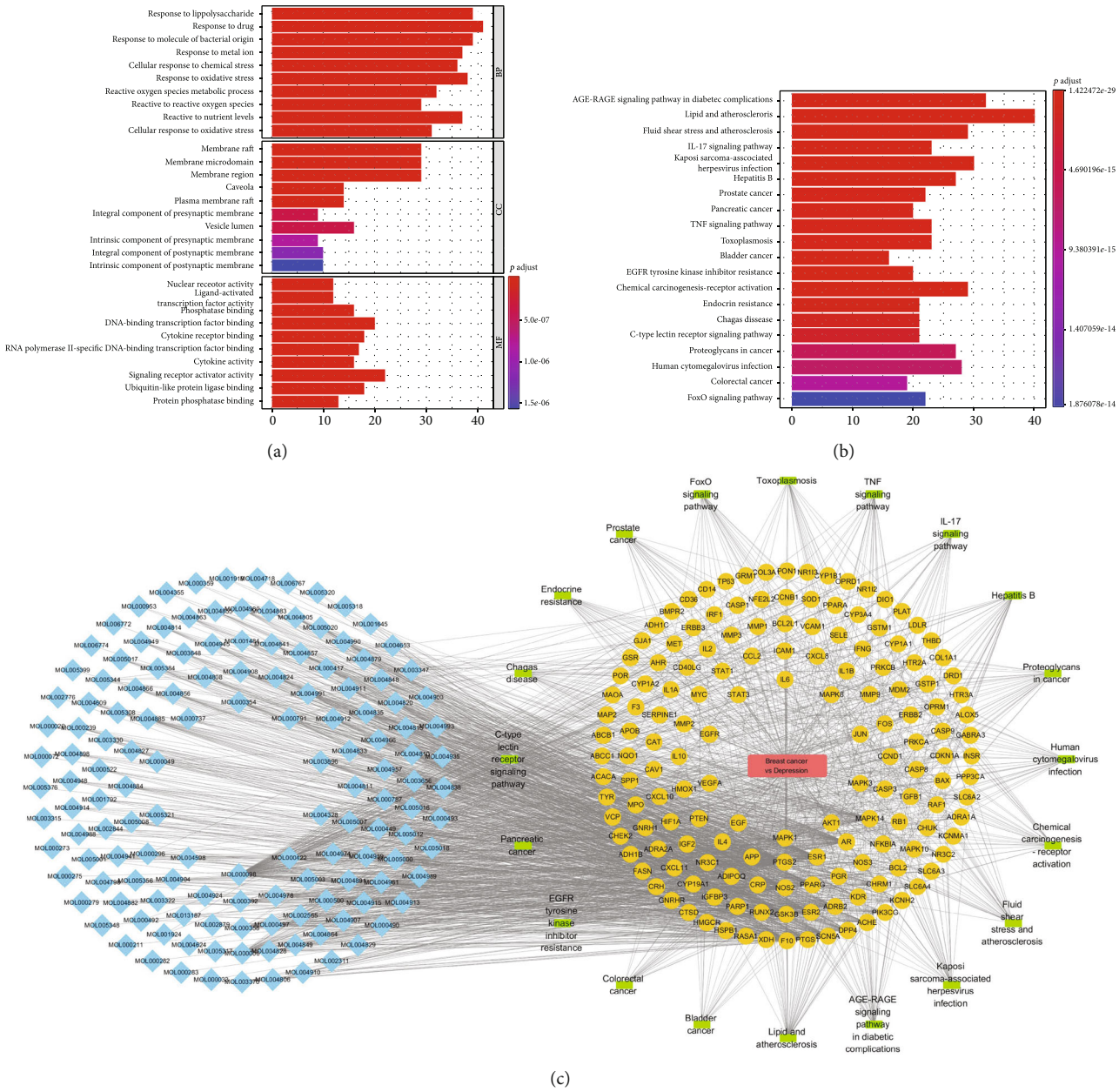

Figure 2: The GO data of enrichment and KEGG analysis. (a) GO analysis was performed to investigate the cellular biological process. (b) KEGG analysis was performed to investigate the most enriched pathways. (c) The network of constituents-diseases-pathways-targets.

while quercetin or Pac+Flu partially rescued this phenomenon (Figures 5(d)–5(j)). Furthermore, the contents of 5-HT, DA, and NE in mice were much higher in the BCRD and depression group, which was rescued in the presence of quercetin or Pac+Flu (Figures 5(k)–5(m)).

3.6. Quercetin Promoted an Antitumor Immune Response in BCRD Mice. A xenograft mouse model was constructed to assess the effect of quercetin on immune response in BCRD mice. The result indicated that BCRD further increased the tumor sizes and weight in breast cancer mice, while this phenomenon was notably revised by quercetin or Pac+Flu (Figures 6(a)–6(c)). In addition, BCRD significantly induced the injury in tissues, and the effect of BCRD was significantly inhibited in the presence of quercetin or Pac+Flu (Figure 6(d)). Meanwhile, the content of CA153 in BCRD mice was markedly inhibited by Pac+Flu or quercetin (Figure 6(e)), and BCRD-induced decrease in CD4+ and CD8+ was also restored by quercetin or Pac+Flu (Supplementary Figure 2, Figures 6(f) and 6(g)). Furthermore, BCRD greatly reduced IFN-γ and IL-2 levels and increased IL-10 in mice, which was notably rescued by quercetin or Pac+Flu (Figures 6(h)–6(j)).

3.7. Quercetin Partially Reversed Serum Metabolism in BCRD Mice. As revealed in Figures 7(a)–7(c), the metabolites in different experimental groups were divided into different clusters. The volcano plot showed that 115 metabolites

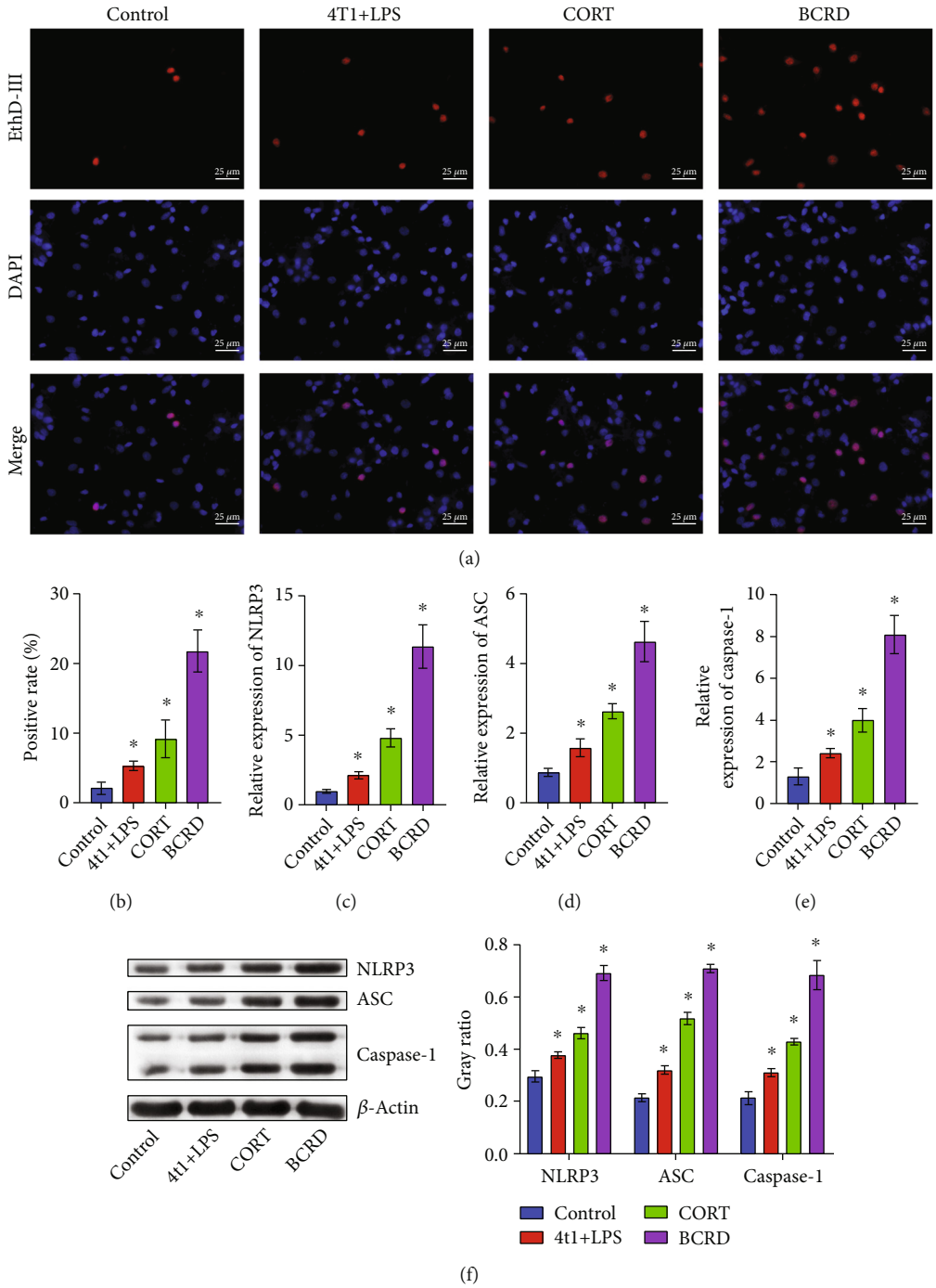

Figure 3: The occurrence of BCRD induced the pyroptosis of neurons. Neurons were treated with LPS+4T1, LPS+4T1+BCRD, or LPS+4T1 +CORD. (a, b) EthD-III staining was used to observe the membrane pores of neurons. (c–e) Caspase-1, ASC, and NLRP3 levels in neurons were assessed by RT-qPCR. (f) ASC, caspase-1, and NLRP3 levels in neurons were investigated by western blot. β-Actin was applied for quantification. $^{*}p < 0.05$ compared with control.

varied significantly among the three groups (Figure 7(d)). We noticed that quercetin effectively reversed the levels of certain metabolites in BCRD, such as argininosuccinic acid, L-asparagine, gamma-aminobutyric acid, succinic acid, and uracil (Supplementary Figure 3). KEGG analysis showed that these differential metabolites were mainly enriched in arginine biosynthesis, alanine, aspartate and glutamate metabolism, and D-glutamine and D-glutamate metabolism (Figure 7(e)).

4. Discussion

BCRD seriously impairs the quality of life of patients. It was reported that traditional Chinese medicine could inhibit

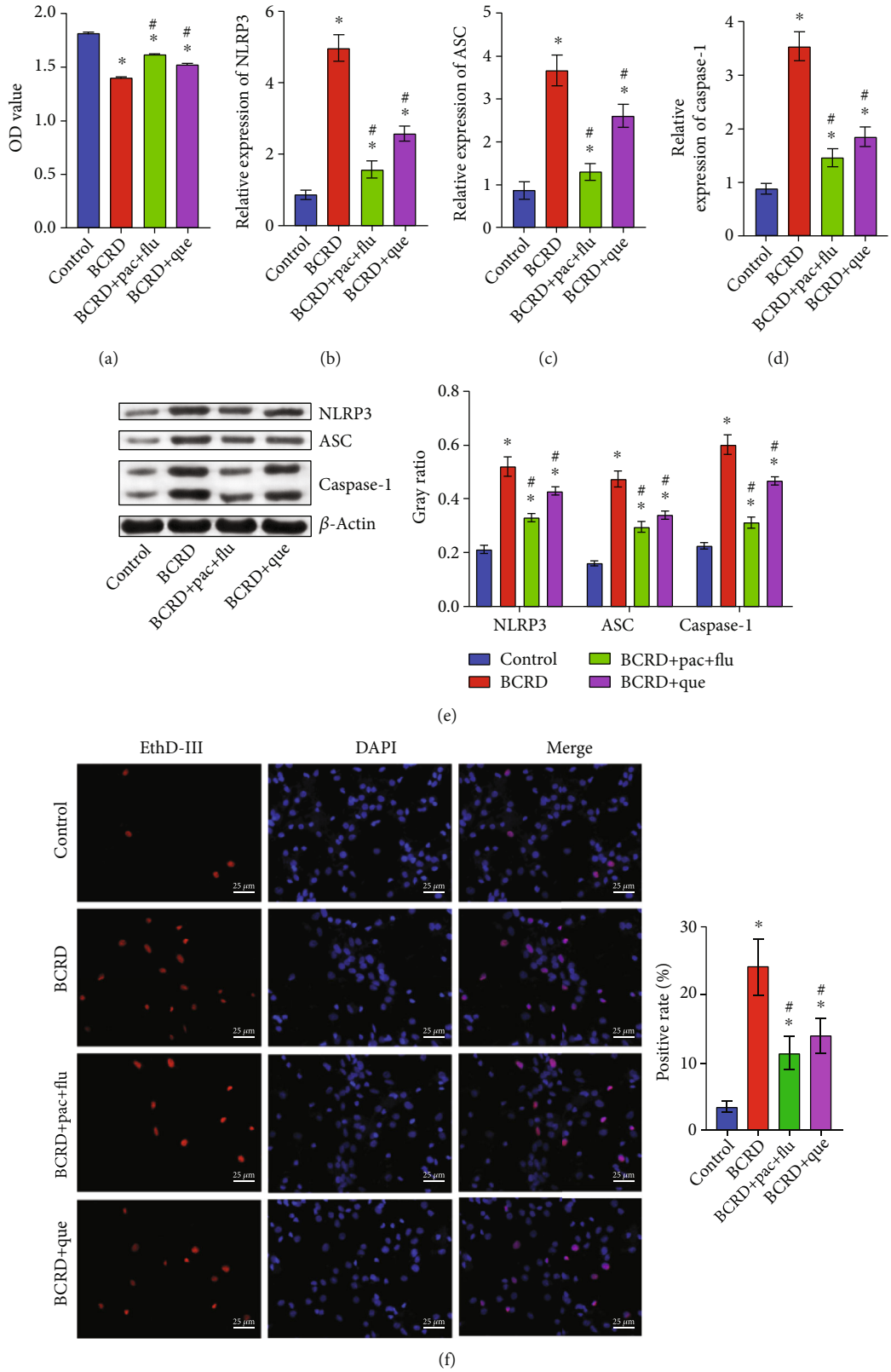

Figure 4: Quercetin significantly reversed BCRD-induced cell pyroptosis. Neurons were divided into BCRD, BCRD+quercetin, or BCRD +Pac+Flu. (a) The viability of neurons was assessed by the CCK8 assay. (b–d) The levels of NLRP3, ASC, and caspase-1 in neurons were investigated by RT-qPCR. (e) ASC, NLRP3, and caspase-1 levels in neurons were investigated by western blot. β-Actin was applied for quantification. (f) The pyroptosis of hippocampal neurons was evaluated by EthD-III staining $^{*}p < 0.05$ compared with control. $^{\#}p < 0.05$ compared with BCRD.

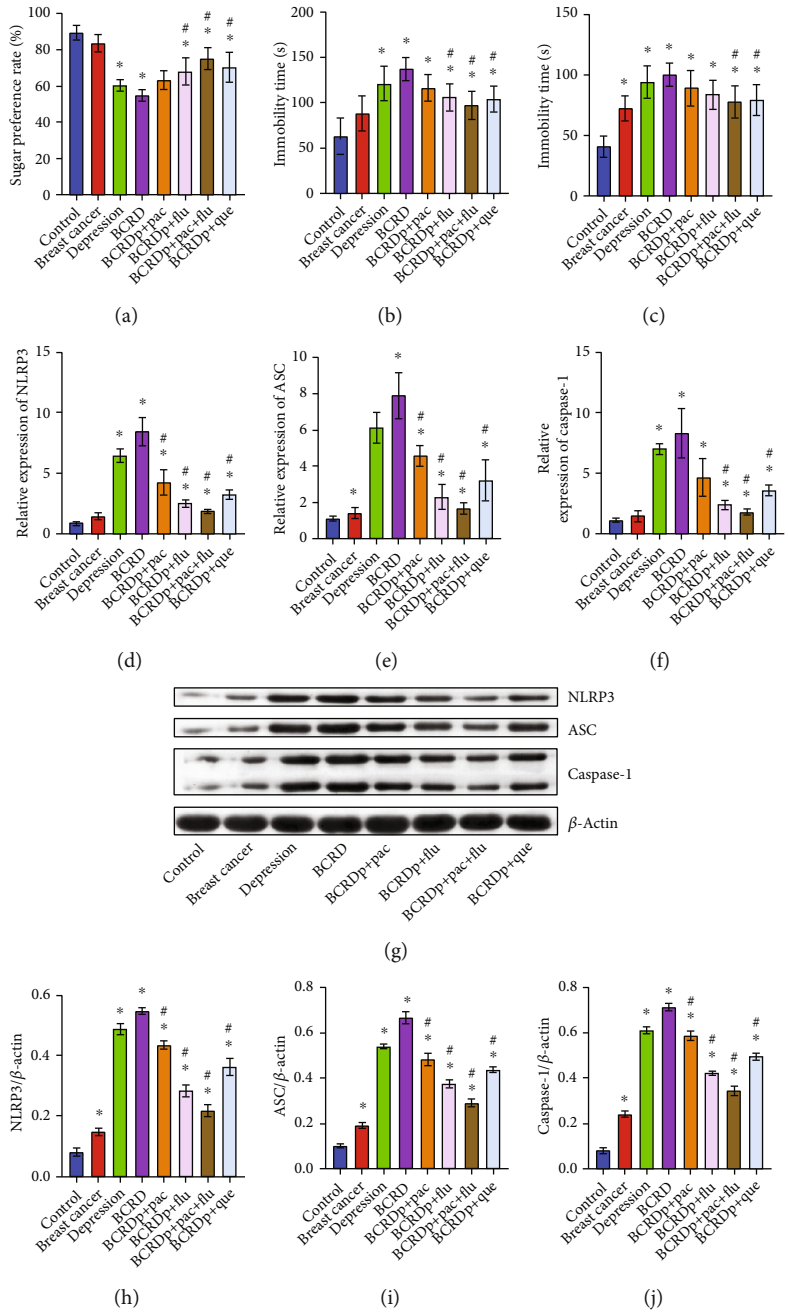

Figure 5: Continued.

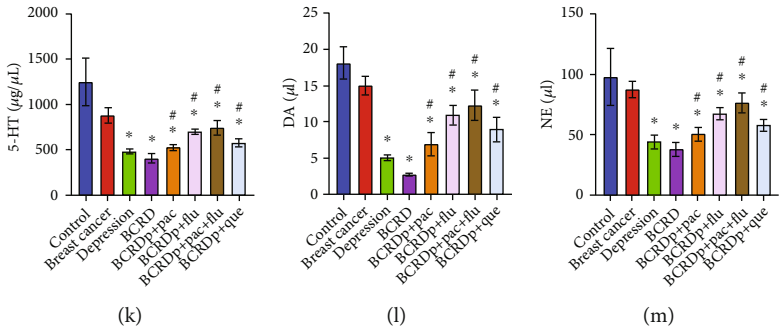

Figure 5: Quercetin alleviated neuron injury and depressive behavior in BCRD mice. (a) The sugar preference rate of mice was detected. (b) The immobility time was recorded after the forced swimming test. (c) The immobility time was recorded after the tail suspension test. (d–f) ASC, NLRP3, and caspase-1 levels in neurons were assessed by RT-qPCR. (g–j) NLRP3, ASC, and caspase-1 levels in neurons were investigated by western blot. β-Actin was applied for quantification. (k–m) The contents of 5-HT, DA, and NE in mice were detected by ELISA. $^{*}p < 0.05$ compared with control. $^{\#}p < 0.05$ compared with BCRD ($n = 6$).

cancer and depression development [7, 19]. However, the function of traditional Chinese medicine in BCRD needs to be further analyzed. In this research, the Xiaoyao Kangai Jieyu Formula could inhibit the progression of BCRD. In addition, quercetin was identified as the key active constituent of the Xiaoyao Kangai Jieyu Formula. Additionally, this work found the association between quercetin and serum metabolism in BCRD. Thus, we explored the function of quercetin, the active ingredient of Xiaoyao Kangai Jieyu Formula, in BCRD. Our findings suggest that quercetin may be used as a new agent for BCRD treatment.

This study assessed the mechanisms of the Xiaoyao Kangai Jieyu Formula on BCRD, and downstream proteins and the active constituents were predicted. The Xiaoyao Kangai Jieyu Formula active constituent-target network revealed the pharmacological foundation of the Xiaoyao Kangai Jieyu Formula. The targets and active constituents were hypothesized in this section. Flavonoids are the main active constituents of the Xiaoyao Kangai Jieyu Formula. Moreover, quercetin is known to be a polyphenolic flavonoid that has antitumor activity, and it exerts in the source of vegetal food and multiple traditional Chinese medicines [20, 21]. In vivo and in vitro study accumulation has paid attention to the chemopreventive activity and mechanisms underlying the function of quercetin BCRD.

Meanwhile, quercetin has multiple biological activities. For example, quercetin attenuates LPS-induced depression-like behavior and learning memory impairment in rats, which may be related to its modulation in the imbalance of hippocampal Copine 6 and TREM1/2 expression associated with brain-derived neurotrophic factor [22]. Quercetin could inhibit the behavior of chronic unpredictable mild stress-induced depression through involving nuclear factor-E2-related factor 2 [23]. Numerous studies have indicated that quercetin plays a therapeutic role in a variety of cancers. For example, quercetin inhibits cervical cancer cell invasion by reducing UBE2S expression in cervical cancer [24]. Quercetin targets specific signaling pathways, which is considered a promising component for treating glioblastoma multiforme [25]. Besides, quercetin has also been shown to have positive anticancer effects in ovarian cancer [26]. These studies suggest that quercetin is a prospective candidate in the treatment of both depression and cancer.

Recent studies indicated that pyroptosis plays a crucial role in the cellular process [27, 28]. Caspase-1, NLRP3, and ASC are known to be the important modulators in cell pyroptosis [29, 30]. Meanwhile, IL-1β is also a pyroptosis-related cytokine [31, 32]. Caspase-1 was often upregulated during the onset of neuronal injury, suggesting that the promotion of pyroptosis might be associated with neuronal injury [33, 34]. Our study revealed that quercetin could reverse the neuron pyroptosis via upregulating cleaved caspase-1, NLRP3, and ASC. Isoglycyrrhizin, a flavonoid similar to quercetin, has recently been demonstrated to improve depression by inhibiting NLRP3-mediated cellular pyroptosis via the miRNA-27a/SYK/NF-κB axis [35]. In this work, we firstly found the correlation between quercetin and pyroptosis in BCRD, suggesting that quercetin reversed the neuron injury during the progression of BCRD through promoting pyroptosis.

It has been reported that disruption to metabolism could lead to the progression of depression [36]. This study found that argininosuccinic acid, L-asparagine, gamma-aminobutyric acid, succinic acid, and uracil could be inhibited by quercetin in BCRD mice. L-Asparagine was known to be the key marker in cardiovascular diseases [37]. An excessive increase in gamma-aminobutyric acid could cause metabolic disorders, which further resulted in the development of diabetes [38]. Succinic acid played a key role in the chronic diseases of the elder people [39], and uracil was the key marker in the metabolic cycle [40]. Thus, our finding revealed that the progression of BCRD might be closely correlated with the metabolic disorder, and quercetin has been shown to partially regulate the abnormalities of relevant metabolites in BCRD.

There are some limitations in this work as follows: (1) the mechanisms by which quercetin regulates the progression of BCRD remain unclear and (2) the relation between quercetin and serum metabolism-related signaling is needed to be analyzed. Hence, more analysis is essential in the future.

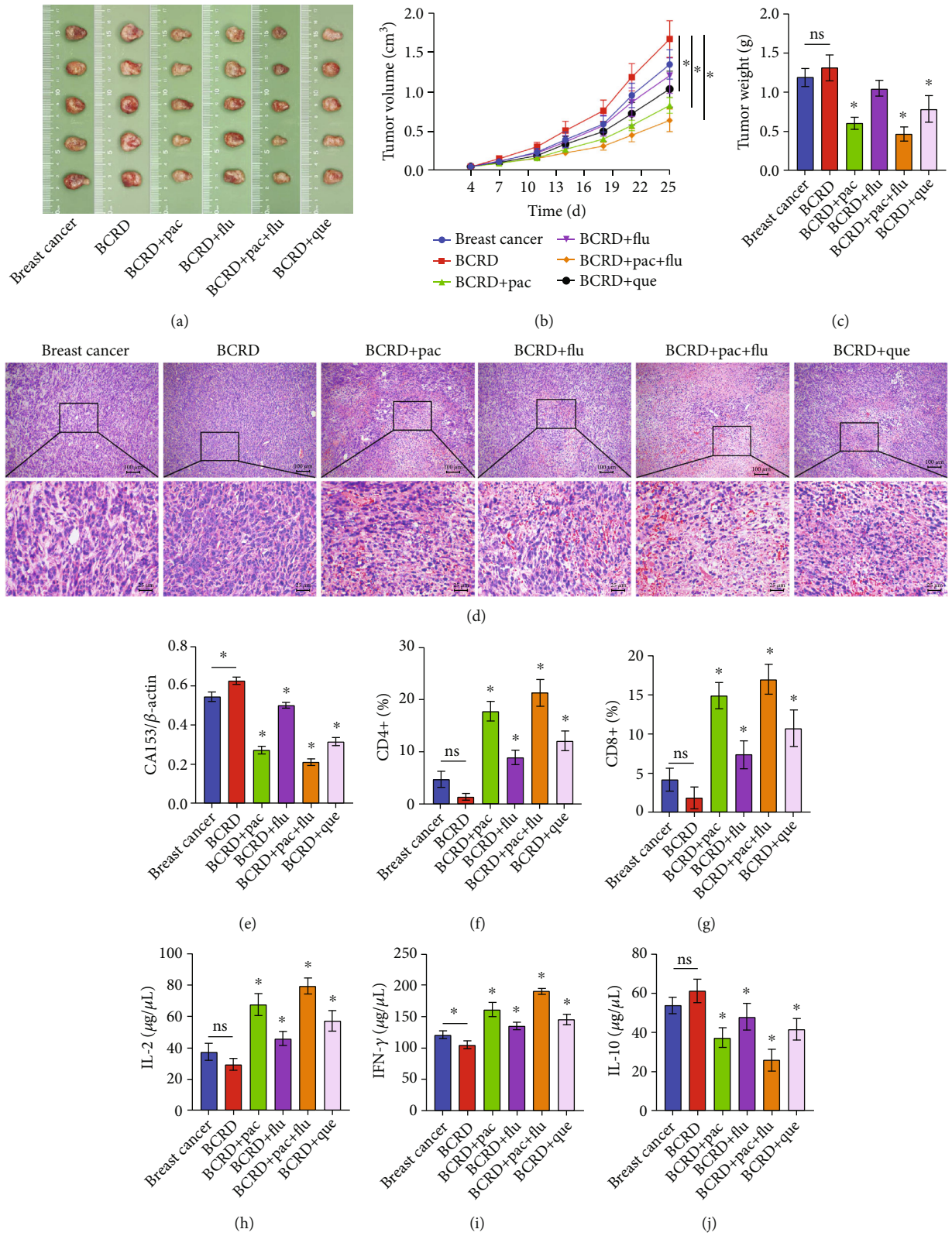

Figure 6: Quercetin promoted an anti-tumor immune response in BCRD mice. (a) The tumor tissues of mice were collected. (b) The tumor volume was calculated. (c) The tumor weight was recorded. (d) The histological change in mice was detected by H&E staining. (e) The expression of CA153 was assessed. (f, g) The ratio of CD4+ and CD8+ in mice was assessed by flow cytometry. (h–j) IL-2, IFN-γ, and IL-10 levels in mice were investigated by ELISA. $^{*}p < 0.05$ compared with breast cancer ($n = 6$).

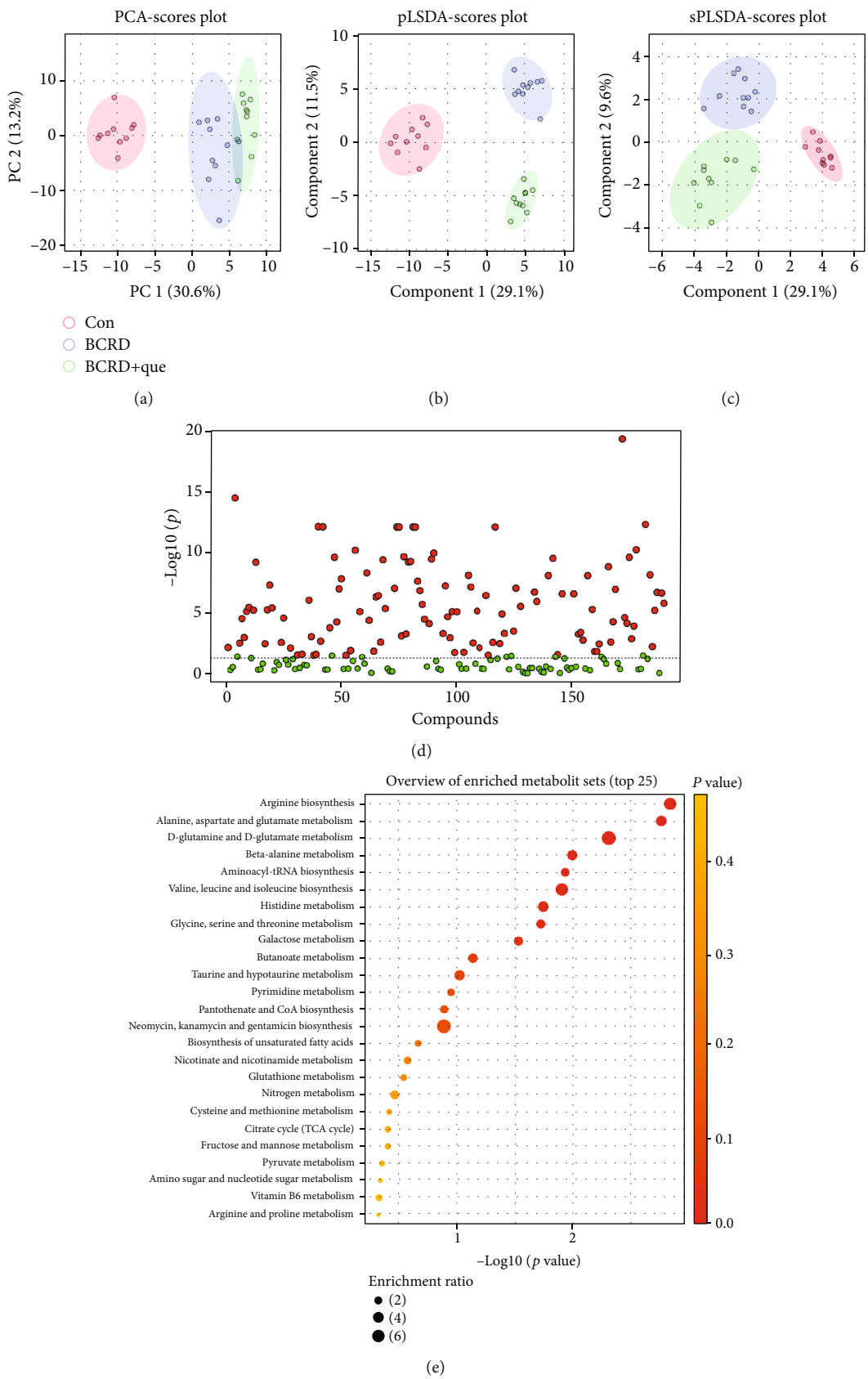

Figure 7: Quercetin might promote the antitumor immune response in BCRD mice via regulation of serum metabolism. (a) Principal component analysis. (b) Partial least squares discriminant analysis (PLS-DA). (c) Sparse partial least squares discriminant analysis (SPLS-DA). (d) Differential metabolites are represented by a volcano plot. (e) KEGG pathway enrichment analysis of differential metabolites.

5. Conclusions

To sum up, quercetin, the active ingredient of the Xiaoyao Kangai Jieyu Formula, effectively mitigated the progression of BCRD by inhibiting pyroptosis, promoting immune response, and improving serum metabolism.

Data Availability

The data used to support the findings of this study are available from the corresponding author upon request.

Conflicts of Interest

There was no competing interest to declare.

Authors' Contributions

Qing Zhu contributed to conceptualization, investigation, methodology, and visualization and wrote the original draft. Lei Yang and Hui Yang contributed to formal analysis, investigation, and validation and wrote the original draft. Yuanshan Han contributed to conceptualization, performed the research, and analyzed the data. Yun Chen and Ying He were responsible for data curation, funding acquisition, project administration, and supervision and reviewed and edited the paper. All authors contributed to the article and approved the submitted version.

Acknowledgments

This study was funded by the National Natural Science Foundation of China (82104846), supported by the Hunan Provincial Natural Science Foundation of China (2019JJ80021), supported by the Scientific Research Project of Hunan Provincial Health Commission (202103101959), and supported by the Science and Technology Innovation Program of Hunan Province (Grant No. 2019SK20321).

Supplementary Materials

Supplementary 1. Supplementary Table 2: the information of key ingredients.

Supplementary 2. Supplementary Figure 1: the network of active ingredient-disease-target.

Supplementary 3. Supplementary Figure 2: CD4+ and CD8+ ratios in mice.

Supplementary 4. Supplementary Figure 3: the heat map of differential metabolites in plasma of mice.

Supplementary 5. Supplementary Figure 4: primary mouse neuronal cell identification. (A) Representative image of primary mouse cortical neurons. (B) IF for identification of primary neurons.

References

[1] X. Luo, Y. Chen, J. Chen et al., "Effectiveness of mobile health-based self-management interventions in breast cancer patients: a meta-analysis," *Supportive Care in Cancer*, vol. 30, no. 3, pp. 2853–2876, 2022.

[2] T. Brown, S. Cruickshank, and M. Noblet, "Specialist breast care nurses for support of women with breast cancer," *Cochrane Database of Systematic Reviews*, vol. 2021, no. 2, p. CD005634, 2021.

[3] S. H. Kim, Y. H. Choe, Y. U. Cho, S. Park, and M. H. Lee, "Effects of a partnership-based, needs-tailored self-management support intervention for post-treatment breast cancer survivors: a randomized controlled trial," *Psycho-Oncology*, 2021.

[4] D. Grujic, C. Giurgi-Oncu, C. Oprean et al., "Well-being, depression, and anxiety following oncoplastic breast conserving surgery versus modified radical mastectomy followed by late breast reconstruction," *International Journal of Environmental Research and Public Health*, vol. 18, no. 17, p. 9320, 2021.

[5] R. B. Semwal, D. K. Semwal, S. Combrinck, and A. Viljoen, "Emodin - a natural anthraquinone derivative with diverse pharmacological activities," *Phytochemistry*, vol. 190, p. 112854, 2021.

[6] A. A. Abdellatef, M. Fathy, A. E. I. Mohammed et al., "Inhibition of cell-intrinsic NF-κB activity and metastatic abilities of breast cancer by aloe-emodin and emodic-acid isolated from Asphodelus microcarpus," *Journal of Natural Medicines*, vol. 75, no. 4, pp. 840–853, 2021.

[7] Z. Li, H. Xu, Y. Xu et al., "Morinda officinalis oligosaccharides alleviate depressive-like behaviors in post-stroke rats via suppressing NLRP3 inflammasome to inhibit hippocampal inflammation," *CNS Neuroscience & Therapeutics*, vol. 27, no. 12, pp. 1570–1586, 2021.

[8] M. S. Wu, X. J. Li, C. Y. Liu et al., "Effects of histone modification in major depressive disorder," *Current Neuropharmacology*, vol. 19, 2021.

[9] P. Meng, Y. Han, Q. Yang et al., "Xiaoyao Kangai Jieyu Fang, a Chinese herbal formulation, ameliorates cancer-related depression concurrent with breast cancer in mice via promoting hippocampal synaptic plasticity," *Evidence-based Complementary and Alternative Medicine*, vol. 2018, 11 pages, 2018.

[10] S. E. Sephton, F. S. Dhabhar, A. S. Keuroghlian et al., "Depression, cortisol, and suppressed cell-mediated immunity in metastatic breast cancer," *Brain, Behavior, and Immunity*, vol. 23, no. 8, pp. 1148–1155, 2009.

[11] A. M. Casaril, M. Domingues, S. R. Bampi et al., "The antioxidant and immunomodulatory compound 3-[(4-chlorophenyl)selanyl]-1-methyl-1H-indole attenuates depression-like behavior and cognitive impairment developed in a mouse model of breast tumor," *Brain, Behavior, and Immunity*, vol. 84, pp. 229–241, 2020.

[12] Y. Takeuchi, D. Ohara, H. Watanabe et al., "Dispensable roles of Gsdmd and Ripk3 in sustaining IL-1β production and chronic inflammation in Th17-mediated autoimmune arthritis," *Scientific Reports*, vol. 11, no. 1, p. 18679, 2021.

[13] L. Gao and Q. Li, "Identification of novel pyroptosis-related lncRNAs associated with the prognosis of breast cancer through interactive analysis," *Cancer Management and Research*, vol. Volume 13, pp. 7175–7186, 2021.

[14] J. Ru, P. Li, J. Wang et al., "TCMSP: a database of systems pharmacology for drug discovery from herbal medicines," *Journal of Cheminformatics*, vol. 6, no. 1, p. 13, 2014.

[15] M. G. Nashed, E. P. Seidlitz, B. N. Frey, and G. Singh, "Depressive-like behaviours and decreased dendritic branching in the

medial prefrontal cortex of mice with tumors: a novel validated model of cancer- induced depression," *Behavioural Brain Research*, vol. 294, pp. 25–35, 2015.

[16] W. Luo, Y. Han, P. Meng et al., "Resatorvid relieves breast cancer complicated with depression by inactivating hippocampal microglia through TLR4/NF-κB/NLRP3 signaling pathway," *Cancer Management and Research*, vol. Volume 12, pp. 13003–13014, 2020.

[17] Y. Zhang, L. Ren, S. Min, F. Lv, and J. Yu, "Effects of N-methyl-D-aspartate receptor (NMDAR) and Ca2+/ calmodulin-dependent protein kinase IIα (CaMKIIα) on learning and memory impairment in depressed rats with different charge by modified electroconvulsive shock," *Ann Transl Med.*, vol. 9, no. 16, p. 1320, 2021.

[18] A. H. Moghaddam, K. Maboudi, B. Bavaghar, S. R. M. Sangdehi, and M. Zare, "Neuroprotective effects of curcumin-loaded nanophytosome on ketamine-induced schizophrenia-like behaviors and oxidative damage in male mice," *Neuroscience Letters*, vol. 765, p. 136249, 2021.

[19] S. Chen, F. Chen, N. Amin et al., "Defects of parvalbumin-positive interneurons in the ventral dentate gyrus region are implicated depression-like behavior in mice," *Brain, Behavior, and Immunity*, vol. 99, pp. 27–42, 2022.

[20] S. Bhandarkar, B. Prabhakar, and P. Shende, "Quercetin-loaded platelets as a potential targeted therapy for glioblastoma Multiforme cell line U373-MG," *Biotechnology Journal*, vol. 16, no. 12, p. e2100271, 2021.

[21] L. Jing, J. Lin, Y. Yang et al., "Quercetin inhibiting the PD-1/PD-L1 interaction for immune-enhancing cancer chemopreventive agent," *Phytotherapy Research*, vol. 35, no. 11, pp. 6441–6451, 2021.

[22] K. Fang, H.-R. Li, X.-X. Chen et al., "Quercetin alleviates LPS-induced depression-like behavior in rats via regulating BDNF-related imbalance of Copine 6 and TREM1/2 in the hippocampus and PFC," *Frontiers in Pharmacology*, vol. 10, p. 1544, 2020.

[23] Y. Guan, J. Wang, X. Wu et al., "Quercetin reverses chronic unpredictable mild stress-induced depression-like behavior *in vivo* by involving nuclear factor-E2-related factor 2," *Brain Research*, vol. 1772, p. 147661, 2021.

[24] T. H. Lin, W. H. Hsu, P. H. Tsai et al., "Dietary flavonoids, luteolin and quercetin, inhibit invasion of cervical cancer by reduction of UBE2S through epithelial-mesenchymal transition signaling," *Food & Function*, vol. 8, no. 4, pp. 1558–1568, 2017.

[25] E. Tavana, H. Mollazadeh, E. Mohtashami et al., "Quercetin: a promising phytochemical for the treatment of glioblastoma multiforme," *BioFactors*, vol. 46, no. 3, pp. 356–366, 2020.

[26] A. Vafadar, Z. Shabaninejad, A. Movahedpour et al., "Quercetin and cancer: new insights into its therapeutic effects on ovarian cancer cells," *Cell & Bioscience*, vol. 10, no. 1, p. 32, 2020.

[27] J. Hou, J. M. Hsu, and M. C. Hung, "Molecular mechanisms and functions of pyroptosis in inflammation and antitumor immunity," *Molecular Cell*, vol. 81, no. 22, pp. 4579–4590, 2021.

[28] B. Zhao, Y. Fei, J. Zhu, Q. Yin, W. Fang, and Y. Li, "PAF receptor inhibition attenuates neuronal pyroptosis in cerebral ischemia/reperfusion injury," *Molecular Neurobiology*, vol. 58, no. 12, pp. 6520–6539, 2021.

[29] Z. Shen, H. Zhou, A. Li et al., "Metformin inhibits hepatocellular carcinoma development by inducing apoptosis and pyroptosis through regulating FOXO3," *Aging*, vol. 13, no. 18, pp. 22120–22133, 2021.

[30] L. Wang, X. F. Jiao, C. Wu et al., "Trimetazidine attenuates dexamethasone-induced muscle atrophy via inhibiting NLRP3/GSDMD pathway-mediated pyroptosis," *Cell death discovery*, vol. 7, no. 1, p. 251, 2021.

[31] A. Dominic, N. T. Le, and M. Takahashi, "Loop between NLRP3 inflammasome and reactive oxygen species," *Antioxidants & Redox Signaling*, 2022.

[32] A. Al Mamun, A. Ara Mimi, Y. Wu et al., "Pyroptosis in diabetic nephropathy," *Clinica Chimica Acta*, vol. 523, pp. 131–143, 2021.

[33] Y. Zhao, Z. Li, E. Lu, Q. Sheng, and Y. Zhao, "Berberine exerts neuroprotective activities against cerebral ischemia/reperfusion injury through up-regulating PPAR-γ to suppress NF-κB-mediated pyroptosis," *Brain Research Bulletin*, vol. 177, pp. 22–30, 2021.

[34] Z. Lyu, Y. Chan, Q. Li et al., "Destructive effects of pyroptosis on homeostasis of neuron survival associated with the dysfunctional BBB-glymphatic system and amyloid-beta accumulation after cerebral ischemia/reperfusion in rats," *Neural Plasticity*, vol. 2021, Article ID 4504363, 11 pages, 2021.

[35] Y. Li, W. Song, Y. Tong et al., "Isoliquiritin ameliorates depression by suppressing NLRP3-mediated pyroptosis via miRNA-27a/SYK/NF-κB axis," *Journal of Neuroinflammation*, vol. 18, no. 1, pp. 1–23, 2021.

[36] M. V. Knott, L. B. Ngwenya, E. A. Correll et al., "Lack of glutamate receptor subunit expression changes in hippocampal dentate gyrus after experimental traumatic brain injury in a rodent model of depression," *International Journal of Molecular Sciences*, vol. 22, no. 15, p. 8086, 2021.

[37] A. Mehta, C. Liu, A. Nayak et al., "Untargeted high-resolution plasma metabolomic profiling predicts outcomes in patients with coronary artery disease," *PLoS One*, vol. 15, no. 8, p. e0237579, 2020.

[38] Y. W. Park, D. K. Deelchand, J. M. Joers et al., "Monitoring the neurotransmitter response to glycemic changes using an advanced magnetic resonance spectroscopy protocol at 7T," *Frontiers in Neurology*, vol. 12, p. 698675, 2021.

[39] R. Frizzo, E. Bortoletto, T. Riello et al., "NMR metabolite profiles of the bivalve Mollusc Mytilus galloprovincialis before and after immune stimulation with Vibrio splendidus," *Frontiers in Molecular Biosciences*, vol. 8, p. 686770, 2021.

[40] Q. Li, X. Deng, N. Jiang et al., "Identification and structure-activity relationship exploration of uracil-based benzoic acid and ester derivatives as novel dipeptidyl peptidase-4 inhibitors for the treatment of type 2 diabetes mellitus," *European Journal of Medicinal Chemistry*, vol. 225, p. 113765, 2021.

Hindawi
Mediators of Inflammation
Volume 2022, Article ID 2567150, 18 pages
https://doi.org/10.1155/2022/2567150

Research Article

Curcumin Targeting NF-κB/Ubiquitin-Proteasome-System Axis Ameliorates Muscle Atrophy in Triple-Negative Breast Cancer Cachexia Mice

Jin Zhang,[1,2] Jin Zheng,[3] Haitao Chen,[4] Xinrong Li,[1] Chenxiao Ye,[1] Fan Zhang,[1] Zewei Zhang,[5] Qinghua Yao,[4,6] and Yong Guo[7]

[1]*The First Clinical Medical College, Zhejiang Chinese Medical University, Hangzhou 310053, China*
[2]*Department of Oncology, Hospital Affiliated to Shaanxi University of Chinese Medicine, Xianyang 712000, China*
[3]*Department of Traditional Chinese Medicine, The Second Hospital Affiliated to Air Force Medical University, Xi'an 710038, China*
[4]*Department of Integrated Traditional Chinese and Western Medicine, Cancer Hospital of the University of Chinese Academy of Sciences/Zhejiang Cancer Hospital, Hangzhou 310022, China*
[5]*Department of Hepatopancreatobiliary Surgery, Cancer Hospital of the University of Chinese Academy of Sciences/Zhejiang Cancer Hospital, Hangzhou 310022, China*
[6]*Key Laboratory of Traditional Chinese Medicine Oncology, Zhejiang Cancer Hospital, Hangzhou 310022, China*
[7]*Department of Oncology, The First Affiliated Hospital of Zhejiang Chinese Medical University, Hangzhou 310003, China*

Correspondence should be addressed to Qinghua Yao; yaoqh@zjcc.org.cn and Yong Guo; guoyong1047@zcmu.edu.cn

Jin Zhang, Jin Zheng, and Haitao Chen contributed equally to this work.

Received 27 September 2021; Revised 22 November 2021; Accepted 8 December 2021; Published 29 January 2022

Academic Editor: Xiaolu Jin

Background. Curcumin is a polyphenol plant-derived compound with anti-inflammatory, antioxidant stress, and anticancer properties that make it have the potential to treat cancer cachexia. However, the role of it in breast cancer cachexia remains unclear. *Methods*. The 4T1 cells were subcutaneously injected into BALB/c mice to induce breast cancer cachexia. After tumor formation, the animals were divided into groups and given curcumin or saline interventions. The therapeutic effect of curcumin on breast cancer cachexia was characterized by tumor growth, changes in body mass and gastrocnemius mass, muscle function test, histopathology, and serum nutrition indexes. Mitochondrial function in muscle tissue was observed by transmission electron microscopy and ATP detection, muscle inflammatory factors were detected by ELISA, muscle differential metabolites were detected by ^{1}HNMR metabolomics, and the muscle tissue ubiquitination levels and NF-KB expression were also analyzed by RT-qPCR and Western blot. *Results*. Dynamic *in vivo* bioluminescence imaging find that curcumin inhibited the growth of tumor in triple-negative breast cancer- (TNBC-) bearing mice, slowed down the loss of body weight and gastrocnemius weight, corrected the mitochondrial dysfunction and malnutrition status, and also significantly improved skeletal muscle function. ELISA analysis found that the level of inflammatory factors in muscle tissue was reduced. ^{1}HNMR metabolomics analysis suggested that curcumin could regulate energy metabolism pathways. RT-qPCR and Western blot analysis found that the expression of myogenic factor myogenin was increased and the expression of myodegradation factor myostatin was decreased in the gastrocnemius; the level of ubiquitination and activation of the NF-κB pathway were also declined. *Conclusions*. Curcumin reduces ubiquitination, inflammation in skeletal muscle by regulating the NF-KB/UPS axis and improves muscle malignant metabolic phenotype and mitochondrial dysfunction, to alleviate muscle atrophy and loss of function in mice with breast cancer cachexia.

1. Introduction

Breast cancer is the most common female tumor disease; its morbidity and mortality rates are increasing year by year, resulting in a serious social and economic burden. Triple-negative breast cancer (TNBC) is a common but aggressive type of breast cancer with limited treatment options [1, 2]. TNBC is characterized by high malignancy, strong aggressiveness, and poor prognosis, and it has more chance to develop cancer cachexia. According to statistics, cachexia is present in more than half of cancer patients, contributing about 40% of cancer-related deaths [3]. The pathogenesis of cancer cachexia involves metabolic disorder, chronic inflammation, and skeletal muscle protein degradation [4, 5]. Weight loss and skeletal muscle atrophy not only are common features of cachexia in cancer patients but also are independent prognostic factors for poor clinical outcomes [6]. Unfortunately, many cancer patients often lack effective treatments [7, 8]; current interventions such as exercise, nutritional supplements, and drugs have not achieved the desired results in reducing muscle wasting [9]. Therefore, it is imperative to explore the effective methods and drugs to prevent cancer cachexia [10].

Skeletal muscle wasting caused by tumor cachexia is a gradual loss of muscle mass and strength [11], mostly due to decreased protein synthesis and/or increased degradation [6, 12]. As a protein degradation pathway, the ubiquitin-proteasome system (UPS) plays an important role in the occurrence of skeletal muscle atrophy [13]. Ubiquitin binds to the substrate of the target protein through ubiquitin-activating enzymes E1, E2, and E3 and activates the proteolytic signaling pathway, for example, the E3 ubiquitin ligase atrogin-1/MAFbx and MuRF1 genes are increased in atrophic skeletal muscle [14–16]. UPS can also mediate mitochondrial dysfunction and lead to skeletal muscle atrophy in cancer patients [17]. Studies have reported that the activation of NF-κB can increase the expression of atrogin-1/MAFbx and MuRF1 in muscle atrophy models; NF-κB also inhibits the expression of mitochondrial genes, thereby reducing mitochondrial biosynthesis [18, 19]. Tumor inflammatory cytokines such as TNF-α and IL-6 can also increase protein degradation by activating NF-κB and UPS pathways to promote skeletal muscle atrophy [20, 21]. More importantly, muscle consumption is critically correlated with the muscle metabolism disorder; the expression levels of glucose, amino acids, and fatty acids in muscle can be changed with chemotherapy [22, 23].

Curcumin is a diketone compound extracted from the dried roots of *Curcuma longa* l. and widely used as a traditional herb medicine in Asia [24, 25]. It has profound anti-inflammatory and anticancer properties and can be served as a NF-κB inhibitor to inhibit inflammatory cytokines and oxidative stress in various diseases [25]. However, limited scientific evidence on the mechanism and efficacy of curcumin hinders its integration into the mainstream of healthcare. As the public's interest on natural phytotherapy and diet therapy related to health and disease increases, this attractive and safe alternative has been extensively studied. Previous studies have also shown that curcumin alleviates postexercise skeletal muscle injury by inhibiting the activity of the ubiquitin-proteasome system [26]. Therefore, we hypothesize that curcumin may be able to improve breast cancer cachexia-related skeletal muscle atrophy.

Hence, in this study, by establishing a TNBC-cachexia mouse model, we performed a series of experiments to investigate the effect of curcumin on cancer cachexia-related skeletal muscle atrophy. We find that curcumin inhibited the growth of tumors and corrects mitochondrial dysfunction and malnutrition status in muscle fibers, as well as skeletal muscle function significant improvement. Further results indicated that curcumin improved the muscle atrophy in TNBC-cachexia mice by regulating the NF-κB/UPS axis. Our study is expected to provide to novel perspective for the nature compound as a candidate agent for cancer cachexia therapy. The schematic diagram of the research is shown in Figure 1.

2. Materials and Methods

2.1. Animal Experiment. Female, 5-week-old BALB/c mice (Zhejiang Chinese Medical University Laboratory Animal Research Center, Hangzhou, China) were given autoclaved chow and water ad libitum under a 12 h light/dark cycle at a room temperature of $24 \pm 2^{\circ}$C and humidity of $55 \pm 10\%$. After 7 days of acclimatization, the mice were randomly divided into three groups ($n = 8$/group): healthy group, model group, and curcumin group. Mice in the model group and the curcumin group were inoculated with 5×10^5 4T1 cells (Cell Bank of the Chinese Academy of Sciences, Shanghai, China); the subcutaneous tumor was formed for 1 week, and treatment intervention began. Mice in the curcumin group were intragastrically treated with 0.2 mL curcumin solution (Sigma, Saint Louis, USA) of 150 mg/mL for 28 days, while the healthy and model groups received an equal amount of normal saline. Record weight and food intake as planned. After 28 days of treatment intervention, experimental samples were collected for the experiment. All animal experiments were conducted with the approval of the Experimental Animal Ethical Committee of the Zhejiang Chinese Medical University.

2.2. Activity Monitoring. On day 28 of intervention, all mice were tested one by one in a $100 \times 100\,\text{cm}^2$ open field facility in random order. Before testing, the arena was cleaned and dried with 75% alcohol. All spontaneous activities were recorded by a motion tracking system (Sony Co., Ltd. Guangzhou, China) for 5 minutes. The experimental results were analyzed using SMART 3.0 (Panlab, Barcelona, Spain), and the total movement distance was used as the evaluation index of athletic ability.

2.3. Muscle Grip Strength Test. The grasping strength of the forelimbs of the mice was measured with a grip strength tester (YLS-13A, Shandong Academy of Medical Sciences, China) on days 0, 14, and 28 after treatment intervention. To reduce variability associated with the operation, the same mice were repeated 5 times and the top 3 peak force measurements were included in the analysis (Unit: gf (gram force)).

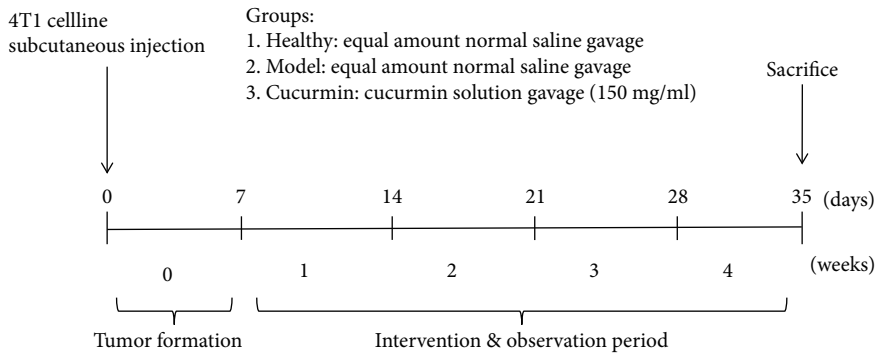

Figure 1: Schematic diagram of the research process.

2.4. Histopathological Assessment. The gastrocnemius muscle was fixed with 4% formalin and further embedded in paraffin and then cut into 4 μm thick sections along the transverse direction of muscle filaments. The gastrocnemius muscle sections were stained with hematoxylin-eosin (HE), and the images were observed and captured under a microscope.

2.5. Transmission Electron Microscopic (TEM) Observation. Prepare gastrocnemius blocks and immediately soak them with 2.5% glutaraldehyde. After 6-8 hours at 4°C, cut into 1 mm thick coronal slices. The samples were washed with PBS and fixed with osmium tetroxide for 1-2 hours. After gradient dehydration with alcohol and acetone, the gastrocnemius muscle was embedded in epoxy resin and sliced into ultrathin sections. Images were obtained by transmission electron microscopy (HT7700, Hitachi, Tokyo, Japan) after double staining with uranyl acetate and lead citrate.

2.6. Gastrocnemius ATP Content Detection. The ATP content in the gastrocnemius muscle of experimental mice was detected using the ATP detection kit (Beyotime, Shanghai, China) for luminescence detection according to the manufacturer's instructions. All luminescence values are finally standardized by the corresponding protein concentration.

2.7. Biochemical Test. Total protein, cholesterol, triglycerides, and albumin were tested by Zhejiang Chinese Medical University Laboratory Animal Research Center using an automatic biochemical analyzer (TBA-40, TOSHIBA, Japan).

2.8. Enzyme-Linked Immunosorbent Assay (ELISA). Weigh the gastrocnemius tissue sample, homogenize it with a lysis buffer containing protease inhibitors on ice, and then centrifuge at 5000 *g* for 5 minutes at 4°C. Collect the supernatant and store it at -20°C. The concentration of IL-6 and TNF-α was determined according to the manufacturer's protocol using IL-6 and TNF-α ELISA kit (Elabscience, Wuhan, China).

2.9. Gastrocnemius Tissue Sample Preparation for Metabolic Profiling. Take out the gastrocnemius muscle from the liquid nitrogen, accurately weigh 100 mg, and add 800 μL MeOH/H_2O solution (v/v, 3 : 1). Then, use an electric homogenizer to homogenize at a frequency of 1/30 for 5 minutes to extract polar metabolites. Centrifuge at 4°C and 13,000 rpm for 10 min, and collect the supernatant. Then, 500 μL of supernatant was dried in a vacuum centrifugal concentrator (Labconco, USA) and resuspended in 600 μL of 10% deuterium water (D2O, 99.8%, Sigma, USA) and 0.05 mM sodium 3-trimethylsilyl-propionate-d4 (TMSP-2,2,3-d4; Sigma, USA) for nuclear magnetic resonance analysis.

2.10. ^{1}H NMR Spectroscopy Analysis and Data Processing. 600 μL supernatants from each sample were introduced for NMR spectroscopic analysis performed on a Bruker 600 MHz AVANCE III spectrometer equipped with a 5 mm BBFO probe and lock performed on the D2O signal at 25°C. ^{1}H NMR spectra were received using NOESYPR1D pulse sequence with water suppression. The data were processed using Bruker Topspin 3.2. All free induction decays (FIDs) from ^{1}H NMR of the muscle were multiplied by a 0.3 Hz exponential line broadening before Fourier transformation. All the obtained NMR spectra were manually phased, baseline corrected, and chemical shift referenced to TSP ($\delta = 0.0$) within MestReNova 6.1 (Mestrelab Research SL, Spain). The analyzed spectrum region was 0.0–9.0 ppm without 4.5–5.0 ppm to eliminate the effects of imperfect water suppression. The characteristic peaks of all muscle metabolites were determined based on the network database of metabolomics, including Biological Magnetic Resonance Bank (https://www.bmrb.wisc.edu/metabolomics) and Human Metabolome Database (https://www.hmdb.ca/). The pathway enrichment analysis of differential metabolites is performed in the MetaboAnalyst 5.0 database (https://www.metaboanalyst.ca/).

2.11. Real-Time qPCR. RNA was extracted from the muscle samples using RNA-Quick Purification Kit (esunbio, Shanghai, China) according to the manufacturer's protocol, and the RNA was reverse transcribed into cDNA by RevertAid First Strand cDNA Synthesis Kit (Thermo Scientific™, Massachusetts, USA). Real-time PCR (RT-PCR) analyses were performed by the ABI 7900HT real-time PCR system (Applied Biosystems, San Francisco, USA); use Super SYBR Green qPCR Master Mix (esunbio, Shanghai, China). The β-actin expression was used to normalize the expression levels, and results were calculated based on the comparative cycle threshold method ($2^{-\Delta\Delta ct}$). The primer sequences are listed in Table 1 ($5'$–$3'$).

Table 1: Primers' table.

Gene name	Forward primer	Reverse primer
β-Actin	TGCTGTCCCTGTATGCCTCTG	TGATGTCACGCACGATTTCC
Myostatin	AGTGGATCTAAATGAGGGCAGT	GTTTCCAGGCGCAGCTTAC
Myogenin	GAGACATCCCCCTATTTCTACCA	GCTCAGTCCGCTCATAGCC
Atrogin-1	CAGCTTCGTGAGCGACCTC	GGCAGTCGAGAAGTCCAGTC
MuRF1	GTGTGAGGTGCCTACTTGCTC	GCTCAGTCTTCTGTCCTTGGA
Nk-kB	AGCGGGAACTGAGTGAGATGA	GCACCCAGGTTGTATCGGG

2.12. Western Blotting. About 80 mg gastrocnemius tissue was lysed in RIPA Lysis Buffer (Cell Signaling, Boston, USA) for 10 minutes on ice. The lysate homogenate was centrifuged, and the protein concentration was measured with the BCA Protein Assay Kit (Beyotime, Shanghai, China). After that, the protein samples were loaded and electrophoresed in 10% SDS-PAGE and transferred to PVDF membranes (Millipore, United States). After that, the membranes were blocked in 5% nonfat milk powder for 2 h before incubation with primary antibodies overnight at 4°C. The primary antibody was purchased from Abcam (Cambridge, UK) and diluted at 1 : 1000, including anti-GAPDH, anti-GDF8/myostatin, anti-MuRF1, anti-atrogin-1 (Fbx32), anti-NF-κB (p65), and anti-NF-κB p65 (phosphorylation S536). Then, the membranes were incubated with the appropriate secondary antibody. The blots were visualized with enhanced chemiluminescence.

2.13. Statistical Analysis. The partial least-squares discriminant analysis (PLS-DA) was performed using SIMCA software, version 14.1 The differential metabolites were filtered by variable influence on projection (VIP) selection according to the PLS-DA and the filtering conditions VIP > 1 and $p < 0.05$. Differences between the two groups were analyzed by unpaired Student's t-test. All values were expressed as mean ± SEM. $p < 0.05$ was considered statistically significant.

3. Result

3.1. Curcumin Inhibited the Tumor Growth of TNBC-Bearing Mice. We used dynamic *in vivo* bioluminescence imaging monitoring to evaluate the mouse growth changes of breast cancer tumor at the beginning, middle, and end of the experiment (Figure 2(a)). *In vivo* bioluminescence imaging results showed that the bioluminescence values of tumor-bearing mice in the curcumin group were significantly lower than those of the model control group at 2 and 4 weeks (Figure 2(b), $p = 0.0205 < 0.05$; $p = 0.0056 < 0.01$). In addition, as shown in Figures 2(c)–2(f), it could also be found that the tumor volume of the curcumin group mice was significantly smaller than that of the model group, and the tumor weight of the mice also reached the same conclusion. These data strongly suggest that curcumin inhibits the tumor growth of breast cancer.

3.2. Curcumin Alleviated Body Weight Loss and Improved Malnutrition in TNBC-Bearing Mice. From the ninth day until the end of the experiment, the bodyweight of the tumor-bearing mice in the curcumin group was significantly larger than that of the model group, but lower than that of the healthy group, as well as the final bodyweight (Figures 3(a) and 3(b)). In addition, the weekly eating status and some nutritional indicators of each group mice were also evaluated. The results showed that the average weekly food intake of mice in the healthy group and the curcumin group was greater than that of the model group within 4 weeks, with statistical difference in the 3rd and 4th weeks (Figure 3(c), $p < 0.05$). The level of nutritional indicators of mice in the model group was significantly lower than that in the healthy group, including total protein, albumin, cholesterol, and triglyceride (Figures 3(d)–3(g), $p < 0.01$), while these indicators were significantly improved after curcumin treatment, including total protein (Figure 3(d), $p = 0.0249$), albumin (Figure 3(e), $p = 0.0131$), cholesterol (Figure 3(f), $p = 0.0011$), and triglyceride (Figure 3(g), $p = 0.0039$). In addition, the weight of the main organs of mice in the model group was significantly lower than that of the healthy group, while curcumin administration partly recovered these organs' weights (Figure 3(h), $p < 0.05$).

3.3. Curcumin Reduced the Skeletal Muscle Loss in Tumor-Bearing Mice and Improves Muscle Function. We measured the grip strength of the forelimbs of the three groups of mice. Compared with that of the healthy group, the grip strength of the model group mice was decreased rapidly, while curcumin administration enhanced the gripping strength, with statistical differences at 2 and 4 weeks (Figure 4(a), curcumin vs. model: $p = 0.047$ and $p = 0.0011$, respectively). In addition, Figure 4(b) indicates that the movement distance of the model group mice was significantly shorter than that of the healthy group ($p < 0.0001$), while this in the curcumin group was significantly decreased (Figure 4(b), $p = 0.0102$). Furthermore, we found that the reduced gastrocnemius weight in the model group mice was significantly recovered by curcumin administration (Figure 4(c), $p < 0.0001$). The lowered gastrocnemius index of the model group mice was also recovered in the curcumin group (Figure 4(d), $p = 0.0214$).

In Figures 4(e) and 4(f), HE staining analysis showed that the healthy group muscle fibers were evenly arranged, showing a dense polygonal structure with regular muscle

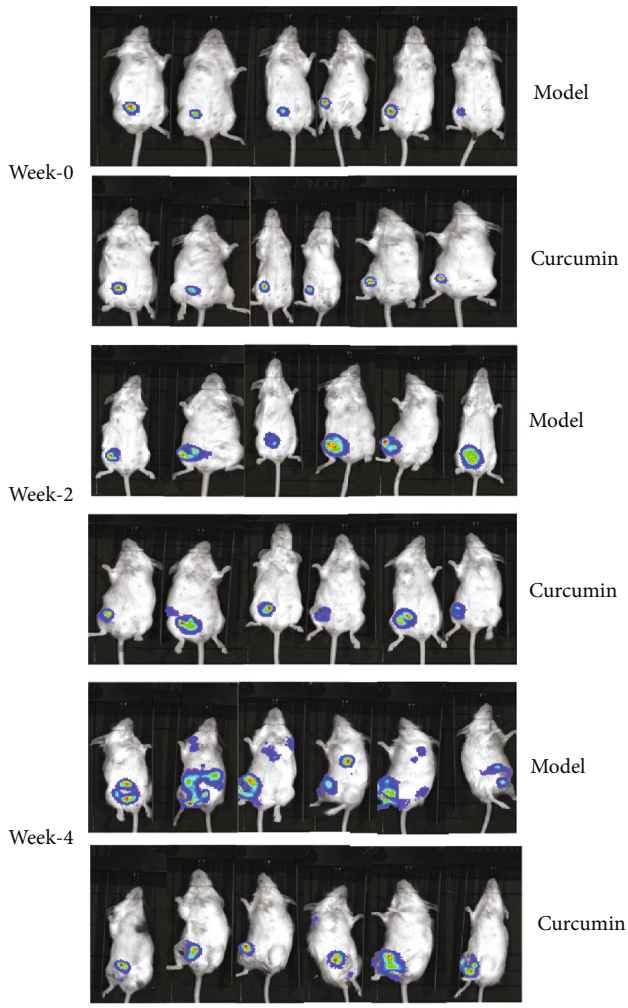

(a)

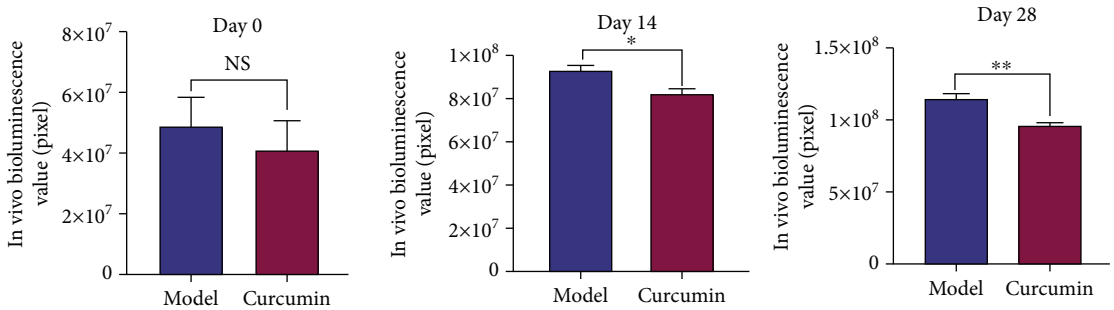

(b)

Figure 2: Continued.

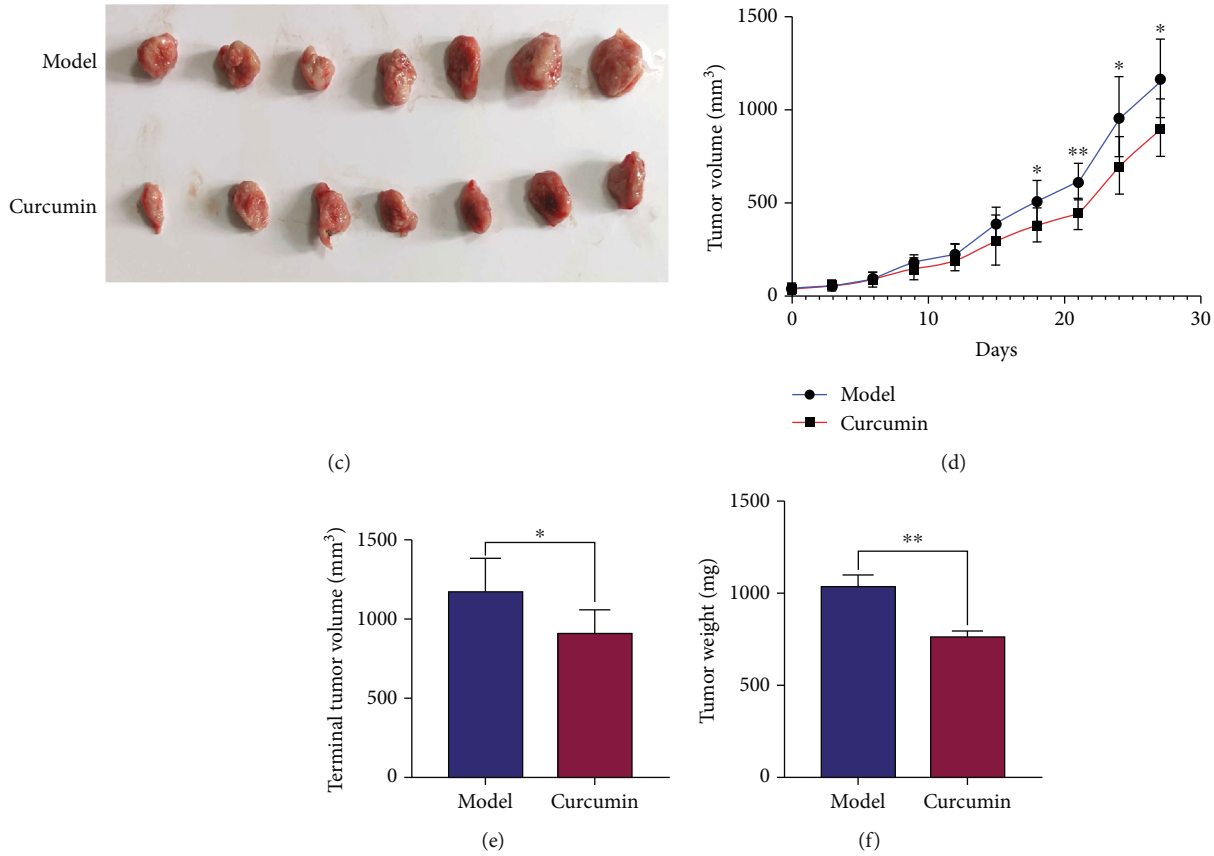

Figure 2: Curcumin inhibits the proliferation of triple-negative breast cancer. (a) In vivo bioluminescence imaging of the breast cancer-bearing mice on day 0, day 14, and day 28 after intervention ($n = 6$/group). (b) Statistical analysis of bioluminescence value of tumor-bearing mice on day 0, day 14, and day 28 after intervention ($n = 6$/group). (c) Comparison of in situ tumor morphology between tumor-bearing model mice and curcumin treatment mice. (d) Model group and curcumin treatment group tumor growth curve during the intervention period ($n = 8$/group). (e, f) Statistical analysis of terminal tumor volume and bodyweight in the model group and the curcumin group ($n = 8$/group). NS: not significant; $^{*}p < 0.05$ and $^{**}p < 0.01$ by t-test, compared to the model group. Data were shown as mean ± standard errors of the mean.

spaces. The muscle fibers in the model group were different in thickness, with an increased diameter and disordered arrangement, and the gaps were increased significantly after muscle fiber atrophy. The cross-sectional area of muscle fibers was also significantly smaller than that in the healthy group (Figure 4(e), $p < 0.0001$). Compared with the model group, the muscle fiber density and area of the mice in the curcumin group were significantly increased, the arrangement was orderly, the muscle fiber gap was significantly reduced (Figure 4(e), $p = 0.0055$), and the condition of muscle atrophy was improved.

3.4. Curcumin Alleviates Mitochondrial Dysfunction and Increases ATP Production in the Gastrocnemius Tissue of Tumor-Bearing Mice. TEM was used to examine the ultrastructure of muscle fibers to assess mitochondrial damage. The result in Figure 5(a) showed that the nuclei (reddish-brown) in the muscle fibers of the mice of the healthy group did not exhibit pyknosis, the mitochondria did not aggregate, and they were evenly distributed between myofibrils (green), mitochondria (reddish-brown) have regular morphology, myofibrils (green) line up neatly, sarcomeres Z-line (orange), H-band (blue) clear. In the model group, Figure 5(b) shows nuclei pyknosis separated from the cytoplasm, mitochondrial aggregation, injury swelling and expansion (reddish-brown), myofibrils (green) broken, sarcomere blurred, sarcomere Z-line (orange), sarcomere H-band (blue) blurred, edema, and voids (purple). In the curcumin group (Figure 5(c)), the number of mitochondria (reddish-brown) was reduced compared with that in the healthy group, and the swelling was obvious. The mitochondrial ridges disappeared and vacuoles were formed, distributed among the myofibrils, but no mitochondrial aggregation was observed. The myofibrils were in normal shape, and the overall shape was slightly worse than that in the normal group. The myofibrils (green) are arranged in a continuous and orderly manner, with no apparent rupture. In addition, the ATP content in the gastrocnemius of the model group is significantly lower than that in the control group, and curcumin treatment improved ATP content (Figure 5(d), $p < 0.05$).

3.5. Curcumin Intervention Alleviated the Malignant Metabolic Phenotype of Muscle Tissue in Tumor-Bearing

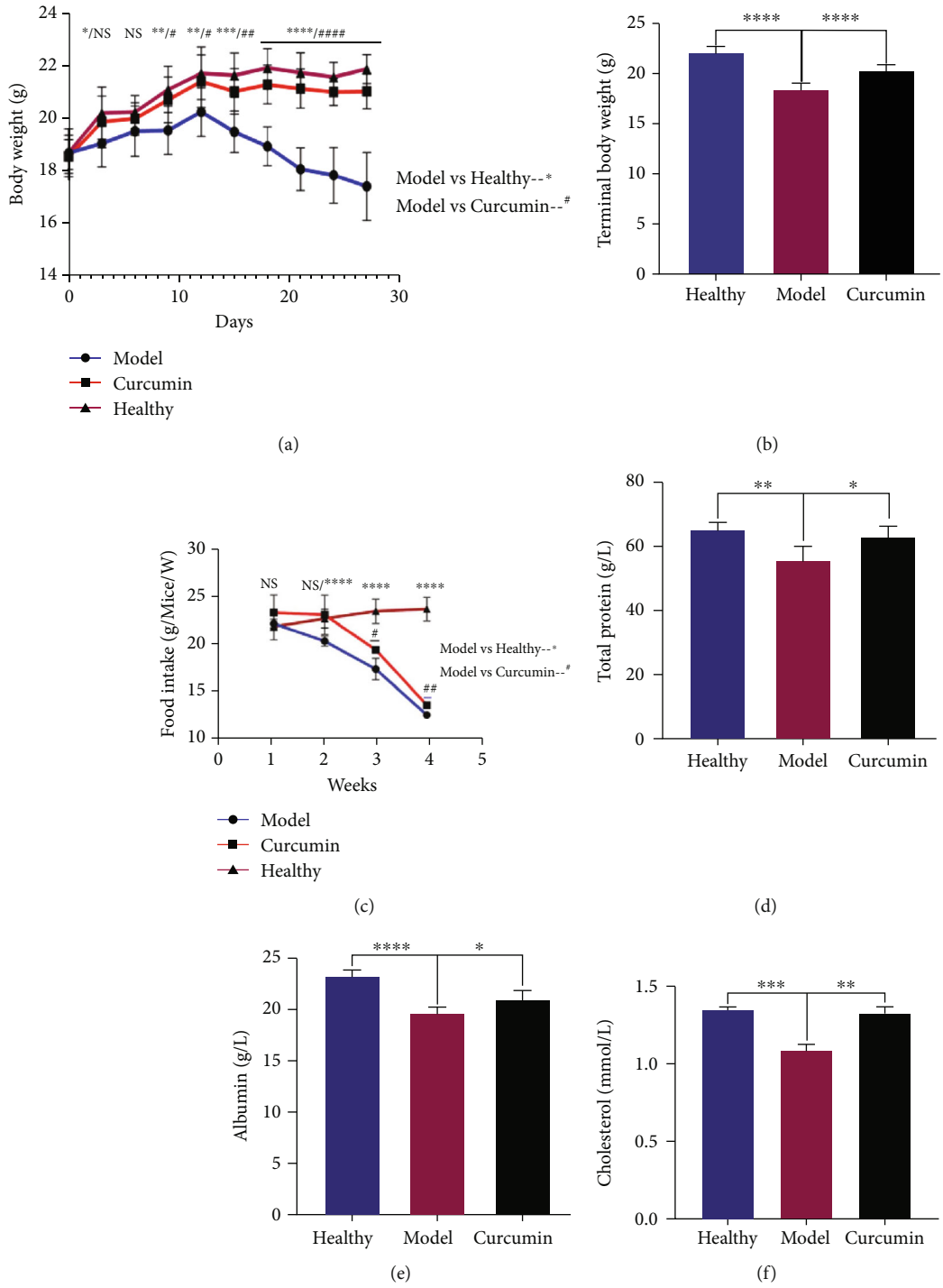

Figure 3: Continued.

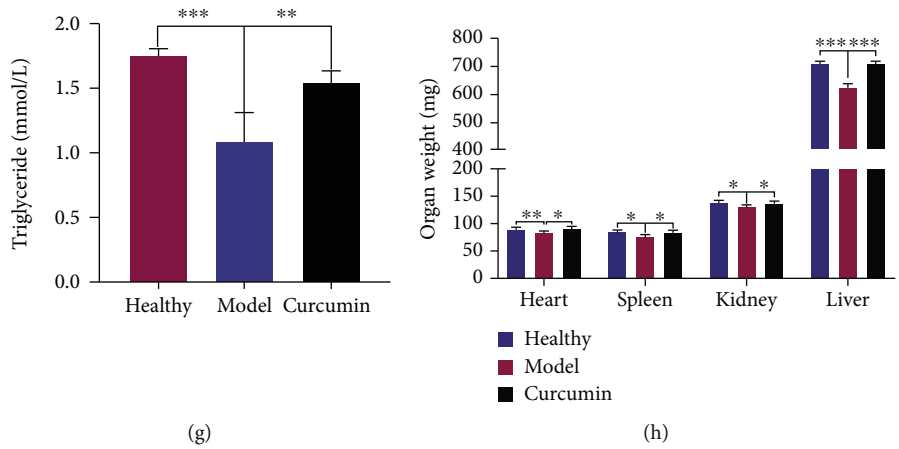

Figure 3: Curcumin alleviates the weight and organ loss and improved malnutrition in tumor-bearing mice. (a) Body weight change curves of the three groups during the 4-week intervention period. (b) Statistical analysis of the terminal body weight of three groups of mice. (c) Statistical analysis of the food intake of the 3 groups of mice during the 4-week observation period. (d–g) Statistical analysis of serum total protein, albumin, cholesterol, and triglyceride of mice in the healthy group, the model group, and the curcumin group at the end of the experiment. (h) Statistical analysis of the weight of the main organs of the three groups of mice at the end of the experiment. $n = 8$ /group. NS: not significant; $^{*}p < 0.05$, $^{**}p < 0.01$, $^{***}p < 0.001$, and $^{****}p < 0.0001$ by t-test, compared to the model group. Data was shown as mean ± standard errors of the mean.

Mice. The above results indicate that curcumin significantly improved the cachexia phenotype of the skeletal muscle of TNBC tumor-bearing mice. To further analyze the underlying mechanism, we performed ^{1}HNMR metabonomic analysis on the gastrocnemius tissue, and the unsupervised partial least-squares discriminant analysis (PLS-DA) score plots showed that the curcumin group and the model group have a good degree of discrimination, which also shows that the metabolic patterns between the two groups are different (Figure 6(a)). The verification plots based on the two sets of ^{1}HNMR spectra illustrated that the PLS-DA model is robust and reliable (Figure 6(b), the R2X, R2Y, and Q2 values of the model are 0.551, 0.989, and 0.889, respectively). Then, six different metabolites were screened according to the conditions of VIP > 1 and $p < 0.05$, including lysine, isobutyrate, AMP, 3-hydroxyphenylacetate, pyruvic acid, and creatine (Figure 6(c)). Based on the differential metabolites, related metabolic pathways were identified by KEGG and HMDB databases (Figure 6(d)). We specifically analyzed the top three metabolic pathways with significant differences, including pyruvate metabolism, glycolysis/gluconeogenesis, and glyoxylate and dicarboxylate metabolism, and these pathways are considered to be the metabolic pathways most relevant to curcumin treatment (for more information, please see supplementary data (Table S1)).

3.6. Curcumin Decreased the Inflammatory Factors and Myodegradable Factors and Increased the Myogenic Factor Expression in the Muscle Tissues. We measured the levels of inflammatory cytokines TNF-α and IL-6 in gastrocnemius tissue; the results indicated that the increased levels of TNF-α and IL-6 levels in the model group were significantly decreased by curcumin administration (Figures 7(a) and 7(b); $p = 0.0006$, $p = 0.016$). RT-qPCR results showed that the expression of the negative regulator myostatin of muscle in the model group was significantly higher than that of the healthy group (Figure 7(c), $p = 0.0397$), while the myostatin of the curcumin group was less than that in the model group (Figure 7(c), $p = 0.0496$), while the expression of myogenin had opposite results in these groups (Figure 7(d)). The results of myostatin protein expression in Figure 7(e) were consistent with Figure 7(c).

3.7. Curcumin Treatment Reduced Ubiquitination and NF-κB Activity in Muscle Tissue of Tumor-Bearing Mice. The ubiquitination-related gene expression was detected, and RT-qPCR results suggest that the expression of atrogin-1 and MuRF-1 in the model group was significantly higher than that in the healthy group (Figures 8(a) and 8(b); $p = 0.0427$, $p = 0.0290$), and this expression was significantly downregulated in the curcumin-treated group compared with the model group (Figures 8(a) and 8(b); $p = 0.0098$, $p = 0.0378$). The RT-qPCR analysis also observed that the NF-κB in the gastrocnemius of the model group was significantly increased (Figure 8(c), $p = 0.0028$), while its expression in the curcumin group mice was downregulated compared with that in the model group (Figure 8(c), $p = 0.0186$). Western blot results for the detection of the protein expression of atrogin-1, MuRF-1, and p-NF-κB p65 were consistent with the aforementioned RT-qPCR results (Figures 8(d)–8(i)).

4. Discussion

Most advanced cancer patients fit the category of tumor cachexia [27], and weight loss, especially the loss of skeletal muscle mass, is the main feature [28]. These features caused by tumor cachexia not only lead to poor tolerance of patients to multiple treatments but also have negative impact on the quality of life and prognosis of patients [29]. However, currently, there are very few methods or drugs to treat cancer cachexia. Curcumin is a food derivative with multiple

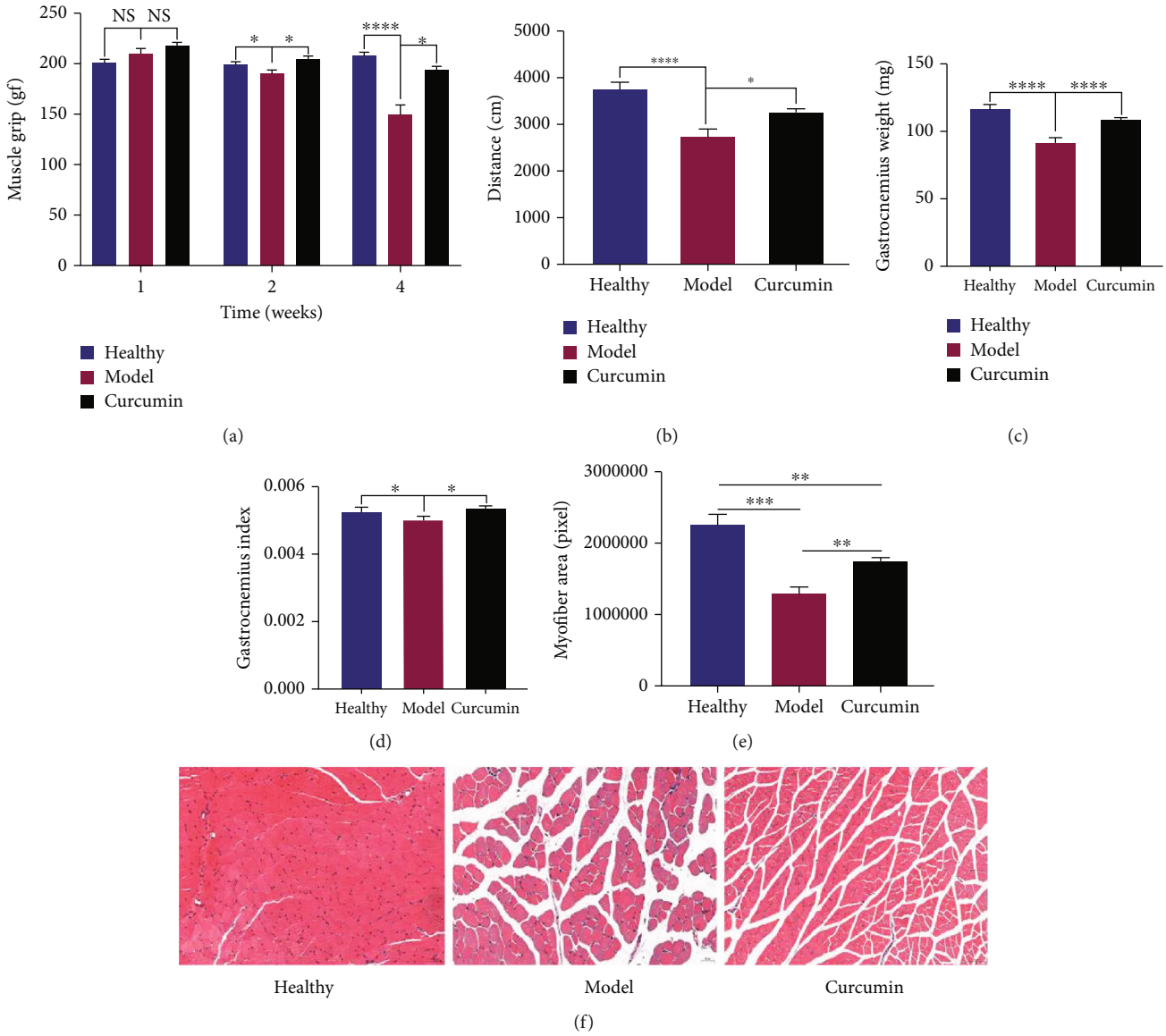

Figure 4: Curcumin reduces skeletal muscle loss and improved muscle function in tumor-bearing mice. (a) Statistical analysis of forelimb grip strength of three groups of mice at 0, 2, and 4 weeks after intervention ($n = 8$/group). (b) Statistical analysis of movement distance within 5 min in three groups of mice at the end of the experiment ($n = 8$/group). (c) Statistical analysis of gastrocnemius muscle weight in three groups of mice at end of the experiment ($n = 8$/group). (d) Comparative analysis of the gastrocnemius index of the three groups of mice at the end of the experiment ($n = 8$/group). (e) Statistical analysis of muscle fiber cross-sectional area in gastrocnemius HE sections of three groups of mice ($n = 5$/group). (f) HE staining analysis of gastrocnemius muscle in three groups (×200 magnification; scale bar: 50 μm, $n = 5$/group). NS: not significant; $^{*}p < 0.05$, $^{**}p < 0.01$, $^{***}p < 0.001$, and $^{****}p < 0.0001$ by t-test, compared to the model group. Data was shown as mean ± standard errors of the mean.

biological targets and different cellular effects. It has anti-inflammatory, antioxidant, and anticancer properties. However, there are few studies on whether curcumin inhibits TNBC through these mechanisms and also reduces tumor cachexia-related skeletal muscle loss or weight loss. Given this, we conducted this study.

Dynamic bioluminescence imaging and tumor volume growth curve find that curcumin inhibited the growth and progression of TNBC tumor in tumor-bearing mice. These data strongly suggest that curcumin has an inhibitory effect on the growth of breast tumors and also suggest that curcumin has the potential to treat breast cancer cachexia. The gradual decrease in body weight is the earliest symptom of cachexia. In our study, 10 days after tumor inoculation in the model group, mouse weight and food intake began to be significantly lower than those of the healthy control group, and their hair color was dim, the spirit was listless, and vitality was decreased, which was consistent with the symptoms of cancer cachexia, while the weight and food intake of mice in the curcumin treatment group were gradually recovered from the 9th day of administration to the end of the experiment. The nutritional status is also a critically important factor of cancer cachexia [30]. Cholesterol and triglycerides are major sources of lipid energy in the

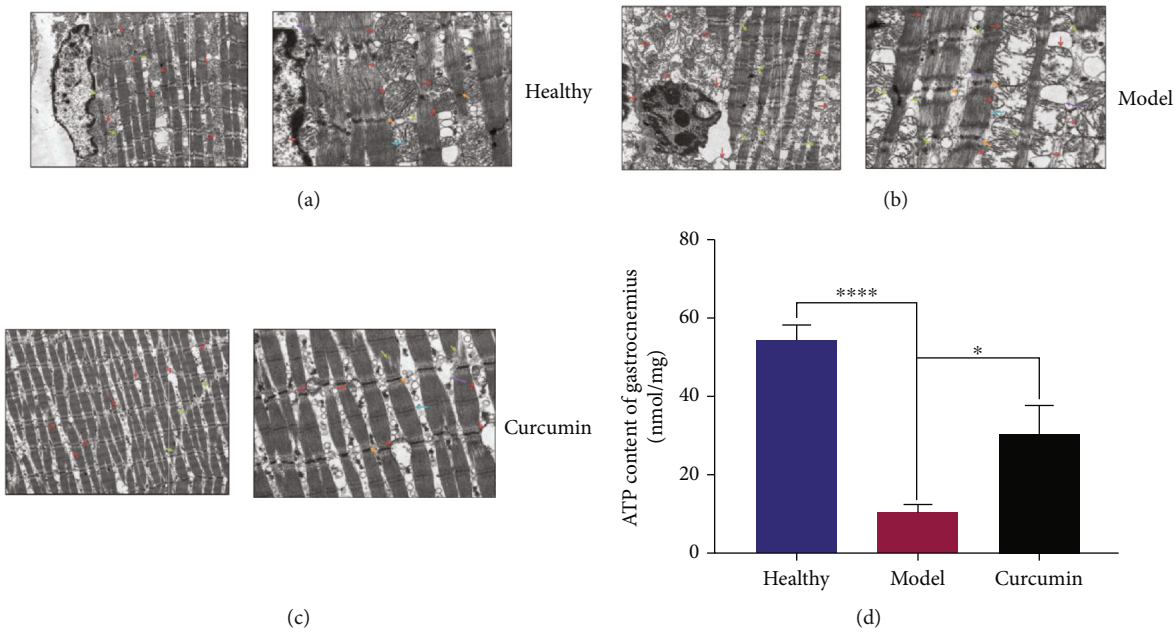

Figure 5: Curcumin alleviates mitochondrial dysfunction and increased ATP production in gastrocnemius of TNBC mice. (a–c) Transmission electron microscope observation of the gastrocnemius in the healthy group, the model group and the curcumin group (green: myofibrils; orange: sarcomere Z-line; blue: H band; reddish-brown: mitochondria; purple: edema; left: 20,000x magnification; right: 50,000x magnification). (d) Statistical analysis of ATP content in gastrocnemius tissue of mice in three groups ($n = 4$/group). $^{*}p < 0.05$ and $^{****}p < 0.0001$ by t-test, compared to the model group. Data were shown as mean ± standard errors of the mean.

body. Serum albumin serves as a nitrogen source to provide nutrition for tissues; serum total protein is often used to monitor the nutritional status of the body. The results showed that curcumin treatment significantly improved the malnutrition status; serum total protein, albumin, cholesterol, and triglyceride levels were higher than those in the model group. Therefore, it can be considered that curcumin not only inhibits the proliferation and progression of TNBC in tumor-bearing mice but also improves the nutritional status and weight loss, thus alleviating cancer cachexia.

Skeletal muscle loss is a typical feature of tumor cachexia [6]. The gastrocnemius in the calf muscles is the most common and earliest skeletal muscle involved, so we collected the gastrocnemius muscles of three groups of mice for downstream experiments. We found that the gastrocnemius muscle of the model group mice was significantly lost compared with that of the healthy group, but after curcumin treatment, the gastrocnemius muscle weight loss of the tumor-bearing mice was partially restored, and the gastrocnemius muscle index was higher than that of the model group mice. In addition, HE staining analysis of gastrocnemius muscle also found that the muscle fibers of the model group had smaller diameters and cross-sectional area, disordered arrangement, and significantly larger gaps, but these conditions were improved in the muscle fibers of the curcumin-treated mice. The forelimb grip and movement distance measurement of mice also confirmed the above results, the model group mice's movement distance per unit time was shortened, and the forelimb grip was continuously lost; these conditions were partially reversed after curcumin treatment. These results indicated the denser muscle fibers and stronger muscle strength of mice after curcumin administration.

The degradation of muscle protein caused by mitochondrial dysfunction is closely related to the skeletal muscle atrophy caused by cachexia [17, 31]. Uncoupling protein-2 and uncoupling protein-3 can destroy the inner and outer membrane of mitochondria, thereby reducing the mitochondrial ATP synthesis required for muscle energy metabolism [32]. In addition, the NF-κB signaling pathway inhibits mitochondrial gene expression, thereby reducing mitochondrial biosynthesis, oxidative phosphorylation, and ATP production [33, 34]. We used TEM to observe the differences in mitochondrial morphology in the gastrocnemius muscles of different groups of mice, to verify whether curcumin reversed the loss of cachexia skeletal muscle is related to the improvement of mitochondrial function. The observation results suggested that there was significant mitochondrial dysfunction in atrophic muscle fibers of model mice compared with healthy mice, and curcumin intervention partially alleviated this phenomenon. Moreover, mitochondria are important productive organelles in cells, and mitochondrial dysfunction is bound to affect the production of ATP in muscles, leading to muscle atrophy [35]. In this study, except for the observed mitochondrial dysfunction in model mouse gastrocnemius muscles, the ATP content in the model mice was also decreased, but it was partly recovered in the curcumin group. These results indicated that the mitochondrial function of muscle fibers in mice treated with curcumin was improved, which also brought about an increase in ATP production.

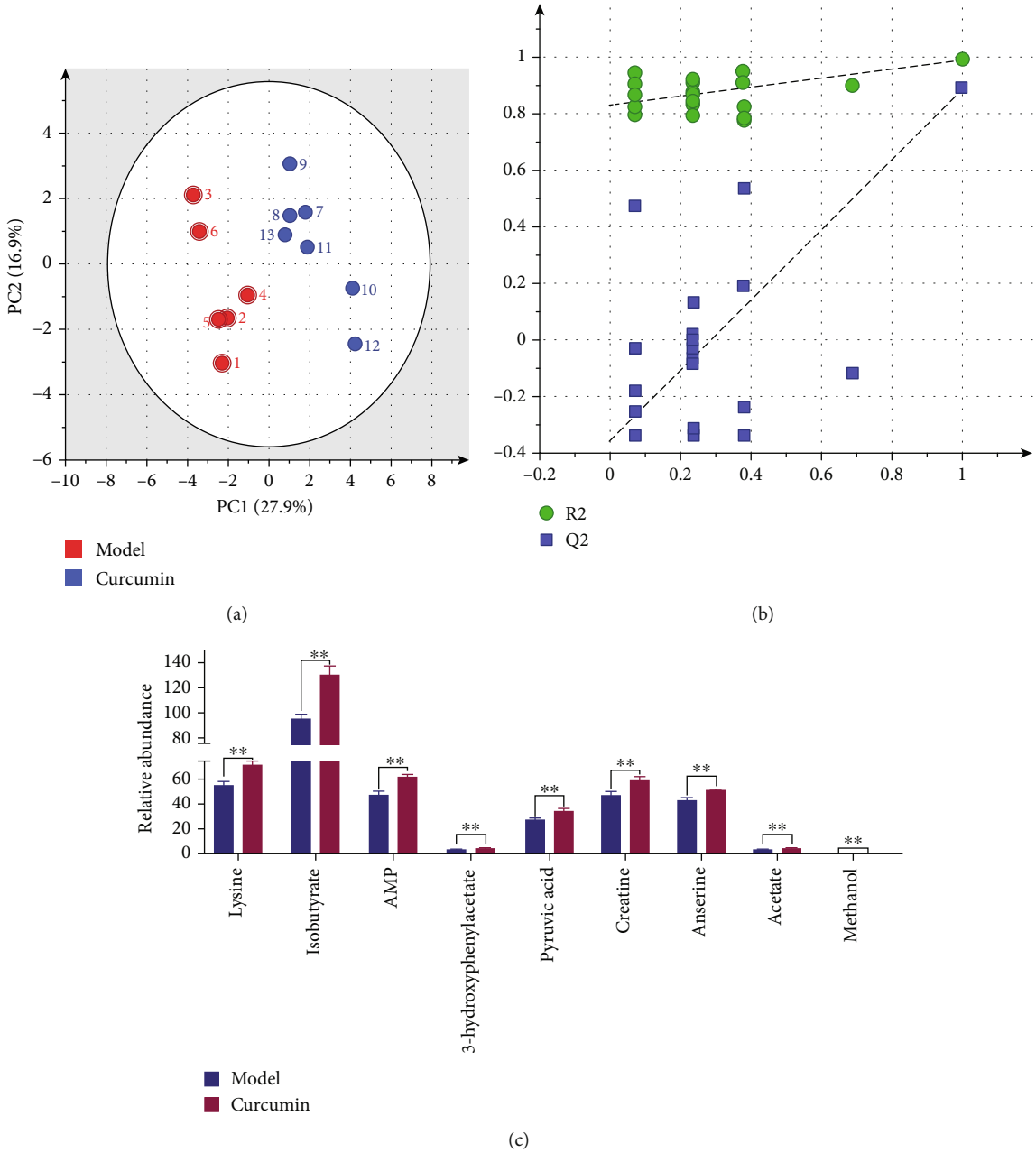

Figure 6: Continued.

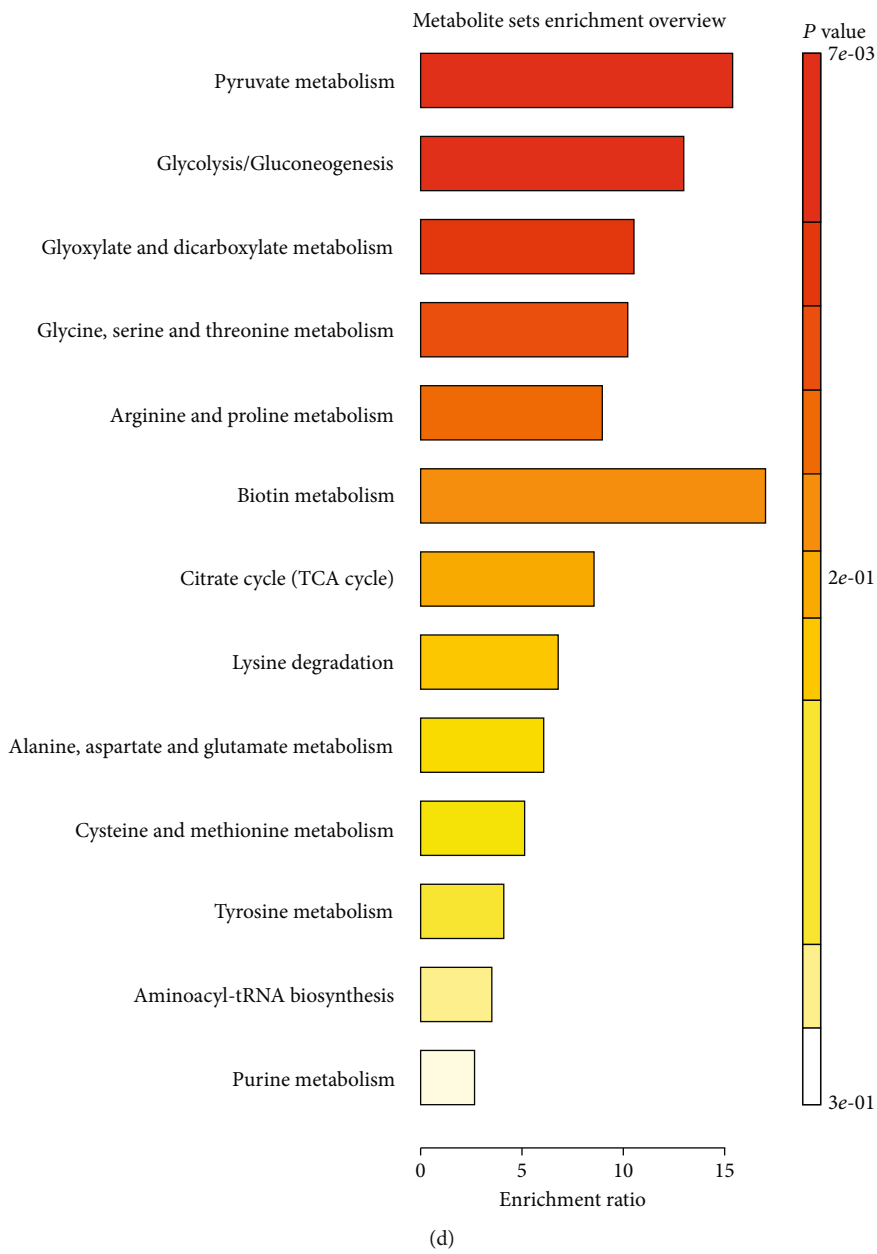

Figure 6: Metabolomics analysis of gastrocnemius tissue in tumor-bearing mice after curcumin intervention. (a) PLS-DA scatter plot of gastrocnemius samples in the model group and the curcumin group ($n = 8$/group). (b) Validation plot of gastrocnemius samples obtained from the model and curcumin groups ($n = 8$/group). (c) Gastrocnemius differential metabolites filtered by the conditions of VIP > 1 and $p < 0.05$. (d) Pathway analysis of differential metabolites; $^{**}p < 0.01$ by t-test, compared to the model group. Data were shown as mean ± standard errors of the mean.

Metabolic disorders are evident in the progression of skeletal muscle loss in patients with tumor dystrophy, so amelioration of specific metabolic defects is also a potential way to alleviate dystrophy [36]. We used ^{1}HNMR metabonomic analysis to explore the changes of metabolites after curcumin improved muscle loss in dyscrasia mice, and a total of 6 significant differential metabolites were screened (AMP, lysine, isobutyrate,3-hydroxyphenylacetate, pyruvic acid, and creatine). AMP provides chemical energy by binding phosphate groups to form adenosine diphosphate (ADP) and adenosine triphosphate (ATP), and a reduction in AMP has been observed in atrophic muscle [37]. Lysine is a key substance that helps other nutrients to be fully absorbed and utilized by the human body. Carnitine deficiency caused by its lack is a common protein deficiency [38]. Isobutyrate is a kind of short-chain fatty acid. Studies have confirmed that the increase in butyrate synthesis by intestinal microbes is closely related to the increase in skeletal muscle index [39]. Fatty acids, glucose, and lactic acid can be metabolized into pyruvate, which is transported to the mitochondria by the mitochondrial pyruvate carrier (MPC) for the citric acid cycle [40]. Sufficient research has proved that creatine can

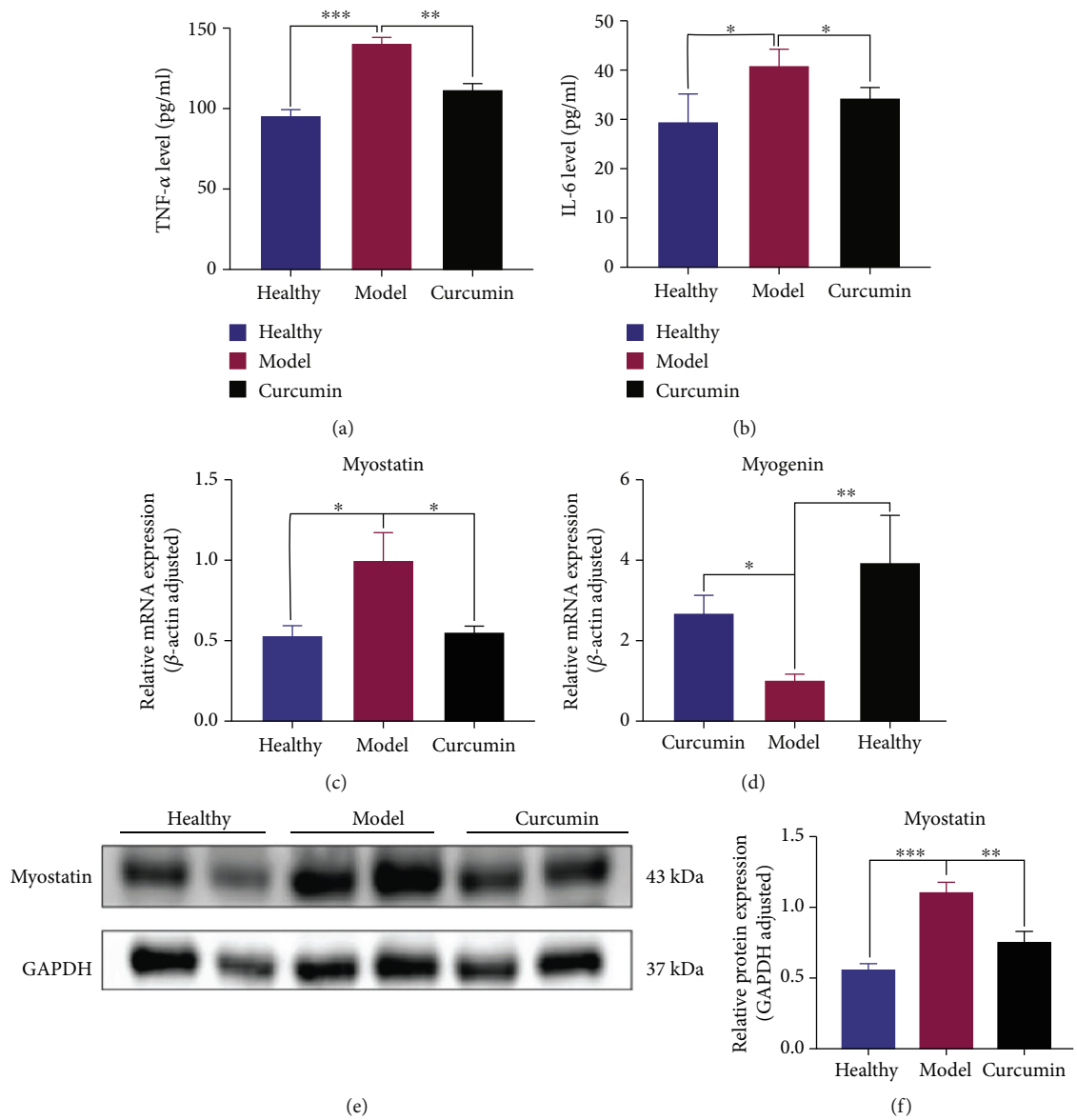

Figure 7: Curcumin decreased inflammatory factors, increased the expression of myogenic factors, and decreased the expression of myodegradable factors in the muscle tissue of tumor-bearing mice. (a, b) Statistical analysis of TNF-α and IL-6 levels in gastrocnemius of three groups of mice ($n = 4$/group). (c, d) Statistical analysis of myostatin and myogenin mRNA expression in gastrocnemius of mice in three groups. (e, f) Statistical analysis of myostatin and myogenin protein expression difference in gastrocnemius of the three groups. NS: not significant; $^{*}p < 0.05$, $^{**}p < 0.01$, and $^{***}p < 0.001$ by t-test, compared to the model group. Data was shown as mean ± standard errors of the mean.

promote muscle anabolism and is used as a supplement to reduce the loss of muscle mass and function in various acute and chronic diseases [41]. No studies have confirmed the effect of 3-hydroxyphenylacetate in alleviating muscle atrophy, and further studies are needed to confirm the effect. In KEGG analysis, these differential metabolites were enriched into the pyruvate metabolism, glycolysis/gluconeogenesis, and glyoxylate and dicarboxylate metabolism. Glycolysis/gluconeogenesis is also closely related to pyruvate metabolism. Pyruvate is an intermediate product of glucose metabolism, which is reduced to lactic acid for energy in the cytoplasm or oxidized into the mitochondria to generate acetyl-CoA and enter the TCA (tricarboxylic acid) cycle, realizing the mutual transformation of sugars, fats, and amino acids in the body [42]. Glyoxylic acid cycling improves the ability of organisms to utilize acetyl-CoA and is a reaction process closely related to the conversion of fats to carbohydrates. These three pathways are all related to the regulation of energy metabolism. Therefore, we believe that curcumin can reduce skeletal muscle loss through the regulation of energy metabolism in mice with cancer cachexia.

Inflammatory cytokines are thought to contribute to induce muscle atrophy and muscle metabolism disorders [43]. We found that the levels of IL-6 and TNF-α in

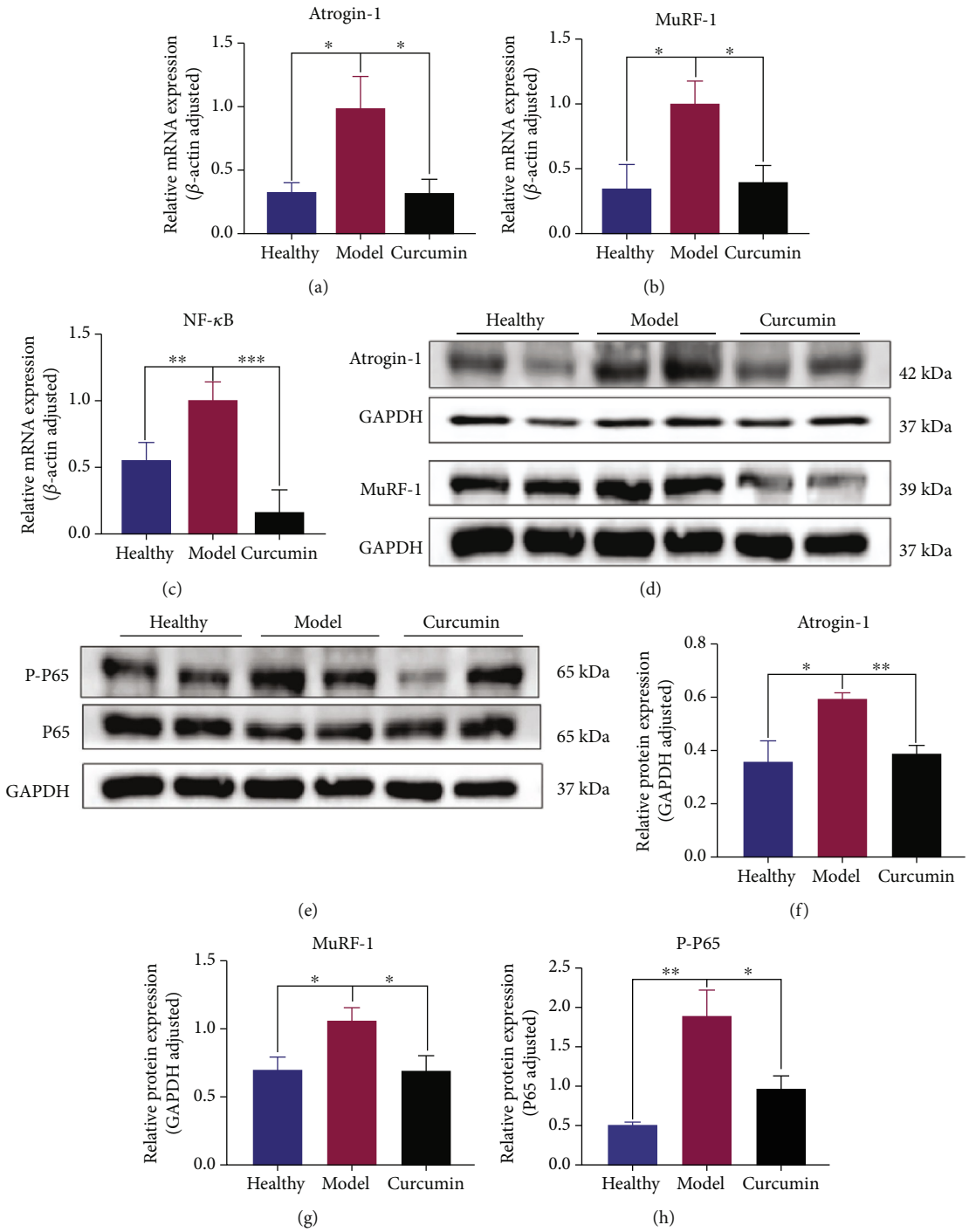

Figure 8: Continued.

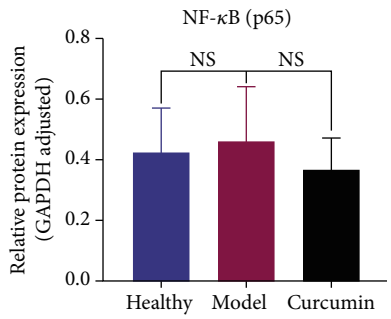

(i)

Figure 8: Curcumin treatment reduces ubiquitination and NF-κB activity in muscle tissue of tumor-bearing mice. (a–c) Statistical analysis of atrogin-1, MuRF-1, and NF-κB mRNA expression of mouse gastrocnemius in three groups. (d) Western blot bands of atrogin-1 and MuRF-1 protein in gastrocnemius of the three groups. (e) Western blot bands of P65 and P-P65 protein in gastrocnemius of the three groups. (f–i) Statistical analysis of atrogin-1, MuRF-1, P-65, and PP-65 protein expressions in gastrocnemius of three groups of mice. NS: not significant; $^{*}p < 0.05$, $^{**}p < 0.01$, and $^{***}p < 0.001$ by t-test, compared to the model group. Data was shown as mean ± standard errors of the mean.

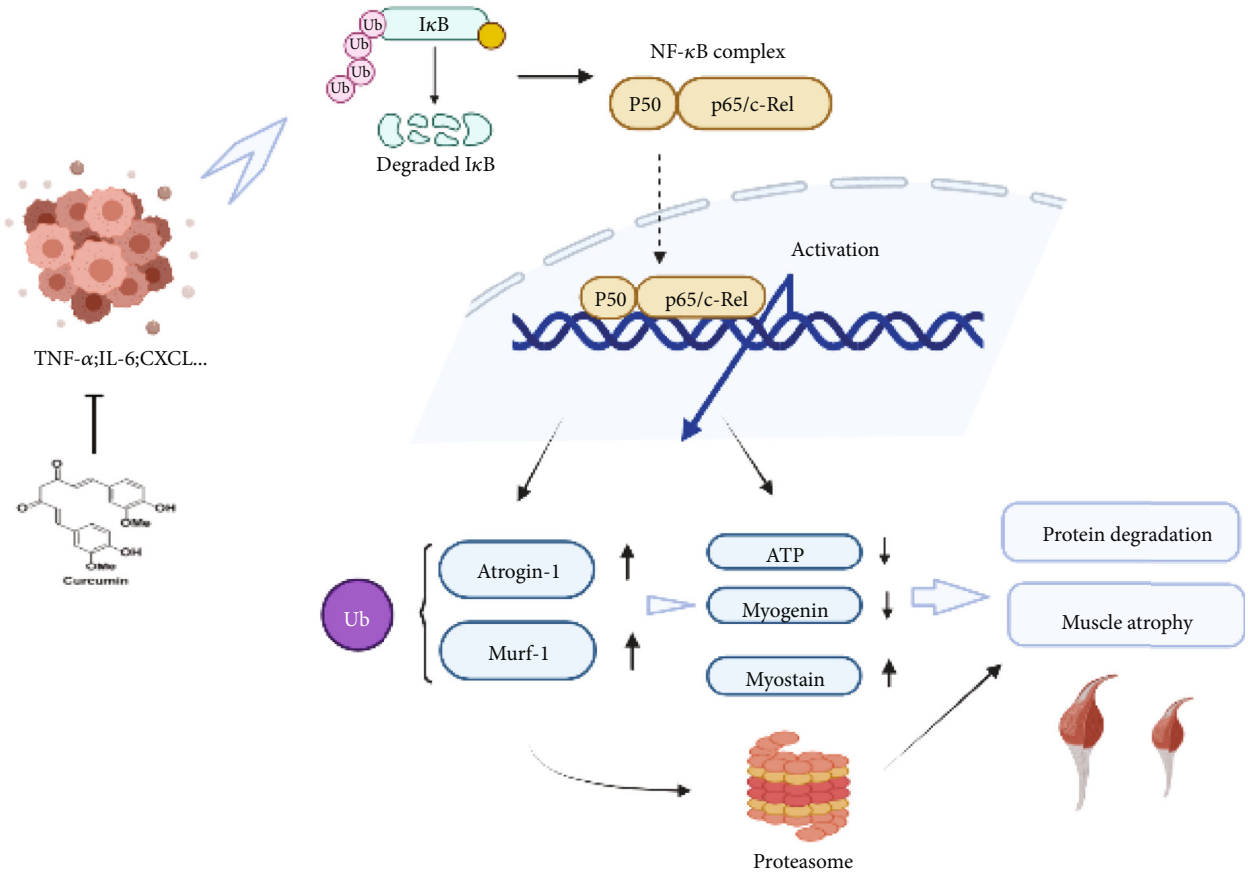

Figure 9: Therapeutic mechanism of curcumin on muscle atrophy in triple-negative breast cancer cachexia.

gastrocnemius of mice in model group gastrocnemius were significantly higher than those in the healthy group, while curcumin partially inhibited elevated levels of IL-6 and TNF-α in tumor-bearing mice, which indicate the anti-inflammation ability of curcumin in TNBC-cachexia. Myostatin and myogenin are important regulators of muscle proteolysis and synthesis, and they play a key role in maintaining the steady-state balance of muscle mass [44]. Our results showed that myostatin expression was higher in the model group but dropped significantly in the curcumin group. Myogenin had opposite results. Therefore, we suggest that curcumin may reduce the expression of muscle degrading factor myostatin and increase the myogenic factor myogenin to achieve the effect of reducing cachexia-related muscle atrophy.

Degradation of muscle proteins through the ubiquitin-proteasome pathway is also a form of muscle atrophy. Previous studies have shown that atrogin-1 and MuRF-1, two muscle-specific E3 ubiquitin ligases, are overexpressed in skeletal muscle in cancer-induced muscle atrophy [45, 46]. In addition, *in vitro* experiments have shown that increased myostatin is often accompanied by increased MAFbx expression [47]. We used RT-qPCR and WB analysis to verify whether curcumin alleviated muscle loss in mice with tumor cachexia by reducing the level of ubiquitination. The results showed that the expression levels of atrogin-1 and MuRF-1 in the gastrocnemius muscle of the model group were significantly higher than those in the healthy group; curcumin reversed this increasing trend. It was consistent with these previous reports and also indicated a regulation role of curcumin on atrogin-1 and MuRF-1. The release of inflammatory factors in the tumor microenvironment can activate the NF-κB pathway, which not only directly induces muscle atrophy but also mediates the transcription of atrogin-1 and MuRF-1, leading to increased protein degradation, which indicates that NF-KB is expected to become a therapeutic target for muscular dystrophy [20, 48]. The RT-qPCR analysis found that NF-κB transcription expression was increased in the model group, while the curcumin group decreased its expression. Western blot results of phosphorylated NF-κB (P-P65) observed the similar tendency. Therefore, we speculate that activation of the NF-κB pathway is one of the mechanisms of curcumin in reducing tumor cachexia and muscle loss.

Based on the above results, we demonstrate that curcumin not only inhibits the proliferation of TNBC but also reduces the weight and skeletal muscle loss associated with tumor-cachexia. The experimental conclusions suggest that its anticachexia effect may be through reducing the expression of inflammatory factors, inhibiting the activation of the NF-κB pathway, reducing the level of ubiquitination in muscle tissue, alleviating fiber mitochondrial dysfunction, improving the malnutrition status and the energy metabolism of muscle tissue reduces the degradation of muscle and increases its synthesis (Figure 9). These mechanisms interact with each other and work together to improve the quality and function of skeletal muscle.

5. Conclusion

In conclusion, curcumin not only inhibits the proliferation of TNBC but also targets the NF-κB/UPS axis ameliorating muscle atrophy in TNBC-cachexia mice.

Abbreviations

ADP: Adenosine diphosphate
AMP: Adenosine monophosphate
ATP: Adenosine triphosphate
BCA: Bicinchoninic acid
ELISA: Enzyme-linked immunosorbent assay
FDR: False discovery rate
FIDs: Free induction decays
gf: Gram force
HE: Hematoxylin-eosin
^{1}HNMR: H-nuclear magnetic resonance
IL-6: Interleukin-6
KEGG: Kyoto Encyclopedia of Genes and Genomes
MPC: Mitochondrial pyruvate carrier
NF-κB: Nuclear factor-k-gene binding
PLS-DA: The partial least-squares discriminant analysis
PVDF: Polyvinylidene fluoride
RT-PCR: Reverse transcription-polymerase chain reaction
SDS-PAGE: Sodium dodecyl sulfate-polyacrylamide gel electrophoresis
SEM: Standard error of the mean
TCA cycle: Tricarboxylic acid cycle
TEM: Transmission electron microscopy
TNBC: Triple-negative breast cancer
TNF-α: Tumor necrosis factor α
UPS: Ubiquitin-proteasome system
VIP: Variable influence on projection
WB: Western blot.

Data Availability

The datasets used and/or analyzed during the current study are available from the corresponding author on reasonable request.

Ethical Approval

All animal studies were performed in Zhejiang Chinese Medical University Laboratory Animal Center, according to protocols approved by the Institutional Animal Care and Use Committee of Zhejiang Chinese Medical University.

Conflicts of Interest

The authors declare that they have no competing interests. The authors declare that the research was conducted in the absence of any commercial or financial relationships that could be construed as a potential conflict of interest.

Authors' Contributions

Jin Zhang performed the research, acquired and analyzed the data, and wrote the first version of the manuscript; Haitao Chen and Xinrong Li analyzed the data and contributed to the manuscript writing; Jin Zheng, Chenxiao Ye, and Zewei Zhang discussed the data and edited the manuscript; Fan Zhang performed the ^{1}HNMR measurements; Qinghua Yao and Yong Guo supervised the study and designed the research. The authors read and approved the final manuscript. Jin Zhang, Jin Zheng, and Haitao Chen contributed equally to this work.

Acknowledgments

Thanks are due to the Zhejiang Chinese Medical University for providing the experimental place and equipment and all the participating researchers for their hard work. This work was supported by the National Natural Science Foundation

of China (81973805), Natural Science Foundation Project of Zhejiang Province (LY21H290001), and Zhejiang Medical and Health Platform Project (2021KY569).

Supplementary Materials

Supplementary Table S1 is provided. *(Supplementary Materials)*

References

[1] H. A. Wahba and H. A. El-Hadaad, "Current approaches in treatment of triple-negative breast cancer," *Cancer Biology & Medicine*, vol. 12, no. 2, pp. 106–116, 2015.

[2] P. F. Peddi, M. J. Ellis, and C. Ma, "Molecular basis of triple negative breast cancer and implications for therapy," *International journal of breast cancer*, vol. 2012, Article ID 217185, 7 pages, 2012.

[3] K. C. H. Fearon, D. J. Glass, and D. C. Guttridge, "Cancer cachexia: mediators, signaling, and metabolic pathways," *Cell Metabolism*, vol. 16, no. 2, pp. 153–166, 2012.

[4] P. Schwartsburd, "Cancer-induced reprogramming of host glucose metabolism: "vicious cycle" supporting cancer progression," *Frontiers in Oncology*, vol. 9, pp. 218–218, 2019.

[5] R. D. Dolan, A. S. Almasaudi, L. B. Dieu, P. G. Horgan, S. T. McSorley, and D. C. McMillan, "The relationship between computed tomography-derived body composition, systemic inflammatory response, and survival in patients undergoing surgery for colorectal cancer," *Journal of Cachexia, Sarcopenia and Muscle*, vol. 10, no. 1, pp. 111–122, 2019.

[6] A. M. Ryan, C. M. Prado, E. S. Sullivan, D. G. Power, and L. E. Daly, "Effects of weight loss and sarcopenia on response to chemotherapy, quality of life, and survival," *Nutrition*, vol. 67-68, article 110539, 2019.

[7] X. Feng, Z. Wang, F. Wang et al., "Dual function ofVGLL4 in muscle regeneration," *The EMBO Journal*, vol. 38, no. 17, 2019.

[8] K. Fearon, F. Strasser, S. D. Anker et al., "Definition and classification of cancer cachexia: an international consensusvol. 12, no. 5, pp. 489–495.

[9] K. M. Herremans, A. N. Riner, M. E. Cameron, and J. G. Trevino, "The microbiota and cancer cachexia," *International Journal of Molecular Sciences*, vol. 20, no. 24, p. 6267, 2019.

[10] S. Bins, S. L. W. Koolen, and R. H. J. Mathijssen, "Pembrolizumab exposure–response assessments challenged by association of cancer cachexia and catabolic clearance—letter," *Clinical Cancer Research*, vol. 25, no. 10, pp. 3192–3192, 2019.

[11] L. B. Bindels and N. M. Delzenne, "Muscle wasting: the gut microbiota as a new therapeutic target?," *The International Journal of Biochemistry & Cell Biology*, vol. 45, no. 10, pp. 2186–2190, 2013.

[12] R. Barreto, D. L. Waning, H. Gao, Y. Liu, T. A. Zimmers, and A. Bonetto, "Chemotherapy-related cachexia is associated with mitochondrial depletion and the activation of ERK1/2 and p 38 MAPKs," *Oncotarget*, vol. 7, no. 28, pp. 43442–43460, 2016.

[13] S. Acharyya and D. C. Guttridge, "Cancer cachexia signaling pathways continue to emerge yet much still points to the Proteasome: Fig 1," *Clinical Cancer Research*, vol. 13, no. 5, pp. 1356–1361, 2007.

[14] S. C. Bodine, E. Latres, S. Baumhueter et al., "Identification of ubiquitin ligases required for skeletal muscle atrophy," *Science*, vol. 294, no. 5547, pp. 1704–1708, 2001.

[15] M. D. Gomes, S. H. Lecker, R. T. Jagoe, A. Navon, and A. L. Goldberg, "Atrogin-1, a muscle-specific F-box protein highly expressed during muscle atrophy," *Proceedings of the National Academy of Sciences of the United States of America*, vol. 98, no. 25, pp. 14440–14445, 2001.

[16] C. J. Wray, J. M. V. Mammen, D. D. Hershko, and P. O. Hasselgren, "Sepsis upregulates the gene expression of multiple ubiquitin ligases in skeletal muscle," *The International Journal of Biochemistry & Cell Biology*, vol. 35, no. 5, pp. 698–705, 2003.

[17] J. L. Halle, G. S. Pena, H. G. Paez et al., "Tissue-specific dysregulation of mitochondrial respiratory capacity and coupling control in colon-26 tumor-induced cachexia," *American Journal of Physiology. Regulatory, Integrative and Comparative Physiology*, vol. 317, no. 1, pp. R68–R82, 2019.

[18] A. R. Kelleher, T. J. Fairchild, and S. Keslacy, "STZ-induced skeletal muscle atrophy is associated with increased p 65 content and downregulation of insulin pathway without NF-κB canonical cascade activation," *Acta Diabetologica*, vol. 47, no. 4, pp. 315–323, 2010.

[19] J. J. Hulmi, M. Silvennoinen, M. Lehti, R. Kivelä, and H. Kainulainen, "Altered REDD1, myostatin, and Akt/mTOR/FoxO/MAPK signaling in streptozotocin-induced diabetic muscle atrophy," *American Journal of Physiology-Endocrinology and Metabolism*, vol. 302, no. 3, pp. E307–E315, 2012.

[20] G. Zhang, Z. Liu, H. Ding, H. Miao, J. M. Garcia, and Y. P. Li, "Toll-like receptor 4 mediates Lewis lung carcinoma-induced muscle wasting via coordinate activation of protein degradation pathways," *Scientific Reports*, vol. 7, no. 1, pp. 2273–2278, 2017.

[21] A. Nicolini, P. Ferrari, M. C. Masoni et al., "Malnutrition, anorexia and cachexia in cancer patients: a mini-review on pathogenesis and treatment," *Biomedicine & Pharmacotherapy*, vol. 67, no. 8, pp. 807–817, 2013.

[22] O'Connell, Pin, Couch, and Bonetto, "Treatment with soluble activin receptor type IIB alters metabolic response in chemotherapy-induced cachexia," *Cancers*, vol. 11, no. 9, p. 1222, 2019.

[23] F. Pin, R. Barreto, M. E. Couch, A. Bonetto, and T. M. O'Connell, "Cachexia induced by cancer and chemotherapy yield distinct perturbations to energy metabolism," *Journal of Cachexia, Sarcopenia and Muscle*, vol. 10, no. 1, pp. 140–154, 2019.

[24] T. W. Corson and C. M. Crews, "Molecular understanding and modern application of traditional medicines: triumphs and trials," *Cell*, vol. 130, no. 5, pp. 769–774, 2007.

[25] J. Epstein, I. R. Sanderson, and T. T. Macdonald, "Curcumin as a therapeutic agent: the evidence fromin vitro, animal and human studies," *The British Journal of Nutrition*, vol. 103, no. 11, pp. 1545–1557, 2010.

[26] T. D. Cardaci, S. B. Machek, D. T. Wilburn, P. S. Hwang, and D. S. Willoughby, "Ubiquitin proteasome system activity is suppressed by curcumin following exercise-induced muscle damage in human skeletal muscle," *Journal of the American College of Nutrition*, vol. 40, no. 5, pp. 401–411, 2021.

[27] J. M. Argilés, S. Busquets, B. Stemmler, and F. J. López-Soriano, "Cancer cachexia: understanding the molecular basis," *Nature Reviews Cancer*, vol. 14, no. 11, pp. 754–762, 2014.

[28] S. Acharyya, K. J. Ladner, L. L. Nelsen et al., "Cancer cachexia is regulated by selective targeting of skeletal muscle gene products," *The Journal of Clinical Investigation*, vol. 114, no. 3, pp. 370–378, 2004.

[29] K. Fearon, J. Arends, and V. Baracos, "Understanding the mechanisms and treatment options in cancer cachexia," *Nature Reviews Clinical Oncology*, vol. 10, no. 2, pp. 90–99, 2013.

[30] K. Amano, T. Morita, J. Miyamoto, T. Uno, H. Katayama, and R. Tatara, "Perception of need for nutritional support in advanced cancer patients with cachexia: a survey in palliative care settings," *Supportive Care in Cancer*, vol. 26, no. 8, pp. 2793–2799, 2018.

[31] M. J. Tisdale, "Loss of skeletal muscle in cancer: biochemical mechanisms," *Frontiers in Bioscience*, vol. 6, no. 3, pp. D164–D174, 2001.

[32] P. Collins, C. Bing, P. McCulloch, and G. Williams, "Muscle UCP-3 mRNA levels are elevated in weight loss associated with gastrointestinal adenocarcinoma in humans," *British Journal of Cancer*, vol. 86, no. 3, pp. 372–375, 2002.

[33] P. Puigserver, J. Rhee, J. Lin et al., "Cytokine Stimulation of Energy Expenditure through p38 MAP Kinase Activation of PPARγ Coactivator-1," *Molecular Cell*, vol. 8, no. 5, pp. 971–982, 2001.

[34] R. F. Johnson, I. Witzel, and N. D. Perkins, "p53-Dependent regulation of mitochondrial energy production by the RelA subunit of NF-κB," *Cancer Research*, vol. 71, no. 16, pp. 5588–5597, 2011.

[35] C. Chinopoulos and V. Adam-Vizi, "Mitochondria as ATP consumers in cellular pathology," *Biochimica et Biophysica Acta (BBA) - Molecular Basis of Disease*, vol. 1802, no. 1, pp. 221–227, 2010.

[36] S. Lahiri, H. Kim, I. Garcia-Perez et al., "The gut microbiota influences skeletal muscle mass and function in mice," *Science Translational Medicine*, vol. 11, no. 502, 2019.

[37] S. G. Miller, P. S. Hafen, and J. J. Brault, "Increased adenine nucleotide degradation in skeletal muscle atrophy," *International Journal of Molecular Sciences*, vol. 21, no. 1, p. 88, 2020.

[38] D. Rudman, C. W. Sewell, and J. D. Ansley, "Deficiency of carnitine in cachectic cirrhotic patients," *The Journal of Clinical Investigation*, vol. 60, no. 3, pp. 716–723, 1977.

[39] W. Q. Lv, X. Lin, H. Shen et al., "Human gut microbiome impacts skeletal muscle mass via gut microbial synthesis of the short-chain fatty acid butyrate among healthy menopausal women," *Journal of Cachexia, Sarcopenia and Muscle*, vol. 12, no. 6, pp. 1860–1870, 2021.

[40] Y. Zhang, P. V. Taufalele, J. D. Cochran et al., "Mitochondrial pyruvate carriers are required for myocardial stress adaptation," *Nature Metabolism*, vol. 2, no. 11, pp. 1248–1264, 2020.

[41] K. K. Harmon, J. R. Stout, D. H. Fukuda, P. S. Pabian, E. S. Rawson, and M. S. Stock, "The application of creatine supplementation in medical rehabilitation," *Nutrients*, vol. 13, no. 6, p. 1825, 2021.

[42] T. Golias, M. Kery, S. Radenkovic, and I. Papandreou, "Microenvironmental control of glucose metabolism in tumors by regulation of pyruvate dehydrogenase," *International Journal of Cancer*, vol. 144, no. 4, pp. 674–686, 2019.

[43] N. Shyh-Chang, *Metabolic changes during cancer cachexia pathogenesis*, Springer, Singapore: Singapore, 2017.

[44] F. Jeanplong, J. J. Bass, H. K. Smith et al., "Prolonged underfeeding of sheep increases myostatin and myogenic regulatory factor Myf-5 in skeletal muscle while IGF-I and myogenin are repressed," *The Journal of Endocrinology*, vol. 176, no. 3, pp. 425–437, 2003.

[45] J. Lagirand-Cantaloube, N. Offner, A. Csibi et al., "The initiation factor eIF3-f is a major target for atrogin 1/MAFbx function in skeletal muscle atrophy," *The EMBO Journal*, vol. 27, no. 8, pp. 1266–1276, 2008.

[46] T. N. Stitt, D. Drujan, B. A. Clarke et al., "The IGF-1/PI3K/Akt pathway prevents expression of muscle atrophy-induced ubiquitin ligases by inhibiting FOXO transcription factors," *Molecular Cell*, vol. 14, no. 3, pp. 395–403, 2004.

[47] S. Lokireddy, I. W. Wijesoma, S. K. Sze, C. McFarlane, R. Kambadur, and M. Sharma, "Identification of atrogin-1-targeted proteins during the myostatin-induced skeletal muscle wasting," *American Journal of Physiology. Cell Physiology*, vol. 303, no. 5, pp. C512–C529, 2012.

[48] D. Cai, J. D. Frantz, N. E. Tawa Jr. et al., "IKKβ/NF-κB Activation Causes Severe Muscle Wasting in Mice," *Cell*, vol. 119, no. 2, pp. 285–298, 2004.

Hindawi
Mediators of Inflammation
Volume 2021, Article ID 2979124, 10 pages
https://doi.org/10.1155/2021/2979124

Research Article

Mesenchymal Stem Cell-Derived Exosomes Modulate Chondrocyte Glutamine Metabolism to Alleviate Osteoarthritis Progression

Kai Jiang,[1] Ting Jiang,[1] Yang Chen,[2] and Xinzhan Mao[1]

[1]*Department of Orthopedics, The Second Xiangya Hospital, Central South University, China*
[2]*Department of Orthopedics, The Third Xiangya Hospital, Central South University, China*

Correspondence should be addressed to Xinzhan Mao; xinzhan.mao@csu.edu.cn

Received 28 May 2021; Revised 21 October 2021; Accepted 22 November 2021; Published 27 December 2021

Academic Editor: Xiaolu Jin

Osteoarthritis (OA) had a high incidence in people over 65 years old, and there is currently no drug that could completely cure it. This study is aimed at studying the role of exosomes in regulating glutamine metabolism in the treatment of OA. First, we identified the exosomes extracted from the mouse OA model's bone marrow mesenchymal stem cells (MSC). *In vitro*, compared with the control group, the cell apoptosis in the OA group increased, while the cell proliferation of the OA group was suppressed. After exosomal treatment, cell apoptosis and cell proliferation were reversed. Inflammatory factors (TNFα, IL-6), glutamine metabolic activity-related proteins (c-MYC, GLS1), glutamine, and GSH/GSSG were increased in the OA group. The overexpression of c-MYC reduced the therapeutic effect of exosomes. At the same time, we found that chondrocyte functional factors (collagen II, Aggrecan) were improved under the treatment of exosomes. However, oe-c-MYC reversed the therapeutic effect of exosomes. *In vivo*, we found that the running capacity of the mice in the OA group was reduced, and the cartilage tissue was severely damaged. In addition, TNFα, IL-6, and chondrocyte apoptosis increased, while the metabolism of collagen II, Aggrecan, and glutamate decreased in the OA group. After exosomal treatment, the mice's exercise capacity, tissue damage, inflammation, and chondrocyte function were improved, and glutamate metabolism was increased. This study showed that exosomes regulated the level of chondrocyte glutamine metabolism by regulating c-MYC, thereby alleviating OA.

1. Introduction

Osteoarthritis (OA) is a common delayed and degenerative disease. Among the elderly over 60 years old, about 10% of men and 18% of women are deeply troubled by it [1]. Age, obesity, metabolic syndrome, genetic susceptibility, disorganization, acute joint injury, and decreased sex hormone levels may be risk factors for OA [2, 3]. Pain is the biggest symptom of OA patients. In addition, OA can also cause joint swelling and spasm, which limit people's daily activities [3]. So far, there is no way to cure OA completely. People can only relieve pain and stiffness by changing risk factors, such as physical therapy (PT) and pharmaceutical treatment [3]. For example, previous studies have shown that weight loss can effectively reduce the knee load of OA patients to improve OA symptoms [4]. Another study showed that supervised exercise, personalized manual therapy, and a family exercise program could effectively reduce the OA index and relieve OA symptoms [5]. Some drugs such as glucosamine and chondroitin, acetaminophen, and celecoxib can be used to reduce the pain of OA [6]. However, these treatments can only relieve pain and control symptoms but cannot cure OA. Cartilage cells and inflammation are considered to play an important role in OA, but the current research on the pathogenesis of OA is still not thorough enough. Therefore, we urgently need to study the pathogenesis and treatment of OA.

In recent years, with the increasing research on exosomes, we found that exosomes have extensive and unique advantages in disease diagnosis and treatment [7]. Due to the endogeneity of exosomes, it can prevent the body from producing antibodies to exosomes and make exosomes have

better biocompatibility [7]. And because of the heterogeneity of exosomes, they can easily carry various proteins on the surface and then enter cells [8]. Exosomes secreted by mesenchymal stem cells (MSC) have a significant role in the treatment of skin restenosis [9], myocardial ischemia/reperfusion injury [10], and inflammatory diseases [11].

Glutamine could be hydrolyzed to ammonium ion ($NH4^+$) and glutamic acid, and then, glutamic acid was converted to glutamic acid α-ketopentanate (α-KG) [12]. After that, α-KG entered the tricarboxylic acid cycle (TCA cycle) and generated adenosine triphosphate (ATP) by producing nicotinamide adenine dinucleotide (NADH) and flavin adenine dinucleotide ($FADH_2$) [13]. ATP is an essential fuel for cell activity. Therefore, the higher the content of glutamine, the more conducive to cell activity [13]. Reduced glutathione (GSH) is a metabolite of glutamine [14]. Glutathione depletion results in exacerbation of damage by oxidative and nitrosative stress and increased levels of proinflammatory mediators [15]. The ratio of reduced glutathione to oxidized glutathione (GSH/GSSG) determines the activation of c-Jun n-terminal kinase (JNK) and mitogen-activated protein kinase (MAPK) pathways, thereby determining proinflammatory cell transcription of factor [15]. Moreover, GSH is an antioxidant in the cell, and GSH/GSSG can be used as a marker of cell antioxidant capacity [16]. The transcription of factor c-MYC was widely involved in the key processes of normal cell proliferation, differentiation, and metabolism [17]. Studies have shown that c-MYC can enhance glutamate metabolism by increasing glutaminase (GLS) [17]. But in OA, whether c-MYC could regulate glutamate metabolism was not yet known. Synovial fluid (SF) is located in the articular cavity, which has a lubrication function and contains protein/metabolite markers of systemic diseases [18]. A previous study has shown that the content of glutamine in OA synovial fluid (SF) was higher than that of rheumatoid arthritis (RA), indicating that there were different expressions in glutamine metabolism [18]. Glutamine has an antioxidant function in OA and other inflammatory diseases [2]. Therefore, based on the above research, we intend to explore the role of MSC-exosomes in regulating glutamine metabolism of chondrocytes in OA and provide a new treatment for OA.

2. Materials and Methods

2.1. Animal Experiments. Thirty male Sprague Dawley (SD) rats were purchased from Hunan Sja Laboratory Animal Co., Ltd. The rats were adaptively fed for one week. The rats were randomly divided into three groups: sham group, OA group, and OA+exosome group, with 10 rats in each group. Rats in the sham group were only treated with incision and suture of the joint capsule. The OA model was established by anterior cruciate ligament transection (ACLT) [19]. Ketamine/xylazine was injected intraperitoneally according to body weight. The corneal reflex and toe reflex were observed. After the disappearance, the skin of both hind limbs was prepared, iodophor alcohol disinfection was carried out, and a sterile operation sheet was laid. The skin, fascia, and tendon were cut along the left and right knee joints' inner edge of the patellar tendon to dislocate the patella laterally. The anterior cruciate ligament was cut under direct vision. After the operation, the incision was sutured layer by layer and the skin around the incision was disinfected with alcohol. Four weeks later, cartilage wear was determined. The OA+exosome group rats were used to establish the ACLT model of bilateral hind limb joint injury. Four weeks later, after cartilage wear was determined; 100 μg of exosomes in 50 μl of PBS was injected into the joint cavity of the bilateral hind. After euthanasia, the tissue and peripheral blood were collected.

2.2. Preparation of Exosomes. According to the method of 2.1, the OA rat model was established, and MSCs were isolated from bone marrow. The MSCs were cultured in the DMEM medium containing 10% fetal bovine serum (FBS; GIBCO) and 1% penicillin-streptomycin. When the cell density was about 80%, the MSCs were digested by trypsin and passaged in two. The MSCs were cultured, and exosomes were prepared. After cells were cultured in a serum-free medium for 24 h, the cell supernatant was collected after centrifuging at 3,000 rpm for 15 min to remove cells and debris. The exosomes were precipitated from the supernatant by centrifugation at 100,000 rpm for 1.5 h at 4°C. The culture supernatant was removed. The sediment at the bottom was the exosomes. The exosomes were carefully immobilized with 1 ml of 2.5% glutaraldehyde for 1 h.

2.3. Cell Culture. Chondrocytes were isolated from rat knee joints. The cells were divided into three groups: control group, OA group, and OA+exosome group. The cells were seeded on a 6-well plate with 3 multiple wells in each group. Control group cells were cultured normally. OA group cells were treated with 10 ng/ml IL-1β [20]; in the OA+exosome group, the OA model was established and the cells were treated with 5 μg/ml exosomes for 48 h. In addition, to study whether MSC-derived exosome regulated chondrocyte glutamate metabolism through c-MYC, we established a c-MYC overexpression cell line of rat chondrocyte. The c-MYC overexpression plasmid oe-c-MYC and the overexpression empty plasmid oe-NC were constructed in HonorGene Co., Ltd., and they were used to treat the cells of the OA+exosome group to detect the regulatory effect of c-MYC on the cells. The cells were divided into five groups: control group, OA group, OA+exosome group, OA+exosome+oe-NC group, and OA+exosome+oe-c-MYC group. The control, OA, and OA+exosome groups were treated with the same way as before. The OA+exosome+oe-NC and OA+exosome+oe-c-MYC groups were transfected with oe-NC and oe-c-MYC, respectively.

2.4. Running Tests. After 4 weeks of modeling, 5 rats in each group were kept and fed until the sixth week. All rats were placed on the treadmill. When the rate was set at 20 m/min, rats in the OA and sham groups did not move. When the rate was set at 15 m/min, the rats in the OA group did not move under 1 mA electrical stimulation while the sham group moved. The treadmill speed was set at 10 m/min, and all rats moved. When the rats stopped moving, we

stimulated them with 1 mA current. All groups of rats were moving 37.69 m. Finally, we counted the number of shocks.

2.5. Hematoxylin-Eosin (HE) Staining. After the knee joint was fixed for 24 h, it was embedded in paraffin. The embedded tissue was sectioned. After baking at 60°C for 12 h, the slides were dewaxed to water. After dyeing with hematoxylin and eosin, gradient alcohol (95-100%) was dehydrated for 5 min. The slides were removed and placed in xylene for 10 min, twice. After sealing with neutral gum, the specimens were observed under a microscope and photographed.

2.6. Safranin Solid Green Staining. Similarly, the tissue sections were dewaxed to water. After the slides were stained with solid green dye solution, they were stained with safranin and washed with distilled water. A hairdryer was used to dry the slides. The slides were placed in xylene for 10 min, twice. Neutral gum was used to mount the sections and observe the slides with a microscope and took photos.

2.7. Terminal Deoxynucleotidyl Transferase-Mediated dUTP-Biotin Nick End Labeling (TUNEL) Assay. Similarly, the tissue sections were dewaxed to water. The slides were stained according to the TUNEL Kit (Shanghai Yisheng biology, No. 40306es50). Each slide was dripped with 100 μl of Proteinase K working solution and reacted at 37°C for 20 min. The slides were rinsed with PBS. 100 μl 1 × Equilibration Buffer was added to each slide, and the slides were incubated at room temperature for 10 min. Most of the 1 × Equilibration Buffer was absorbed with an absorbent paper. Then, 50 μl of TdT buffer was added to the slides. The slides were incubated at room temperature for 60 min, and then they were rinsed with PBS. After the slides were stained, DAPI working solution was used to stain the nucleus for 10 min. After mounting the slides, it was observed and pictures were taken under a microscope. The number of apoptotic cells was counted.

2.8. Immunohistochemical (IHC) Assay. Similarly, the tissue sections were dewaxed to water. According to the manufacturer's instructions, the slides were stained with a two-step Kit (ZSGB-BIO, No. pv-8000). An appropriate amount of endogenous peroxidase blocker was added to the slides. And the slides were incubated for 10 min at room temperature. The slides were rinsed with PBS. The slides were dropped with 100 μl primary antibodies (c-MYC, GLS) and incubated at 37°C for 60 min. PBS was used to rinse the sections. 100 μl of secondary antibodies (anti-rabbit, rabbit, rabbit-IgG antibody-HRP polymer) was added dropwise. And the slides were incubated at room temperature for 20 min. The sections were rinsed with PBS. An appropriate amount of freshly prepared DAB chromogenic solution was added to the slides. Hematoxylin was used to restain the slides for 5-10 min, and the slides were rinsed with distilled water. PBS was used to turn the slides blue. The slices were dehydrated, cleared, and mounted. At last, the slides were observed under a microscope and photos were taken.

2.9. Real-Time Quantitative PCR (RT-qPCR). Trizol kit was used to extract total RNA from tissues and cells. The concentrations of RNA were 100 ng/μl-200 ng/μl, and OD260/OD280 was 1.8-2.0. The HiFscript cDNA synthesis kit was used to reverse the mRNAs into cDNAs according to the manufacturer's instructions. β-Actin was used as an internal control. The reaction was predenatured at 95°C for 10 min. Then, the reaction was denatured at 95°C for 15 s, annealed and extended at 60°C for 30 s and subjected to 40 denaturation cycles. Primer sequences were used as follows: β-actin—F: ACATCCGTAAAGACCTCTATGCC, β-actin—R: TACTCCTGCTTGCTGATCCAC; TNFα—F: CCCCTCTATTTATAATTGCACCT; TNFα—R: CTGGTAGTTTAGCTCCGTTT; IL-6—F: TCACTATGAGGTCTACTCGG; IL-6—R: CATATTGCCAGTTCTTCGTA; Aggrecan—F: ACAGACACCCCTACCCTTGC, Aggrecan—R: CCTCACATTGCTCCTGGTCGAT; c-MYC—F: ACTCGGTGCAGCCCTATTTC, c-MYC—R: GTAGCGACCGCAACATAGGA; and GLS1—F: CTGCTGCAGAGGGTGGAATA, GLS1—R: GAGGTGTGTACTGGACTTGGT.

2.10. Western Blot (WB). According to the instructions of the BCA protein quantification kit, extract the protein of exosomes in the cell or cell supernatant, and determine the protein concentration. The protein was separated by 10% SDS-PAGE gel and then transferred to the PVDF membrane (Millipore, Bedford, MA, USA). 5% skimmed milk powder was prepared with 1 × PBST, and the membrane was immersed and placed at room temperature for 90 min. The primary antibodies TNFα (1 : 1,000, No. ab6671, Abcam), IL-6 (1 : 1,000, rabbit, bs-0782r, bioss), c-MYC (1 : 10,000, rabbit, ab32072, Abcam), GLS1 (1 : 1,000, rabbit, ab156876, Abcam), CD63 (1 : 1,000, rabbit, ab134045, Abcam), CD9 (1 : 1,000, rabbit, ab92726, Abcam), CD81 (1 : 1,000, rabbit, ab109201, Abcam), GM130 (1 : 1,000, rabbit, ab52649, Abcam), and β-actin (1 : 5,000, mouse, 66009-1-Ig, Protein) were diluted in proportion with 1 × PBST; β-actin was an internal control. The membrane was incubated with the primary antibody for 90 min at room temperature. The secondary antibodies HRP goat anti-mouse IgG (1 : 5,000, SA00001-1, Proteintech) and HRP goat anti-rabbit IgG (1 : 6,000, SA00001-2, Proteintech) were diluted with 1 × PBST. The diluted secondary antibody was incubated with the membrane for 90 min at room temperature. ECL was used to develop color exposure. Finally, grayscale analysis was performed.

2.11. Enzyme-Linked Immunosorbent Assay (ELISA). The peripheral plasma of rats in each group was collected. According to the manufacturer's instructions, the ELISA kit (Enzyme Linked Bioengineering Co., Ltd., No. ml059460) was used to detect α-KG. The cell supernatant of each group was collected. The biochemical kits were used to detect GLN (Nanjing Jiancheng Institute of Biology, No. A073-1-1), GSH (Nanjing Jiancheng Institute of Biology, No. A006-2-1), and GSSG (Nanjing Jiancheng Institute of Biology, No. A061-1-1).

2.12. The Cells Were Identified by Flow Cytometry. The cells were cultured in 6-well plates and treated according to the groups. After reaching the predetermined time, the cells

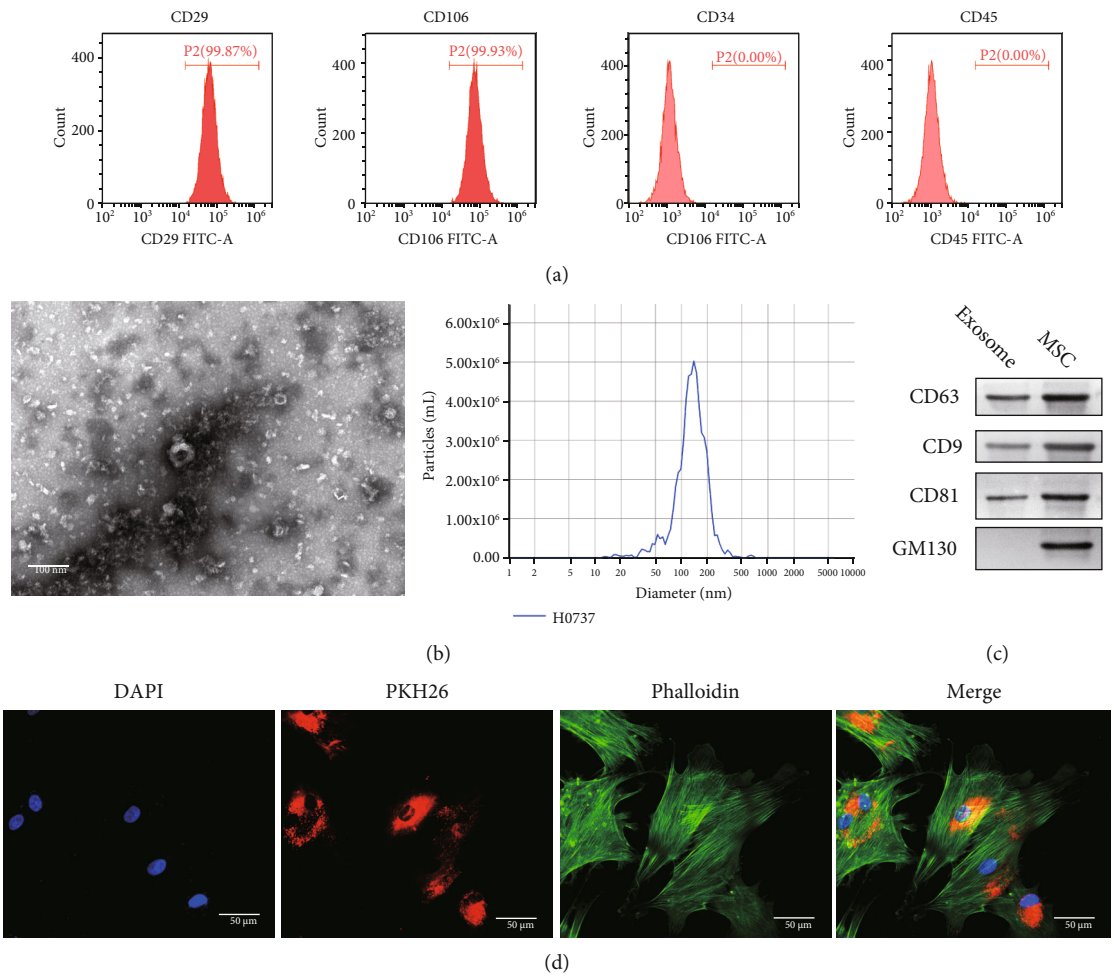

Figure 1: Isolation of bone marrow MSCs and uptake of exosomes. (a) The contents of CD29, CD106, CD34, and CD45 in exosomes were detected by flow cytometry. (b) The diameter of exosomes was detected by an electron microscope. Scale bar = 100 nm. (c) The exosome-associated proteins CD63, CD9, and CD81 were detected by WB. (d) IF was used to detect the uptake of exosomes by chondrocytes. DAPI was blue fluorescence, PKH26 was red fluorescence, phalloidin and was green fluorescence. Scale bar = 50 μm.

were digested. The cells were labeled with CD29, CD106, CD34, and CD45 antibodies, respectively. In MSC, CD29, CD106, and CD34 were positive, while CD34 and CD45 were negative.

2.13. Transmission Electron Microscopy. PBS was used to resuspended exosomes. Approximately 10 μg of exosomes resuspended in PBS was dropped on the para membrane. The exosomes were examined by an electron microscope and photographed.

2.14. Cell Apoptosis Assay. The cells were cultured in 6-well plates and treated according to the groups. After reaching the predetermined time, the cells were digested. After the cells were suspended in binding buffer, 5 μl V-FITC and 5 μl PI were mixed with the cells. After 10 min of dark reaction, mixtures were detected by the flow cytometer.

2.15. Statistical Analysis. All experiments were repeated 3 times, and the data were expressed as the average value ± standard deviation (SD). GraphPad Prism 9.0 was used to analyze the data. For the comparison between the two groups, we used Student's t-test to compare. For more than two independent groups, we used one-way ANOVA to compare. And the Tukey test was added if necessary. $P < 0.05$ was considered statistically significant.

3. Results

3.1. Isolation of Bone Marrow MSCs and Uptake of Exosomes. To determine the therapeutic effect of MSC secreted exosomes on OA, we first established an OA rat model and extracted MSC from the spinal cord. To identify whether the cells were MSC, we used flow cytometry to identify the cells. The results showed that CD29 and CD106 were positive and CD34 and CD45 were negative, which indicated that the cells were indeed MSC (Figure 1(a)) [21]. MSCs were cultured and exosomes were isolated from a serum-free supernatant. The exosomes were identified by electron microscopy (Figure 1(b)). The size of exosomes is generally 40-100 nm [22]. Then, we detected the contents of exosomal marker proteins CD63, CD9, CD81, and GM130 in

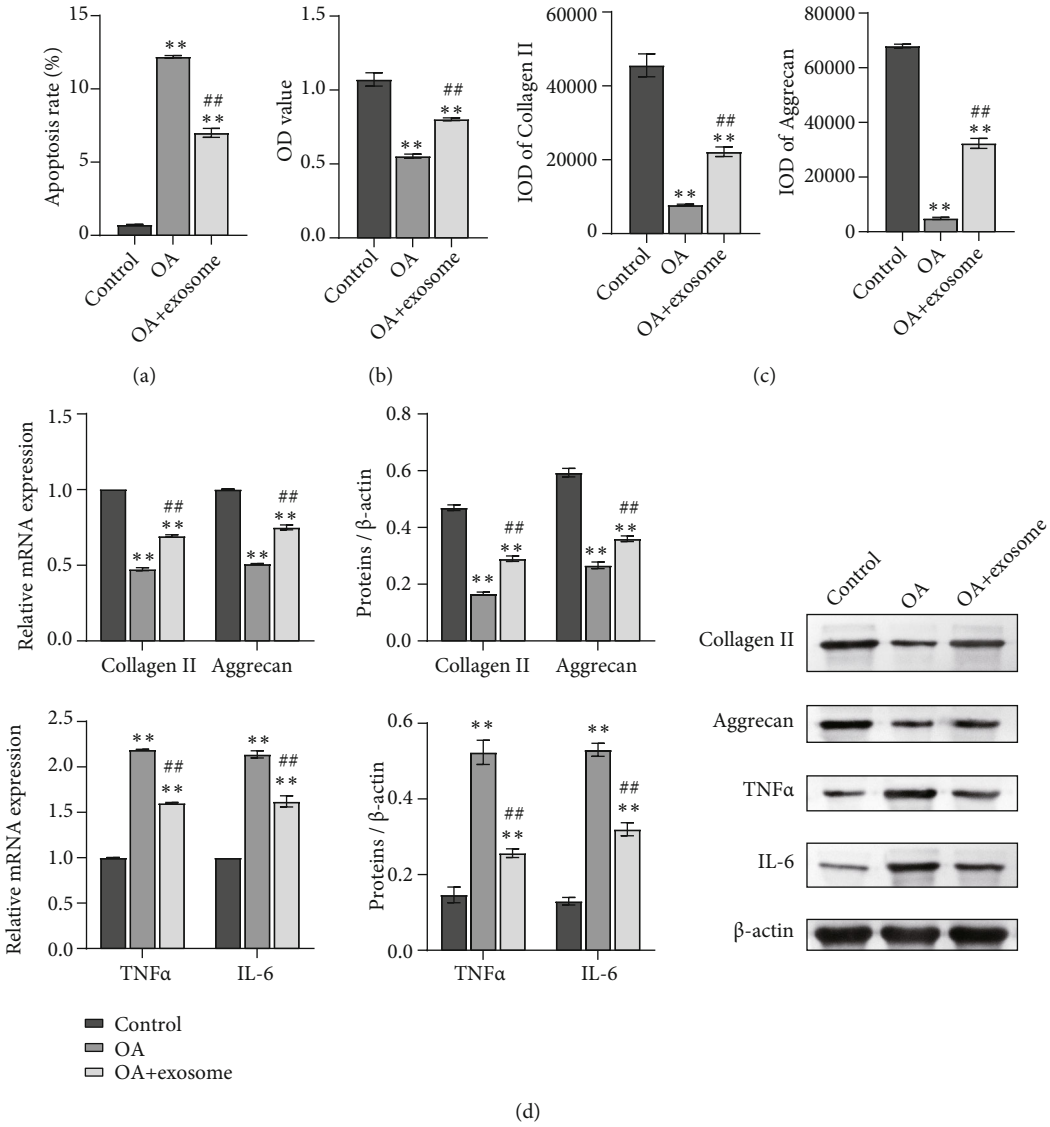

Figure 2: Exosomes affect cell function of OA chondrocytes. (a) Apoptosis was identified by flow cytometry. (b) The CCK8 method was used to detect cell proliferation. (c) Collagen II and Aggrecan of chondrocytes were detected by IF. (d) The mRNA and protein contents of collagen II, Aggrecan, TNFα, and IL-6 were detected by RT-qPCR and WB. $^{**}P < 0.01$ vs. control; $^{\#\#}P < 0.01$ vs. OA.

exosomes and MSC by WB [23]. The results showed that CD63, CD9, and CD81 were expressed in exosomes and MSC, while the GM130 protein was only expressed in MSC (Figure 1(c)). Therefore, the substance we extracted is indeed exosomes. PKH67 is a widely used exosomal marker [24, 25]. Exosomes were labeled with PKH67; cytoskeletons were labeled with F-actin and phalloidin combined with F-actin to prevent its depolymerization and poisoning cells. Fluorescence staining showed that the exosomes could be absorbed by chondrocytes (Figure 1(d)).

3.2. Exosomes Affect Cell Function and Glutamine Metabolism of OA Chondrocytes. To determine whether there are differences in the cell function and glutamate metabolism between the control, OA, and OA+exosome groups, we established the OA rat chondrocyte model *in vitro*. Cell apoptosis rate was identified by flow cytometry. The results showed that the apoptosis rate of the OA group was significantly higher than that of the control group, and exosome treatment reversed the increase of apoptosis (Figure 2(a), Figure S1A). Then, we used the CCK8 assay to detect the proliferation of cells. We found that compared with the control group, the proliferation rate of the OA group decreased, and exosome treatment reversed the effect of OA (Figure 2(b)). Collagen II and Aggrecan of chondrocytes were detected by IF to detect the function of chondrocytes. The results showed that OA decreased the expression of collagen II and Aggrecan, while exosomes played a positive role (Figure 2(c), Figure S1B). Furthermore, we detected the contents of collagen II and Aggrecan by RT-qPCR and WB, and the results were consistent with the results (Figure 2(d)). At the same time, to detect the inflammatory reaction in the cells, we used RT-qPCR and WB to detect the contents of TNFα and IL-6 in the cells

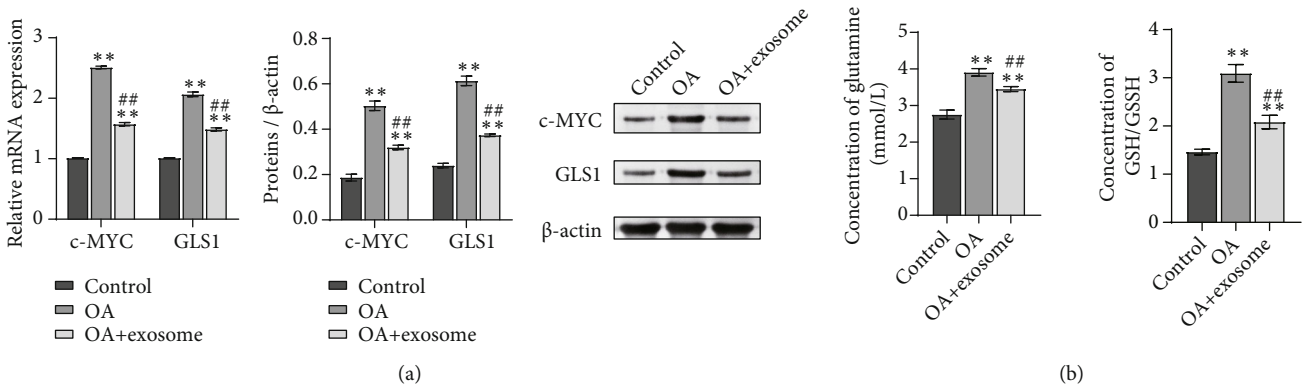

Figure 3: Exosomes affect glutamine metabolism of OA chondrocytes. (a) The contents of c-MYC and GLS1 were detected by biochemical kit. (b) The content of glutamine and GSH/GSSG in cells was detected by biochemical kit. $^{**}P < 0.01$ vs. the control; $^{\#\#}P < 0.01$ vs. OA.

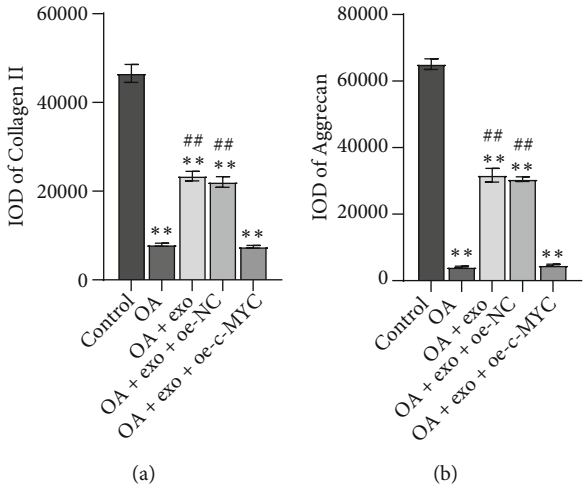

Figure 4: oe-c-MYC decreased the therapeutic effect of exosomes on OA chondrocytes and affected the function of OA chondrocytes. The expressions of collagen II (a) and Aggrecan (b) were detected by IF. $^{**}P < 0.01$ vs. control; $^{\#\#}P < 0.01$ vs. OA.

(Figure 2(d)). We found that exosomes regulated the levels of TNFα and IL-6 and reduced the inflammatory response.

After detecting the changes in cell function, we began to see changes in glutamate metabolism. A biochemical kit was utilized to detect the metabolism of glutamine. We found that the treatment of exosomes reduced the content of c-MYC and GLS1 (Figure 3(a)). In addition, the content of glutamine and GSH/GSSG in the cells was detected. The results showed that glutamine and GSH/GSSG content in the OA group increased while the exosome decreased (Figure 3(b)). These results suggested that exosomes affect glutamine metabolism in OA chondrocytes.

3.3. oe-c-MYC Decreased the Therapeutic Effect of Exosomes on OA Chondrocytes and Affected the Function of OA Chondrocytes and Glutamine Metabolism. A study has shown that exosomes downregulate the expression of c-MYC in breast cancer cells [26], but whether exosomes can affect glutamine metabolism of OA chondrocytes by downregulating c-MYC is unknown. Therefore, we constructed c-MYC overexpression vector (oe-c-MYC) and its control vector (oe-NC). OA+exosome was treated with oe-c-MYC and oe-NC, respectively. The changes of cell function and glutamate metabolism after overexpression of c-MYC were detected. Similarly, to detect cell function changes, we first detected the expressions of collagen II and Aggrecan by IF (Figures 4(a) and 4(b), Figure S2A-B). The results showed that the OA and OA+exosome groups were consistent with those of previous studies, while when exosomes were combined with oe-c-MYC, the positive rates of collagen II and Aggrecan were decreased. The results indicated that oe-c-Myc reduced the therapeutic effect of exosomes on OA chondrocytes and affected the function of cells. Next, to detect the changes in glutamate metabolism in each group, we used RT-qPCR and WB to detect the expression of glutamate metabolism activity-related proteins c-MYC and GLS1 in each group of cells (Figure 5(a)). In the next step, we used ELISA to detect the content of α-KG. The results showed that the α-KG of the OA group was significantly lower than that of the control group. When the exosome increased the content of α-KG, we found that if oe-c-MYC and exosomes were combined with OA chondrocytes, the content of α-KG was reduced again (Figure 5(b)). The contents of GLN and GSH/GSSG were detected by the biochemical kit to detect the difference in glutamine uptake. Exosomes decrease the expression of various indicators, but when combined with oe-c-MYC, their expression increased, hindering the therapeutic effect of exosomes (Figure 5(c)).

3.4. Exosomes Alleviate Joint Injury in OA Rats. The joint injury model of rats was established, and exosomes were injected into both hind limbs' joint cavities to treat OA injury. The three groups were the sham, OA, and OA+exosome groups. Firstly, the motor ability of rats in each group was detected. The results showed that the number of electric shocks in the exosome treatment group was lower than that in the OA group when the movement distance was the same (Figure 6(a)). The knee tissues of rats stained with HE and safranin solid green staining. HE results showed that the joint structure of the sham group was complete, and the chondrocytes were evenly distributed. In the model group,

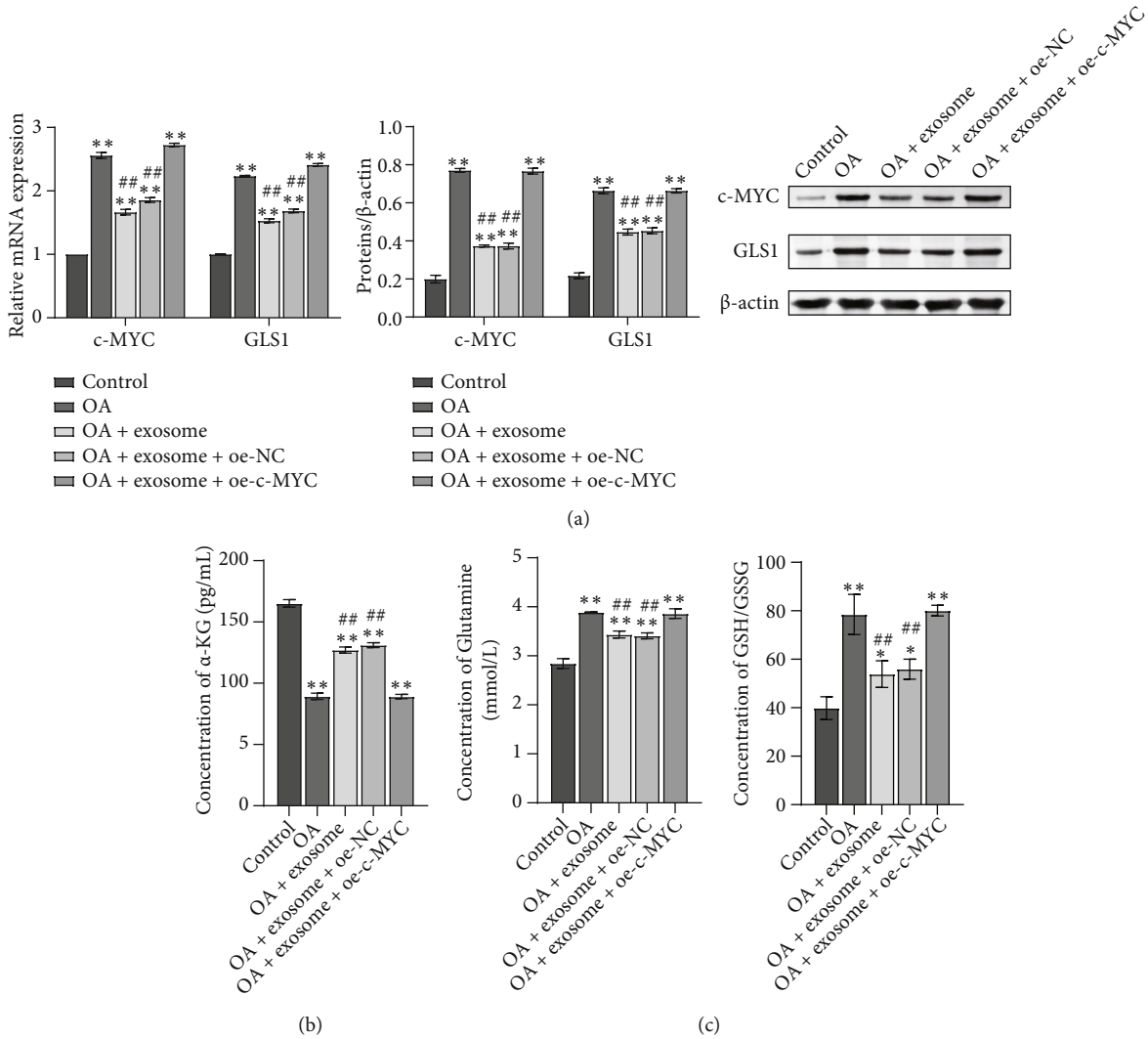

Figure 5: oe-c-MYC decreased the therapeutic effect of exosomes on OA chondrocytes and affected glutamine metabolism. (a) The mRNA and protein contents of c-MYC and GLS1 were detected by RT-qPCR and WB. (b) The content of α-KG was detected by ELISA. (c) The contents of glutamine and GSH/GSSG were detected by the biochemical kit. $^{**}P < 0.01$ vs. control; $^{\#\#}P < 0.01$ vs. OA.

the number of chondrocytes decreased, and the distribution was uneven. After treatment with exosomes, the articular cartilage surface was more complete than that of the model group. The number of cells was distributed evenly, and some had cell clusters (Figure 6(b)). The results of safranin solid green staining showed that the cartilage in the control group and the OA+exosome group was arranged orderly, and the surface structure of cartilage was complete. In the OA group, there were obvious cracks on the surface of the specimens and the arrangement of chondrocytes was disordered (Figure 6(c)). RT-qPCR and WB detected the expression of TNFα and IL-6 in tissues. The results showed that exosomes had a significant effect on OA inflammation (Figure 6(d)). The TUNEL kit was used to stain the tissue, and we found that apoptosis in the OA group increased, and exosomes reversed this increase (Figure 6(e), Figure S3A). Furthermore, we detected the levels of collagen II and Aggrecan in tissues by RT-qPCR and WB. The results showed that the treatment of exosomes reversed the decrease of the expression levels of collagen II and Aggrecan by OA (Figure 6(f)). Finally, in order to detect glutamine metabolism-related proteins c-MYC and GLS1, we carried out IHC staining, RT-qPCR detection, and WB detection on the tissues. The results showed that compared with the sham group, c-MYC and GLS1 increased in the OA group, while exosome decreased this increase (Figures 6(g) and 6(h), Figure S3B). The expression of α-KG in the OA group was lower than that in the sham group, while exosome increased the content of α-KG (Figure 6(i)). These results suggested that exosomes have a positive effect on OA and can regulate glutamine metabolism in the bone and joint.

4. Discussion

OA is a global disease. The limitations of current research on OA treatment have resulted in no reliable drugs to cure OA. Exosomes have been a hot research topic in recent years and have therapeutic effects on many diseases. We found that

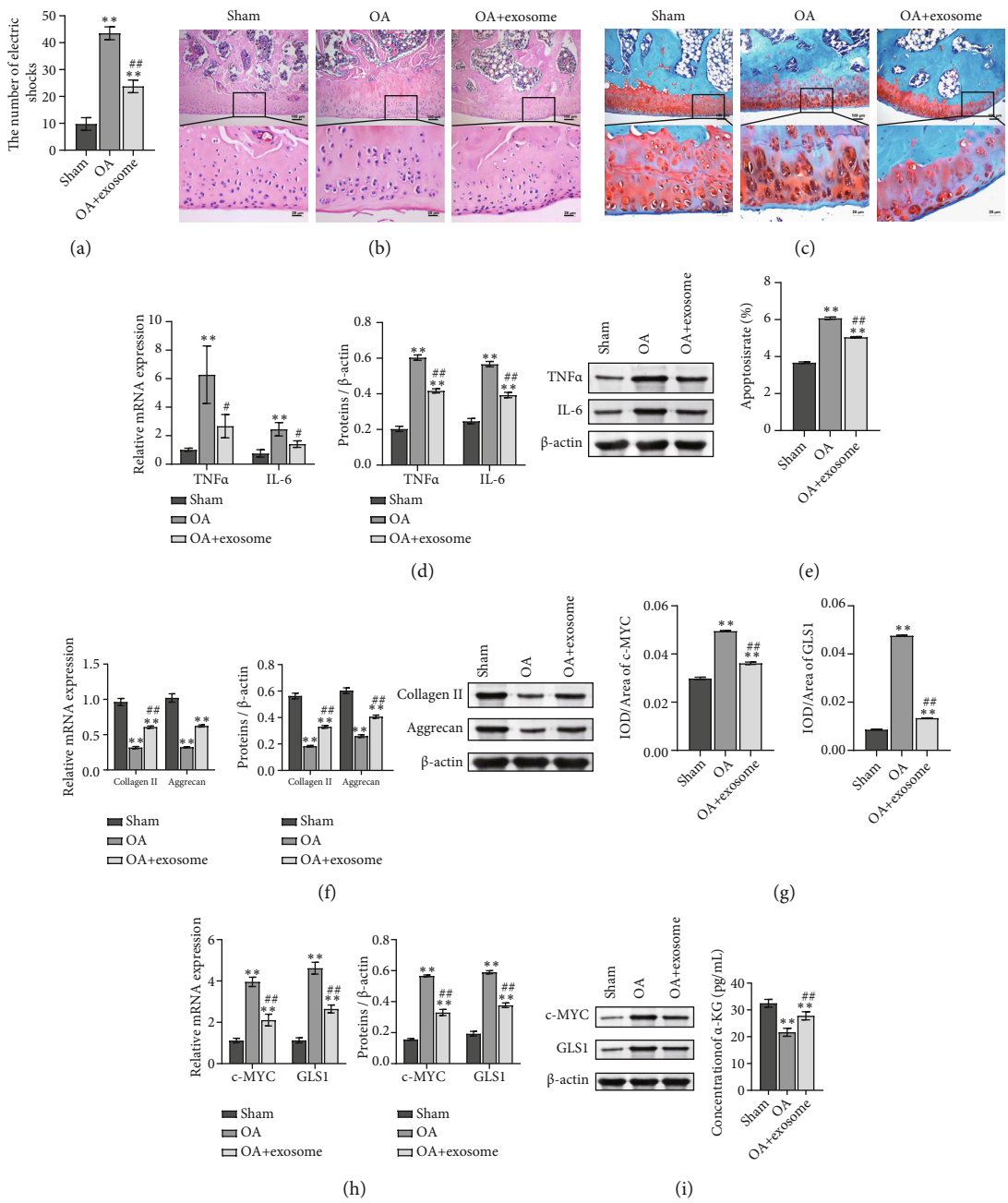

Figure 6: Exosomes alleviate joint injury in OA rats. (a) The movement of mice on the treadmill. When all mice ran 37.69 meters, the number of electric shocks received by the mice was counted. (b) The cartilage was stained with HE. Scale bar = 100 μm and 25 μm. (c) The cartilage was stained with safranin solid green staining. Scale bar = 100 μm and 25 μm. (d) mRNA and protein expressions were detected by RT-qPCR and WB to detect TNFα and IL-6. (e) TUNEL assay was used to detect apoptosis. Scale bar = 25 μm. (f) mRNA and protein expressions of collagen II and Aggrecan were detected by RT-qPCR and WB. (g) The expression of c-MYC and GLS1 was detected by IHC. Scale bar = 100 μm and 25 μm. (h) mRNA and protein expressions of c-MYC and GLS1 were detected by RT-qPCR and WB. (i) α-KG content was detected by ELISA. $^{**}P < 0.01$ vs. sham. $^{\#\#}P < 0.01$ vs. OA.

exosomes can affect the metabolism of glutamine. Inflammation is related to the progression of OA, and anti-inflammatory drugs can prevent the development of OA [27]. For example, quercetin [28] and ABT263 (navitoclax) [29] alleviate OA by inhibiting inflammation. Our research first showed that the occurrence of OA triggered inflammation, and the content of inflammatory factors TNFα and IL-6 increased in the OA model. The exosomes secreted by MSC have a therapeutic effect on OA and can reduce the levels of TNFα and IL-6 in OA. Therefore, in the treatment of OA, exosomes are also equivalent to a new type of anti-inflammatory drug. Exosomes secreted by MSC also have a similar effect in the TMJ-OA treatment, suggesting that exosomes do have anti-inflammatory effects [30].

Apoptosis is positively correlated with the severity of cartilage destruction and matrix depletion [31]. Apoptosis

is programmed cell death and an essential life process [32]. But inappropriate apoptosis is a factor in many human diseases, including neurodegenerative diseases, inflammatory diseases, and cancer [32]. Bao et al. pointed out that rapamycin could improve OA by inhibiting rat chondrocytes from IL-18-induced apoptosis [33]. Wang et al. suggested that propolis could inhibit OA by inhibiting mouse chondrocytes from IL-1β-induced apoptosis [34]. These results showed that we could improve OA by inhibiting cell apoptosis. Our results confirmed this. We detected the apoptosis of chondrocytes in each group of rats. The results showed that the apoptosis of chondrocytes in OA rats increased, while the exosome treatment group could significantly downregulate the apoptosis of chondrocytes.

Glutamic acid metabolism-related proteins c-MYC and GLS1 were used to characterize the activities of glutamic acid metabolism-related enzymes [35]. A study has shown that Gankyrin can upregulate c-MYC by activating β-catenin signal transduction to drive glycolysis and glutamine breakdown [35]. Another study has also shown that the dysregulated XLOC_006390/c-MYC axis increases glutamate metabolism and promotes the progression of pancreatic cancer to a higher stage [36]. In our study, the expression of c-MYC and GLS1 increased in OA, but decreased after treatment with exosomes. It indicated that exosomes affect glutamate metabolism. In addition, when we treated OA chondrocytes with oe-c-MYC and exosomes, the metabolism of glutamate in the cells increased, while the expression of collagen II and Aggrecan decreased, which promoted the progress of OA. Our study showed that oe-c-MYC hindered the therapeutic effect of exosome on OA. Although our study found that MSC-secreted exosomes have a positive therapeutic effect on OA, they still could not cure OA. In the future, we will try to use exosomes in clinical trials of OA and further confirm the therapeutic effect of exosomes on OA. Moreover, we hope that through clinical trials; we can further show that exosomes can reduce the expression of c-MYC to reduce glutamate metabolism, thereby alleviating OA.

5. Conclusion

In this study, the effect of MSC-exosomes on chondrocyte function and glutamine metabolism was systematically studied. At the same time, exosomes can affect arthritis chondrocyte function and glutamate metabolism by downregulating c-MYC. It provided a preliminary basis for the subsequent clinical treatment of OA by exosomes.

Data Availability

All the data is available for publication.

Conflicts of Interest

The authors publicize that there is no potential conflict of interest between them.

Authors' Contributions

KJ and XM designed and performed the experiments. KJ drafted the manuscript. XM, TJ, and YC revised the manuscript and analyzed the data. KJ, TJ, and YC performed the experiments and contributed reagents, materials. All authors have approved the final version of the manuscript.

Supplementary Materials

Supplementary 1. Figure S1: exosomes affect cell function of OA chondrocytes. (A) apoptosis was identified by flow cytometry. (B) Collagen II and Aggrecan of chondrocytes were detected by IF. Scale bar = 25 μm.

Supplementary 2. Figure S2: oe-c-MYC decreased the therapeutic effect of exosomes on OA chondrocytes and affected the function of OA chondrocytes. The expressions of collagen II (A) and Aggrecan (B) were detected by IF. Scale bar = 25 μm.

Supplementary 3. Figure S3: exosomes alleviate joint injury in OA rats. (A) TUNEL assay was used to detect apoptosis. Scale bar = 25 μm. (B) The expression of c-MYC and GLS1 was detected by IHC. Scale bar = 100 μm and 25 μm.

References

[1] A. E. Nelson, "Osteoarthritis year in review 2017: clinical," *Osteoarthritis and Cartilage*, vol. 26, no. 3, pp. 319–325, 2018.

[2] Y. Li, W. Xiao, W. Luo et al., "Alterations of amino acid metabolism in osteoarthritis: its implications for nutrition and health," *Amino Acids*, vol. 48, no. 4, pp. 907–914, 2016.

[3] B. Abramoff and F. E. Caldera, "Osteoarthritis: pathology, diagnosis, and treatment options," *The Medical Clinics of North America*, vol. 104, no. 2, pp. 293–311, 2020.

[4] S. P. Messier, C. Legault, R. F. Loeser et al., "Does high weight loss in older adults with knee osteoarthritis affect bone-on-bone joint loads and muscle forces during walking?," *Osteoarthritis and Cartilage*, vol. 19, no. 3, pp. 272–280, 2011.

[5] G. D. Deyle, S. C. Allison, R. L. Matekel et al., "Physical therapy treatment effectiveness for osteoarthritis of the knee: a randomized comparison of supervised clinical exercise and manual therapy procedures versus a home exercise program," *Physical Therapy*, vol. 85, no. 12, pp. 1301–1317, 2005.

[6] X. Zhu, D. Wu, L. Sang et al., "Comparative effectiveness of glucosamine, chondroitin, acetaminophen or celecoxib for the treatment of knee and/or hip osteoarthritis: a network meta-analysis," *Clinical and Experimental Rheumatology*, vol. 36, no. 4, pp. 595–602, 2018.

[7] Y. Zhang, J. Bi, J. Huang, Y. Tang, S. Du, and P. Li, "Exosome: a review of its classification, isolation techniques, storage, diagnostic and targeted therapy applications," *International Journal of Nanomedicine*, vol. Volume 15, pp. 6917–6934, 2020.

[8] D. M. Pegtel and S. J. Gould, "Exosomes," *Annual Review of Biochemistry*, vol. 88, no. 1, pp. 487–514, 2019.

[9] P. Wu, B. Zhang, H. Shi, H. Qian, and W. Xu, "MSC-exosome: a novel cell-free therapy for cutaneous regeneration," *Cytotherapy*, vol. 20, no. 3, pp. 291–301, 2018.

[10] R. C. Lai, F. Arslan, M. M. Lee et al., "Exosome secreted by MSC reduces myocardial ischemia/reperfusion injury," *Stem Cell Research*, vol. 4, no. 3, pp. 214–222, 2010.

[11] C. R. Harrell, N. Jovicic, V. Djonov, N. Arsenijevic, and V. Volarevic, "Mesenchymal stem cell-derived exosomes and other extracellular vesicles as new remedies in the therapy of inflammatory diseases," *Cell*, vol. 8, no. 12, p. 1605, 2019.

[12] R. W. Moreadith and A. L. Lehninger, "The pathways of glutamate and glutamine oxidation by tumor cell mitochondria. Role of mitochondrial NAD(P)+-dependent malic enzyme.," *The Journal of Biological Chemistry*, vol. 259, no. 10, pp. 6215–6221, 1984.

[13] T. Zhou, Y. Yang, Q. Chen, and L. Xie, "Glutamine metabolism is essential for stemness of bone marrow mesenchymal stem cells and bone homeostasis," *Stem Cells International*, vol. 2019, Article ID 8928934, 13 pages, 2019.

[14] V. J. Sydnor and D. R. Roalf, "A meta-analysis of ultra-high field glutamate, glutamine, GABA and glutathione 1HMRS in psychosis: implications for studies of psychosis risk," *Schizophrenia Research*, vol. 226, pp. 61–69, 2020.

[15] G. Bjørklund, A. A. Tinkov, B. Hosnedlová et al., "The role of glutathione redox imbalance in autism spectrum disorder: a review," *Free Radical Biology & Medicine*, vol. 160, pp. 149–162, 2020.

[16] S. Zhu, D. Makosa, B. Miller, and T. M. Griffin, "Glutathione as a mediator of cartilage oxidative stress resistance and resilience during aging and osteoarthritis," *Connective Tissue Research*, vol. 61, no. 1, pp. 34–47, 2020.

[17] P. Gao, I. Tchernyshyov, T.-C. Chang et al., "c-Myc suppression of miR-23a/b enhances mitochondrial glutaminase expression and glutamine metabolism," *Nature*, vol. 458, no. 7239, pp. 762–765, 2009.

[18] J. R. Anderson, S. Chokesuwattanaskul, M. M. Phelan et al., "1H NMR metabolomics identifies underlying inflammatory pathology in osteoarthritis and rheumatoid arthritis synovial joints," *Journal of Proteome Research*, vol. 17, no. 11, pp. 3780–3790, 2018.

[19] O. H. Jeon, C. Kim, R. M. Laberge et al., "Local clearance of senescent cells attenuates the development of post- traumatic osteoarthritis and creates a pro-regenerative environment," *Nature Medicine*, vol. 23, no. 6, pp. 775–781, 2017.

[20] P. H. Zhou, S. Q. Liu, and H. Peng, "The effect of hyaluronic acid on IL-1β-induced chondrocyte apoptosis in a rat model of osteoarthritis," *Journal of Orthopaedic Research*, vol. 26, no. 12, pp. 1643–1648, 2008.

[21] Y. Liu, L. Lin, R. Zou, C. Wen, Z. Wang, and F. Lin, "MSC-derived exosomes promote proliferation and inhibit apoptosis of chondrocytes via lncRNA-KLF3-AS1/miR-206/GIT1 axis in osteoarthritis," *Cell Cycle*, vol. 17, no. 21-22, pp. 2411–2422, 2018.

[22] I. Wortzel, S. Dror, C. M. Kenific, and D. Lyden, "Exosome-mediated metastasis: communication from a distance," *Developmental Cell*, vol. 49, no. 3, pp. 347–360, 2019.

[23] W. S. Toh, R. C. Lai, B. Zhang, and S. K. Lim, "MSC exosome works through a protein-based mechanism of action," *Biochemical Society Transactions*, vol. 46, no. 4, pp. 843–853, 2018.

[24] G. Sagar, R. P. Sah, N. Javeed et al., "Pathogenesis of pancreatic cancer exosome-induced lipolysis in adipose tissue," *Gut*, vol. 65, no. 7, pp. 1165–1174, 2016.

[25] Q. Li, B. Li, Q. Li et al., "Exosomal miR-21-5p derived from gastric cancer promotes peritoneal metastasis via mesothelial-to-mesenchymal transition," *Cell Death & Disease*, vol. 9, no. 9, p. 854, 2018.

[26] J. Du, J. Fan, C. Dong, H. Li, and B. Ma, "Inhibition effect of exosomes-mediated Let-7a on the development and metastasis of triple negative breast cancer by down-regulating the expression of c-Myc," *European Review for Medical and Pharmacological Sciences*, vol. 23, no. 12, pp. 5301–5314, 2019.

[27] K. Y. Chin and S. Ima-Nirwana, "The role of vitamin E in preventing and treating osteoarthritis - a review of the current evidence," *Frontiers in Pharmacology*, vol. 9, p. 946, 2018.

[28] Y. Hu, Z. Gui, Y. Zhou, L. Xia, K. Lin, and Y. Xu, "Quercetin alleviates rat osteoarthritis by inhibiting inflammation and apoptosis of chondrocytes, modulating synovial macrophages polarization to M2 macrophages," *Free Radical Biology & Medicine*, vol. 145, pp. 146–160, 2019.

[29] H. Yang, C. Chen, H. Chen et al., "Navitoclax (ABT263) reduces inflammation and promotes chondrogenic phenotype by clearing senescent osteoarthritic chondrocytes in osteoarthritis," *Aging (Albany NY)*, vol. 12, no. 13, pp. 12750–12770, 2020.

[30] S. Zhang, K. Y. W. Teo, S. J. Chuah, R. C. Lai, S. K. Lim, and W. S. Toh, "MSC exosomes alleviate temporomandibular joint osteoarthritis by attenuating inflammation and restoring matrix homeostasis," *Biomaterials*, vol. 200, pp. 35–47, 2019.

[31] G. Musumeci, F. C. Aiello, M. A. Szychlinska, M. Di Rosa, P. Castrogiovanni, and A. Mobasheri, "Osteoarthritis in the XXIst century: risk factors and behaviours that influence disease onset and progression," *International Journal of Molecular Sciences*, vol. 16, no. 12, pp. 6093–6112, 2015.

[32] S. Elmore, "Apoptosis: a review of programmed cell death," *Toxicologic Pathology*, vol. 35, no. 4, pp. 495–516, 2007.

[33] J. Bao, Z. Chen, L. Xu, L. Wu, and Y. Xiong, "Rapamycin protects chondrocytes against IL-18-induced apoptosis and ameliorates rat osteoarthritis," *Aging (Albany NY)*, vol. 12, no. 6, pp. 5152–5167, 2020.

[34] B. W. Wang, Y. Jiang, Z. L. Yao, P. S. Chen, B. Yu, and S. N. Wang, "Aucubin protects chondrocytes against IL-1β-induced apoptosis in vitro and inhibits osteoarthritis in mice model," *Drug Design, Development and Therapy*, vol. Volume 13, pp. 3529–3538, 2019.

[35] H. Song and K. H. Park, "Regulation and function of SOX9 during cartilage development and regeneration," *Seminars in Cancer Biology*, vol. 67, Part 1, pp. 12–23, 2020.

[36] J. He, F. Li, Y. Zhou et al., "LncRNA XLOC_006390 promotes pancreatic carcinogenesis and glutamate metabolism by stabilizing c-Myc," *Cancer Letters*, vol. 469, pp. 419–428, 2020.

Hindawi
Mediators of Inflammation
Volume 2021, Article ID 7393029, 12 pages
https://doi.org/10.1155/2021/7393029

Research Article

UBC Mediated by SEPT6 Inhibited the Progression of Prostate Cancer

Ruochen Zhang, Yaojing Yang, Haijian Huang, Tao Li, Liefu Ye, Le Lin, and Yongbao Wei

Shengli Clinical Medical College of Fujian Medical University, Department of Urology, Fujian Provincial Hospital, China

Correspondence should be addressed to Yongbao Wei; weiyb@fjmu.edu.cn

Received 2 September 2021; Revised 25 November 2021; Accepted 29 November 2021; Published 20 December 2021

Academic Editor: Mingliang Jin

Background. Prostate cancer is one of the most common malignancies in men. Protein ubiquitination is an important mechanism for regulating protein activity and level *in vivo*. We aimed to study the mechanism of SEPT6 and UBC action in prostate cancer to identify new targets. *Methods*. The ubiquitin-protein and the ubiquitin coding gene UBA52, UBA80, UBB, and UBC expressions were detected in clinical tissues and cells. Overexpression and knockdown of UBC were performed in prostate cancer DU145 cells. Cell Counting Kit 8 (CCK-8) assay was performed to detect cell proliferation. Cell cycle at 24 h was detected by flow cytometry. Clonal formation assay was used to measure cell clone number. Immunofluorescence (IF) was performed to detect the colocalization of SEPT6 and UBC in prostate cancer cells. Next, we overexpressed or knocked down SEPT6 expression in DU145 cells. Pearson correlation coefficient was applied to analyze the relationship between SEPT6 and UBC in prostate cancer tissue. oe-SEPT6+oe-UBC coexpressing cells were constructed to detect the upstream and downstream relationship between SEPT6 and UBC on prostate cancer cells. The tumor formation experiment was performed to explore SEPT6/UBC effect on prostate cancer. *Results*. UBC was upregulated in prostate cancer tissues and cells. Overexpression of UBC promoted cell survival and proliferation. IF revealed the colocalization of SEPT6 and UBC in prostate cancer cells. UBC expression decreased after oe-SEPT6, while increased after sh-SEPT6, indicating that UBC was downstream of SEPT6. Pearson correlation coefficient analysis showed that SEPT6 was negatively correlated with UBC in prostate cancer tissues. SEPT6 as an upstream gene of UBC regulated prostate cancer cell behavior through UBC. The tumor formation experiment showed that SEPT6 could inhibit tumor growth. *Conclusion*. In general, SEPT6 inhibited UBC expression, thereby reducing the overall ubiquitination level, affecting the expression level of downstream cell proliferation-related genes, and then affecting the progression of prostate cancer.

1. Introduction

Prostate cancer is one of the most common malignancies and the second most common cause of cancer-related death in men [1]. It is a complex, heterogeneous disease with a variable natural history [2]. Prostate cancer is characterized by various biological behaviors translated into different clinical manifestations, ranging from inert microscopic disease to highly aggressive tumors, including a tendency to metastasize [3]. There are three recognized risk factors for prostate cancer: age, race, and genetics [1]. The key problem for prostate cancer patients is detecting recurrent disease and treating metastatic cancer [4]. Prostate-specific antigen (PSA) targeting strategy improved functional imaging can enhance the identification of patients with less metastatic prostate cancer in the short term [5]. However, the diagnostic method of PSA screening for prostate cancer in people has always been controversial and fiercely debated, which is associated with overdiagnosis and overtreatment, accompanied by urinary, sexual, and intestinal dysfunction [6]. Despite the new progress, prostate cancer remains a major medical problem affecting men. Current trends in the treatment of prostate cancer patients increase the need for reliable therapeutic targets and new and innovative strategies for cancer diagnosis and treatment.

Septins are a class of guanosine triphosphate- (GTP-) binding proteins that are highly conserved in eukaryotes and are usually associated with membranes and are involved in cytokinesis, exocytosis, and other cellular processes [7, 8]. Human Septins contain 13 gene families that encode more than 30 protein isotypes with ubiquitous and tissue-specific expression [9]. Septins are involved in various normal cellular processes and may be a key cancer gene and participate in the pathogenesis of multiple diseases, including cancer [10, 11]. Septin6 (SEPT6), also known as SEP2 and KIAA0128, is located in XQ24 [12]. It plays a role in actin dynamics, cell shape, and microtubule regulation [13]. SEPT6 and SEPT7 GTP-binding proteins regulate AP3 and endosomal-sorting complex required for transport- (ESCRT-) dependent multivesicle biogenesis [14]. SEPT6 is involved in the development of hepatocellular carcinoma (HCC) [15] and also plays a role in the occurrence and normal function of leukemia (including neurotransmission) [16]. A previous study has found that SEPT6 is a target gene of microRNA-223-3p (miR-223-3p), which may reverse the biological activity induced by miR-223-3p and may provide a potential therapeutic target for prostate cancer [17]. This suggests that SEPT6 may be a potential therapeutic target.

Ubiquitin is a highly conserved 76 amino acid protein in all eukaryotes [18]. Ubiquitination is catalyzed by a three-enzyme cascade reaction composed of E1 ubiquitin-activating enzyme, E2 ubiquitin-conjugating enzyme, and E3 ubiquitin ligase [19]. Through the action of ubiquitin-protein ligase, ubiquitin is connected to the target protein through the isopeptide bond between the C-terminal glycine residue of ubiquitin and the epsilon amino group of lysine in the substrate protein [20]. Like phosphorylation, ubiquitination of proteins regulates or affects most cellular processes, and defects in this system are associated with many diseases [21]. Ubiquitin C (UBC) is one of the two stress-regulated polyubiquitin genes in mammals and plays a crucial role in maintaining cellular ubiquitin levels, especially under stress conditions [22]. Studies have shown that UBC is an essential source of ubiquitin in the process of cell proliferation and stress and is necessary for fetal liver development, cell cycle progression, and stress tolerance [23]. Ubiquitin-mediated proteasome degradation is an important mechanism for regulating protein metabolism in cells and is of great significance for maintaining normal functions of the body [24]. Ubiquitin proteasome system (UPS) has made some progress in developing potential novel therapies against cancer and neurodegenerative diseases [25, 26], but the specific mechanism of UBC in prostate cancer is rarely studied.

Based on the above studies, the antitumor effect of SEPT6 in prostate cancer may be used as a target for the development of prostate cancer disease. SEPT6 may target the UBC gene to affect prostate cancer, but its effect on prostate cancer cells remains unknown. Therefore, this study is aimed at exploring the role of the expression of SEPT6 and UBC in prostate cancer tissues and cells and at providing new insights for the development of prostate cancer therapy.

2. Material and Methods

2.1. Clinical Tissue Samples. Ten participants came from Fujian Provincial Hospital. Prostate cancer tissues and paracancerous tissues were collected and divided into prostate cancer tissue and paracancerous tissue groups. All subjects gave their informed consent for inclusion before they participated in the study. The study was conducted following the Declaration of Helsinki; written informed consents were obtained from the guardians of these patients.

2.2. Cell Culture and Treatment. Prostate cell lines RWPE-1 and prostate cancer cell lines PC3, CWR22 (22Rv1), VCaP, and DU145 were purchased from the Cell Bank of the Chinese Academy of Sciences. RWPE-1 and VCaP cells were cultured in Dulbecco's Modified Eagle Medium-High Glucose (DMEM-H) containing 10% fetal bovine serum (FBS, Thermo Fisher Scientific). PC3 cells were cultured in Ham's F-12K (Kaighn's) with 10% FBS. CWR22 and DU145 cells were cultured in Roswell Park Memorial Institute (RPMI) 1640 (w/o Hepes) containing 10% FBS. To overexpress UBC and SEPT6, the UBC and SEPT6 sequences were linked to the vector LV003. According to the instructions, UBC and SEPT6 vectors were transfected into DU145 cells using Lipofectamine 3000 reagent. The oe-NC group was transfected with an oe-NC plasmid in DU145 cells. The short hairpin targeting UBC including sh-UBC (1), sh-UBC (2), and sh-UBC (3) and the short hairpin targeting SEPT6 including sh-SEPT6 (1), sh-SEPT6 (2), and sh-SEPT6 (3) synthesized by Sangon Biotech Co., Ltd. (Shanghai, China), and the corresponding negative control sh-NC were used to knock down the expression of UBC and SEPT6. To detect the relationship between the upstream and downstream effects of SEPT6 and UBC on prostate cancer cells, an oe-SEPT6+oe-UBC coexpression cell line was constructed.

2.3. Quantitative Real-Time PCR (qRT-PCR). qRT-PCR was used to detect the mRNA levels of UBA52, UBA80, UBB, UBC, SEPT6, CDK1, CCNA2, MCM10, E2F1, HIST1H1A, HIST1H3B, BRCA1, and AURKB in cells and tissues. Total RNA was extracted by Trizol methods. RNA was reversely transcribed into cDNAs by the instruction of a reverse transcription kit (CW2569, CWBIO, China). SYBR Green qPCR mix (Invitrogen) was performed to test gene's relative expression in ABI 7900 system. The relative level of the gene was calculated by the $2^{-\Delta\Delta Ct}$ method with GAPDH as the internal gene. The primer sequences used in this study are shown in Table 1.

2.4. Western Blot (WB). RIPA lysis buffer (#P0013B, Beyotime Biotechnology) was applied to extract the total protein from prostate cancer tissues and cells. The protein of each group was quantified according to the BCA protein determination kit. The protein was mixed with SDS-PAGE loading buffer (#MB2479, Meilunbio) for 5 min in boiling water at 100°C. The protein was adsorbed on the PVDF membrane by gel electrophoresis, sealed with 5% skim milk solution for 2 h at room temperature, and incubated with diluted primary antibodies at room temperature for 90 minutes. The secondary antibody HRP goat anti-mouse IgG (SA00001-1, 1 : 5000, Proteintech, USA) and HRP goat anti-Rabbit IgG (SA00001-2, 1 : 6000, Proteintech, USA) were incubated with the membrane at room temperature for 90 min. The protein bands were detected by the ChemiScope 6100 system (Clinx

Table 1: The primers used in this study.

Primer ID	5′-3′
UBA52-F	CGGACGCAAACATGCAGAT
UBA52-R	CGGCAAATATCAGACGCTGC
UBA80-F	AGAGACTCGGCGGTTGAAAG
UBA80-R	TCCCCGTAAGGGTTTTCACG
UBB-F	GCGCATAGAGGAGAAGGGAAA
UBB-R	AGGCTTTTCAACTGAGCCCC
UBC-F	CCGGGATTTGGGTCGCAG
UBC-R	TCACGAAGATCTGCATTGTCAAG
SEPT6-F	CACACCTACCATGACTCCCGAA
SEPT6-R	GACTCCGTTGCTGACAAGCTC
CDK1-F	AAACTACAGGTCAAGTGGTAGCC
CDK1-R	TCCTGCATAAGCACATCCTGA
CCNA2-F	ACCAGGAGAATATCAACCCGGAA
CCNA2-R	CCGGACTTCAGTACCGCCAG
MCM10-F	AAGCCTTCTCTGGTCTGCG
MCM10-R	CTGTGGCGTAACCTTCTTCAA
E2F1-F	TGCCCCACCCTCCAATCTGC
E2F1-R	CAAAACCCGGCCCAAACGTCA
HIST1H1A-F	TGGGCATTAAGAGCCTGGTAA
HIST1H1A-R	ACCCGTTGCCTTAGTTTTTGTA
HIST1H3B-F	ATGGCTCGTACTAAACAGACAGC
HIST1H3B-R	TTCCGAATCAGCAACTCGGTC
BRCA1-F	ACCTTGGAACTGTGAGAACTCT
BRCA1-R	TCTTGATCTCCCACACTGCAATA
AURKB-F	CAGTGGGACACCCGACATC
AURKB-R	GTACACGTTTCCAAACTTGCC
β-Actin-F	ACCCTGAAGTACCCCATCGAG
β-Actin-R	AGCACAGCCTGGATAGCAAC

Co., Ltd, Shanghai, China). β-Actin was used as the internal reference for detecting relative expression levels. The primary antibodies were SEPT6 (ab138036, 1 : 750, Abcam, UK), UBA52 (18039-1-AP, 1 : 3000, Proteintech), UBA80 (14946-1-AP, 1 : 750, Proteintech, USA), UBB (10201-2-AP, 1 : 1000, Proteintech, USA), UBC (14415-1-AP, 1 : 2000, Proteintech, USA), ubiquitin (ab7780, 1: 2000, Abcam, UK), Ki67 (ab92742, 1 : 5000, Abcam, UK), PCNA (10205-2-AP, 1 : 3000, Proteintech, USA), and β-actin (66009-1-Ig, 1 : 5000, Proteintech, USA).

2.5. Immunohistochemistry (IHC) and Immunocytochemistry (ICC). Ubiquitin-protein expression was detected by IHC in prostate cancer tissues and paracancerous tissues. The slices were roasted at 60°C for 12 h. Then, the slices were dewaxed to water and heated to repair the antigen. 1% periodic acid was added, and the endogenous enzyme was inactivated for 10 min at room temperature. PBS was washed 3 times for 3 min. Ubiquitin (ab7780, 1 : 100, Abcam, UK) primary antibody was incubated overnight at 4°C, and PBS was washed 3 times for 5 min. The expressions of ubiquitin in prostate cell RWPE-1 and prostate cancer cells PC3, CWR22, VCAP, and DU145 were detected by ICC. The slides were removed and fixed with 4% paraformaldehyde for 30 min. PBS was washed 3 times for 5 min. Then, 0.3% Trolaton was added for 30 min at 37°C. 3% H_2O_2 was added at room temperature for 10 min to inactivate endogenous enzymes. Ubiquitin (ab7780, 1 : 50, Abcam, UK) was incubated overnight at 4°C. PBS was washed 3 times for 5 min. The secondary antibody was incubated at 37°C for 30 min. PBS was washed 3 times for 5 min. DAB was used for color development, hematoxylin was restained for 5-10 min, washed with distilled water, and PBS returned to blue. All levels of alcohol (60-100%) were dehydrated for 5 min. After removal, it was placed in xylene for 10 min and then sealed with neutral gum and observed under the microscope.

2.6. Immunofluorescence (IF). The distribution of SETP6 and UBC in DU145 cells was detected by IF. The slides were removed and washed with PBS 3 times. Then, slides were fixed with 4% paraformaldehyde for 30 min, and PBS was washed 3 times for 5 min. Then, it was permeabilized with 0.5% Triton X-100 at 37°C for 30 min. After washing with PBS, 5% BSA was sealed at 37°C for 1 h, and SEPT6 (PA5-19024, 1 : 50, ThermoFisher) and UBC (ab7780, 1 : 50, Abcam, UK) were incubated overnight at 4°C. PBS was washed 3 times for 5 min. Diluted Donkey Anti-Goat IgG (H+L), FITC conjugate (SA00003-3, 1 : 100, Proteintech, UK), Donkey Anti-Rabbit IgG (H+L), and CoraLite594 conjugate (SA00013-8, 1 : 200, Proteintech, UK) were added. Then, they were incubated at 37°C for 90 min, and PBS was washed 3 times for 5 min. Then, they were dyed with DAPI (Wellbio, China) at 37°C for 10 min. The plates were sealed and observed under a fluorescence microscope.

2.7. Cell Counting Kit 8 (CCK-8) Assay. CCK-8 detected cell proliferation in the control group, oe-UBC group, and sh-UBC group. The cells of different groups were inoculated into 96-well plates with 1×10^4 cells/well density and incubated at 37°C and 5% CO_2 in an incubator. CCK-8 (#NU679, DOJINDO, Japan) was added 10 μL/well to each well. The absorbance value at 450 nm was analyzed by a Bio-Tek enzyme plate (MB-530, Heales, China).

2.8. Cell Cycle Assay. The cell suspension was collected, centrifuged to get cell precipitation, and washed with PBS 2-3 times to make the single-cell suspension, and the number of cells was adjusted to 1×10^6 cells/mL. 150 μL propidium iodide (PI) was added and stained at 4°C for 30 min in the dark. The PI was excited by a 488 nm argon-ion laser and received by a 630 nm pass filter. Ten thousand cells were collected through FSC/SSC scatter plot. The gating technique was used to eliminate adhesion cells and fragments, and the percentage of each cell cycle on the fluorescence histogram of PI was analyzed.

2.9. Clone Formation Assay. The proliferation of the control group, oe-UBC group, and sh-UBC group was detected by clone formation assay. The cells were digested with trypsin, the cell suspension was prepared, and the cells were seeded in 6-well plates at 1×10^5/well. One thousand cells/2 mL were collected from each group and inoculated in a 6-well

plate. The cells were cultured in an incubator at 37°C and 5% CO_2 for 2~3 weeks, and the liquid was changed appropriately during the period. After discarding the medium, the cells were washed twice with PBS. Then, cells were fixed with 4% paraformaldehyde for 15 min, washed twice with PBS, stained with 0.5% crystal violet for 5 min, and washed with distilled water 3 times. The camera took pictures of each hole and counted the number of clones.

2.10. In Vivo Tumorigenesis. Nine BALB/C male nude mice were randomly divided into the NC group, sh-SEPT6 group, and oe-SEPT6 group, with 8 mice in each group. The short hairpin targeting SEPT6 (sh-SEPT6), synthesized by Sangon Biotech Co., Ltd. (Shanghai, China), was used to knock down the expression of SEPT6. To overexpress SEPT6, the SEPT6 sequences were linked to the vector LV003. SEPT6 vector was transfected into prostate cancer DU145 cells using Lipofectamine 3000 reagent according to the instructions. The right side of the mice was subcutaneously injected with 100 μL PBS suspension of 1×10^7 DU145 cells. The tumor volume of each group was detected at 4, 7, 11, 14, 17, 21, 24, and 28 d. After 28 days, the nude mice were sacrificed, and the tumor weight of each group was detected. qRT-PCR was used to detect the expression of SEPT6 and UBC, and WB was used to detect the expression levels of SEPT6, UBC, PCNA, and Ki67.

2.11. Statistical Analysis. Statistical analysis was performed using GraphPad 8.0 software (San Diego, California, USA), and three independent experimental data were expressed as mean ± standard deviation (SD). Differences between two or more groups were analyzed using the Student *t*-test or using one-way analysis of variance (ANOVA). Pearson correlation coefficient studied the correlation between SEPT6 and UBC. $P < 0.05$ was considered statistically significant.

3. Results

3.1. UBC Was Upregulated in Prostate Cancer Tissues and Cells. First, IHC was used to detect ubiquitin-protein (UBC) expression in prostate cancer tissues and paracancerous tissues. UBC expression was elevated in prostate cancer tissues compared with paracancerous tissues (Figure 1(a)). WB and qRT-PCR were then performed to detect ubiquitin-encoding gene UBA52, UBA80, UBB, and UBC expression. The results revealed that UBC was highly expressed in prostate cancer tissues (Figures 1(b) and 1(c)). Then, we detected ubiquitin-protein and ubiquitin-coding gene UBA52, UBA80, UBB, and UBC expression in prostate cell line RWPE-1 (control) and prostate cancer cell lines PC3, CWR22, VCaP, and DU145. The results showed that UBC was also highly expressed in prostate cancer cells (Figures 1(d)–1(f)), consistent with our detection results in prostate cancer tissues and paracancerous tissues and highly expressed in DU145 cells. Therefore, we selected DU145 cells as the research object for subsequent experiments to explore the role of UBC in prostate cancer.

3.2. Overexpression of UBC Promoted Cell Survival and Proliferation. To further study the influence of UBC on prostate cancer cells, the overexpression or knockdown of UBC expression in prostate cancer DU145 cells was divided into the oe-NC and oe-UBC groups or the sh-NC, sh-UBC (1), sh-UBC (2), and sh-UBC (3) groups. First, the knockdown efficiency of UBC and the efficiency of the overexpressed vector were verified by qRT-PCR. qRT-PCR showed that UBC expression increased in the oe-UBC group, while UBC expression in the sh-UBC (1), sh-UBC (2), and sh-UBC (3) groups was decreased. Among them, the expression of UBC was most significantly decreased in the sh-UBC (2) group, so we chose sh-UBC (2) for follow-up studies (Figure 2(a)). WB showed that sh-UBC significantly reduced UBC expression, while UBC expression increased in oe-UBC (Figure 2(b)). IHC revealed sh-UBC significantly reduced ubiquitin expression, while ubiquitin expression increased in oe-UBC (Figure 2(c)). Cell function experiments showed that compared with the NC group, cell proliferation ability and cell clone number of the oe-UBC group were increased, the G0/G1 phase was decreased, and the G2+S phase was increased (Figures 2(d)–2(f)). WB detected proliferation-related protein PCNA and Ki67 expressions. The results showed that compared with the NC group, PCNA and Ki67 expressions were increased in the oe-UBC group but decreased in the sh-UBC group (Figure 2(g)). This confirmed our hypothesis that oe-UBC promotes the proliferation of prostate cancer cells.

3.3. SEPT6 Mediated UBC Expression. Previous study has found that SEPT6 might be a potential therapeutic target for prostate cancer [17]. However, there are few studies on the function of SEPT6 in prostate cancer. Therefore, we wanted to further investigate SEPT6 function in prostate cancer. We found by qRT-PCR that SEPT6 was low expressed in prostate cancer tissues compared with paracancerous tissues (Figure 3(a)). Pearson correlation coefficient analysis showed a negative correlation between SEPT6 and UBC in prostate cancer tissues (Figure 3(b)). Figure 3(c) demonstrated the colocalization of SEPT6 and UBC in prostate cancer cells. Then, we overexpressed or knocked down the expression of SEPT6 in DU145 cells, packaged as lentivirus and transfected into cells, which were divided into the NC and oe-SEPT6 groups or the sh-NC, sh-SEPT6 (1), sh-SEPT6 (2), and sh-SEPT6 (3) groups. The knockdown and overexpression efficiency of SEPT6 was verified by qRT-PCR. qRT-PCR showed that SEPT6 expression increased in the oe-SEPT6 group, while SEPT6 expression in sh-SEPT6 (1), sh-SEPT6 (2), and sh-SEPT6 (3) groups was decreased. The sh-SEPT6 (1) group showed the most obvious decrease in SEPT6 expression, so we selected sh-SEPT6 (1) for subsequent research (Figure 3(d)). UBC expression was decreased after overexpression of SEPT6 and increased after knocking down SEPT6, indicating that UBC expression was mediated by SEPT6 (Figures 3(e) and 3(f)).

3.4. SEPT6 Regulated Prostate Cancer Cell Behavior through UBC. To explore the relationship between SEPT6 and UBC on prostate cancer cells, we constructed an oe-SEPT6+oe-UBC coexpression cells. They were divided into three groups: the NC (DU145 cells), oe-SEPT6, and oe-SEPT6+oe-UBC group. Cell function experiments showed that compared with

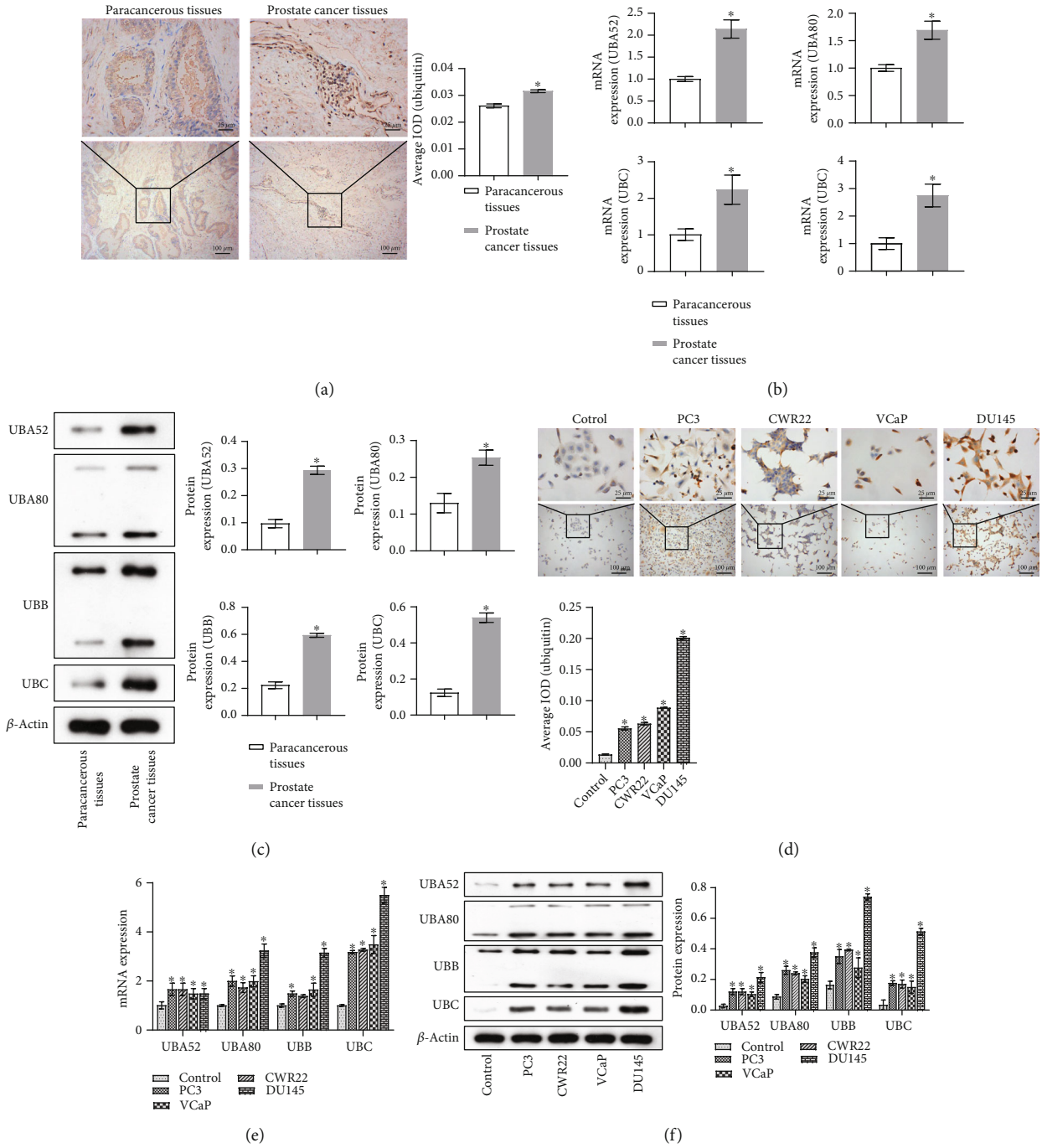

Figure 1: UBC was upregulated in prostate cancer tissues and cells. In prostate cancer tissues and paracancerous tissue, (a) IHC was used to detect ubiquitin-protein (UBC) expression. $^{*}P < 0.05$ vs. paracancerous tissues; scale bar = 25 μm, the magnification is 400 times; scale bar = 100 μm, the magnification is 100 times. (b, c) qRT-PCR and WB were performed to detect ubiquitin-encoding gene UBA52, UBA80, UBB, and UBC expression. $P < 0.05$ vs. paracancerous tissues. In prostate cell line RWPE-1 and prostate cancer cell lines PC3, CWR22, VCAP, and DU145, (d) ICC were used to detect ubiquitin-protein expression. $^{*}P < 0.05$ vs. the control group (prostate cell line RWPE-1); scale bar = 25 μm, the magnification is 400 times; scale bar = 100 μm, the magnification is 100 times. (e, f) qRT-PCR and WB detected ubiquitin-encoding gene UBA52, UBA80, UBB, and UBC expression. $^{*}P < 0.05$ vs. the control group (prostate cell line RWPE-1).

the NC group, cell proliferation ability and cell clone number of the oe-SEPT6 group were decreased, the G0/G1 phase was increased, and the G2+S phase was decreased. However, cell function changes induced by oe-SEPT6 could be reversed after overexpression of UBC (Figures 4(a)–4(c)). WB detected the expression of proliferation-related proteins PCNA and Ki67. The results showed that compared with the NC group, PCNA and Ki67 expressions in the oe-SEPT6 group were reduced,

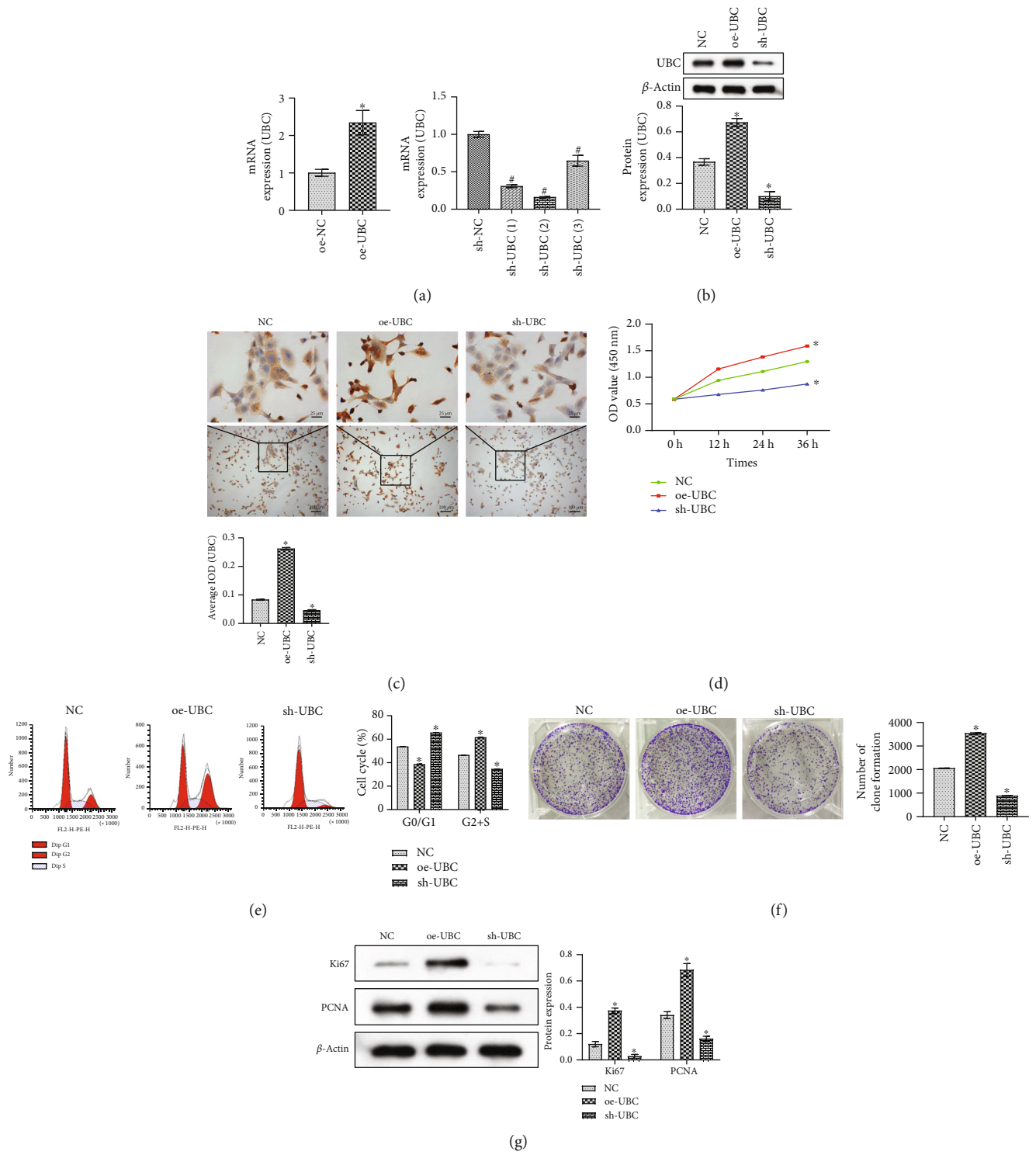

Figure 2: Overexpression of UBC promoted cell survival and proliferation. (a) The overexpression and knockdown efficiency of UBC was detected by qRT-PCR. (b) WB was used to detect UBC expression. (c) IHC was used to detect ubiquitin expression. (d) CCK-8 detected cell proliferation. (e) Cell cycle at 24 h was detected by flow cytometry. (f) Clonal formation assay detected cell clone number. (g) WB was performed to detect proliferation-related protein PCNA and Ki67 expressions. $^{*}P < 0.05$ vs. the NC group; scale bar = 25 μm, the magnification is 400 times; scale bar = 100 μm, the magnification is 100 times.

and oe-UBC could reverse the decrease in the expression of PCNA and Ki67 caused by oe-SEPT6 (Figure 4(d)). Previous studies have shown that UBC reduction plays an important role in cell replication and senescence [27]. We have detected the expression levels of a series of cell cycle CDK1, CCNA2, MCM10, and E2F1 and proliferation-related proteins HIST1H1A, HIST1H3B, BRCA1, and AURKB. As shown in Figures 4(e) and 4(f), cell cycle and proliferation-related

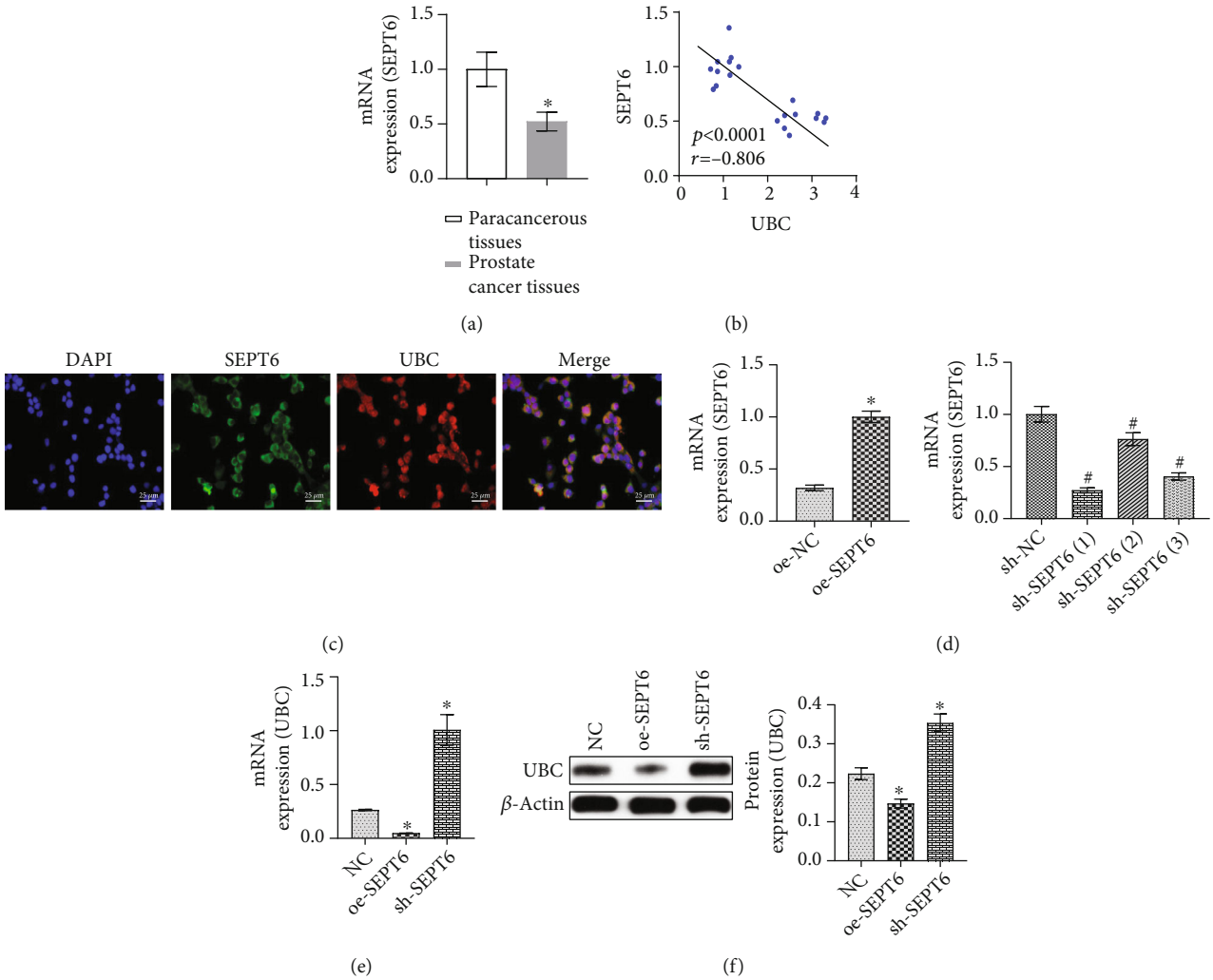

Figure 3: SEPT6 mediated UBC expression. (a) The expression of SEPT6 was detected by qRT-PCR in prostate cancer tissues and paracancerous tissues. $^{*}P < 0.05$ vs. paracancerous tissues. (b) Pearson correlation coefficient analyzed the relationship between SEPT6 and UBC in prostate cancer tissues. (c) IF detected the colocation of SEPT6 and UBC in prostate cancer cells. Scale bar = 25 μm, the magnification is 400 times. (d) The overexpression and knockdown efficiency of SEPT6 was detected by qRT-PCR. $^{*}P < 0.05$ vs. the NC group. (e, f) qRT-PCR and WB detected UBC expression, respectively. $^{*}P < 0.05$ vs. the NC group.

protein expressions were decreased in the oe-SEPT6 group compared with the NC group. Still, the reduced protein levels induced by oe-SEPT6 were reversed after oe-UBC. This showed that SEPT6 could regulate the behavior of prostate cancer cells through UBC.

3.5. SEPT6 Inhibited Tumor Growth in Nude Mice. To further explore the effect of SEPT6/UBC on prostate cancer, a tumor formation experiment was conducted in nude mice, and subcutaneous injection of sh-SEPT6 and oe-SEPT6 treated prostate cancer cells in nude mice. Compared with the NC group, the tumor volume and mass in the sh-SEPT6 group were significantly increased. However, the tumor volume and mass in the oe-SEPT6 group were decreased (Figures 5(a) and 5(b)). qRT-PCR showed that compared with the NC group, UBC expression in the oe-SEPT6 group was decreased, while UBC expression increased in the sh-SEPT6 group (Figure 5(c)). As shown in Figure 5(d), compared with the NC group, SEPT6 expression in the OE-SEPT6 group increased, while UBC expression decreased. In the sh-SEPT6 group, SEPT6 expression also decreased, and UBC expression increased. WB results showed that the expressions of ubiquitin and proliferation-related proteins PCNA and Ki67 were raised in the sh-SEPT6 group compared with the NC group. In the oe-SEPT6 group, ubiquitin and proliferation-related protein PCNA and Ki67 expressions were decreased. These results suggested that the SEPT6/UBC pathway could regulate the proliferation of tumor cells in vivo, thus affecting tumor progression.

4. Discussion

Recently, more and more groups have focused on the function of Septins in mammals. Septin can form filamentous

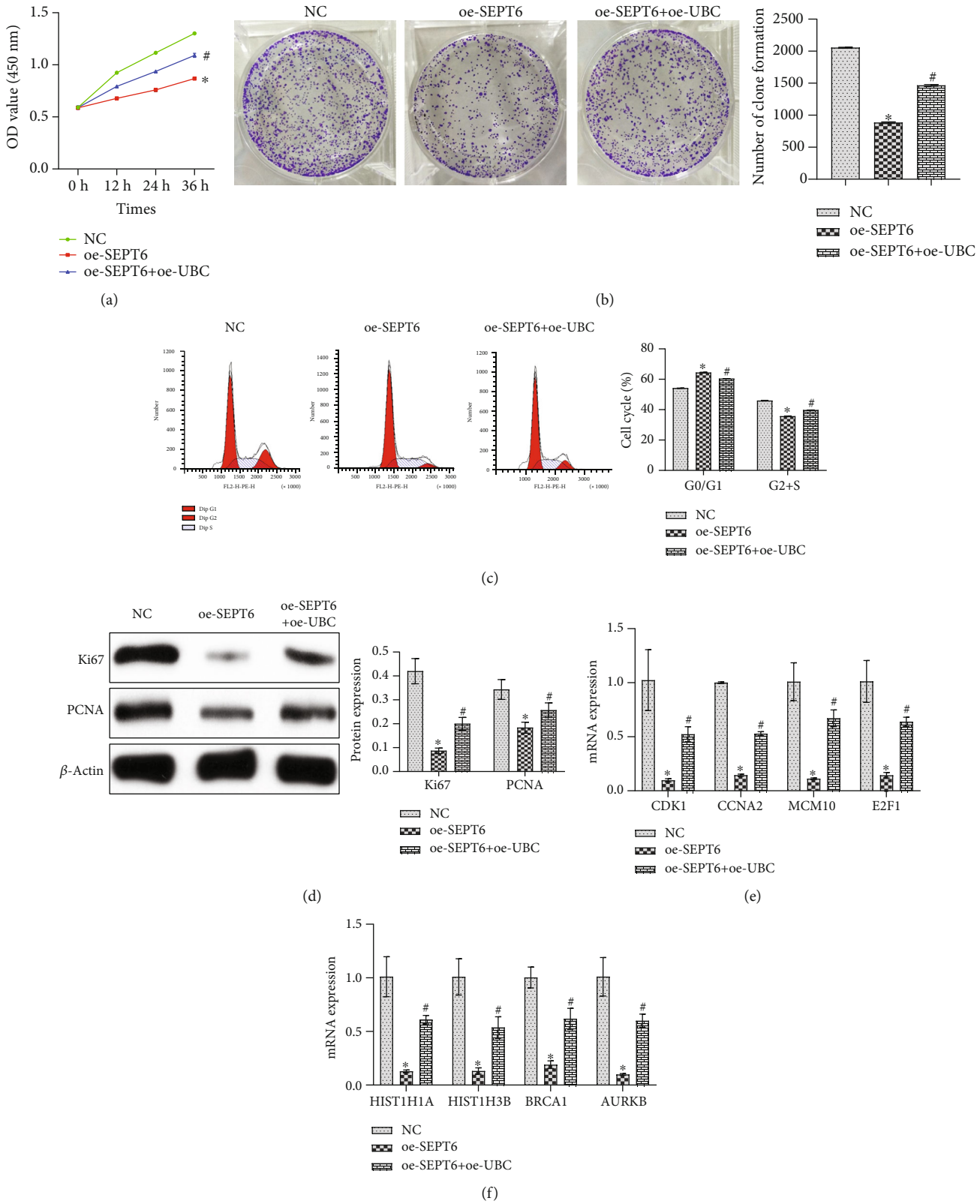

Figure 4: SEPT6 regulated prostate cancer cell behavior through UBC. (a) CCK-8 was used to detect cell proliferation. (b) Clonal formation assay detected cell clone number. (c) Cell cycle at 24 h was detected by flow cytometry. (d) WB was performed to detect proliferation-related protein PCNA and Ki67 expressions. (e) The expression levels of cell cycle proteins CDK1, CCNA2, MCM10, and E2F1 were detected by qRT-PCR. (f) qRT-PCR detected proliferation-related protein HIST1H1A, HIST1H3B, BRCA1, and AURKB expressions. $^{*}P < 0.05$ vs. the NC group; $^{\#}P < 0.05$ vs. the oe-SEPT6 group.

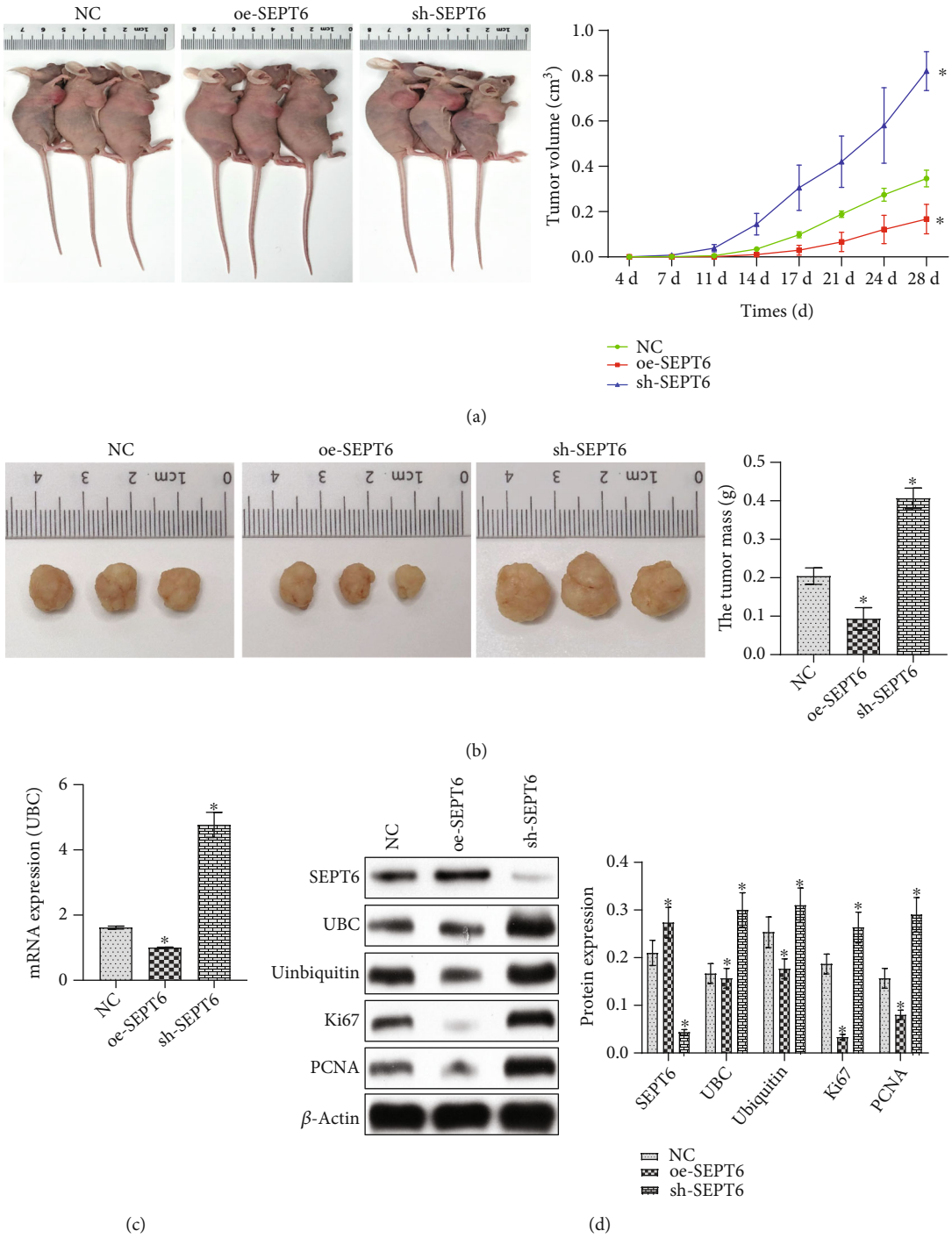

Figure 5: SEPT6 inhibited tumor growth in nude mice. (a) The tumor volume of each group was detected at the time points of 4, 7, 11, 14, 17, 21, 24, and 28 d. (b) Nude mice were sacrificed on day 28, and tumor mass was measured in each group. (c) UBC expressions were detected by qRT-PCR. (d) WB was performed to detect SEPT6, UBC, ubiquitin, PCNA, and Ki67 expressions. $^*P < 0.05$ vs. the NC group.

structures and higher structures on the cortex of eukaryotic cells and bind with actin and microtubule cytoskeleton network [28]. Septins in mammals have been reported to play a key role in the cell cycle and proliferation [29]. Although Septins are essential for cytokines, apoptosis, and proliferation, their molecular mechanisms in cellular processes have not been further investigated. Our study found that SEPT6 inhibited the ubiquitin-coding gene UBC expression, affected the expression level of downstream cell proliferation-related genes, and thus affected the malignant of prostate cancer.

Posttranslational modification plays an important role in regulating the Septin-septin interaction and controlling the formation of high-order septin complexes, and such modifications include SUMOylation, acetylation, ubiquitination, and phosphorylation [30]. The covalence modification of proteins by ubiquitination is the main regulatory

mechanism of protein degradation and quality control, endocytosis, vesicle transport, cell cycle control, stress response, DNA repair, growth factor signal transduction, transcription, gene silencing, and other biological fields [31]. There are four genes encoding ubiquitin in human beings, namely, UBA52, UBA80, UBB, and UBC. The amino acid sequences of ubiquitin-protein encoded by these four genes are completely the same. The only difference is that the repetition times of the ubiquitin-coding sequence in each gene are different [32, 33]. In our study, we found that UBC expression was upregulated in prostate cancer tissues and cells. At the same time, overexpression of UBC could promote cell survival and proliferation, indicating that UBC affects the function of prostate cancer cells.

SEPT6 has already been studied in cellular function. It is reported that the loss of SEPT6 could enhance hematopoietic stem cell engraftment potential [34]. LSD1-mediated SEPT6 protein activates the TGF-β1 pathway and regulates metastasis of non-small-cell lung cancer [35]. Notably, SEPT6 knockdown inhibited apoptosis in prostate cancer cells and promoted migration and invasion [17]. This might be due to the genetic specificity of the cell that determines the function of SEPT6. However, there are few studies on the function of SEPT6 in prostate cancer. Therefore, we wanted to further investigate SEPT6 function in prostate cancer. Proteasome and ubiquitin-mediated systems are functionally involved in many human diseases such as malignancy. It has been reported that changes in proteasome and ubiquitin gene expression are involved in the cancerous state of human kidneys [36]. However, there is little research on SEPT6 and UBC in prostate cancer. Our study found that SEPT6 was negatively correlated with UBC. Furthermore, we found the colocalization of SEPT6 and UBC in prostate cancer cells and the expression of UBC decreased when SEPT6 was overexpressed. Therefore, we speculated that SEPT6 might mediate UBC expression.

Studies have shown that targeting Septin has a strong potential to moderate harmful bystander or homeostasis cytokine-driven proliferation without affecting traditional antigen presentation-driven proliferation [37]. However, UBC regulates a series of genes that control cell cycle and proliferation, such as CDK1, CCNA2, MCM10, E2F1, BRCA1, HIST1H1A, and HIST1H3B, and induces replication of aging genes in HBM-MSCs [27]. Through cell experiments, we found that the expression levels of the cell cycle and proliferation-related proteins decreased after oe-SEPT6, but overexpression of SEPT6 and UBC could increase the protein levels. This indicates that SEPT6, as an upstream gene of UBC, could regulate the behavior of prostate cancer cells through UBC and affect cell proliferation. Through tumor formation experiments, it is found that SEPT6 could inhibit tumor growth. It shows that the SEPT6/UBC pathway could regulate the proliferation of prostate cancer cells, thereby affecting the progress of prostate cancer. However, it is still necessary to further study the role of SEPT6 and UBC in the progression of prostate cancer. In addition, there are some limitations in our study. We only used one prostate cancer cell line DU145 to study the mechanism of SEPT6 and UBC. In fact, more than two prostate cancer cell lines should be taken to study the mechanism of SEPT6 and UBC. However, due to the limitation of funds, we cannot solve this problem well at present. In the future, we will use more than two cell lines to further verify our results. On the other hand, we only investigated the effect of SEPT6 on tumorigenesis in nude mice but did not investigate the role of UBC. Due to the limitation of funds, we will construct cells that interfere with or overexpress UBC to further investigate the effect of UBC on tumorigenesis in vivo in the future.

In conclusion, SEPT6 inhibited UBC expression, thereby reducing the overall ubiquitination level, affecting the expression level of downstream cell proliferation-related genes, and thus affecting the malignancy of prostate cancer. This study provided a reference and basis for the clinical treatment and prognosis of prostate cancer in the future and provided a new target for the treatment of prostate cancer.

Data Availability

All data used to support the findings of this study are available from the corresponding author upon request.

Ethical Approval

The study was conducted following the Declaration of Helsinki. The study was approved by the Ethics Committee of Fujian Provincial Hospital (K-2019-12-028).

Consent

Written informed consents were obtained from the guardians of these patients.

Conflicts of Interest

The authors have no conflict of interest to declare.

Authors' Contributions

Ruochen Zhang and Yaojing Yang contributed equally to this work.

Acknowledgments

This study was supported by the Fujian Provincial Hospital. This study was supported by the high-level hospital foster grants from Fujian Provincial Hospital, Fujian province, China (2020HSJJ18), and the Startup Fund for scientific research, Fujian Medical University (2019QH1154). In addition, we appreciate WELL BIOLOGICAL SCIENCE (http://www.wellbiology.com/, Changsha, China) greatly for their help in experimental methodology for this study.

References

[1] M. Nguyen-Nielsen and M. Borre, "Diagnostic and therapeutic strategies for prostate cancer," *Seminars in Nuclear Medicine*, vol. 46, no. 6, pp. 484–490, 2016.

[2] E. M. Sebesta and C. B. Anderson, "The surgical Management of prostate cancer," *Seminars in Oncology*, vol. 44, no. 5, pp. 347–357, 2017.

[3] A. Lancia, T. Zilli, V. Achard et al., "Oligometastatic prostate cancer: the game is afoot," *Cancer Treatment Reviews*, vol. 73, pp. 84–90, 2019.

[4] U. Haberkorn, M. Eder, K. Kopka, J. W. Babich, and M. Eisenhut, "New strategies in prostate cancer: prostate-specific membrane antigen (PSMA) ligands for diagnosis and therapy," *Clinical Cancer Research*, vol. 22, no. 1, pp. 9–15, 2016.

[5] C. C. Foster, R. R. Weichselbaum, and S. P. Pitroda, "Oligometastatic prostate cancer: reality or figment of imagination?," *Cancer*, vol. 125, no. 3, pp. 340–352, 2019.

[6] G. H. Tan, G. Nason, K. Ajib et al., "Smarter screening for prostate cancer," *World Journal of Urology*, vol. 37, no. 6, pp. 991–999, 2019.

[7] M. Ihara, H. Tomimoto, H. Kitayama et al., "Association of the Cytoskeletal GTP-binding Protein Sept4/H5 with Cytoplasmic Inclusions Found in Parkinson's Disease and Other Synucleinopathies∗," *The Journal of Biological Chemistry*, vol. 278, no. 26, pp. 24095–24102, 2003.

[8] A. E. Zeraik, M. Staykova, M. G. Fontes et al., "Biophysical dissection of schistosome septins: insights into oligomerization and membrane binding," *Biochimie*, vol. 131, pp. 96–105, 2016.

[9] L. Dolat, Q. Hu, and E. T. Spiliotis, "Septin functions in organ system physiology and pathology," *Biological Chemistry*, vol. 395, no. 2, pp. 123–141, 2014.

[10] M. Liu, S. Shen, F. Chen, W. Yu, and L. Yu, "Linking the septin expression with carcinogenesis," *Molecular Biology Reports*, vol. 37, no. 7, pp. 3601–3608, 2010.

[11] D. Connolly, I. Abdesselam, P. Verdier-Pinard, and C. Montagna, "Septin roles in tumorigenesis," *Biological Chemistry*, vol. 392, no. 8-9, pp. 725–738, 2011.

[12] E. A. Peterson and E. M. Petty, "Conquering the complex world of human septins: implications for health and disease," *Clinical Genetics*, vol. 77, no. 6, pp. 511–524, 2010.

[13] S. Mostowy and P. Cossart, "Septins: the fourth component of the cytoskeleton," *Nature Reviews. Molecular Cell Biology*, vol. 13, no. 3, pp. 183–194, 2012.

[14] S. Traikov, C. Stange, T. Wassmer et al., "Septin6 and Septin7 GTP binding proteins regulate AP-3- and ESCRT-dependent multivesicular body biogenesis," *PLoS One*, vol. 9, no. 11, article e109372, 2014.

[15] L. Xiangji, X. Feng, C. Qingbao et al., "Knockdown of HBV surface antigen gene expression by a lentiviral microRNA-based system inhibits HBV replication and HCC growth," *Journal of Viral Hepatitis*, vol. 18, no. 9, pp. 653–660, 2011.

[16] R. Ono, M. Ihara, H. Nakajima et al., "Disruption of Sept6, a fusion partner gene of MLL, does not affect ontogeny, leukemogenesis induced by MLL-SEPT6, or phenotype induced by the loss of Sept4," *Molecular and Cellular Biology*, vol. 25, no. 24, pp. 10965–10978, 2005.

[17] Y. Wei, J. Yang, L. Yi et al., "MiR-223-3p targeting SEPT6 promotes the biological behavior of prostate cancer," *Scientific Reports*, vol. 4, p. 7546, 2014.

[18] Z. Bai, M. Wei, Z. Li, and W. Xiao, "Drosophila Uev1a is dually required for Ben-dependent DNA-damage response and fly mobility," *Cellular Signalling*, vol. 74, article 109719, 2020.

[19] C. M. Pickart, "Mechanisms underlying ubiquitination," *Annual Review of Biochemistry*, vol. 70, no. 1, pp. 503–533, 2001.

[20] A. A. Perelygin, F. A. Kondrashov, I. B. Rogozin, and M. A. Brinton, "Evolution of the mouse polyubiquitin-C gene," *Journal of Molecular Evolution*, vol. 55, no. 2, pp. 202–210, 2002.

[21] P. Cohen and M. Tcherpakov, "Will the ubiquitin system furnish as many drug targets as protein kinases?," *Cell*, vol. 143, no. 5, pp. 686–693, 2010.

[22] H. Park, M. S. Yoon, and K. Y. Ryu, "Disruption of polyubiquitin gene Ubc leads to defective proliferation of hepatocytes and bipotent fetal liver epithelial progenitor cells," *Biochemical and Biophysical Research Communications*, vol. 435, no. 3, pp. 434–440, 2013.

[23] K. Y. Ryu, R. Maehr, C. A. Gilchrist et al., "The mouse polyubiquitin gene UbC is essential for fetal liver development, cell-cycle progression and stress tolerance," *The EMBO Journal*, vol. 26, no. 11, pp. 2693–2706, 2007.

[24] C. Pohl and I. Dikic, "Cellular quality control by the ubiquitin-proteasome system and autophagy," *Science*, vol. 366, no. 6467, pp. 818–822, 2019.

[25] X. Huang and V. M. Dixit, "Drugging the undruggables: exploring the ubiquitin system for drug development," *Cell Research*, vol. 26, no. 4, pp. 484–498, 2016.

[26] N. M. Weathington and R. K. Mallampalli, "Emerging therapies targeting the ubiquitin proteasome system in cancer," *The Journal of Clinical Investigation*, vol. 124, no. 1, pp. 6–12, 2014.

[27] J. Kim, Y. Kim, H. Choi et al., "Ubiquitin C decrement plays a pivotal role in replicative senescence of bone marrow mesenchymal stromal cells," *Cell Death & Disease*, vol. 9, no. 2, p. 139, 2018.

[28] A. A. Bridges and A. S. Gladfelter, "Septin Form and Function at the Cell Cortex∗," *The Journal of Biological Chemistry*, vol. 290, no. 28, pp. 17173–17180, 2015.

[29] K. Ong, C. Wloka, S. Okada, T. Svitkina, and E. Bi, "Architecture and dynamic remodelling of the septin cytoskeleton during the cell cycle," *Nature Communications*, vol. 5, no. 1, p. 5698, 2014.

[30] H. Y. Wang, C. H. Lin, Y. R. Shen, T. Y. Chen, C. Y. Wang, and P. L. Kuo, "Protein kinase A-mediated septin7 phosphorylation disrupts septin filaments and ciliogenesis," *Cell*, vol. 10, no. 2, p. 361, 2021.

[31] J. H. Hurley, S. Lee, and G. Prag, "Ubiquitin-binding domains," *The Biochemical Journal*, vol. 399, no. 3, pp. 361–372, 2006.

[32] J. Y. Lee, M. Tokumoto, Y. Fujiwara, and M. Satoh, "Involvement of ubiquitin-coding genes in cadmium-induced protein ubiquitination in human proximal tubular cells," *The Journal of Toxicological Sciences*, vol. 40, no. 6, pp. 901–908, 2015.

[33] C. P. Grou, M. P. Pinto, A. V. Mendes, P. Domingues, and J. E. Azevedo, "The de novo synthesis of ubiquitin: identification of deubiquitinases acting on ubiquitin precursors," *Scientific Reports*, vol. 5, no. 1, 2015.

[34] K. Senger, G. Marka, K. Soller, V. Sakk, M. C. Florian, and H. Geiger, "Septin 6 regulates engraftment and lymphoid differentiation potential of murine long-term hematopoietic stem cells," *Experimental Hematology*, vol. 55, pp. 45–55, 2017.

[35] Y. Hong, X. Li, and J. Zhu, "LSD1-mediated stabilization of SEPT6 protein activates the TGF-β1 pathway and regulates non-small-cell lung cancer metastasis," *Cancer Gene Therapy*, 2021.

[36] H. Kanayama, K. Tanaka, M. Aki et al., "Changes in expressions of proteasome and ubiquitin genes in human renal cancer cells," *Cancer Research*, vol. 51, no. 24, pp. 6677–6685, 1991.

[37] A. M. Mujal, J. K. Gilden, A. Gérard, M. Kinoshita, and M. F. Krummel, "A septin requirement differentiates autonomous and contact-facilitated T cell proliferation," *Nature Immunology*, vol. 17, no. 3, pp. 315–322, 2016.

Hindawi
Mediators of Inflammation
Volume 2021, Article ID 7681252, 14 pages
https://doi.org/10.1155/2021/7681252

Research Article

Effect of Garlic Organic Sulfides on Gene Expression Profiling in HepG2 Cells and Its Biological Function Analysis by Ingenuity Pathway Analysis System and Bio-Plex-Based Assays

Chenghao Lv,[1,2] Caiqiong Wang,[2] Ping Li,[2] Yiwen Huang,[2] Xiangyang Lu,[1] Meng Shi,[2] Chaoxi Zeng,[2] and Si Qin[1,2]

[1]*College of Bioscience and Biotechnology, Hunan Agricultural University, Changsha, Hunan 410128, China*
[2]*Lab of Food Function and Nutrigenomics, College of Food Science and Technology, Hunan Agricultural University, Changsha 410128, China*

Correspondence should be addressed to Chaoxi Zeng; chaoxizeng@hunau.edu.cn and Si Qin; qinsiman@hotmail.com

Received 10 September 2021; Revised 23 October 2021; Accepted 26 October 2021; Published 30 November 2021

Academic Editor: Deguang Song

Garlic organic sulfides are dietary bioactive components with multiple biofunctions to prevent chronic diseases/inflammation and promote human health. DADS (diallyl disulfide), DATS (diallyl trisulfide), and DTS (diallyl tetrasulfide) are typical organic sulfides with similar structures from garlic. However, the structure-activity relationship of garlic organic sulfides remained unknown. The aim of the present study was to investigate the effect of DADS, DATS, and DTS on the gene expression profiling of human hepatocellular carcinoma cells (HepG2) by application of microarray and specialized analysis software, GO, Bio-Plex-based cytokines assay and IPA and analyze their structure-activity relationship according to antioxidant, anti-inflammatory, and metabolic-related properties. According to the microarray data, with the increase of S atom in garlic organic sulfides, its biological activity was gradually enhanced. In the general catalog of GO, garlic organic sulfides mainly affect biological process, molecular function, and cellular component. RT-qPCR results indicated that the microarray data is trustworthy, and the structure-activity analysis data found that more sulfur atoms have more powerful properties; thus, microarray data of DTS was preceded to the subsequent IPA analysis. The results of IPA analysis showed that the top 5 signaling pathways and molecular functions were disturbed by DTS; the molecular functions with the highest scores affected by DTS are cancer, cell apoptosis, and cell proliferation, which imply that the occurrence or metabolism of these diseases is related to the differential expression of the above-mentioned related genes and the activation of signaling channels, and the core of the most significant molecular network is inflammation. Finally, the results found that the secretions of 6 cytokines in macrophages were significantly inhibited by DTS treatment. This is the first study that analyzed the structure-activity relationship of garlic organic sulfides, which will provide useful genetic information for its multi-biofunction and promote their clinical application in the near future.

1. Introduction

Garlic organic sulfides are dietary bioactive components with the functions to prevent chronic diseases/inflammation and promote human health. DADS (diallyl disulfide), DATS (diallyl trisulfide), and DTS (diallyl tetrasulfide) are typical organic sulfides with similar structures to garlic, possessing two, three, and four sulfur atoms, respectively. They are natural compounds with low toxicity, and recent studies found that they have potent bioactive properties such as antioxidation, anticancer, and anti-inflammation activities. However, their structure-activity relationships remained unknown.

Experimental studies have shown that daily consumption of garlic is beneficial to human health, such as reducing the risk of esophageal cancer, gastric cancer, and prostate cancer [1, 2]. A large number of animal studies have shown that garlic has a wide range of biological activities including

antioxidant [3, 4], anti-inflammatory, and anticancer activities [5, 6]. In addition, garlic can also be used to treat indigestion and fever, and it has antibacterial property [7]. It is also used as a food preservative in Asia [8].

The main biologically active substance of garlic is garlic organic sulfides (OSCS), which has a pungent smell and spicy taste. Garlic organic sulfur compounds can be divided into fat-soluble organic sulfur compounds and water-soluble organic sulfur compounds. Fat-soluble organic sulfides are classified into monosulfur compounds (DAS), disulfide compounds (DADS), trisulfide compounds (DATS), and tetrasulfide compounds (DTS) according to the number of S atoms [9].

Recent epidemiological investigations have shown that eating garlic can reduce the risk of different types of malignant tumors by inhibiting inflammatory factors [2, 10]. Cell culture experiments have shown that garlic sulfide S-allyl-L-cysteine (SAC) can inhibit the production of NO and the expression of iNOS [11]. In RAW264.7 cells induced by LPS, red garlic organic sulfide can inhibit the production of NO and the expression of iNOS [12]. In BV2 microglia cells stimulated by LPS, DADS can also inhibit the production of NO and PGE2 [13]. In addition, Liu et al. compared the effects of DAS, DADS, and DATS on the inhibition of NO production and iNOS expression and found the inhibitory effects in the order of DATS>DADS>DAS, which indicates that the inhibitory effect may be similar to that of S in garlic organic sulfide [14]. In RAW264.2 cells stimulated by LPS, DATS exhibited the best inhibitory effect on inflammation when compared to GSAC, SAC, DAS, and DADS [15]. Therefore, the structural difference of organic sulfide in garlic may be the key factor affecting its biological activity.

Garlic organic sulfides also exert anti-inflammatory effects by inhibiting the expression of proinflammatory factors. Allicin can inhibit the expression of proinflammatory factors induced by TNF-α [16]. DADS can also inhibit the expression of proinflammatory factors, induced by LPS, such as IL-1β and TNF-β [13]. In RAW264.7 cells induced by LPS, DATS inhibited the expression of IL-6, IL-10, IL-12, KC, MCP-1, and TNF-α [15].

Experimental data from several studies indicate that the expression of proinflammatory factors such as iNOS and COX2 is related to the NF-κB signaling pathway. DADS was reported to attenuate the expression of the NF-κB signaling pathway [17]. However, DADS can inhibit the expression of transcription factors p65, c-Jun, and c-fos in the nucleus [18]. On the other hand, allicin can downregulate the transcription factors p65 of the upstream kinase IKKα/β and downregulate IκB and attenuate the nuclear translocation of p65 [15]. These experimental studies show that DATS can inhibit the inflammatory response induced by LPS and downregulate the IKK-mediated NF-κB signaling pathway.

Mitogen-activated protein kinases (MAPKs), including JNK, p38, and ERK, play a key role in the inflammatory responses [19]. Therefore, in some chronic inflammatory diseases including rheumatoid arthritis, psoriasis, inflammatory bowel disease, and chronic obstructive pulmonary disease, inhibiting the expression of MAPKs is an effective treatment. Some studies have shown that DADS can attenuate the MAPK signaling pathway induced by LPS and thereby slowing down the inflammatory responses [13]. Allicin can inhibit the ERK signaling pathway and thereby inhibit the proliferation of cancer cells [20]. DADS and DATS can inhibit the activity of AP-1 mediated by JNK and ERK and promote the expression of GST protein and mRNA [21]. DATS attenuates AP-1 activity and COX-2 expression by inhibiting JNK and Akt signaling pathways [22]. DATS can also inhibit the phosphorylation of TAK1, the common upstream regulator of IKKα/β and MAPK signaling pathways [13, 15]. In addition, it also inhibits the phosphorylation of AKT1, an upstream protein kinase that activates IKK [23, 24]. These experiments show that garlic organic sulfide can inhibit the MAPK and NF-κB signaling pathway mediated by AKT1/TAK1 and thereby inhibiting the inflammatory responses.

In this study, we investigated the effects of DADS, DATS, and DTS on the gene expression profiling of human hepatocellular carcinoma cells (HepG2) by application of microarray and specialized analysis software, GO and IPA, and analyzed their structure-activity relationship according to antioxidant, anti-inflammatory, and metabolic-related properties. Finally, LPS-induced RAW264.7 macrophages were treated with DTS to verify its inhibitory effect on inflammation and maintenance of redox balance.

2. Materials and Methods

2.1. Cell and Cell Cultures. HepG2 cells were cultured in DMEM medium containing 10% fetal bovine serum (FBS), and the temperature was maintained at 37 cu with stable 5% CO_2 gas supply. Discard the old culture medium in the 25 cm^2 petri dish, add about 1 ml 0.01 M PBS with a pipette, shake gently to rinse the cell surface, and wash away the remaining FBS to prevent it from affecting the trypsin digestion. Use the pipette tip to suck off the PBS (not directly poured), add 1 ml of 0.05% pancreatin solution to cover the bottom of the bottle, incubate for 1 minute, then discard most of the pancreatin, and keep it at 37 t in an incubator for 2 minutes. By using the inverted microscope, the digestion of the cells was observed. It was observed that the cells gradually shrink and became rounded, the cell connection disappeared, the spacing increased, and a few cells were fallen off the bottle wall. At this time, we quickly added 2 ml fully grown DMEM/F12 medium (containing 10% FBS), gently pipetted with a disposable sterile straw to make it into a cell suspension. Transfer the digested cells into a centrifuge tube, and centrifuge it at 1,000 rpm or 800 rpm for 5 minutes. Aspirate the supernatant with a pipette, to the cell pellet adding 3-4 ml DMEM/F12 medium containing 10% FBS to fully suspend the cells (gently mix the front, back, left, and right); if necessary, add antibiotics (commonly used penicillin), and then put them into 3-4 petri dishes to make the total amount of liquid in each bottle reach 5 ml. Keep the well-mixed cell culture dish carefully into an incubator at 37 with 5% CO_2, and continue culturing.

2.2. Cell Toxicity Determination. MTT assay was used to check the cytotoxicity of DSs. HepG2 cells were seeded on a 96-well plate at a density of 104 cells per well and then pre-incubated at 37°C for 24 h; then the specified dose (0.5 μM, 10 μM, and 20 μM) of garlic organic sulfide compound was added and incubated for another 24 h. Then, add MTT to the plate (final concentration is 0.5 mg/ml) and incubate for 4 h, add acidic isopropanol (HCl in isopropanol is 0.04-0.10 N) to dissolve formazan crystals, and use a microplate reader (Thermo Scientific, USA) to measure the optical density (OD) at 575 nm. Cell viability was determined by comparing the OD value of DSs-treated cells with that of untreated cells.

2.3. RNA Extraction and Microarray. HepG2 cells were precultured in a petri dish for 24 hours and then treated with DADS, DATS, and DTS at a concentration of 10 μM dissolved in 0.1% DMSO for 10 hours. Total RNA was extracted using the Isogen RNA kit (Nippon Gene Co., Tokyo, Japan) according to the instructions, and the RNA quality was evaluated by automatic capillary gel electrophoresis on the Agilent Bioanalyzer 2100 (Palo Alto, CA, USA). These total RNA samples were labeled according to the standard single-cycle amplification, and labeling protocol was developed by Affymetrix (Santa Clara, CA, USA), and cRNA was labeled at 40°C for 2 hours. After amplification and labeling, the Affymetrix Gene Chip Human U133 plus 2.0 Array system was used for gene chip testing. The Affymetrix Gene Chip Human U133 plus 2.0 chip contained more than 44 K oligonucleotides, and the hybridization fluorescence was scanned using the Affymetrix scanner.

2.4. GO Ontology and IPA Analysis of Microarray Data. The gene chip results were first classified according to the Gene Ontology ID (GO ID) (http://www.geneontology.org/). Gene Ontology is a major bioinformatics method that is aimed at standardizing genes and gene products across species and database representation of attributes. Then, through the Ingenuity Pathway Analysis (IPA) system (http://www.ingenuity.com) for analysis.

2.5. Bio-Plex-Based Assays of Inflammatory Cytokine. HepG2 cells were precultured and starved accordingly to eliminate the effect of FBS. The cells were treated with 10-20 μM of DTS for half hour before exposure to 1 μg/ml LPS for additional 12 h. The 27 cytokines' detection, including IL-1α, IL-1β, IL-2, IL-4, IL-5, IL-6, IL-7, IL-8, IL-9, IL-10, IL-12, IL-13, IL-15, IL-17, RANTES, PDGF-BB, FGF basic, IP-10, TNF-α, Eotaxin, IFN-γ, MCP-1, MIP-1α, MIP-1β, GM-CSF, and VEGF, was performed by using Bio-Plex Pro Human Cytokine 27-Plex Panel kit (Bio-Rad Laboratories) and Bio-Plex cytokines assay system (Bio-Plex 200, Bio-Rad) according to the manufacturer's instructions, and the results were analyzed by the Bio-Plex manager software (version 4.0).

2.6. Statistical Analysis. All the experimental data in the present study were repeated at least three or four times. Significances or differences of treated vs. control were analyzed by using Student's t-test, and $p < 0.05$ was considered significant.

3. Results and Discussions

3.1. Gene Expression Profiling. In the source data of the gene chip by DADS treatment, the expression of 3 genes changed by 5 times or more, and the expression of all 3 genes was upregulated. The fold change of the expression of 2 genes was between 4 and 5 times, and the expression of all 2 genes was upregulated. The expression changes of 13 genes were between 3 and 4 times, and the expression of all 13 genes was upregulated. The expression of 110 genes varied from 2-fold to 3-fold, 85 of which were upregulated and 25 were downregulated. In the source data of the experimental group treated by DADS, out of 54675 genes, there were 128 genes (accounting for 0.23%, 128 : 54675) that showed the expression change higher than 2 times (Table 1).

In the source data of the gene chip by DATS treatment, the expression of 4 genes had a fold change greater than or equal to 5 times, the expression of 3 genes was upregulated, and the expression of 1 gene was downregulated. The expression changes of 7 genes were between 4-fold and 5-fold, 6 genes were upregulated, and 1 gene was downregulated. The expression changes of 32 genes were between 3 times and 4 times, 18 genes were upregulated, and 14 genes were downregulated. The expression of 201 genes varied between 2-fold and 3-fold, 99 of which were upregulated and 102 genes were downregulated. In general, in the source data of the experimental group processed by DATS, 244 genes (0.45%, 244 : 54675) out of 54675 genes had expression changes higher than 2 times (Table 1).

In the source data of the gene chip by DTS treatment, the expression of 4 genes changed by 5 times or more, and the expression of all 4 genes was upregulated. The expression changes of 8 genes were between 4-fold and 5-fold, 7 genes were upregulated, and 1 gene was downregulated. The expression changes of 29 genes were between 3 times and 4 times, 21 genes were upregulated, and 8 genes were downregulated. The expression of 203 genes varied between 2-fold and 3-fold, of which 115 genes were upregulated and 88 genes were downregulated. In general, in the source data of the experimental group processed by DTS, there were 244 genes (0.45%, 244 : 54675) out of the 54675 genes whose expression has changed more than 2 times (Table 1).

The number of downregulated genes in the DATS group was more than that in the DTS group. However, the number of genes upregulated in the DTS group is significantly higher than that in the DATS group and gene expression of the DADS group changed more than 2 times, and the number of upregulated genes increased in the order of DTS>DATS>DADS.

3.2. GO Ontology Analysis of Microarray Data. In this study, we first used the free analysis tool GO (Gene Ontology) on the whole network to analyze the gene chip data. This analysis method is based on one or more GO numbers corresponding to each gene to find each gene in the official catalog of GO categories, and it has the following three

Table 1: Changes of DSs-related gene expression in Hep G2 cells.

	Fold of change	DADS/ control	DATS/ control	DTS/ control
Up	5<	3	3	4
	4	2	6	7
	3	13	18	21
	2	85	99	115
Down	2	25	102	88
	3	0	14	8
	4	0	1	1
	5<	0	1	0
Total	Up	103	126	147
	Down	25	118	97
	Total ($\pm 2^3$ fold change)	128	244	244

major categories, namely, biological process, cellular component, and molecular function. Each major category contains 6 subcategories. For classification, each category also has a corresponding GO number. Since this experiment was intended to study the results of the differential expression of hepatocarcinoma genes after treatment with DADS, DATS, and DTS and their relationship with physiological activity, only genes with significant changes in differential expression are selected for the overall analysis. According to the results of previous studies, we selected genes whose changes were greater than 2 times for statistical analysis. There were 616 genes whose expression changes were greater than 2 times, accounting for 1.13% of the total number of genes. The results of GO analysis showed that there are 32, 27, and 25 subgroup genes are disturbed by garlic organic sulfides treatment in the total three categories including biological processes, cell composition, and molecular function. The most significantly disturbed genes are related to protein binding in DTS group, which indicated that DTS can significantly affect the intracellular signal pathway.

3.3. DADS/DATS/DTS Regulates the Expressions of Genes

3.3.1. DADS/DATS/DTS Regulates the Expressions of Liver Drug Metabolizing Enzymes. To understand the effect of garlic organic sulfide on HepG2 cells and predict its metabolism in the liver, we studied the gene expression changes of drug metabolizing enzymes and transporters in cells treated with DADS, DATS, and DTS. Phase I enzymes are mainly responsible for binding heterologous substances to carriers on the cell surface during drug metabolism. Phase II enzymes function to enhance their water solubility or expose specific binding sites to facilitate binding to transporters. Transport enzymes are to transport the foreign material out of the cell and excrete it from the body through the blood circulation. In this study, changes were observed in gene expression of 35 drug metabolizing enzymes and transporters. Coenzyme I related to typical phase I enzymes represents FMO5 and NCF2, and related to phase II coenzymes, it is worth noting that the differentially expressed phase II coenzymes also include GCLC, GCLM, SQSTM1, and other antioxidant enzymes. There are 10 genes related to proteins such as the ATP and SLC families (Table 2). In the DTS treatment group, the upregulated expression of phase I coenzyme was more than 2 times that of NCF2. GCLC, GCLM, SQSTM1, and HMOX1 were found to be more than 2 times upregulated in phase II coenzyme or antioxidant protein. SlC6A6 and SLC2A2 are the genes that express more than 2 times in transporters.

3.3.2. DADS/DATS/DTS Regulates the Expressions of Inflammation-Related Genes. To understand the effect of garlic organic sulfide on HepG2 cells and predict its effect on inflammation in the liver, we studied the expression changes of inflammation-related genes in cells treated with DADS, DATS, and DTS. The typical inflammatory cell pathways affected by DSs are the NF-κB signaling pathway, IL-6 signaling pathway, and IL-2 signaling pathway. According to gene chip data, gene expression changes more than 2 times, and genes related to inflammatory cell pathways include TLR6, FOS, SOCS1, BCL10, and TNFAIP3. Among them, DSs had the greatest impact on the expression changes of FOS genes. The expression changes of FOS genes in the DTS treatment group were higher than 4 times, and both the DADS and DATS experimental groups were more than 3 times (Table 3).

3.3.3. DADS/DATS/DTS Regulates the Expressions of Genes Related to Glucose and Lipid Metabolism. To understand the effect of garlic organic sulfides on glycolipid metabolism, we studied changes in the expression of genes related to glycolipid metabolism in cells treated with DADS, DATS, and DTS. Among the genes related to glucose and lipid metabolism, GCLC, GCLM, SLC2A2, and GCKR showed more than 2 times of expression changes after DS_S treatment. In the DATS and DTS groups, the expression of SLC2A2 gene changed more than 3 times and the gene was downregulated (Table 4).

3.3.4. DADS/DATS/DTS Regulates the Expression of Genes Related to Cell Proliferation and Apoptosis. To understand the effect of garlic organic sulfide on cell proliferation and apoptosis, we investigated the changes in gene expressions related to cell proliferation and apoptosis in HepG2 cells treated with DADS, DATS, and DTS. After DSs treatment, the expression of apoptosis-related genes changed more than 2 times, including F2RL2, HSPA1A///HSPA1B, GCLC, GCLM, SLC2A2, EGR1, FOS, BCL10, TLR6 and NCF2. According to the data from the gene chip, DSs can promote the expression of apoptosis genes, especially the F2RL2 gene, HSPA1A///HSPA1B gene, FOS gene, and NCF2 gene. The gene expression change multiples are more than 3 times, and the F2RL2 gene expression within the multiple is even more than 14 times. DSs can also downregulate the expression of SLC2A2 gene. The expression of cell proliferation-related genes changed more than 2-fold, including F2RL1, SOCS1, FOS, FOSL1, HSPA1A, JAG1, and SPP1 genes. From the data of the gene chip, we can see that the most

Table 2: Changes in gene expression of drug metabolizing enzymes and transporters in DSs-treated cells.

Gene symbol	Gene title	Fold	Change
Detoxification: phase I drug			
		3.42	
FMO5	Flavin containing monooxygenase 5	2.82	Down
		3.58	
		4.29	
NCF2	Neutrophil cytosolic factor 2 (65 kDa, chronic granulomatous disease, autosomal 2)	3.88	Up
		3.16	
Detoxification: phase II and antioxidant proteins			
		2.32	
SQSTM1	Sequestosome 1	2.46	Up
		2.20	
		2.01	
HMOX1	Heme oxygenase (decycling) 1	2.22	Up
		2.65	
		2.32	
GCLC	Glutamate-cysteine ligase, catalytic subunit	2.51	Up
		2.49	
		2.36	
GCLM	Glutamate-cysteine ligase, modifier subunit	2.40	Up
		2.58	
Detoxification: phase III			
		2.17	
SLC2A2	Solute carrier family 2 (facilitated glucose transporter), member 2	3.24	Down
		3.01	
		3.18	
SLC6A6	Solute carrier family 6 (neurotransmitter transporter, taurine), member 6	3.82	Up
		3.17	

typical gene that affects cell proliferation is the F2RL2 gene (Table 5).

3.3.5. Real Time Quantitative-PCR Analysis. To verify the accuracy of the gene chip results and compare the structure-activity relationship of the three compounds, we further verified the expression of typical drug metabolizing enzymes and antioxidant protein-related genes in HepG2 cells treated with the above three organic sulfides of garlic and analyzed whether the number of sulfur atoms is the same as the change trend of the expression of the genes.

After treating HepG2 cells with the same concentrations of the samples, the total RNA was extracted and then reverse transcribed into cDNA. Finally, the target genes were detected with a fluorescent kit and a real-time fluorescent quantitative PCR. Statistical analysis of the data can provide useful information. Due to the high cost of RT-PCR experiments, only 6 typical genes for drug metabolizing enzymes and antioxidant proteins were selected for RNA transcription level verification. The selected genes were NCF2, SQSTM1, HMOX1, GCLC, and GCLM. And SLC6A6 belongs to the genes corresponding to phase I/II antioxidant proteins and phase III transporter (Figure 1).

The selected genes showed similar expressions between the DNA chip and RT-PCR data, and the trend of differential expression of the genes was the same. Among them, the expression level of anti-inflammatory factor IL11 increased by 4.21 times in real-time PCR, while it increased by 3.33 times in the DNA chip. The reason for the difference in expression multiples is that the results of RT-PCR were obtained from real-time fluorescence measurement, which can record more minutes and precise gene differential expression in real time, so the measured difference multiple is larger and more precise. Compared with treatment by DADS and DATS, DTS can significantly upregulate the expression of SQSTM1, HMOX1, GCLC, and GCLM. These data indicate that treatment of HepG2 cells by DTS can indeed enhance the expression of their antioxidant genes, reduce inflammation, and increase the expression of genes related to metabolic regulation.

3.4. IPA Analysis of Microarray Data. To further analyze the potential relationship between significantly changed genes and biological functions, we input the gene chip data into the IPA system, and then the system outputs an analysis report: including typical pathways that are significantly

Table 3: DSs regulate the expression of inflammation-related genes.

Gene symbol	Gene title	Fold	Change
		2.11	
TLR6	Toll-like receptor 6	2.34	Up
		2.05	
		3.16	
FOS	v-fos FBJ murine osteosarcoma viral oncogene homolog	3.88	Up
		4.13	
		2.07	
SOCS1	Suppressor of cytokine signaling 1	2.68	Down
		2.08	
		2.11	
BCL10	B-cell CLL/lymphoma 10	2.32	Up
		3.05	
		2.01	
TNFAIP3	Tumor necrosis factor, alpha-induced protein 3	2.13	Down
		2.24	
		2.17	
PRKACB	Protein kinase, cAMP-dependent, catalytic, beta	2.34	Up
		2.69	
		2.08	
TNFRSF10D	Tumor necrosis factor receptor superfamily, member 10d, decoy with truncated death domain	2.68	Up
		2.83	

Table 4: DSs regulate the expression of genes related to glucose and lipid metabolism.

Gene symbol	Gene title	Fold	Change
		2.32	
GCLC	Glutamate-cysteine ligase, catalytic subunit	2.51	Up
		2.49	
		2.29	
GCLM	Glutamate-cysteine ligase, modifier subunit	2.40	Up
		2.48	
		2.17	
SLC2A2	Solute carrier family 2 (facilitated glucose transporter), member 2	3.24	Down
		3.01	
		2.07	
GCKR	Glucokinase (hexokinase 4) regulator	2.04	Up
		2.95	

affected, molecular networks, biological functions, and molecules; due to the limitation of study, only some important issues were selected for analysis in this part.

3.4.1. Main Typical Affected Signaling Pathways. The typical approach affected by DTS processing can help locate its main signal channel. The most affected signal channel in the DTS treatment group is glutamate metabolism, and its p value takes the negative logarithm to the maximum value of 3.47; the second affected channel is acute phase response signal.

The p value of NRF2-mediated oxidative stress response activated by DTS takes a negative logarithm of 3.08. It is a very essential and complex signal transmission pathway. Nuclear factor Nrf2 (also called Nfe212) is a transcription factor that regulates the redox state of cells. Nrf2 has the ability to promote the expression of various protective genes of cells in response to various stimuli (including redox signals, inflammation, growth factors, and energy supply changes), which makes it play a key role in cell adaptation. Experimental evidence shows that Nrf2 can profoundly affect metabolism: Nrf2 protects the liver from steatosis by

Table 5: DSs regulate the expression of genes related to cell proliferation and apoptosis.

Gene symbol	Gene title	Fold	Change
		14.14	
F2RL2	Coagulation factor II (thrombin) receptor-like 2	15.28	Up
		15.01	
		4.29	
HSPA1A///HSPA1B	Heat shock 70 kDa protein 1A///heat shock 70 kDa protein 1B	4.30	Up
		3.68	
		2.32	
GCLC	Glutamate-cysteine ligase, catalytic subunit	2.51	Up
		2.49	
		2.29	
GCLM	Glutamate-cysteine ligase, modifier subunit	2.40	Up
		2.48	
		2.17	
SLC2A2	Solute carrier family 2 (facilitated glucose transporter), member 2	3.24	Down
		3.01	
		2.11	
TLR6	Toll-like receptor 6	2.34	Up
		2.05	
		3.16	
FOS	v-fos FBJ murine osteosarcoma viral oncogene homolog	3.88	Up
		4.14	
		2.07	
SOCS1	Suppressor of cytokine signaling 1	2.68	Down
		2.08	
		4.29	
NCF2	Neutrophil cytosolic factor 2 (65 kDa, chronic granulomatous disease, autosomal 2)	3.12	Up
		3.16	
		2.06	
VDR	Vitamin D (1,25-dihydroxyvitamin D3) receptor	2.69	Down
		2.86	
		3.20	
SPP1	Secreted phosphoprotein 1 (osteopontin, bone sialoprotein I, early T-lymphocyte activation 1)	2.64	Up
		2.82	
		2.19	
FOSL1	FOS-like antigen 1	2.39	Up
		2.34	
		2.76	
JAG1	Jagged 1 (Alagille syndrome)	3.59	Up
		4.01	

promoting fatty acid oxidation and inhibiting adipogenesis and can promote the formation of fat in peripheral tissues by activating C/EBPb and PPARg. The effect of Nrf2 on lipid metabolism and its obvious ability to inhibit gluconeogenesis indicate that CNC-bZIP factor contributes to metabolic flexibility; that is, it helps to promote organism's lipid oxidation and carbohydrate oxidation as an energy ability to convert. Therefore, the effects of DTS on the metabolism of foreign substances, C21-steroid hormones, glycerophospholipids, glycerolipids, and glutamate may all be related to NRF2, which further confirms that the expression of drug metabolism enzymes is significantly affected by DTS treatment. At the same time, Nrf2 can also be used as a stress-activated transcription factor that mediates drug metabolism enzymes. Nrf2 can control the expression of many phase I and phase II drug metabolism enzymes, as well as other multidrug resistance-related protein (MRP) transporters including MRP2, MRP3, MRP4, and MRP5 expressions. In

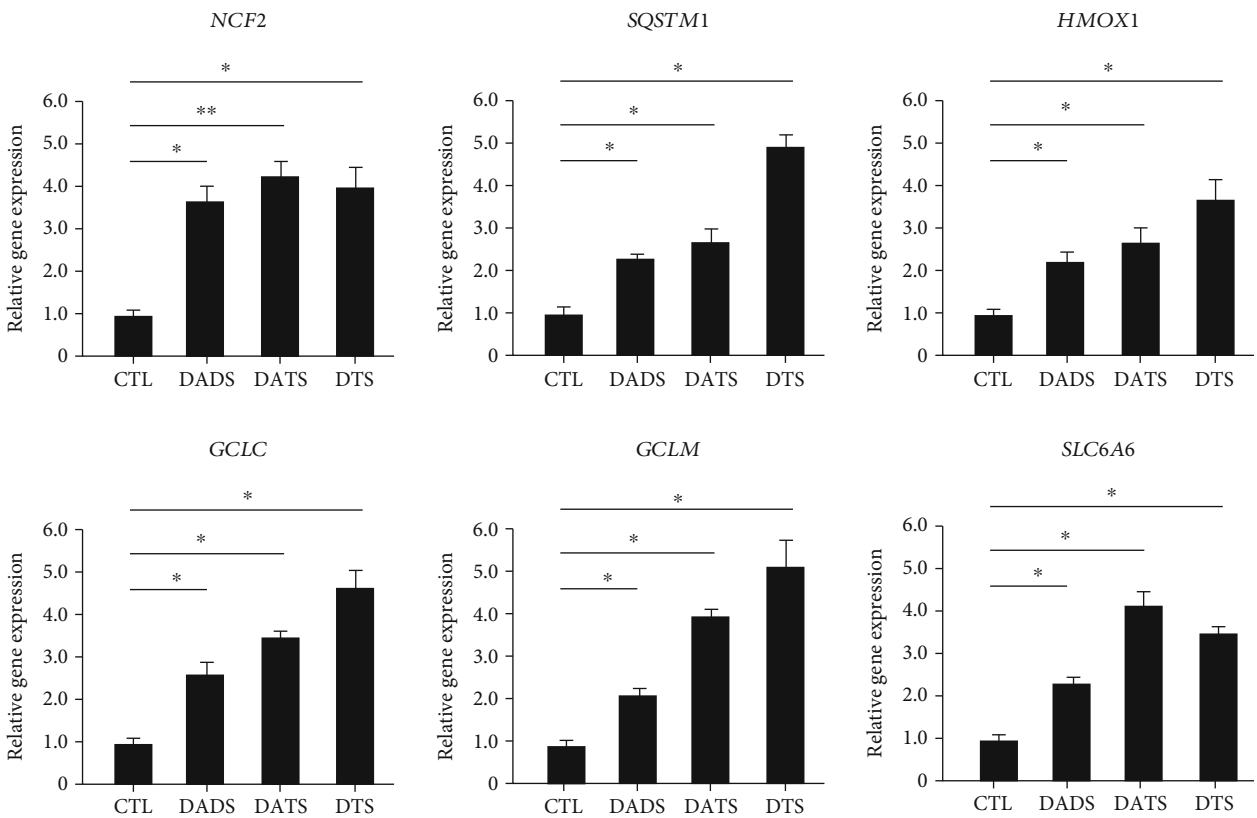

Figure 1: RT-PCR results of typical genes in HepG2 cells treated with DADS/DATS/DTS.

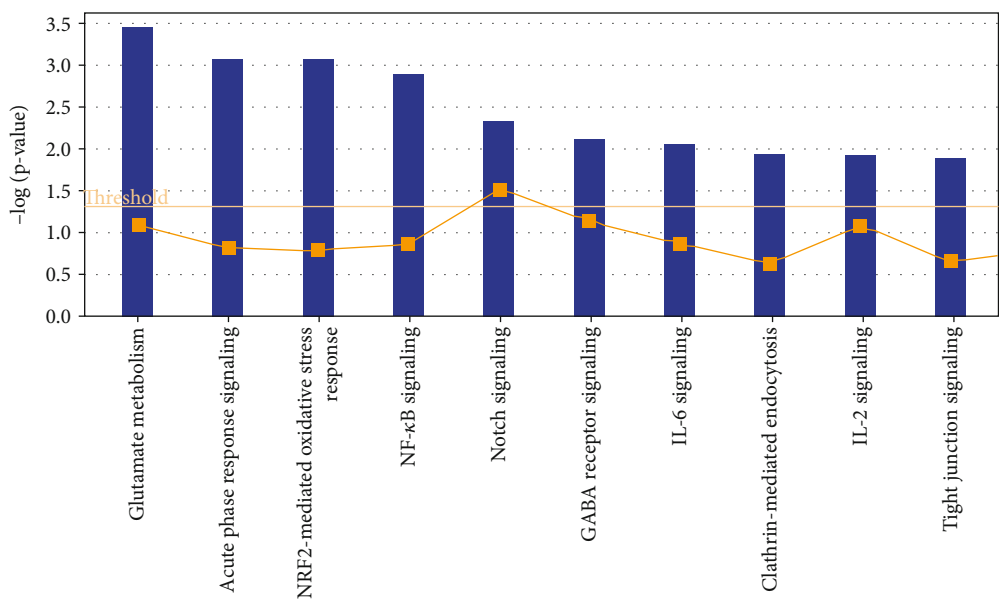

Figure 2: Top 10 typical cell pathways affected by DTS treatment.

addition to regulating the basic and induced expression of drug metabolism enzymes, Nrf2 also controls the key components of the endogenous antioxidant system: many drug metabolism enzymes and antioxidant systems require NADPH as a cofactor, including aldehyde ketone reductase (AKR), NQO1, GSR1, and TXNRD1, and it is worth noting that NADPH produces enzymes glucose-6-phosphate dehydrogenase (G6PD), 6-phosphogluconate dehydrogenase (PGD), isocitrate dehydrogenase (IDH)1, and malic enzyme (the processes of ME)1 which are regulated by Nrf2.

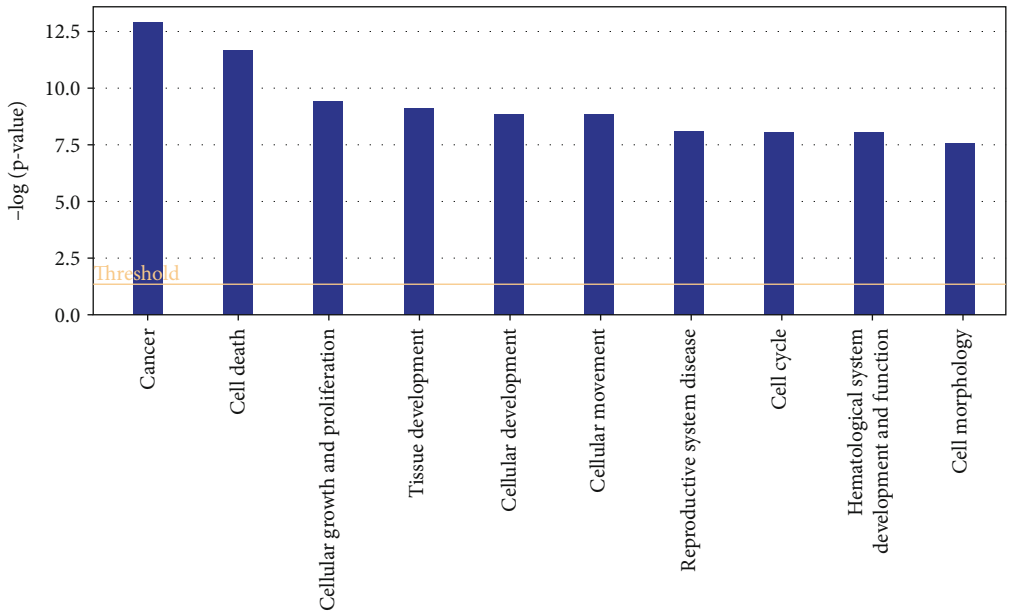

Figure 3: Top 10 molecular functions changed by DTS treatment.

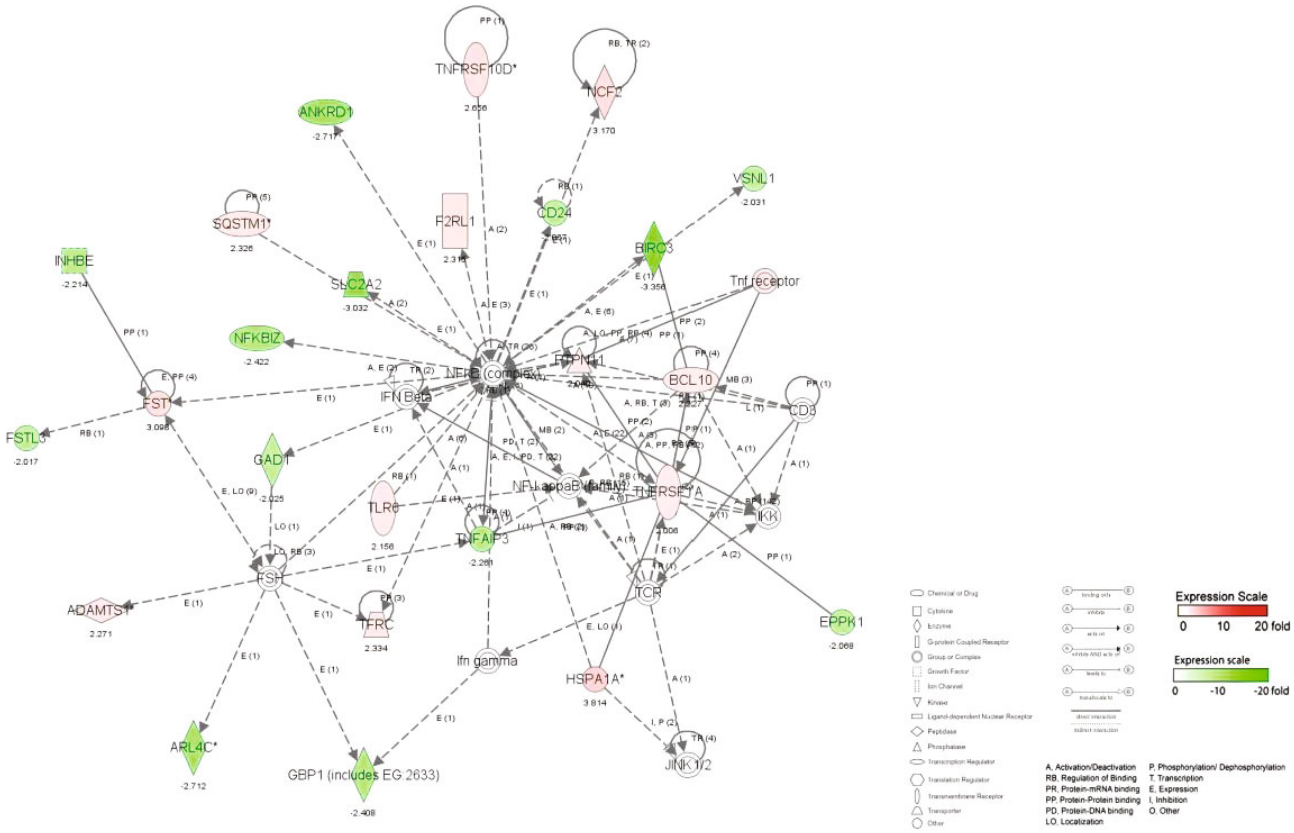

Figure 4: The most significant molecular network affected by DTS.

Therefore, the high activity of Nrf2 can ensure that the expression of the enzyme-catalyzed reduction reaction is combined with the supply of cofactors. In addition, other signal channels that can be significantly activated in the DTS treatment group are NF-κB signaling, IL-6 signaling, and IL-2 signaling. These three cell pathways are all inflammatory

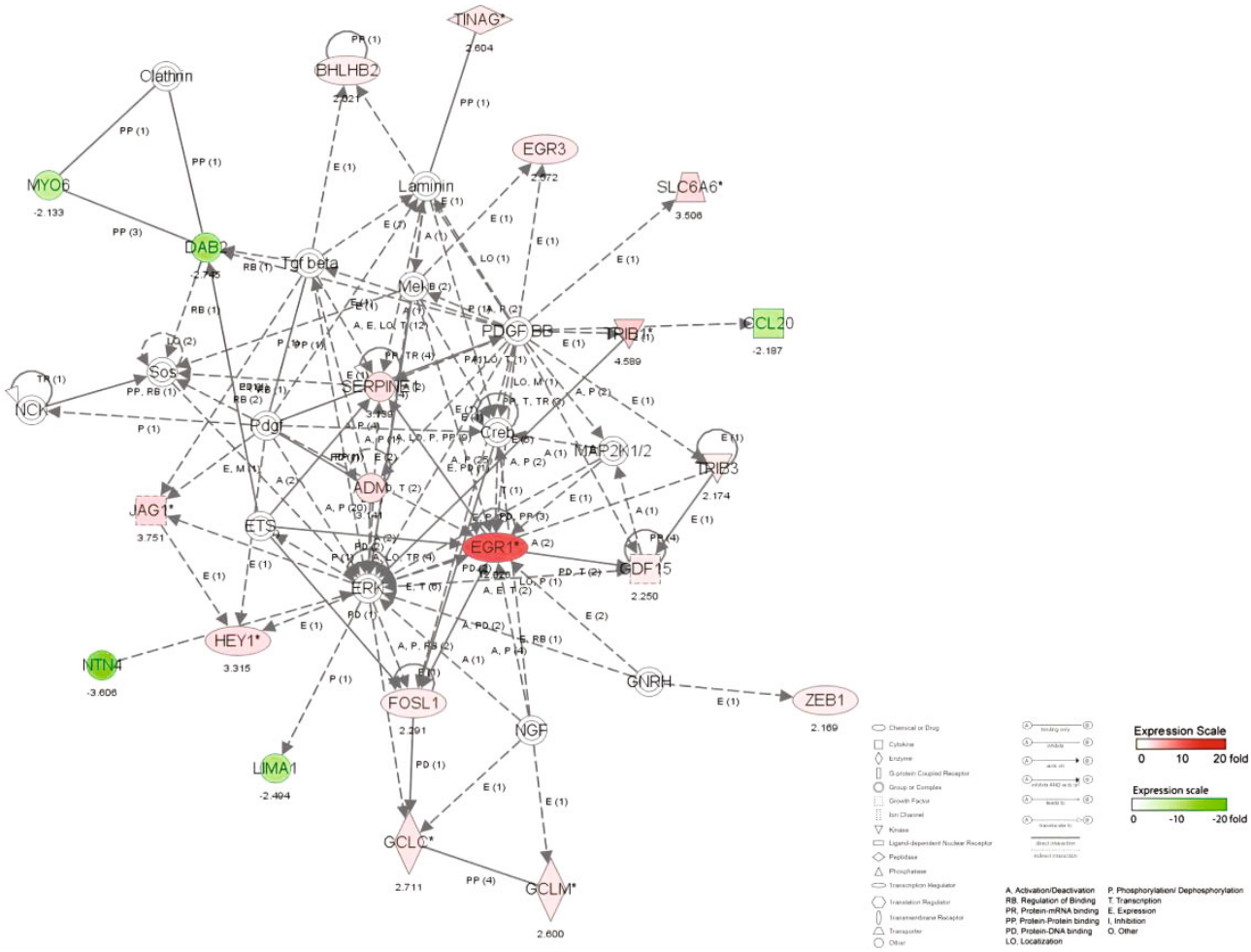

Figure 5: The second most significant molecular network affected by DTS.

cell pathways. Therefore, DTS can also activate inflammatory cell pathways, showing its anti-inflammatory potential (Figure 2).

3.4.2. Top 10 Molecular Functions Changed by DTS Treatment. The 10 major molecular functions affected by DTS are Cancer, Cell Death, Cellular Growth and Proliferation, Tissue Development, Cellular Development, Cellular Movement (Cell Movement), Reproductive System Disease, Cell Cycle, Hematological System Development and Function, and Cell Morphology. DTS changed the expression of F2RL1, SLC2A2, FOS, PALLD, TRIB1, and other genes more than 2 times. DTS can significantly affect cell proliferation and apoptosis and cell cycle arrest. In addition, the expression changes of DTS on cancer-related genes such as FOSL1, JAG1, FLRT2, and BCL10 are also more than 2-fold, indicating that DTS may have an anticancer effect (Figure 3).

3.4.3. Molecular Network and Signal Channel Analysis. The 10 most significant molecular networks after DTS treatment are shown in Table 3. Among them, the most affected by DTS are Gene Expression, Protein Synthesis, and Cell Death (scoring: 49 points). Three main biological functions are involved in this network: gene expression, protein synthesis, and cell apoptosis, followed by Cardiovascular System Development and Function, Tissue Morphology, and Amino Acid Metabolism (scoring: 39 points).

To determine the relevant molecular networks and signal channel of differentially expressed genes, in this study, we used the IPA biological software to perform typical signal channels and network analysis on the upregulated, downregulated, and integrated data sets and constructed a comparison between the DTS treatment group and the non-DTS treatment control group. The captions illustrate the classification attributes of molecules of different shapes. The metabolites marked in red in the figure are upregulated metabolites, and the metabolites marked in green are downregulated metabolites. The solid line represents the direct interaction between the two molecules, and the dashed line represents the indirect interaction between the two molecules. Relationship, networks, and signal channels describe the functional relationships between gene products based on known interactions reported in the literature.

There are 35 genes involved in the construction of the most significant molecular network affected by DTS; 25 genes are differentially expressed. NF-κB, as the central position gene of this molecular network, controls the transcriptional activity of multiple inflammatory factors and the

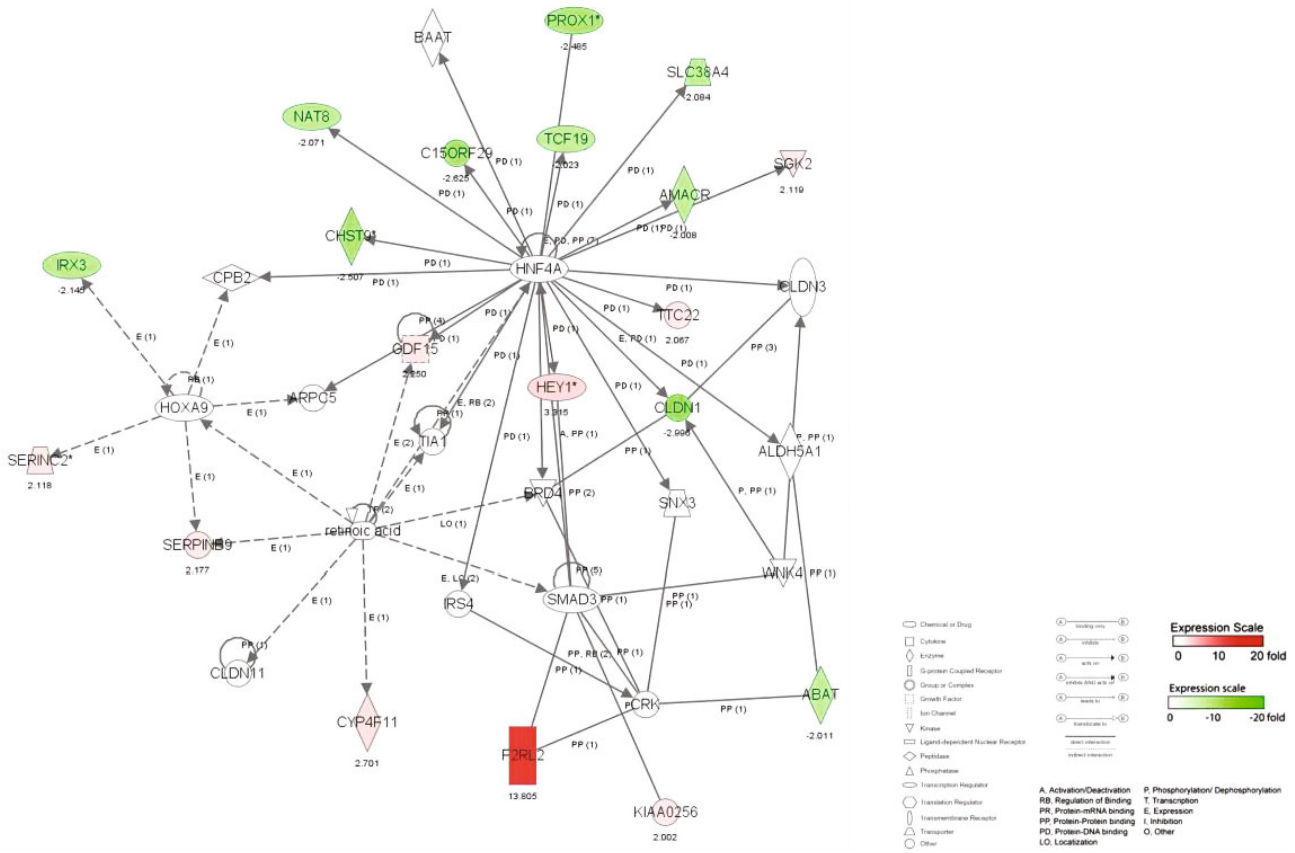

Figure 6: The third most significant molecular network affected by DTS.

expression of antioxidant genes. Among them, there are 12 upregulated genes, and the most significant gene of upregulated fold change is HSPA1A. There are 13 downregulated genes, and the gene with the most significant downregulation fold change is BIRC3. In the molecular network, the upregulated expression of HSPA1A was indirectly affected by NF-κB, which had the largest fold change of 3.8. It promotes the correct folding of newly translated and misfolded proteins and stabilizes or degrades mutant proteins. It helps DNA repair. Its functions contribute to biological processes, including signal transduction, apoptosis, protein homeostasis, cell growth, and differentiation. It is associated with a large number of cancers, neurodegenerative diseases, cellular senescence and aging, and inflammatory diseases such as diabetes type 2 and rheumatoid arthritis.

In this molecular network, NCF2 (neutrophil cytoplasmic factor 2) is upregulated after being indirectly affected by NF-κB. NCF2 is also called NADPH oxidase and is a multiprotein complex with 67 kilodalton molecular subunits. It is related to chronic diseases, especially chronic inflammation. The deletion induced by Alu duplication in the NCF2 gene is a new mechanism that causes p67-hypoxic chronic granulomatous disease (CGD). Chronic granulomatosis is associated with life-threatening infections and disorders. The downregulated expression of BIRC3 was indirectly affected by NF-κB, and the fold change was the largest, which was 3.35. BIRC3 is a member of the apoptosis family, which inhibits cell apoptosis by interfering with the activation of caspase (Figure 4).

There are 35 genes involved in the construction of the second most significant molecular network, of which 21 genes are differentially expressed. ERK, as the central position gene of this molecular network, controls the transcription activity of multiple inflammatory factors and the expression of antioxidant genes. Among them, there are 16 upregulated genes, and the gene with the most significant upregulated fold change is EGR1. There are 5 downregulated genes, and the most significant gene of downregulated fold change is NTN4 (Figure 5).

There are 35 genes involved in the construction of the network, of which 19 genes are differentially expressed. HNF4A, as the central location gene of this molecular network, controls the transcriptional activity of multiple inflammatory factors and the expression of antioxidant genes. Among them, there are 9 upregulated genes, and the most significant gene with upregulated fold change is F2RL2. There are 10 downregulated genes, and the gene with the most significant downregulation fold change is CLDN1 (Figure 6).

3.5. Effect of DTS on Secretion of Inflammatory Cytokines. Since cytokines play an important role in inflammation, the LPS-induced RAW264.7 cell model was constructed to detect the secretion profile of typical cytokines by Bio-Plex

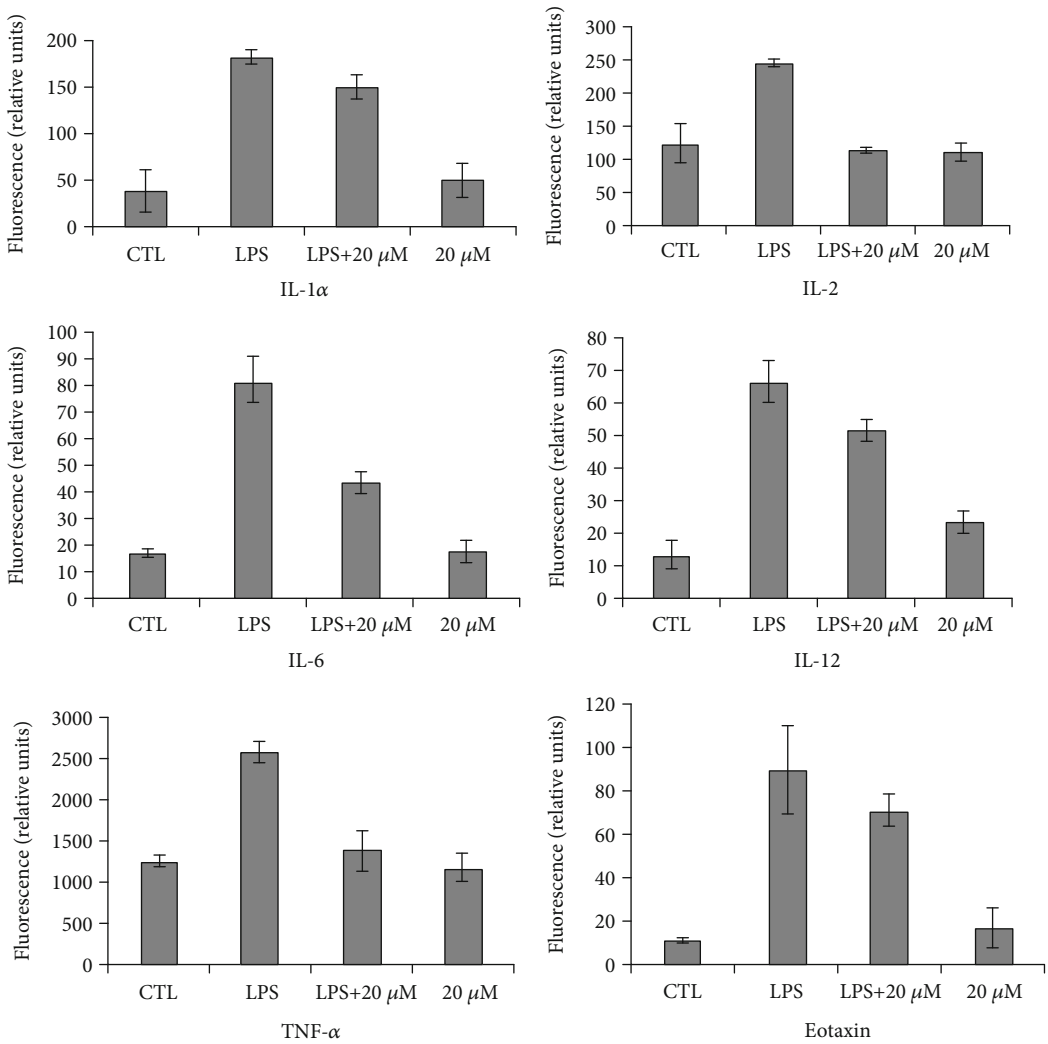

Figure 7: Influence of DTS on the production of inflammatory cytokines.

2000 proteome detecting instrument, including the expression levels of 23 inflammatory cytokines, to further verify the results of gene chip analysis and understand the regulation of DTS on the protein expression level of cytokines network. As shown in Figure 7, the most 6 inflammatory factors with significant changes were listed, including IL-1α, IL-2, IL-6, IL-12, TNF-α, and Eotaxin, which were significantly decreased in a dose-dependent manner after DTS treatment of 10 or 20 μ M ($P < 0.05$); meanwhile, the other cytokines had no significant change (data not shown).

IL-1α and IL-6 are important proinflammatory factors. LPS was activated NF-κB by activating monocyte MAPK signaling pathway to activate IL-1 gene expression, in which P38 plays an important role in IL-1 secretion. On the other hand, IL-1 also induces the activation of ERK1/2, P38, and JNK, which in turn activates NF-κB and regulates the expression of inflammation-related genes. The effect of IL-6 is closely related to STAT3, which plays an important role in cell proliferation and differentiation. Therefore, IL-6 can not only promote the development of inflammation but also accelerate the proliferation and growth of normal cells and tumor cells. The result indicated that DTS inhibited the expression of pro-inflammatory cytokines in macrophages, which was similar to the result of gene chip. In inflammatory response models, TNF-α is an important inflammatory factor, which can bind its receptor TNFRα to form trimer-mediated association of cohesive protein TRADD. TRADD recruits the corresponding protein and induces NF-κB activation through TRAF2 and RIP molecules. Therefore, the significantly decreased expression of TNF-α in this study indicates that the DTS can inhibit the inflammatory response via NF-κB inactivation.

4. Conclusions

Treatment with DADS, DATS, and DTS resulted in the differential expression of genes in liver cancer cells. Most of the genes whose expression changes were greater than 2 times are distributed between upregulated and downregulated expressions 2-3 times. Among the three experimental groups, EGR1, NCF2, and F2RL2 were found while the gene expression changes were more than 4 times. Among

the three categories classified according to the GO catalog, the molecular function category contained the largest number of genes with differential expression greater than 2 times, indicating that DADS, DATS, and DTS acted on liver cancer cells and have the greatest impact on their molecular functions. The function with the largest number of genes included is protein binding, indicating that the molecular signaling pathways in cells are significantly affected by DADS, DATS, and DTS. In the DTS treatment group, the gene upregulated and expressed more than 2 times of the phase I coenzyme is NCF2. The genes with upregulated expression of phase II coenzyme or antioxidant proteins more than 2-fold include GCLC, GCLM, SQSTM1, and HMOX1.

Glutamate Metabolism (glutamate metabolism), Acute Phase Response Signaling (acute stress response), NRF2-mediated Oxidative Stress Response (NRF2-mediated oxidative stress response) are the most significant typical signal channels that are changed by DTS. The activation of these signal channel is related to Nrf2-mediated oxidative stress. The ten major molecular functions affected by DTS are Cancer, Cell Death, Cellular Growth and Proliferation, Tissue Development, Cellular Development, Cellular Movement (cell movement), Reproductive System Disease (reproductive system disease), Cell Cycle (cell cycle), Hematological System Development and Function (blood system development and function), and Cell Morphology (cell morphology). The molecular functions with the highest scores affected by DTS are cancer, cell apoptosis, and cell proliferation, which prove that the occurrence or metabolism of these diseases is related to the differential expression of the above-mentioned related genes and the activation of signal channels.

Through the analysis of the molecular network that has the greatest impact on DTS, it is concluded that the molecular functions involved in the first three molecular networks correspond to the signal channels and diseases analyzed above. In particular, the core of the first molecular network is inflammation. The results of Bio-Plex kit for the detection of inflammatory cytokine secretion were consistent with the results of gene chip hybridized for the differential expression of inflammatory cytokine genes, which proved that the results of gene chip were reliable, and also verified that DTS could reduce the secretion of proinflammatory cytokines from the perspective of proteomics.

Data Availability

All data included in this study are available upon request by contacting the corresponding author.

Conflicts of Interest

The authors declare that there is no conflict of interest.

Authors' Contributions

Chenghao Lv and Caiqiong Wang are the co-first authors and contributed to the work equally.

Acknowledgments

This work was partially supported by the National Key Research and Development Program of China (2019YF C1604903), Natural Science Foundation of China (3110 1268), Natural Science Foundation of Hunan Province (2019JJ40132), and Double First-Class Construction Project of Hunan Agricultural University (SYL201802025) to Si Qin.

References

[1] C. M. Gao, T. Takezaki, J. H. Ding, M. S. Li, and K. Tajima, "Protective effect of allium vegetables against both esophageal and stomach cancer: a simultaneous case-referent study of a high-epidemic area in Jiangsu Province, China," *Japanese Journal of Cancer Research*, vol. 90, no. 6, pp. 614–621, 1999.

[2] A. W. Hsing, A. P. Chokkalingam, Y. Gao et al., "Allium vegetables and risk of prostate cancer: a population-based study," *Journal of the National Cancer Institute*, vol. 94, no. 21, pp. 1648–1651, 2002.

[3] S. K. Banerjee, P. K. Mukherjee, and S. K. Maulik, "Garlic as an antioxidant: the good, the bad and the ugly," *Phytotherapy Research*, vol. 17, no. 2, pp. 97–106, 2003.

[4] V. Dhawan and S. Jain, "Effect of garlic supplementation on oxidized low density lipoproteins and lipid peroxidation in patients of essential hypertension," *Molecular and Cellular Biochemistry*, vol. 266, no. 1/2, pp. 109–115, 2004.

[5] X. Wu, F. Kassie, and V. Mersch-Sundermann, "Induction of apoptosis in tumor cells by naturally occurring sulfur-containing compounds," *Mutation Research*, vol. 589, no. 2, pp. 81–102, 2005.

[6] A. Arunkumar, M. R. Vijayababu, N. Srinivasan, M. M. Aruldhas, and J. Arunakaran, "Garlic compound, diallyl disulfide induces cell cycle arrest in prostate cancer cell line PC-3," *Molecular and Cellular Biochemistry*, vol. 288, no. 1-2, pp. 107–113, 2006.

[7] A. A. Powolny and S. V. Singh, "Multitargeted prevention and therapy of cancer by diallyl trisulfide and related allium vegetable-derived organosulfur compounds," *Cancer Letters*, vol. 269, pp. 305–314, 2008.

[8] L. Shamseer, T. L. Charrois, and S. Vohra, "Complementary, holistic, and integrative medicine: garlic," *Pediatrics in Review*, vol. 27, no. 12, pp. e77–e80, 2006.

[9] V. Lanzottl, "The analysis of onion and garlic," *Journal of Chromatography. A*, vol. 1112, no. 1-2, pp. 3–22, 2006.

[10] S. Kalayarasan, P. N. Prabhu, N. Sriram, R. Manikandan, M. Arumugam, and G. Sudhandiran, "Diallyl sulfide enhances antioxidants and inhibits inflammation through the activation of Nrf2 against gentamicin-induced nephrotoxicity in Wistar rats," *European journal of pharmacology*, vol. 606, no. 1-3, pp. 162–171, 2009.

[11] K. M. Kim, S. B. Chun, M. S. Koo et al., "Differential regulation of NO availability from macrophages and endothelial cells by the garlic component S-allyl cysteine," *Free Radical Biology and Medicine*, vol. 30, no. 7, pp. 747–756, 2001.

[12] H. J. Park, B. T. Jeon, H. C. Kim et al., "Aged red garlic extract reduces lipopolysaccharide-induced nitric oxide production in RAW 264.7 macrophages and acute pulmonary inflammation through haeme oxygenase-1 induction," *Acta Physiologica*, vol. 205, no. 1, pp. 61–70, 2012.

[13] H. Y. Park, N. D. Kim, G. Y. Kim et al., "Inhibitory effects of diallyl disulfide on the production of inflammatory mediators and cytokines in lipopolysaccharide-activated BV2 microglia," *Toxicology and Applied Pharmacology*, vol. 262, no. 2, pp. 177–184, 2012.

[14] K. L. Liu, H. W. Chen, R. Y. Wang, Y. P. Lei, L. Y. Sheen, and C. K. Lii, "DATS Reduces LPS-Induced iNOS Expression, NO Production, Oxidative Stress, and NF-κB Activation in RAW 264.7 Macrophages," *Journal of Agricultural and Food Chemistry*, vol. 54, no. 9, pp. 3472–3478, 2006.

[15] S. X. You, E. Nakanishi, H. Kuwata et al., "Inhibitory effects and molecular mechanisms of garlic organosulfur compounds on the production of inflammatory mediators," *Molecular Nutrition & Food Research*, vol. 57, no. 11, pp. 2049–2060, 2013.

[16] A. Lang, M. Lahav, E. Sakhnini et al., "Allicin inhibits spontaneous and TNF-α induced secretion of proinflammatory cytokines and chemokines from intestinal epithelial cells," *Clinical Nutrition*, vol. 23, no. 5, pp. 1199–1208, 2004.

[17] J. George, M. Singh, A. K. Srivastava, K. Bhui, and Y. Shukla, "Synergistic growth inhibition of mouse skin tumors by pomegranate fruit extract and diallyl sulfide: Evidence for inhibition of activated MAPKs/NF-κB and reduced cell proliferation," *Toxicology*, vol. 49, no. 7, pp. 1511–1520, 2011.

[18] P. Pratheeshkumar, P. Thejass, G. Kutan, and J. Environ, "Diallyl Disulfide Induces Caspase-Dependent Apoptosis via Mitochondria-Mediated Intrinsic Pathway in B16F-10 Melanoma Cells by Up-Regulating P53, Caspase-3 and Down-Regulating Pro-Inflammatory Cytokines and Nuclear Factor- $\kappa\beta$-Mediated Bcl-2 Activation," *Journal of environmental pathology and toxicology*, vol. 29, no. 2, pp. 113–125, 2010.

[19] M. Terajima, T. Inoue, K. Magari, H. Yamazaki, Y. Higashi, and H. Mizuhara, "Anti-inflammatory effect and selectivity profile of AS1940477, a novel and potent p38 mitogen-activated protein kinase inhibitor," *European Journal of Pharmacology*, vol. 698, no. 1-3, pp. 455–462, 2013.

[20] J. H. Cha, Y. J. Choi, S. H. Cha, C. H. Choi, and W. H. Cho, "Allicin inhibits cell growth and induces apoptosis in U87MG human glioblastoma cells through an ERK-dependent pathway," *Oncology Reports*, vol. 28, no. 1, pp. 41–48, 2012.

[21] C. W. Tsai, H. W. Chen, J. J. Yang, L. Y. Sheen, C. K. Lii, and J. Agric, "Diallyl Disulfide and Diallyl Trisulfide Up-Regulate the Expression of the π Class of GlutathioneS-Transferase via an AP-1-Dependent Pathway," *Food Chemistry*, vol. 55, no. 3, pp. 1019–1026, 2007.

[22] S. Shrotriya, J. K. Kundu, H. K. Na, and Y. J. Surh, "Diallyl Trisulfide Inhibits Phorbol Ester–Induced Tumor Promotion, Activation of AP-1, and Expression of COX-2 in Mouse Skin by Blocking JNK and Akt Signaling," *Cancer Research*, vol. 70, no. 5, pp. 1932–1940, 2010.

[23] S. Sato, H. Sanjo, K. Takeda et al., "Essential function for the kinase TAK1 in innate and adaptive immune responses," *Nature Immunology*, vol. 6, no. 11, pp. 1087–1095, 2005.

[24] Y. G. Lee, J. Lee, S. E. Byeon et al., "Functional role of Akt in macrophage-mediated innate immunity," *Frontiers in Bioscience*, vol. 16, no. 1, pp. 517–530, 2011.

Hindawi
Mediators of Inflammation
Volume 2021, Article ID 8481013, 7 pages
https://doi.org/10.1155/2021/8481013

Review Article

Role and Function of T Cell-Derived Exosomes and Their Therapeutic Value

Yuanyuan Shao, Xiaofeng Pan, and Rong Fu

Department of Hematopathology, Tianjin Medical University General Hospital, 154 Anshan Street, Tianjin 300052, China

Correspondence should be addressed to Rong Fu; furong8369@tmu.edu.cn

Received 24 September 2021; Revised 29 October 2021; Accepted 2 November 2021; Published 12 November 2021

Academic Editor: Deguang Song

Exosomes are membrane-bound extracellular vesicles that are produced in the endosomal compartment of most eukaryotic cells. Containing proteins, RNA, and DNA, exosomes mediate intercellular communication between different cell types by transferring their contents and thus are involved in numerous physiological and pathological processes. T cells are an indispensable part of adaptive immunity, and the functions of T cell-derived exosomes have been widely studied. In the more than three decades since the discovery of exosomes, several studies have revealed that T cell-derived exosomes play a novel role in cell-to-cell signaling, especially in inflammatory responses, autoimmunity, and infectious diseases. In this review, we will summarize the function of T cell-derived exosomes and their therapeutic potential.

1. Introduction

In 1982, Harding et al. discovered exosomes while observing the maturation of mammalian reticulocytes [1]; subsequently, Johnstone et al. coined the term "exosome" in 1987 [2, 3]. They observed the accumulation of "membrane-bound vesicles" in the lumen of multivesicular endosomes (MVE) as a result of the inward invagination of its limiting membrane. After the infusion of MVE with the cellular membrane, "vesicular inclusions" were released into the extracellular space. As a comparison with exosomes, ectosomes are released from the plasma membrane as shedding vesicles.

Exosomes are membrane-bounded extracellular vesicles (EVs) usually of 30 nm to 150 nm in diameter produced in the endosomal compartment of most eukaryotic cells [4]. According to Exocarta (http://www.exocarta.org), an online database of exosomes, more than 9760 proteins (from the cytoplasm, membrane, Golgi apparatus, and reticulum), as well as more than 3000 mRNAs and have identified as exosomal cargo [5, 6]. Suppressive or promotive factors can be transferred by T cell-derived exosomes to other cells *via* membrane vesicle trafficking, thus influencing a variety of immune responses, including adaptive immunity and immune responses to pathogens and cancer [7, 8].

1.1. The Function of T Cell-Derived Exosomes. The process of exosome secretion in T lymphocytes can be initiated by increased intracellular Ca^{2+} concentration, which is induced by external stimuli [9]. The exosomes released by activated human T lymphocytes are characterized by bioactive Fas ligand (FasL) and APO ligand in their aqueous core, which promote activation-induced cell death [10]. Jurkat T cell-derived exosomes constitutively express natural-killer group 2 member D (NKG2D) ligand, which inhibits natural killer cell (NK) cytotoxicity during thermal and oxidative stress [11]. It has also been found that exosomes derived from Jurkat T cells can regulate proliferation and the physiological functions of endothelial cells, primarily through a CD47-dependent pathway [12]. Structural studies of T lymphocyte-derived exosomes have yielded significant insights into their typical surface molecules, which include glucocorticoid-induced tumor necrosis factor receptor (GITR) [13], major histocompatibility complex

(MHC)-I and MHC-II [14], lymphocyte function-associated antigen- (LFA-) 1/2 [15], tumor susceptibility gene 101 (TSG101) [16], APO-1/CD95 (Fas), FasL [17], C-X-C motif chemokine receptor 4 (CXCR4) [18], and T cell receptor (TCR) [19].

Proteomics studies have shown that there are some constant proteins in most T cell-derived exosomes, including glyceraldehyde-3-phosphate dehydrogenase (GAPDH), enolase, specific heat-shock proteins, CD81, CD63, major luminal proteins (including tubulin isoforms and actin), annexins, and proteins involved in immunological processes such as human leukocyte antigen-I (HLA-I), components of the TCR/CD3 complex, β2-microglobulin, and specific integrins [20, 21]. Studies have also detected membrane-associated ATPase valosin-containing proteins (VCP) in leukemic T cells, but not normal T cells from healthy donors [20]. Moreover, some miRNAs with regulatory functions are also present in exosomes, with several specifically enriched miRNAs. The activity of the major exosomal heterogeneous nuclear riboprotein A2/B1 largely contributes to this phenomenon [22]. Recent studies have found that exosomal DNA can also be present in T cell-derived exosomes [23].

During T cell activation, a specific set of tRNA fragments (tRFs) derived from the $5'$-terminus and $3'$-internal region of tRNAs without variable loops are released in exosomes; 45% of tRFs but fewer than 1% of miRNAs from the corresponding cellular RNAs were significantly enriched in exosomes. And T cell activation was blocked when this process was inhibited [24].

CD3+ T cell-derived exosomes can stimulate and promote the proliferation of resting CD3+ T cells. These exosomes can also induce a relative increase in CD8+ T cells with the help of interleukin-2. Moreover, these exosomes may inhibit HIV through human chemokine (C-C Motif) ligand 5 (CCL5)/regulated upon activation normal T cell expressed and secreted (RANTES) [24].

The function of exosomes may resemble their cell of origin. T cells can secrete CD63+ exosomes to antigen-presenting cells (APCs) during immune synapse formation, which causes an antigen-driven unidirectional transfer of miRNAs. This process is highly dependent on sphingomyelinase-2 [8]. And this immunological synapse can promote the efficiency of exosome transfer, mostly in a neutral sphingomyelinase-2-dependent pathway.

Moreover, T cell-derived exosomes can prime dendritic cells (DCs) for antiviral responses. Antigen-bearing DCs initiate antipathogen programs when they form immunological synapses with T cells. The exosomes can induce antiviral responses through genomic and mitochondrial DNA. After fusion with target cells, they can activate the cyclic GMP-AMP synthase (cGAS)/signaling adaptor protein (STING) cytosolic DNA-sensing pathway and induce the expression of interferon regulatory factor 3- (IRF3-) dependent interferon regulated genes. Moreover, the DCs gain resistance to viral infection after exosome uptake [23]. Additionally, metastasis of esophageal cancer cells is promoted by T cell-derived exosomes from irradiated infiltrating esophageal carcinoma patients [25].

Exosomes derived from human T cells may participate in the pathogenesis of nonobese diabetes mellitus. These exosomes transfer the active form of microRNAs (miR-155, miR-142-5p, and miR-142-3p) to pancreatic β cells, inducing apoptosis by inhibiting the expression of genes involved in chemokine signaling (Ccl2, Ccl7, and Ccl10) exclusively in β cells. The recruited immune cells exacerbate β cell death when these genes are activated [26]. Exosomes may also show immunosuppressive properties that are against the function of the cell of origin. This phenomenon is presumably predicated by the type of target cell they interact with. For example, CD40L and inducible costimulator protein (ICOS) can be highly expressed after the activation of CD4+ T cells. Nevertheless, DCs will undergo apoptosis and even T cell responses will be silenced after binding of the main effector molecule FasL by DCs through CD54/LFA-1 and pMHV-II/TCR [27, 28].

1.2. T Cell-Derived Exosomes in Diseases. Using a novel method to isolate and characterize exosomes derived from T cells even in a limited amount of sample [29], exosomes have been found to be involved in the pathogenesis of numerous inflammatory diseases.

Oral lichen planus (OLP) is a chronic inflammatory disease with uncertain etiology. It is currently thought to be T cell mediated. In patients with OLP, T cell-derived exosomes that contain macrophage inflammatory protein- (MIP-) 1α/β can drive the trafficking of CD8+ T cells after binding with CC chemokine receptor (CCR)1/5, contributing to the development of OLP [30]. Moreover, T cell-derived exosomes from OLP patients exhibited an aberrant cytokine profile. An *in vitro* study showed that those aberrant cytokines can trigger apoptosis in keratinocytes [31].

Sjören's syndrome is a chronic autoimmune disease in which the body's leukocytes destroy moisture producing glands. In Sjören's syndrome patients, activated T cell-derived exosomes containing miR-142-3p can be transferred into glandular cells. miR-142-3p can alter intracellular Ca^{2+} signaling and destroys the protein production in salivary gland cells, thus directly impairing epithelial cell function [32]. Studies have also found that T cell-derived exosomes participate in the pathogenesis of hypertension (HTN). In an angiotensin-induced HTN animal model, CD3+ T cell-derived exosomes entered peripheral circulation and the kidneys. They also found that the concentration of exosomes was positively correlated with high blood pressure [33].

1.3. CD4+ T Cell-Derived Exosomes. CD4+ T cells can produce cytokines and interact with other cells such as NK cells, macrophages, and CD8+ T cells. The peptides presented by class II MHC can stimulate the TCR of CD4+ T cells to make them exert their functions, which include activating other immune cells. Th1 cells, which are CD4+ T cells against intracellular pathogens, can produce immunoglobulin G2A (IgG2a) antibodies to optimize the clearance of viruses and extracellular bacteria by stimulating the conversion of immunoglobulins in B cells.

Exosome secretion is promoted *in vitro* by CD28 and TCR costimulation. However, when other stimuli such as

phorbol 12-myristate 13-acetate (PMA) and ionomycin were used, this effect was not found. This might be because cells produce exosomes as a physiological response [34]. Moreover, T cells can regulate the release of distinct exosome subpopulations under different activation statuses [35].

In ischemic heart disease patients, circulating exosomes containing miR-142-3p from activated CD4+ T cells can boost post ischemic ventricular remodeling by activating myofibroblasts, primarily *via* the phosphatidylserine receptor [36]. Activated T lymphocytes can also infiltrate atherosclerotic plaques in patients with ischemic heart disease. These exosomes can enhance cholesterol accumulation in monocytes, which is observed in cell coculture. Endogenous phosphatidylserine receptor facilitates exosome internalization. And the subsequent increase in the production of the proinflammatory cytokine TNF-α parallels cholesterol accumulation in monocytes [37].

Furthermore, specific proteins involved in the RAS signaling pathway are enriched in exosomes and can drive ERK phosphorylation in recipient immune cells [38]. Antigen-specific T cell exosomes may serve as a new type of immunosuppressive reagent that be used for transplantation rejection and treating autoimmune diseases [39].

CD4+ T cell-derived exosomes can also be applied in clinical practice as novel biomarkers for disease development. In chronic hepatitis B patients, exosomes derived from CD4+ and CD8+ T cells are released into serum, while in patients with nonalcoholic steatohepatitis (NASH) or nonalcoholic liver disease (NAFLD), high level of macrophage/monocyte-derived and invariant natural killer (iNKT) cell-derived exosomes are released into the serum [40].

Follicular helper T cells (Tfhs) constitute another subpopulation of CD4+ T cells that regulate the development of antigen-specific B cell immunity in the germinal center of secondary lymphoid follicles. Tfhs are closely involved in the development of antibody-mediated rejection (AMR) after renal transplantation. Tfhs-derived CD4+ CXCR5+ CXCR3- exosomes, which mediate B cell proliferation and differentiation, were significantly increased in the AMR group compared with those in the non-AMR group [41].

1.4. CD8+ T Cell-Derived Exosomes. CD8+ T cells play an essential role in protecting against infectious agents by killing infected cells following recognition of microbial peptides presented by MHC class I molecules on the surface of target cells. Major efforts are underway to harness tumor-specific CD8+ T cells to treat cancer cells. After target cell recognition, cytotoxic granules are released into the immunological synapse formed between killer cells and their targets.

The granules secreted by cytotoxic T lymphocytes (CTLs) contain perforins (referred to as membrane-perturbing proteins), granulysin, and granzymes. The perforin pore gives granzymes access to the cytosol of target cells, where they induce cell death pathways.

Exosomes derived from CD8+ T cells also contain granzymes and perforin. These granzymes can be directly transferred when CTLs fuse with the membrane of target cells or through endocytosis [42]. Typically, during immune synapse formation with target cells, exosomes are released from CTLs to assist in killing target cells [43].

Generally, CTLs secrete extracellular vesicles following antigen stimulation. If treated with IL-12, CTLs can secrete exosomes with various diameters that are selectively enriched for certain exosomal proteins. The proteins inside exosomes may display altered catalytic and binding activities [44]. Additionally, CTL-derived exosomes can strengthen the effects of weak antigen stimulation on CTLs and activate bystander CTLs in the absence of antigens.

Macrophages are a type of leukocyte that engulf and digest cancer cells, cellular debris, microbes, foreign substances, and anything that is recognized as "foreign protein" in the process of phagocytosis. Treatment with trinitrophenol- (TNP-) specific exosomes, which carry miRNA-150 derived from CD8+ T cells, impairs functional interactions between innate and adaptive immune responses *in vivo*, as well as phagocytic activity *in vitro* [45].

Moreover, macrophages lose contact sensitivity when cocultured with CD8+ T cell-derived exosomes. At the same time, the proliferation of effector T cells may be inhibited and regulatory T cell (Treg) induction may be promoted [46]. CD8+ T cells deliver miRNA-150 *via* exosomes to antigen-primed macrophages, which suppresses delayed-type hypersensitivity in a mouse model [47]. Except for delivering cytotoxic molecules to targets, in patients with melanoma, the ERK and NF-κB pathways are activated by CD8+ T cell-derived exosomes, resulting in the expression of matrix metalloproteinase (MMP) 9 and tumor cells becoming invasive *in vitro*. However, this does not affect tumor cell apoptosis or proliferation [48]. CD8+ T cell-derived exosomes with membrane expression of FasL can promote the invasion and metastasis of Fas+ tumor cells through MMP-9-mediated extracellular matrix degradation [45].

Exosomes from CD8+ T cells not only inhibit the CD8+ CTL responses mediated by antigen-specific DCs by affecting the function of target cells through the endocytosis of APCs and B cells but also inhibit antitumor immunity in an antigen-dependent manner [49]. Activated CD8+ T cells can secrete exosomes that interrupt fibroblastic stroma-mediated tumor cell invasion and metastasis by the apoptotic depletion of mesenchymal tumor stromal cells [47]. However, it has been argued that exosomes from exhausted CD8+ T cells possibly participate in the prevention of tumor growth, invasion, and metastasis [50]. Functional analysis has indicated that differently expressed lncRNAs from a variety of exosomal sources actively participate in regulating the diverse CD8+ T cell responses by altering biosynthetic processes, gene expression, and metabolism [51].

1.5. Treg-Derived Exosomes. Tregs are another type of CD4+ T cells with a prominent suppressive function rather than providing helper activity. These cells express CD3, CD4, and CD25 on their surface and are indispensable for specific immune tolerance [52, 53]. According to their origin, Tregs can be subdivided into "induced" regulatory T cells (iTregs) or thymically derived Tregs (tTregs). In the microenvironment, a variety of immune cells such as macrophages, DCs, NK T cells, CD4+ T cells, CD8+ T cells, and B cells are

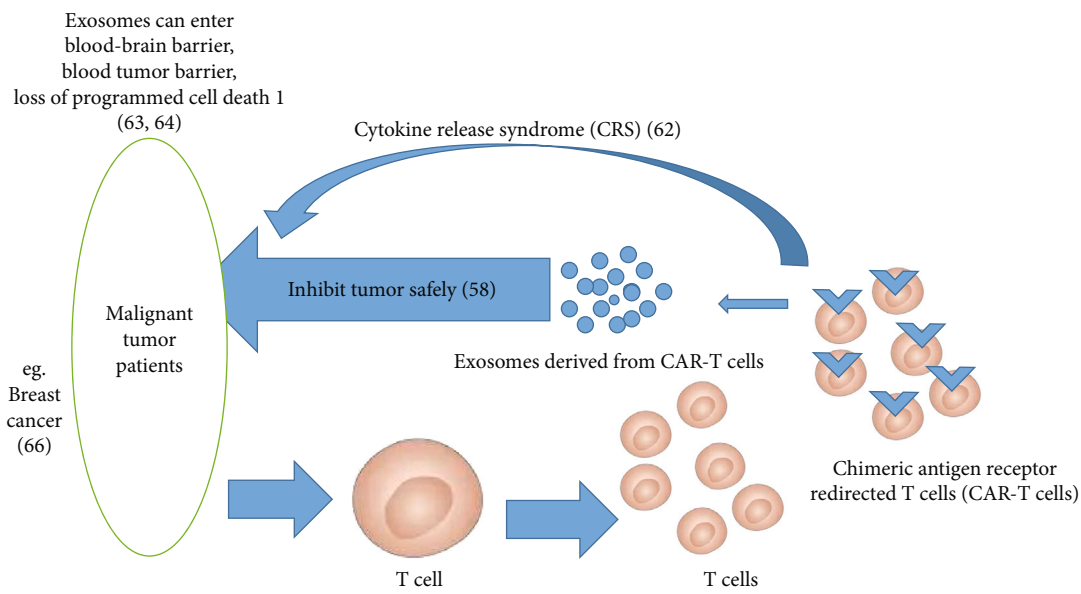

Figure 1: CAR-T cell-derived exosomes for tumor treatment.

inhibited by various subtypes of Tregs. Tregs can specifically inhibit immune responses through several mechanisms. For example, Tregs can secrete suppressor cytokines including IL-10 and TGF-β [54, 55], consume the local IL-2 concentration, and induce apoptosis or cell cycle arrest through direct cellular contact.

Compared with other T cell subtypes, Tregs secrete more exosomes, with more membranous molecules such as CD25, CTLA4, and CD73. The Rab family proteins are indispensable for exosome release by T cells. It has been reported that Rab27b double-knockout (Rab27-DKO) Tregs cannot secrete exosomes, which makes them unable to suppress Th1 function [56]. Treg-derived exosomes primarily achieve their suppressive functions through CD73 and the subsequent release of adenosine to suppress inflammation [57–59].

Other functional molecules isolated from Treg-derived exosomes include let-7d, let-7b, and miR-155. These can be transferred to Th1 cells to inhibit their proliferation and cytokine release [56]. Thus, Treg-derived exosomes and their cargo may represent promising antitumor targets. Treg-derived exosomes can also inhibit DCs. When exosomes containing miR-142-3p and miR-150-5p are engulfed by DCs, the DCs will secrete less IL-10 and IL-6 following lipopolysaccharide (LPS) stimulation [60]. Treg-derived exosomes also regulate intracellular immunity, which can be applied to increase allograft kidney survival [61].

Tregs also inhibit cytotoxic T lymphocytes *via* exosomes, which can be reversed by GW4869, an EXO inhibitor. This inhibition is related to regulation of interferon and perforin [50]. Apart from tumor suppression, Treg-derived exosomes can prolong the survival of liver transplantation patients [61].

1.6. Chimeric Antigen Receptor T Cell-Derived Exosomes. On the basis of the basic characteristics of antigen recognition and immune cell signaling, chimeric antigen receptors (CARs) have been successfully designed and applied to treat malignant blood diseases.

CAR-T cell therapy comes with unprecedented efficacy in hematologic malignancies. However, after interacting with tumor cells, CAR-T cell-induced cytokine release syndrome (CRS) commonly manifests with high fever, nausea, tachycardia, hypotension, rash, headache, shortness of breath, and bone marrow suppression [62]. Patients may develop hypogammaglobulinemia and B cell aplasia as a result of the elimination of healthy B cells by CAR-T cells. However, these mild clinical manifestations are acceptable toxicities. When antibodies are injected or CAR-T cell therapy is combined with bone marrow transplantation, this clinical manifestation can be managed. However, CAR-T cell toxicity management is still a challenge, especially central nervous system toxicity.

Studies have found that exosomes derived from CAR-T cells display the functions of reducing the toxicity induced by CAR-T cells and can cross the blood-brain barrier and blood-tumor barrier [63], as well as loss of programmed cell death 1 (PD1) protein, which means that recombinant PD-L1 treatment fails to weaken the antitumor effect [64]. CAR-containing exosomes express high levels of cytotoxic molecules and inhibit tumor cells. This has been verified in a preclinical study, which showed its relative safety [58]. Anticancer drugs can kill target cells by being loaded into exosomes derived from CAR-T cells because of their superior potential compared with that of CAR-T cells to penetrate the extracellular matrix (ECM) of solid tumors [63, 65]. For instance, CAR-containing exosomes significantly inhibited the growth of both endogenous and exogenous mesothelin-positive triple-negative breast cancer cells without obvious side effects while displaying a high tumor inhibition rate (Figure 1) [66].

2. Conclusions

In conclusion, the current research into T cell-derived exosomes is still in the exploratory stage. Whether T cell-

derived exosomes will have a major role in the future for clinical diagnosis or treatment remains to be determined. We reviewed CD4+ T cell-, CD8+ T cell-, and Treg-derived exosomes, as well as those from other issues. Better experimental models and systematic studies are needed, especially in autoimmune diseases, before T cell-derived exosomes can transition from the laboratory to the clinic.

Data Availability

This review does not contain any original data. The data cited could be found in the reference papers.

Conflicts of Interest

The authors declare that they have no conflicts of interest.

Authors' Contributions

Yuanyuan Shao and Xiaofeng Pan contributed equally to this work.

Acknowledgments

We thank James P. Mahaffey, PhD, from Liwen Bianji (Edanz) (http://www.liwenbianji.cn/), for editing the English text of a draft of this manuscript. This work was supported by the National Natural Science Foundation of China (grant numbers 81800120, 81700117, and 81870101).

References

[1] C. Harding and P. Stahl, "Transferrin recycling in reticulocytes: pH and iron are important determinants of ligand binding and processing," *Biochemical and Biophysical Research Communications*, vol. 113, no. 2, pp. 650–658, 1983.

[2] B. T. Pan and R. M. Johnstone, "Fate of the transferrin receptor during maturation of sheep reticulocytes in vitro: selective externalization of the receptor," *Cell*, vol. 33, no. 3, pp. 967–978, 1983.

[3] R. M. Johnstone, M. Adam, J. R. Hammond, L. Orr, and C. Turbide, "Vesicle formation during reticulocyte maturation. Association of plasma membrane activities with released vesicles (exosomes).," *The Journal of Biological Chemistry*, vol. 262, no. 19, pp. 9412–9420, 1987.

[4] C. Théry, K. W. Witwer, E. Aikawa et al., "Minimal information for studies of extracellular vesicles 2018 (MISEV 2018): a position statement of the International Society for Extracellular Vesicles and update of the MISEV2014 guidelines," *Journal of Extracellular Vesicles*, vol. 7, no. 1, article 1535750, 2018.

[5] H. Kalra, R. J. Simpson, H. Ji et al., "Vesiclepedia: a compendium for extracellular vesicles with continuous community annotation," *PLoS Biology*, vol. 10, no. 12, article e1001450, 2012.

[6] G. Raposo and W. Stoorvogel, "Extracellular vesicles: exosomes, microvesicles, and friends," *Journal of Cell Biology*, vol. 200, no. 4, pp. 373–383, 2013.

[7] I. Langley, E. Adams, B. Doulla, and S. B. Squire, "Operational modelling to guide implementation and scale-up of diagnostic tests within the health system: exploring opportunities for parasitic disease diagnostics based on example application for tuberculosis," *Parasitology*, vol. 141, no. 14, pp. 1795–1802, 2014.

[8] M. Mittelbrunn, C. Gutiérrez-Vázquez, C. Villarroya-Beltri et al., "Unidirectional transfer of microRNA-loaded exosomes from T cells to antigen- presenting cells," *Nature Communications*, vol. 2, no. 1, p. 282, 2011.

[9] A. Savina, M. Furlán, M. Vidal, and M. I. Colombo, "Exosome Release Is Regulated by a Calcium-dependent Mechanism in K562 Cells," *Journal of Biological Chemistry*, vol. 278, no. 22, pp. 20083–20090, 2003.

[10] I. Monleón, M. J. Martínez-Lorenzo, L. Monteagudo et al., "Differential secretion of Fas ligand- or APO2 ligand/TNF-related apoptosis-inducing ligand-carrying microvesicles during activation-induced death of human T cells," *Journal of Immunology*, vol. 167, no. 12, pp. 6736–6744, 2001.

[11] M. Hedlund, O. Nagaeva, D. Kargl, V. Baranov, and L. Mincheva-Nilsson, "Thermal- and oxidative stress causes enhanced release of NKG2D ligand-bearing immunosuppressive exosomes in leukemia/lymphoma T and B cells," *PLoS One*, vol. 6, no. 2, article e16899, 2011.

[12] S. Kaur, S. P. Singh, A. G. Elkahloun, W. Wu, M. S. Abu-Asab, and D. D. Roberts, "CD47-dependent immunomodulatory and angiogenic activities of extracellular vesicles produced by T cells," *Matrix Biology*, vol. 37, pp. 49–59, 2014.

[13] Y. Xie, X. Zhang, T. Zhao, W. Li, and J. Xiang, "Natural $CD8^+25^+$ regulatory T cell- secreted exosomes capable of suppressing cytotoxic T lymphocyte-mediated immunity against B16 melanoma," *Biochemical & Biophysical Research Communications*, vol. 438, no. 1, pp. 152–155, 2013.

[14] N. Masafumi, "Antigen presentation by MHC-dressed cells," *Frontiers in Immunology*, vol. 5, p. 672, 2015.

[15] A. di Pace, N. Tumino, F. Besi et al., "Characterization of human NK cell-derived exosomes: role of DNAM1 receptor in exosome-mediated cytotoxicity against tumor," *Cancers*, vol. 12, no. 3, p. 661, 2020.

[16] Q. Wang, G. Yu, H. He et al., "Differential expression of circular RNAs in bone marrow-derived exosomes from essential thrombocythemia patients," *Cell Biology International*, vol. 45, no. 4, pp. 869–881, 2021.

[17] M. N. Theodoraki, A. Matsumoto, I. Beccard, T. K. Hoffmann, and T. L. Whiteside, "CD44v3 protein-carrying tumor-derived exosomes in HNSCC patients' plasma as potential noninvasive biomarkers of disease activity," *OncoImmunology*, vol. 9, no. 1, article 1747732, 2020.

[18] X. Li, Y. Zhang, Y. Wang et al., "Exosomes derived from CXCR4-overexpressing BMSC promoted activation of microvascular endothelial cells in cerebral ischemia/reperfusion injury," *Neural Plasticity*, vol. 2020, Article ID 8814239, 13 pages, 2020.

[19] V. Vignard, M. Labbé, N. Marec et al., "MicroRNAs in tumor exosomes drive immune escape in melanoma," *Cancer Immunology Research*, vol. 8, no. 2, pp. 255–267, 2020.

[20] A. Bosque, L. Dietz, A. Gallego-Lleyda et al., "Comparative proteomics of exosomes secreted by tumoral Jurkat T cells and normal human T cell blasts unravels a potential tumorigenic role for valosin-containing protein," *Oncotarget*, vol. 7, no. 20, pp. 29287–29305, 2016.

[21] D. Perez-Hernandez, C. Gutiérrez-Vázquez, I. Jorge et al., "The Intracellular interactome of tetraspanin-enriched microdomains reveals their function as sorting machineries toward

exosomes," *Journal of Biological Chemistry*, vol. 288, no. 17, pp. 11649–11661, 2013.

[22] C. Villarroya-Beltri, C. Gutiérrez-Vázquez, F. Sánchez-Cabo et al., "Sumoylated hnRNPA2B1 controls the sorting of miRNAs into exosomes through binding to specific motifs," *Nature Communications*, vol. 4, no. 1, 2013.

[23] T. Daniel, F. Baixauli, C. Villarroya-Beltri et al., "Priming of dendritic cells by DNA-containing extracellular vesicles from activated T cells through antigen-driven contacts," *Nature Communications*, vol. 9, no. 1, pp. 1–7, 2018.

[24] N. T. Chiou, R. Kageyama, and K. M. Ansel, "Selective Export into Extracellular Vesicles and Function of tRNA Fragments during T Cell Activation," *Cell Reports*, vol. 25, no. 12, pp. 3356–3370.e4, 2018.

[25] H. Min, X. Sun, X. Yang et al., "Exosomes derived from irradiated esophageal carcinoma-infiltrating T cells promote metastasis by inducing the epithelial–mesenchymal transition in esophageal cancer cells," *Pathology & Oncology Research*, vol. 24, no. 1, pp. 11–18, 2018.

[26] C. Guay, J. K. Kruit, S. Rome et al., "Lymphocyte-derived exosomal microRNAs promote pancreatic β cell death and may contribute to type 1 diabetes development," *ScienceDirect*, vol. 29, no. 2, pp. 348–361.e6, 2019.

[27] S. Durlanik, L. Loyal, R. Stark et al., "CD40L expression by CD4+but not CD8+T cells regulates antiviral immune responses in acute LCMV infection in mice," *European Journal of Immunology*, vol. 46, no. 11, pp. 2566–2573, 2016.

[28] T. C. Metzger, H. Long, S. Potluri et al., "ICOS promotes the function of CD4+ effector T cells during anti-OX40-mediated tumor rejection," *Cancer Research*, vol. 76, no. 13, pp. 3684–3689, 2016.

[29] I. Azoulay-Alfaguter and A. Mor, "Isolation and characterization of T lymphocyte-exosomes using mass spectrometry," in *Immunometabolism*, S. Mishra, Ed., vol. 2184 of Methods in Molecular Biology, pp. 91–102, Humana, New York, NY, 2020.

[30] J.-Y. Yang, J. Zhang, R. Lu, Y.-Q. Tan, G.-F. du, and G. Zhou, "T cell–derived exosomes induced macrophage inflammatory protein-1α/β drive the trafficking of $CD8^+$ T cells in oral lichen planus," *Journal of Cellular and Molecular Medicine*, vol. 24, no. 23, pp. 14086–14098, 2020.

[31] J. Y. Yang, Y. Q. Tan, and G. Zhou, "T cell-derived exosomes containing cytokines induced keratinocytes apoptosis in oral lichen planus," *Oral Diseases*, 2021.

[32] J. Cortes-Troncoso, S. I. Jang, P. Perez et al., "T cell exosome-derived miR-142-3p impairs glandular cell function in Sjögren's syndrome," *JCI insight*, vol. 5, no. 9, 2020.

[33] S. la Salvia, L. Musante, J. Lannigan, J. C. Gigliotti, T. H. le, and U. Erdbrügger, "T cell-derived extracellular vesicles are elevated in essential HTN," *American Journal of Physiology. Renal Physiology*, vol. 319, no. 5, pp. F868–F875, 2020.

[34] N. Blanchard, D. Lankar, F. Faure et al., "TCR activation of human T cells induces the production of exosomes bearing the TCR/CD3/ζ complex," *Journal of Immunology*, vol. 168, no. 7, pp. 3235–3241, 2002.

[35] E. J. van der Vlist, G. J. A. Arkesteijn, C. H. A. van de Lest, W. Stoorvogel, E. N. M. Nolte-'t Hoen, and M. H. M. Wauben, "$CD4^+$ T cell activation promotes the differential release of distinct populations of nanosized vesicles," *Journal of Extracellular Vesicles*, vol. 1, no. 1, 2012.

[36] L. Cai, G. Chao, W. Li et al., "Activated $CD4^+$ T cells-derived exosomal miR-142-3p boosts post-ischemic ventricular remodeling by activating myofibroblast," *Aging*, vol. 12, no. 8, pp. 7380–7396, 2020.

[37] L. Zakharova, M. Svetlova, and A. F. Fomina, "T cell exosomes induce cholesterol accumulation in human monocytes via phosphatidylserine receptor," *Journal of Cellular Physiology*, vol. 212, no. 1, pp. 174–181, 2007.

[38] I. Azoulay-Alfaguter and A. Mor, "Proteomic analysis of human T cell-derived exosomes reveals differential RAS/MAPK signaling," *European Journal of Immunology*, vol. 48, no. 11, pp. 1915–1917, 2018.

[39] H. Zhang, Y. Xie, W. Li, R. Chibbar, S. Xiong, and J. Xiang, "$CD4^+$ T cell-released exosomes inhibit $CD8^+$ cytotoxic T-lymphocyte responses and antitumor immunity," *Cellular & Molecular Immunology*, vol. 8, no. 1, pp. 23–30, 2011.

[40] M. Kornek, M. Lynch, S. H. Mehta et al., "Circulating microparticles as disease-specific biomarkers of severity of inflammation in patients with hepatitis C or nonalcoholic steatohepatitis," *Gastroenterology*, vol. 143, no. 2, pp. 448–458, 2012.

[41] J. Yang, L. Bi, X. He et al., "Follicular helper T cell derived exosomes promote B cell proliferation and differentiation in antibody-mediated rejection after renal transplantation," *Bio Med Research International*, vol. 2019, pp. 1–9, 2019.

[42] P. J. Peters, J. Borst, V. Oorschot et al., "Cytotoxic T lymphocyte granules are secretory lysosomes, containing both perforin and granzymes," *Journal of Experimental Medicine*, vol. 173, no. 5, pp. 1099–1109, 1991.

[43] P. J. Peters, H. J. Geuze, H. A. D. van Donk et al., "Molecules relevant for T cell-target cell interaction are present in cytolytic granules of human T lymphocytes," *European Journal of Immunology*, vol. 19, no. 8, pp. 1469–1475, 1989.

[44] L. Li, S. M. Jay, Y. Wang, S. W. Wu, and Z. Xiao, "IL-12 stimulates CTLs to secrete exosomes capable of activating bystander $CD8^+$ T cells," *Scientific Reports*, vol. 7, no. 1, article 13365, 2017.

[45] K. Nazimek, B. Nowak, J. Marcinkiewicz, M. Ptak, W. Ptak, and K. Bryniarski, "Enhanced generation of reactive oxygen intermediates by suppressor T cell-derived exosome-treated macrophages," *Folia Medica Cracoviensia*, vol. 54, no. 1, pp. 37–52, 2014.

[46] N. Seo, Y. Shirakura, Y. Tahara et al., "Activated CD8+ T cell extracellular vesicles prevent tumour progression by targeting of lesional mesenchymal cells," *Nature Communications*, vol. 9, no. 1, p. 435, 2018.

[47] K. Bryniarski, W. Ptak, A. Jayakumar et al., "Antigen-specific, antibody-coated, exosome-like nanovesicles deliver suppressor T-cell microRNA-150 to effector T cells to inhibit contact sensitivity," *Journal of Allergy & Clinical Immunology*, vol. 132, no. 1, pp. 170–181.e9, 2013.

[48] Z. Cai, F. Yang, L. Yu et al., "Activated T cell exosomes promote tumor invasion via Fas signaling pathway," *Journal of Immunology*, vol. 188, no. 12, pp. 5954–5961, 2012.

[49] Y. Xie, H. Zhang, W. Li et al., "Dendritic cells recruit T cell exosomes via exosomal LFA-1 leading to inhibition of $CD8^+$ CTL responses through downregulation of peptide/MHC class I and Fas ligand-mediated cytotoxicity," *Journal of Immunology*, vol. 185, no. 9, pp. 5268–5278, 2010.

[50] X. Wang, H. Shen, Q. He, W. Tian, A. Xia, and X. J. Lu, "Exosomes derived from exhausted CD8+ T cells impaired the

anticancer function of normal CD8+ T cells," *Journal of Medical Genetics*, vol. 56, no. 1, pp. 29–31, 2019.

[51] W. Ptak, K. Nazimek, P. W. Askenase, and K. Bryniarski, "From mysterious supernatant entity to miRNA-150 in antigen-specific exosomes: a history of hapten-specific T suppressor factor," *Archivum Immunologiae et Therapiae Experimentalis*, vol. 63, no. 5, pp. 345–356, 2015.

[52] E. M. Shevach, "Mechanisms of Foxp3$^+$ T Regulatory Cell-Mediated Suppression," *Immunity*, vol. 30, no. 5, pp. 636–645, 2009.

[53] H. Bour-Jordan and J. A. Bluestone, "Regulating the regulators: costimulatory signals control the homeostasis and function of regulatory T cells," *Immunological Reviews*, vol. 229, no. 1, pp. 41–66, 2009.

[54] S. Budhu, D. A. Schaer, Y. Li et al., "Blockade of surface-bound TGF-β on regulatory T cells abrogates suppression of effector T cell function in the tumor microenvironment," *Science Signaling*, vol. 10, no. 494, 2017.

[55] R. Kapur, M. Kim, R. Aslam et al., "T regulatory cells and dendritic cells protect against transfusion-related acute lung injury via IL-10," *Blood*, vol. 129, no. 18, pp. 2557–2569, 2017.

[56] I. S. Okoye, S. M. Coomes, V. S. Pelly et al., "MicroRNA-containing T-regulatory-cell-derived exosomes suppress pathogenic T helper 1 cells," *Immunity*, vol. 41, no. 3, p. 503, 2014.

[57] L. A. Smyth, K. Ratnasothy, J. Y. S. Tsang et al., "CD73 expression on extracellular vesicles derived from CD4$^+$CD25$^+$Foxp3$^+$ T cells contributes to their regulatory function," *European Journal of Immunology*, vol. 43, no. 9, pp. 2430–2440, 2013.

[58] A. Clayton, S. al-Taei, J. Webber, M. D. Mason, and Z. Tabi, "Cancer exosomes express CD39 and CD73, which suppress T cells through adenosine production," *Journal of Immunology*, vol. 187, no. 2, pp. 676–683, 2011.

[59] Y. U. A. N. Y. U. A. N. Yang, V. E. S. N. A. BUCAN, H. E. I. K. E. Baehre, J. U. L. I. A. N. E. von der Ohe, A. N. N. A. Otte, and R. A. L. F. Hass, "Acquisition of new tumor cell properties by MSC-derived exosomes," *International Journal of Oncology*, vol. 47, no. 1, pp. 244–252, 2015.

[60] A. Chersi, R. A. Houghten, M. C. Morganti, and E. Muratti, "Recognition of HLA class II molecules by antipeptide antibodies elicited by synthetic peptides selected from regions of HLA-DP antigens," *Zeitschrift Für Naturforschung C Journal of Biosciences*, vol. 42, no. 11-12, pp. 1313–1318, 1987.

[61] X. Yu, C. Huang, B. Song et al., "CD4$^+$CD25$^+$ regulatory T cells- derived exosomes prolonged kidney allograft survival in a rat model," *Cellular Immunology*, vol. 285, no. 1-2, pp. 62–68, 2013.

[62] A. E. Obstfeld, N. V. Frey, K. Mansfield et al., "Cytokine release syndrome associated with chimeric-antigen receptor T-cell therapy; clinicopathological insights," *Blood*, vol. 130, no. 23, pp. 2569–2572, 2017.

[63] T. Yang, P. Martin, B. Fogarty et al., "Exosome delivered anticancer drugs across the blood-brain barrier for brain cancer therapy in Danio rerio," *Pharmaceutical Research*, vol. 32, no. 6, pp. 2003–2014, 2015.

[64] F. Wenyan, C. Lei, S. Liu et al., "CAR exosomes derived from effector CAR-T cells have potent antitumour effects and low toxicity," *Nature Communications*, vol. 10, no. 1, 2019.

[65] X.-J. Tang, X.-Y. Sun, K.-M. Huang et al., "Therapeutic potential of CAR-T cell-derived exosomes: a cell-free modality for targeted cancer therapy," *Oncotarget*, vol. 6, no. 42, pp. 44179–44190, 2015.

[66] P. Yang, X. Cao, H. Cai et al., "The exosomes derived from CAR-T cell efficiently target mesothelin and reduce triple-negative breast cancer growth," *Cellular Immunology*, vol. 360, article 104262, 2021.

Hindawi
Mediators of Inflammation
Volume 2021, Article ID 5587428, 13 pages
https://doi.org/10.1155/2021/5587428

Research Article

The Correlation between Gut Microbiota and Serum Metabolomic in Elderly Patients with Chronic Heart Failure

Zhenhua Wang,[1] Zhaoling Cai,[1] Markus W. Ferrari,[2] Yilong Liu,[1] Chengyi Li,[1] Tianzhang Zhang,[1] and Guorong Lyu[3,4]

[1]*Department of Cardiology, Second Affiliated Hospital of Fujian Medical University, Quanzhou, Fujian 362000, China*
[2]*Department of Internal Medicine 1, Helios-HSK Clinics, Wiesbaden D-65193, Germany*
[3]*Department of Ultrasound Medicine, Second Affiliated Hospital of Fujian Medical University, Quanzhou, Fujian 362000, China*
[4]*Collaborative Innovation Center for Maternal and Infant Health Service Application Technology of Education Ministry, Quanzhou Medical College, Quanzhou, Fujian 362000, China*

Correspondence should be addressed to Zhenhua Wang; wzh0522@yeah.net and Guorong Lyu; lgr_feus@sina.com

Received 14 July 2021; Accepted 6 October 2021; Published 27 October 2021

Academic Editor: Peng Bin

Objective. Chronic heart failure (CHF) refers to a state of persistent heart failure that can be stable, deteriorated, or decompensated. The mechanism and pathogenesis of myocardial remodeling remain unknown. Based on 16S rDNA sequencing and metabolomics technology, this study analyzed the gut microbiota and serum metabolome in elderly patients with CHF to provide new insights into the microbiota and metabolic phenotypes of CHF. *Methods*. Blood and fecal samples were collected from 25 elderly patients with CHF and 25 healthy subjects. The expression of inflammatory factors in blood was detected by ELISA. 16S rDNA sequencing was used to analyze the changes in microorganisms in the samples. The changes of small molecular metabolites in serum samples were analyzed by LC-MS/MS. Spearman correlation coefficients were used to analyze the correlation between gut microbiota and serum metabolites. *Results*. Our results showed that the IL-6, IL-8, and TNF-α levels were significantly increased, and the IL-10 level was significantly decreased in the elderly patients with CHF compared with the healthy subjects. The diversity of the gut microbiota was decreased in the elderly patients with CHF. Moreover, *Escherichia Shigella* was negatively correlated with biocytin and RIBOFLAVIN. *Haemophilus* was negatively correlated with alpha-lactose, cellobiose, isomaltose, lactose, melibiose, sucrose, trehalose, and turanose. *Klebsiella* was positively correlated with bilirubin and ethylsalicylate. *Klebsiella* was negatively correlated with citramalate, hexanoylcarnitine, inosine, isovalerylcarnitine, methylmalonate, and riboflavin. *Conclusion*. The gut microbiota is simplified by the disease, and serum small-molecule metabolites evidently change in elderly patients with CHF. Serum and fecal biomarkers could be used for elderly patients with CHF screening.

1. Introduction

Chronic heart failure (CHF) is a very common multifactor syndrome. Although there are many therapies that are currently used, CHF remains a disease with high morbidity and high mortality. CHF affects not only the heart and blood circulation but also the musculoskeletal, neuroendocrine, metabolic, and immune systems. CHF is associated with altered gut function, including intestinal morphology, permeability, and absorption capacity [1]. Increased gut permeability and bacterial biofilm formation may lead to chronic inflammation and malnutrition. CHF is also considered to be a state of chronic inflammation. The plasma levels of pro-inflammatory factors, such as tumor necrosis factor- (TNF-) α, are related to the severity of disease in CHF patients and can be used to predict survival rates [2, 3]. In fact, it has been found that the wall thickness and permeability of the small intestine and large intestine of CHF patients increase, and the increase in bacterial populations (e.g., *Bacteroides*, *Prevotella*, and *Clostridium*) that adhere to the intestinal mucosa,

and the transfer of bacteria or their toxins from the intestine to the blood is directly associated with systemic inflammation [4]. The excessive growth of pathogenic bacteria and *Candida* in the intestine of CHF patients and the increase in intestinal mucosal permeability were found to be related to the severity of clinical disease, venous blood congestion, and inflammation [5]. Chronic systemic inflammation often occurs in CHF patients, and this inflammatory state is closely related to changes in intestinal morphology, function, and bacterial flora.

In addition, recent studies have reported that the gut and the heart are an axis of mutual regulation, and the blood is the bridge between the two interactions [6, 7]. After intestinal barrier function is damaged, bacteria translocate and introduce bacterial products in circulation, which can lead to atherosclerosis and CHF. On the other hand, the damage to heart function in CHF affects the intestinal microcirculation, which leads to intestinal mucosal barrier dysfunction and increased bacterial translocation. The emergence of the heart-gut axis as a new concept once again showed that the gut is closely related to the occurrence and development of cardiovascular diseases [8]. The gut microbiota plays a crucial role in maintaining homeostasis in the host, because its large number of gene products can supplement the physiological processes of the host [9, 10]. Evidence suggests that the gut microbiota has potential clinical significance in the pathophysiology of CHF [11]. Heart failure (HF) patients showed a significant decrease in the diversity of the gut microbiome and downregulation of key gut bacteria. The above studies indicated that changes in the gut microbiome are potential factors involved in the pathogenesis and progression of HF.

The imbalance of gut microbial metabolites leads to intestinal malnutrition, heart dysfunction, and other diseases in CHF patients. There are at least 6,500 low-molecular-weight metabolites in humans, in addition to proteins and genes, that play important roles in biological systems [12]. The latest progress in this field has enabled us to understand the key role of previously unknown metabolites or metabolic pathways in maintaining homeostasis under physiological and stress conditions [13, 14]. The progression of HF promotes the use of glucose rather than fatty acids, and in the late stages of HF, the heart becomes unable to effectively use any of the substrates. In HF patients, due to the decrease in cardiac output or insufficient perfusion, myocardial hypoxia leads to an increase in hypoxia-inducible factor-1α (HIF-1α), which inhibits pyruvate dehydrogenase (PDH) and promotes cardiac glycolysis without activating glucose oxidation, leading to an increase in the circulating levels of pyruvate and lactic acid and is a prognostic indicator of death [15, 16]. Metabolomics has shown good performance in identifying diagnostic disease markers, which may help to provide new insights into the metabolic processes associated with CHF.

As the global population ages, chronic diseases are placing an increasing burden on public health systems. Studies have shown one to two in every 100 adults in the general population, and more than one in 10 people aged over 70 years are diagnosed with heart failure [17]. At present, there are few studies on the combined use of 16S rDNA sequencing and LC-MS metabolomics to analyze the gut microbiota and serum metabolome in CHF patients, especially the elderly patients. Therefore, our study focused on chronic heart failure in the elderly. In this study, microbiome analysis and metabolomics were used to explore changes in the gut microbiota and serum metabolome during the healthy and CHF to screen effective fecal and serum biomarkers, so as to provide new ideas and insights for elucidating the metabolic process related to CHF.

2. Materials and Methods

2.1. Study Subjects. Twenty-five CHF patients (H group) and 25 healthy subjects (C group) participated in the experiments. According to current guidelines, the diagnosis of CHF is based on symptoms, clinical signs, and recorded left ventricular dysfunction during exercise. All patients were clinically stable (according to the New York Heart Association (NYHA) functional rating) and had received constant medication for at least 4 weeks prior to evaluation. The study sequentially collected information on medications taken by CHF patients and on the NYHA classification of the disease. All healthy subjects did not take any drugs. The study excluded subjects who had infection, rheumatoid arthritis, renal failure, major valvular heart disease, intestinal disease, cancer, or autoimmune disease. None of the subjects had any known immune system diseases, and none had received immunomodulatory therapy. The clinical data of subjects in different groups are shown in Table 1. The electrocardiogram (ECG) of the 25 healthy and 25 CHF subjects in the healthy and CHF groups was also used as a diagnostic reference of CHF. This study was approved by the ethical review committee of our hospital, and informed consent was obtained from each study participant.

2.2. 16S rDNA Sequencing. Fecal samples were collected from 20 healthy subjects and 22 CHF patients by using stool sampling cups. All the fecal samples were stored at -80°C. Microbial genomic DNA was extracted from each fecal sample at 200 mg using the QIAamp ® Fast DNA Stool Mini Kit (Qiagen) according to the manufacturer's protocol. An Agilent 4200 Tapestation Kit (Agilent Technologies) was used to determine the quality of the extracted DNA, and then, the Nextera XT DNA Sample Prep Kit (Illumina) was used to generate sequencing libraries. The bacterial V3/V4 region (F: CCTACGGGNGGCWGCAG and R: GACTACHVGGGTATCTAATCC) was amplified. An Agilent 4200 Tapestation was used to confirm the quality of the libraries, and targeted sequencing of the samples was performed on the HiSeq 2500 platform (Illumina). FastQC (0.11.9) was used for quality control of the original high throughput sequence data. Trim-galore (0.6.5) and CutAdapt (2.8) were used to perform low-quality filtering and joint removal. Cluster analysis was performed with 97% similarity after obtaining effective sequences, and each cluster was called an operational taxonomic unit (OTU). QIIME 2 (2020-2) software and a 16S rDNA sequence database (SILVA-132-99) were used to perform taxonomic annotation and quantitative

Table 1: Clinical parameters of subjects.

	CHF ($n = 25$)	Healthy ($n = 25$)	P value
Age (years)	65 ± 3.17	65 ± 3.07	0.941
Gender (male/female)	14/11	13/12	
BMI (kg/m^2)	29.7 ± 1.44	29.1 ± 1.33	0.768
Smoking			0.733
Never	10	12	
Past	11	10	
Current	4	3	
CRP (mg/L)	11.1 ± 2.06	4.22 ± 1.12	0.006
NT-proBNP (pg/mL)	6564.5 ± 1187.23	109.2 ± 45.91	<0.001
NYHA class			
I	2		
II	5		
III	7		
IV	11		

CHF: chronic heart failure; BMI: body mass index; NYHA: New York Heart Association; CRP: cAMP receptor protein; NT-proBNP: N-terminal pro-B type natriuretic peptide. The unpaired T test was used between the two groups conforming to the normal distribution. P value < 0.05 was considered statistically significant.

statistics for the representative sequences of each OTU. A rank abundance curve was used to explain the two aspects of species abundance and species evenness. Qiime 2 software was used to calculate the alpha diversity index (Chao1 index) of each sample and to draw the ranked abundance curve based on ASV and the dilution curve based on alpha diversity. R software was used to draw a boxplot of differences in alpha diversity (R phyloseq package) between groups for the Wilcoxon test (between two groups) method. The MicrobiomeAnalyst platform [18, 19] (https://www.microbiomeanalyst.ca/) was used for bioinformatics analysis.

2.3. LC-MS/MS Analysis and Annotation. Blood samples from 25 healthy subjects and 25 CHF patients were used for metabolomic analysis. The blood from all participants was centrifuged at 1150 × g and 4°C for 10 min in a centrifuge tube coated with heparin. The supernatant was then aliquoted (100 μL) into a labeled test tube and stored at -80°C before preparation for metabolomics analysis. Each aliquot (100 μL) was mixed with 300 μL of cold acetonitrile and then vortexed for 30 s before analysis. The mixture was deproteinized by centrifugation at 4°C (21130 × g, 30 mins), and 1 μL of supernatant was injected into a UPLC instrument. After each operation, the needle was cleaned for 5 s. An HPLC system (1290, Agilent Technologies) and a UPLC BEH Amide column (1.7 μm, 2.1 × 100 mm, Waters) combined with a TripleTOF 6600 (Q-TOF, AB Sciex) and a QTOF 6550 were used for LC-MS/MS analysis. The mobile phases consisted of 25 mM NH_4OAc and 25 mM NH_4OH (pH = 9.75) (A) and acetonitrile (B) in water. The elution gradient was as follows: 0 min 95% B; 7 min, 65% B; 9 min, 40% B; 9.1 min, 95% B; 12 min, 95% B, delivered at a rate of 0.5 mL/min. The injection volume was 2 μL. In this mode, the acquisition software (Analyst TF 1.7, AB Sciex) continuously evaluates the full-scan survey MS data and triggers the acquisition of MS/MS spectra based on preselected criteria. In each cycle, 12 precursor ions with an intensity greater than 100 were selected and fragmented with collision energy (CE) of 30 V (15 MS/MS events, each product ion had a cumulative time of 50 milliseconds). ESI source conditions were set as follows: ion source gas 1 was 60 psi, ion source gas 2 was 60 psi, curtain gas was 35 psi, source temperature was 650°C, ion spray voltage floating (ISVF) was 5000 V, and positive and negative voltages were 4000 V. The raw data were converted to MZXML format using ProteoWizard and processed using an internal program, which was developed by R software and based on XCMS for peak detection, extraction, alignment, and integration. Then, the internal MS2 database (BiotreeDB) was applied for metabolite annotation. The critical value of the annotation was set to 0.3. QC samples were used to demonstrate the stability of the LC-MS system. MetaboAnalyst [20] (https://www.metaboanalyst.ca/) and Kyoto Encyclopedia of Genes and Genomes [21] (KEGG, https://www.kegg.jp/) were used for bioinformatics analysis.

2.4. ELISA. Blood samples were collected from 20 healthy subjects and 22 CHF patients. The level of IL-6 (CSB-E04638h, Cusabio biotech, China), IL-8 (CSB-E04641h, Cusabio biotech, China), IL-10 (CSB-E04593h, Cusabio biotech, China), and TNF-α (CSB-E04740h, Cusabio biotech, China) in the blood samples was determined by ELISA kit according to the manufacturer's instructions, and all samples analyses were repeated three times.

2.5. Statistical Analysis. Statistical analysis of the data was performed using SPSS 21.0 (IBM, USA) and Graphpad prism 8.0 statistical software. The Gpower software (Cristian-Albrechts University, Kiel, Germany) was used to calculate the experimental validity when selecting samples. All the data are presented as the means ± standard deviations (SDs). Statistical significance between two groups within experiments was determined by unpaired two-tailed Student's t

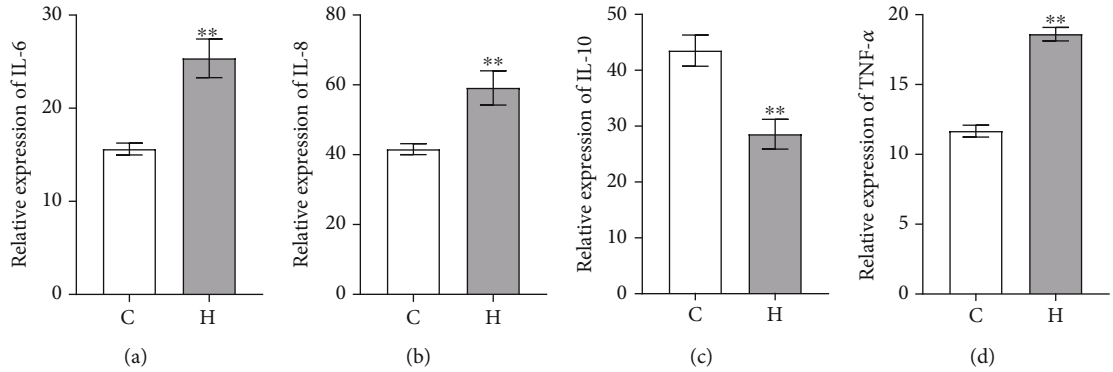

Figure 1: The levels of inflammatory factors in blood were detected. (a) The expression levels of IL-6. (b) The expression levels of IL-8. (c) The expression levels of IL-10. (d) The expression levels of TNF-α. $^{**}P < 0.01$ vs. healthy group. C: healthy group; H: CHF group.

tests. A P value < 0.05 was considered to be statistically significant. Analysis of similarities (ANOSIM) is a nonparametric test method based on permutation tests and rank-sum tests and is used to test whether the difference between groups is significantly greater than that within groups, so as to judge whether the grouping is meaningful. LDA effect size (LefSe, Galaxy Version 1.0) robustly identifies microbes that are significantly different among biological classes, and additional tests were performed to assess these differences with the LDA value and $P < 0.05$. Spearman correlation coefficients ($P < 0.05$) and heatmaps were used to analyze the correlation among gut microbiota, serum metabolomic, and inflammatory factors by Graph prism (8.0) software.

3. Result

3.1. The Characteristics of Subjects. Twenty-five healthy subjects and 25 CHF patients participated in this study, and their clinical information was statistically analyzed. The clinical data of all the participants are shown in Table 1. The calculation results of Gpower software showed that the effectiveness of the experiment could reach 80% in the case of 25 cases in each group. The results of clinical data showed that there were no significant differences in age, gender, BMI, or smoking habits between the two groups. The NYHA class disease rating showed that CHF patients had high disease severity. The CRP and NT-proBNP levels of CHF patients were significantly higher than those of healthy subjects. To further analyze the levels of inflammatory factors in CHF patients and healthy subjects, ELISAs were performed, and the results showed that compared with the levels in the healthy group, the levels of IL-6, IL-8, and TNF-α in the CHF group were significantly higher, while the expression of IL-10 was significantly lower (Figure 1).

3.2. Compositional Alteration of the Gut Microbiota in CHF Patients and Healthy Subjects. To further analyze whether the structure of the gut microbiota of patients with chronic heart failure has changed, 16S rDNA sequencing was used to detect the fecal microorganisms of CHF patients and healthy subjects. As the OTU rank index increased, the relative abundance gradually decreased, indicating that the species richness and evenness of all the tested samples were high (Figure 2(a)). The rank-sum test of the Chao1 index showed that the fecal microbial diversity of CHF patients was significantly reduced compared with that of the healthy subjects (Figure 2(b)). Taxonomic composition analysis based on OTUs showed that there were 11 common microbial phyla in the feces of healthy subjects and CHF patients (Figure 2(c), Supplementary Figure 1A). There were 3 phylum-specific microorganisms in healthy subjects and 1 phylum-specific microorganism in the feces of CHF patients (Figure 2(c), Supplementary Figure 1A). Analysis of the genera showed that there were 161 common genus-level microorganisms in the feces of the healthy subjects and CHF patients (Figure 2(d), Supplementary Figure 1B). There were 69 genus-level microorganisms in the feces of healthy subjects and 30 genus-level microorganisms in the feces of CHF patients (Figure 2(d), Supplementary Figure 1B). These results indicate that the diversity of the gut microbiota decreased in CHF patients.

3.3. Differences of the Gut Microbiota between CHF Patients and Healthy Subjects. To investigate taxonomic and functional differences caused by changes in microbial structure, ANOSIM was first used to analyze the differences between groups. ANOSIM showed that the R value was 0.262, which is greater than 0 and close to 1, and the P value was 0.001, which is less than 0.05, indicating that the difference between groups was greater than that within groups, the difference between groups was obvious, and the grouping was meaningful (Figure 3(a)). To study the differences in the structure of the gut microbiota between groups in depth, LEfSe was used to estimate the impact of the relative abundance of each species on the difference effect and to determine the species with significantly different effects on sample division. The LDA ring-mounted evolutionary branch diagram clearly showed the taxonomic relationship between CHF patients and healthy subjects. The changes at the genus level showed that *Ruminococcus gnavus group* (LDA = 4.42, $P = 0.0209$), *Escherichia Shigella* (LDA = 5.01, $P = 0.0034$), *Ruminococcaceae UCG 005* (LDA = 3.16, $P = 0.0473$), *Ruminococcaceae UCG 002* (LDA = 3.90, $P = 0.0072$), *Lactobacillus* (LDA = 4.50, $P = 0.0303$), *Atopobium* (LDA = 2.48, $P = 0.0409$), *Romboutsia* (LDA = 3.85, $P = 0.0054$), *Streptococcus* (LDA = 4.80, $P = 0.0122$), *Haemophilus* (LDA = 3.10, $P = 0.0058$), and

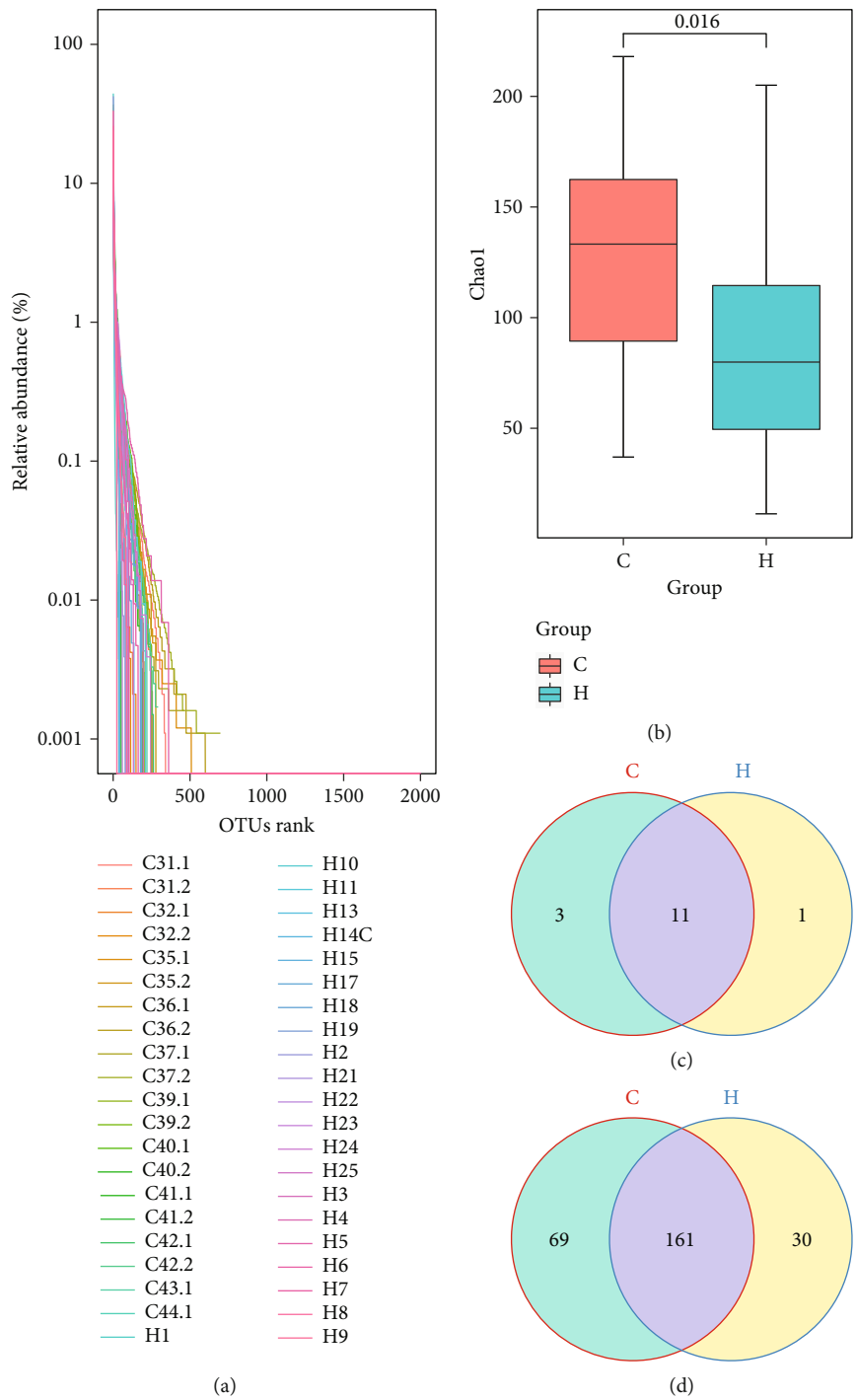

Figure 2: Changes of fecal microbiome. (a) The rank abundance curve. (b) The changes of Chao 1 index. (c) Venn diagram showed microbiota at the phylum level. (d) Venn diagram showed microbiota at genus level. C: healthy group; H: CHF group.

Klebsiella (LDA = 4.11, $P = 0.0018$) were significantly enriched in the feces of CHF patients, suggesting that they may be fecal biomarkers for CHF (Figure 3(b)). Functional prediction of gut microbiota showed amino acid metabolism, metabolism of cofactors and vitamins, energy metabolism, replication and repair, and metabolism of terpenoids and polyketides pathways were significantly enriched in the healthy group, and membrane transport and signal transduction pathways were significantly enriched in CHF group at L2 pathways (Supplementary Figure 2A). At L3 pathways, ABC transporters, beta lactam resistance (environmental information processing), and bacterial secretion system pathways were significantly enriched in the healthy group, thiamine metabolism, NOD-like receptor signaling pathway, and beta alanine metabolism pathways were significant enriched in the CHF group (Supplementary Figure 2B). The

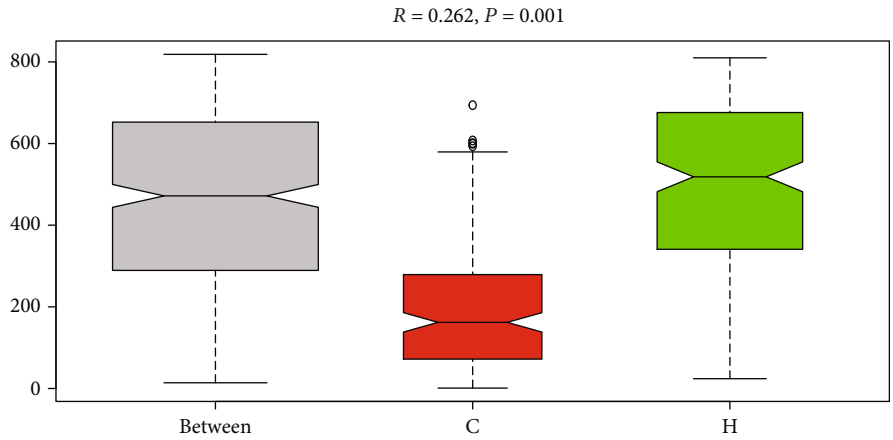

(a)

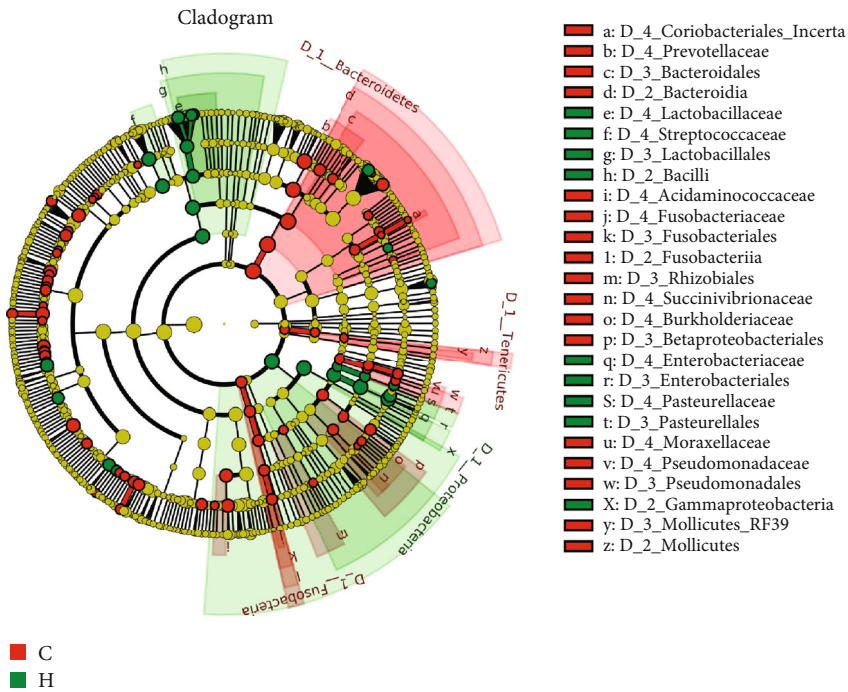

(b)

Figure 3: Differential microbial and functional analysis of feces. (a) ANOSIM showed the differentia in groups. (b) Ring-mounted evolutionary branch diagram showed the different microbiota ($P < 0.05$, LDA > 2.28). C: healthy group; H: CHF group.

results showed that the intestinal flora function of the CHF patients had changed.

3.4. Serum Metabolomic Profile in CHF Patients and Healthy Subjects. We further performed metabolic profiling of serum samples from subjects by using high-throughput liquid chromatography-mass spectrometry (LC/MS). The cluster of QC samples in the PCA score plot demonstrated satisfactory stability and repeatability of the metabolic profiling method (Figure 4(a)). As demonstrated by the PLS-DA score plot, clear separation of control versus CHF samples was observed (Figure 4(b)). Subsequently, heatmap showed a total of 90 potential biomarkers of the CHF group were identified (Figure 4(c)). All of the results indicate that the CHF serum metabolic phenotype was altered compared to the healthy phenotype.

3.5. Different Serum Metabolomic of CHF Patients and Healthy Subjects. There are 50 metabolites changed with $P < 0.05$ and $\log 2(\mathrm{FC}) > 1.0$, including 27 and 23 metabolites that were enriched in the CHF and healthy groups, respectively (Figure 5(a)). The ethylsalicylate, N-formyl-L-methionine, galacturonate, cellobiose, sucrose, turanose, alpha-lactose, lactose, trehalose, isomaltose, melibiose, 3-amino-5-hydroxybenzoate, 1,11-undecanedicarboxylic acid, D-glucurono-6,3-lactone, adenosine, 4-acetamidobutanoate, homocitrulline, N-acetylglutamate, bilirubin, bilirubin, ascorbate, mesoporphyrin IX, 5-methoxysalicylic acid, vanillic acid, 2-pyrocatechuic acid, gentisic acid, and furosemide

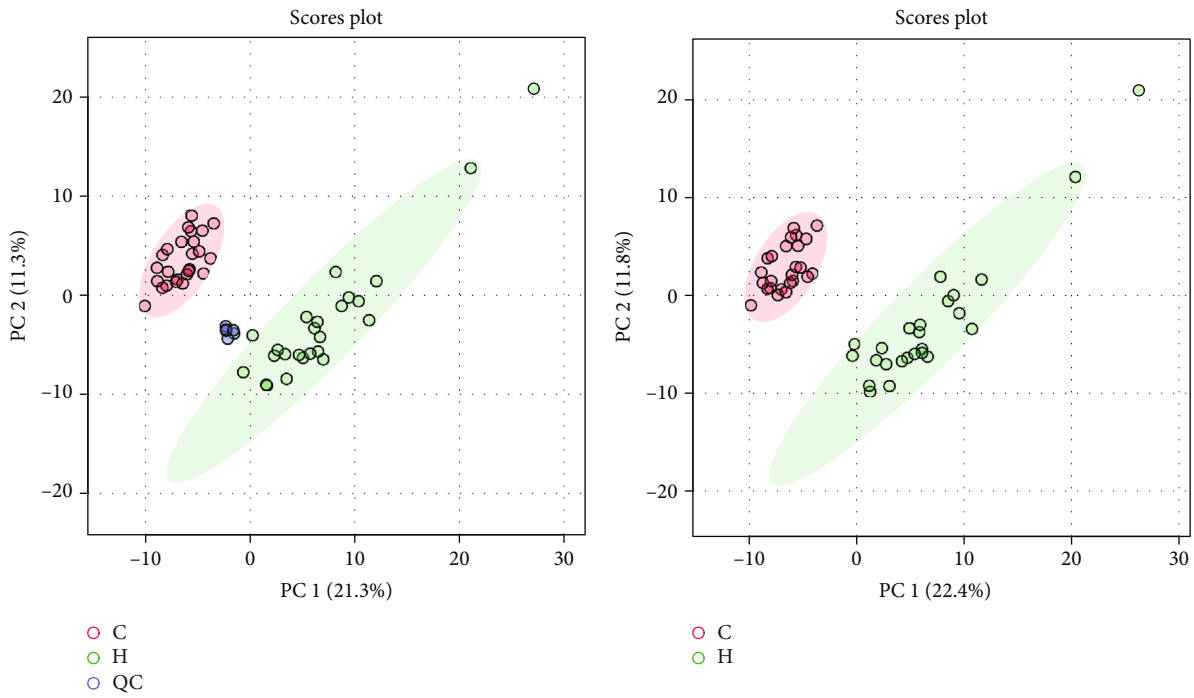

(a) (b)

Figure 4: Continued.

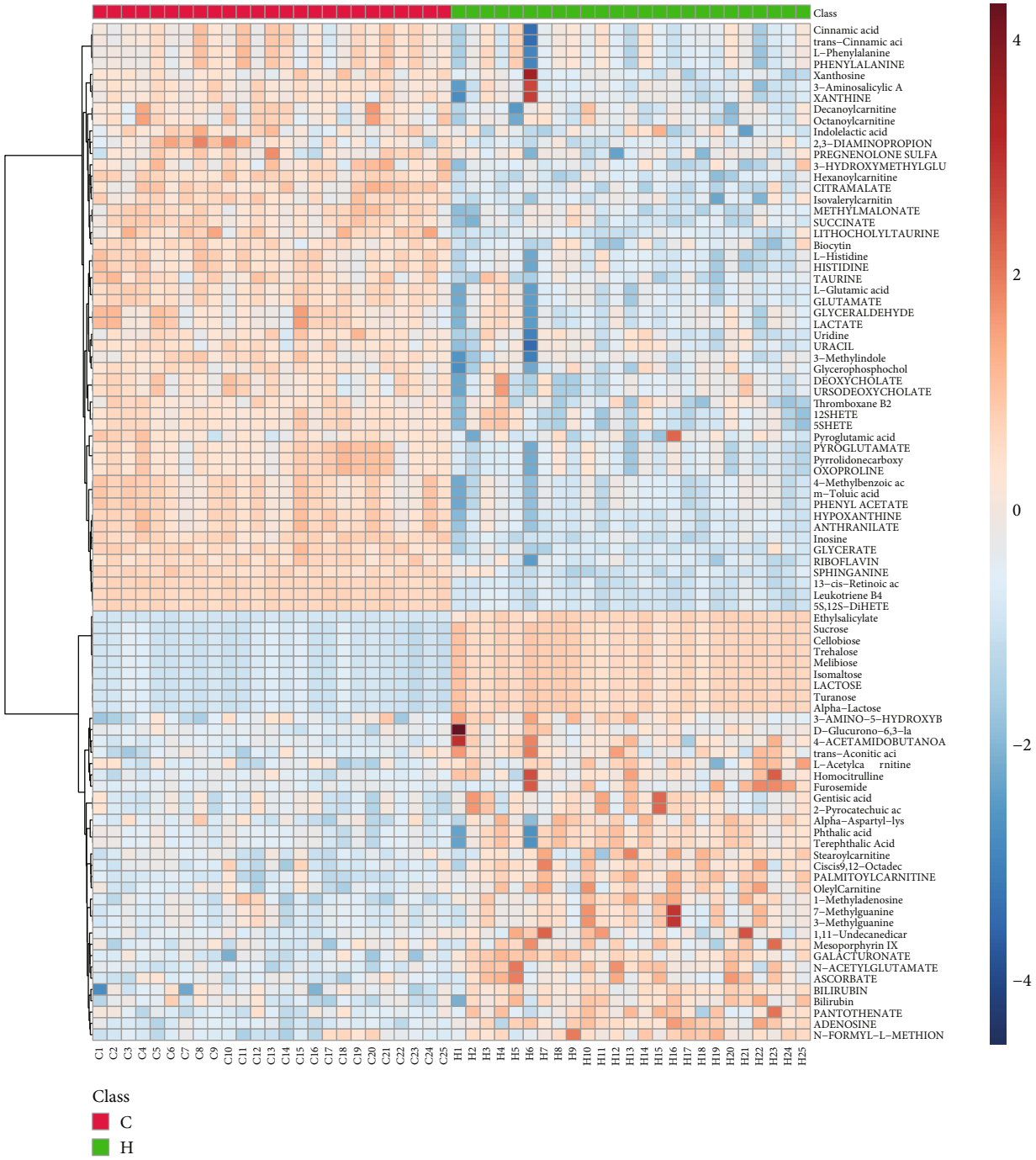

(c)

Figure 4: Metabolomic analyses of serum samples. (a) The PCA score plot using the first two components. (b) The PLS-DA scores plot based on fecal metabolic profiles in the healthy and CHF group. (c) Heatmap showed the differential proportion of 90 metabolites in the sample of CHF and healthy groups. The different colors of the circle represent different groups, blue circle: QC sample, green circle: CHF group, red circle: healthy group. C: healthy group; H: CHF group.

were significantly enriched in the CHF group (Figure 5(b)). The citramalate, isovalerylcarnitine, pyroglutamate, 13-cis-retinoic acid, 5S,12S-DiHETE, leukotriene B4, inosine, 4-methylbenzoic acid, m-toluic acid, phenyl acetate, anthranilate, hypoxanthine, hexanoylcarnitine, sphinganine, lithocholyltaurine, methylmalonate, succinate, glycerate, glutamate, L-glutamic acid, riboflavin, biocytin, and thromboxane B2 were significantly enriched in the healthy group (Figure 5(b)). All the results indicated that 23 and 27 separately enriched metabolites in the healthy and CHF groups, respectively, may be biomarkers that could contribute to early screening of chronic heart failure patients.

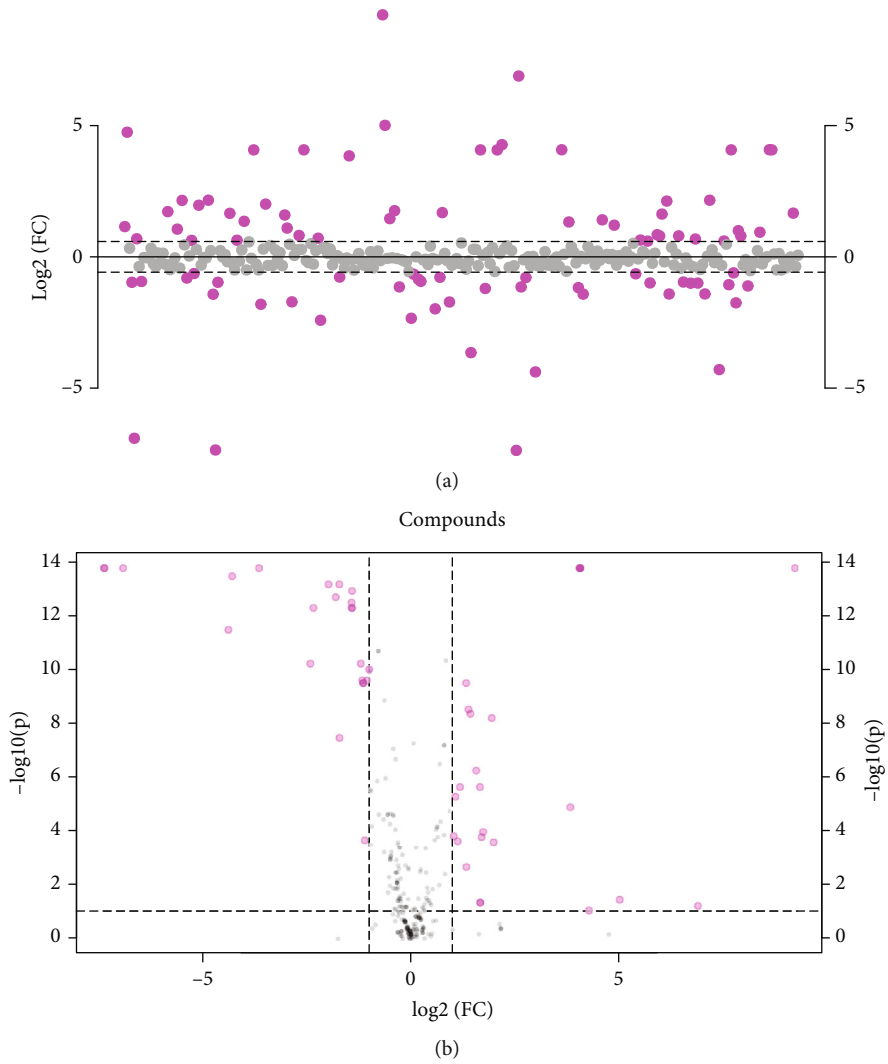

Figure 5: The characteristics and correlation of serum metabolites. (a) The different metabolites associated with CHF were confirmed (log 2(FC) > 1.0) (pink). (b) Volcano map showed the different metabolites in CHF and healthy groups.

3.6. The Correlation among Gut Microbiota, Serum Metabolomic, and Inflammatory Factors. We analyzed the correlation between gut microbiota and serum metabolomic. We found *Escherichia Shigella* was negatively correlated with biocytin and riboflavin (Figure 6). *Haemophilus* was negatively correlated with alpha-lactose, cellobiose, isomaltose, lactose, melibiose, sucrose, trehalose, and turanose (Figure 6). *Klebsiella* was positively correlated with bilirubin (bilirubin) and ethylsalicylate (Figure 6). *Klebsiella* was negatively correlated with citramalate, hexanoylcarnitine, inosine, isovalerylcarnitine, methylmalonate, and riboflavin (Figure 6). We also analyzed the correlation among inflammatory factors, gut microbiota, and serum metabolites. The results showed that IL-6 was positively correlated with alpha-lactose, bilirubin, cellobiose, ethylsalicylate, isomaltose, lactose, melibiose, sucrose, trehalose, turanose, and *Klebsiella* (Figure 7). IL-6 was negatively correlated with biocytin, citramalate, hexanoylcarnitine, inosine, isovalerylcarnitine, methylmalonate, and riboflavin (Figure 7). IL-8 was positively correlated with bilirubin and ethylsalicylate (Figure 7). IL-8 was negatively correlated with biocytin, citramalate, hexanoylcarnitine, inosine, methylmalonate, and riboflavin (Figure 7). IL-10 was positively correlated with biocytin, citramalate, hexanoylcarnitine, inosine, isovalerylcarnitine, methylmalonate, and riboflavin (Figure 7). IL-10 was negatively correlated with alpha-lactose, bilirubin, cellobiose, ethylsalicylate, isomaltose, lactose, melibiose, sucrose, trehalose, turanose, and *Escherichia Shigella* (Figure 7). TNF-α was positively correlated with alpha-lactose, bilirubin, cellobiose, ethylsalicylate, isomaltose, lactose, melibiose, sucrose, trehalose, turanose, and *Klebsiella* (Figure 7). TNF-α was negatively correlated with biocytin, citramalate, hexanoylcarnitine, inosine, isovalerylcarnitine, methylmalonate, riboflavin, and *Haemophilus* (Figure 7). All the results showed that gut microbiota, serum metabolomic, and inflammatory factors were correlated in chronic heart failure patients.

4. Discussion

In 132 patients with chronic systolic heart failure, plasma measurements of asymmetric/symmetric dimethylarginine (ADMA, SDMA), N-monomethylarginine, and methyllysine

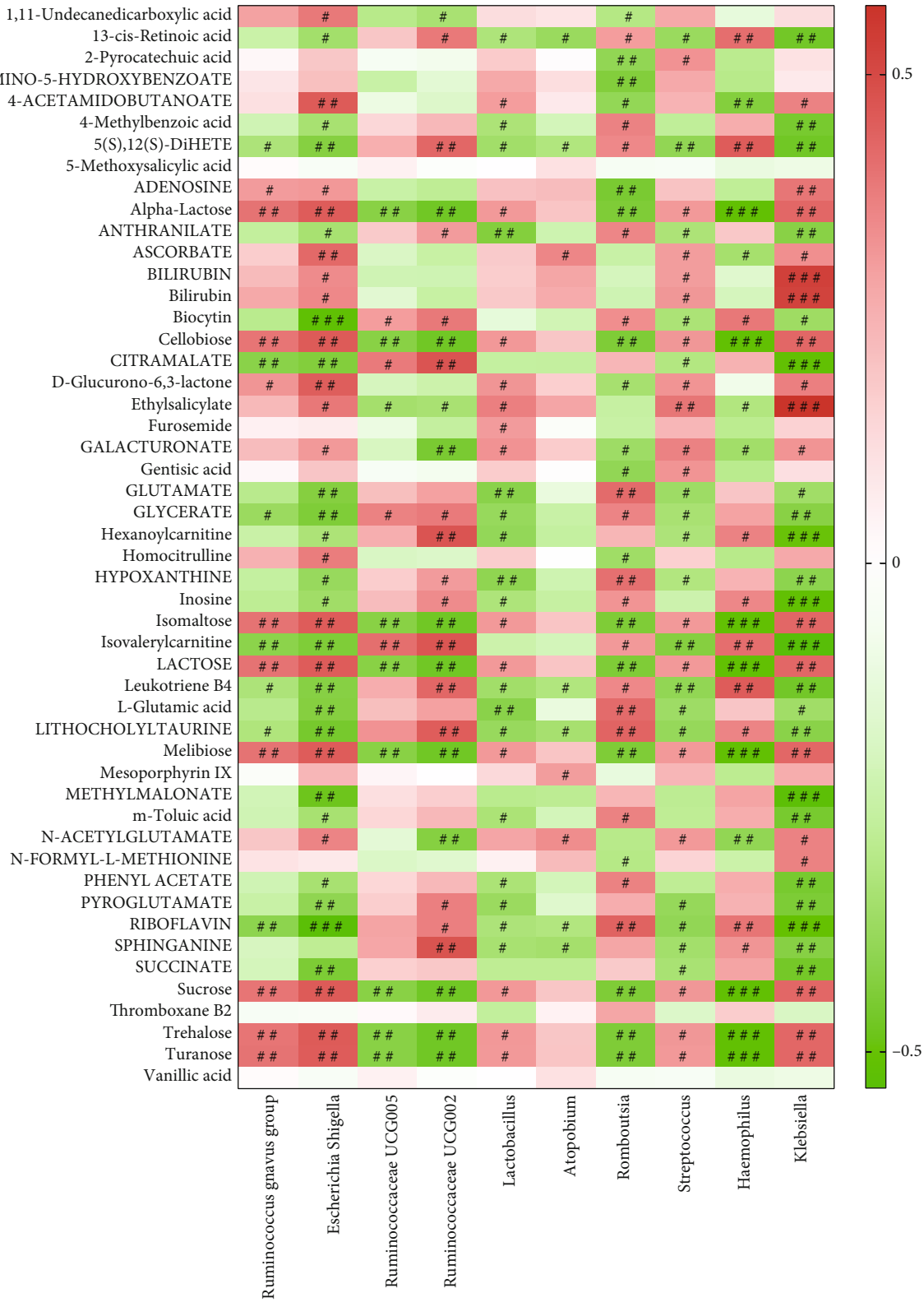

Figure 6: The correlation between gut microbiota and serum metabolomic. Red represents positive correlation, and green represents negative correlation. $^{\#}P < 0.05$; $^{\#\#}P < 0.01$; $^{\#\#\#}P < 0.001$.

have shown that elevated levels of methylated arginine metabolites (demmethyllysine) are associated with left ventricular diastolic dysfunction, and elevated levels of ADMA were associated with later right ventricular systolic dysfunction [22]. Heart failure (HF) and its risk factors promote dysregulation of the intestinal flora, causing damage to the

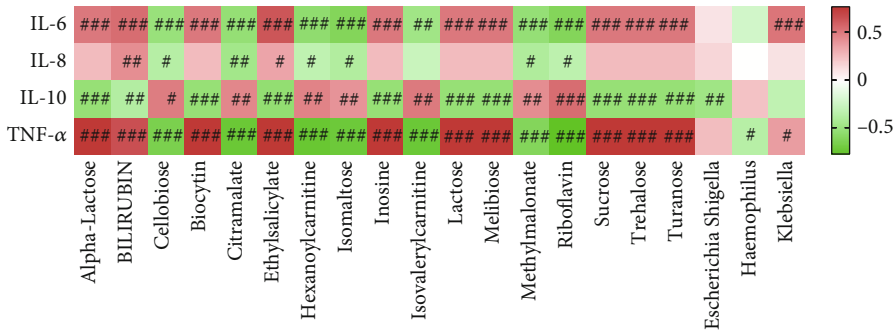

Figure 7: The correlation among gut microbiota, serum metabolites, and inflammatory factors. Red represents positive correlation, and green represents negative correlation. $^{\#}P < 0.05$; $^{\#\#}P < 0.01$; $^{\#\#\#}P < 0.001$.

intestinal barrier, and the entry of LPS and other components of the flora into the bloodstream, leading to chronic inflammation, which in turn exacerbates heart failure [7]. It was reported that the structure of the gut microbiota was disordered, and the permeability of the gut was increased in CHF patients [11, 23]. Increased intestinal permeability might cause bacteria and their toxins to enter the blood and cause inflammation [24]. Analysis of inflammation factors showed that the levels of IL-6, IL-8, and TNF-α were significantly higher and that of IL-10 was lower in CHF patients than in healthy subjects. As a marker of systemic inflammation, the CRP level was elevated in HF patients, but was within the normal range in healthy controls [5]. The CRP (11.1 ± 2.06 mg/L) and NT-proBNP (6564.5 ± 1187.23 pg/mL) levels of CHF patients were significantly higher than those of healthy subjects. Under normal and healthy physiological conditions, the gut is stable and strictly controlled [25]. Our study showed that the diversity and number of gut microbiota were decreased in the CHF patients, which was consistent with previous studies.

Recently, studies have shown that the gut microbiota can affect the cardiovascular system, and that arrhythmias can aggravate the development of HF [26]. The imbalance of the gut microbiota and intestinal malnutrition was directly related to the origin of various processes of acute or chronic host dysfunction. In addition, studies have reported that the development of CHF is often accompanied by enrichment of pathogens in the gut microbiota [5, 11, 26, 27]. Compared with healthy individuals, CHF patients had more colonizing pathogenic bacteria, including *Campylobacter*, *Salmonella*, *Escherichia Shigella*, *Yersinia enterocolitica*, and *Candida species* [28]. Compared with patients with mild HF, more patients with moderate to severe HF contain *Candida*, *Campylobacter*, and *Shigella species* [28]. Artery atherosclerosis in patients with ischemic stroke and transient ischemic attack case-control study found that patients with stroke and transient ischemic attack more opportunistic pathogens, such as *Enterobacter*, *Megasphaera*, *Oscillibacter*, and *Desulfovibrio*, and fewer commensal or beneficial genera including *Bacteroides*, *Prevotella*, and *Faecalibacterium* [29]. *Eubacterium rectale* and *Dorea longicatena* were less abundant in the HF patients than in that of healthy subjects [30]. Compared to younger HF patients, the *Faecalibacterium* was depleted, while *Lactobacillus* was enriched in the gut of older HF patients [30]. The LDA ring-mounted evolutionary branch diagram clearly showed that *Escherichia Shigella*, *Ruminococcaceae*, *Lactobacillus*, *Atopobium*, *Romboutsia*, *Streptococcus*, *Haemophilus*, and *Klebsiella* were significantly enriched in the feces of CHF patients. Our study found that the more potential pathogenic bacteria and less beneficial bacteria enriched in the gut microbiota of CHF patients. Whether these reduced beneficial bacteria have a potential effect on chronic heart failure remains to be seen. We will further explore the potential role of probiotics or prebiotics in chronic heart failure in animal models, with a view to developing new treatments for chronic heart failure based on the "heart-gut axis" or "gut-heart axis" theory.

Metabolites derived from the intestinal tract and gut microbiota are nutrients that are directly or indirectly digested, absorbed, and utilized by the host [31, 32]. The correlation between gut microbiota and plasma metabolite showed plasma sphingosine 1-phosphate was positively correlated with several CHF-enriched bacteria such as *Veillonella*, *Coprobacillus*, and *Streptococcus*, while plasma-reduced metabolite ricinoleic acid was positively correlated with *Butyricicoccus* enriched in healthy [27]. Our study found *Escherichia Shigella* was negatively correlated with serum biocytin and riboflavin. *Haemophilus* was negatively correlated with serum alpha-lactose, cellobiose, isomaltose, lactose, melibiose, sucrose, trehalose, and turanose. *Klebsiella* was positively correlated with serum bilirubin (bilirubin) and ethylsalicylate, while negatively correlated with serum citramalate, hexanoylcarnitine, inosine, isovalerylcarnitine, methylmalonate, and riboflavin. There were some studies of plasma metabolite in HF disease. Lysophosphatidylcholine 18 : 2, cholesteryl ester 18 : 1, alanine, choline, and fructose were correlated with B-type natriuretic peptide or left ventricular ejection fractions [33]. Orotic acid and N-methylproline were a distinct metabolic signature for differentiated individuals with HF with preserved ejection fraction versus HF with reduced ejection fraction [34]. Norvaline,1-pyrroline-2-carboxylate, lysophosphatidylinositol (16 : 0/0 : 0), phosphatidylglycerol (6 : 0/8 : 0), fatty acid esters of hydroxy fatty acid (24 : 1), and phosphatidylcholine (18 : 0/18 : 3) may have the potential to differentiate patients with dilated cardiomyopathy and ischemic cardiomyopathy, which were common causes of HF [35]. Studies have shown

that the gut microbiota in the elderly CHF patients may be related to serum metabolite.

Functional prediction of gut microbiota showed amino acid metabolism, metabolism of cofactors and vitamins, energy metabolism, replication and repair, and metabolism of terpenoids and polyketides pathways were significantly enriched in the healthy group, and membrane transport and signal transduction pathways were significantly enriched in CHF group at L2 pathways. At L3 pathways, ABC transporters, beta lactam resistance (environmental information processing), and bacterial secretion system pathways were significantly enriched in the healthy group, and thiamine metabolism, NOD-like receptor signaling pathway, and beta alanine metabolism pathways were significantly enriched in the CHF group. Studies have shown that skeletal muscle mass and strength are extremely low in 20% of patients with CHF [36]. Supplementation of essential amino acids (EAA) can prevent muscle strength and performance decline and improve quality of life and survival in patients with CHF, which may be a feasible treatment strategy [36]. But we did not analyze the correlation between metabolites and functional pathways due to the limited time and funding issues in this research. In the future, we will perform experiments and analysis to investigate the relationship between microbial function and metabolism.

In conclusion, our study found that the diversity and quantity of gut microbiota in elderly patients with CHF were reduced, the potential pathogenic bacteria were enriched, the beneficial bacteria were depleted, and the changes of serum metabolic map were accompanied. Our study may provide insignificance for the treatment of elderly patients with CHF, but it uncovers the relationship between gut microbiota and serum metabolites in elderly patients with CHF.

5. Conclusion

The diversity of the gut microbiota in CHF patients was decreased, and the disease tended to reduce the complexity of microbiota. Imbalance of the gut microbiota and serum metabolites profiles was the basic characteristics in elderly patients with CHF.

Data Availability

The data that support the findings of this study are available from the corresponding author upon reasonable request.

Ethical Approval

This study was approved by the Second Affiliated Hospital of Fujian Medical University (2020347), Quanzhou, Fujian, China.

Consent

Written informed consent was obtained from all subjects.

Conflicts of Interest

The authors declare that there is no conflict of interest regarding the publication of this article.

Authors' Contributions

Zhenhua Wang and Guorong Lyu performed the study design, data acquisition, statistical analysis, and writing of the manuscript. Yilong Liu and Chengyi Li performed the sample collection and contributed to writing the manuscript. Zhaoling Cai and Tianzhang Zhang performed the study design, data interpretation, and writing of the manuscript. Markus W. Ferrari performed the data interpretation and writing of the manuscript. All authors read and approved the final manuscript. Zhenhua Wang and Zhaoling Cai are co-first author.

Acknowledgments

This study was supported by Natural Science Foundation of Fujian Province, P.R.C (2020J01238), Medical Elite Cultivation Program of Fujian, P.R.C (2015-ZQN-ZD-24), Quanzhou High-level Talent Innovation and Entrepreneurship Project (2018C052R), Jinjiang Science and Technology Project (2016S002), Research Project of Collaborative Innovation Center for Maternal and Infant Health Service Application Technology (XJM1802).

Supplementary Materials

Supplementary Figure 1: the relative abundance of gut microbiota at phylum and genus level. (a) Relative abundance of microbiota in samples at phylum level. (b) Heatmap showed relative abundance of microbiota in samples at the genus level. C: healthy group; H: CHF group. Supplementary Figure 2: The different pathway at L2 and L3 level in healthy and CHF group. (a) The enriched pathway at L2 level. (b) The enriched pathway at L3 level. C: healthy group; H: CHF group. *(Supplementary Materials)*

References

[1] A. Sandek, J. Bauditz, A. Swidsinski et al., "Altered intestinal function in patients with chronic heart failure," *Journal of the American College of Cardiology*, vol. 50, no. 16, pp. 1561–1569, 2007.

[2] M. Rauchhaus, W. Doehner, D. P. Francis et al., "Plasma cytokine parameters and mortality in patients with chronic heart failure," *Circulation*, vol. 102, no. 25, pp. 3060–3067, 2000.

[3] B. Levine, J. Kalman, L. Mayer, H. M. Fillit, and M. Packer, "Elevated circulating levels of tumor necrosis factor in severe chronic heart failure," *The New England Journal of Medicine*, vol. 323, no. 4, pp. 236–241, 1990.

[4] A. Sandek, I. Bjarnason, H. D. Volk et al., "Studies on bacterial endotoxin and intestinal absorption function in patients with chronic heart failure," *International Journal of Cardiology*, vol. 157, no. 1, pp. 80–85, 2012.

[5] E. Pasini, R. Aquilani, C. Testa et al., "Pathogenic gut flora in patients with chronic heart failure," *JACC: Heart Failure*, vol. 4, no. 3, pp. 220–227, 2016.

[6] R. Gerhard and R. Giuseppe, "The heart and the gut," *European Heart Journal*, vol. 35, no. 7, pp. 426–430, 2014.

[7] S. Madan and M. R. Mehra, "Gut dysbiosis and heart failure: navigating the universe within," *European Journal of Heart Failure*, vol. 22, no. 4, pp. 629–637, 2020.

[8] T. Kamo, H. Akazawa, J.-i. Suzuki, and I. Komuro, "Novel concept of a heart-gut axis in the pathophysiology of heart failure," *Korean Circulation Journal*, vol. 47, no. 5, pp. 663–669, 2017.

[9] T. Kitai, J. Kirsop, and W. H. W. Tang, "Exploring the microbiome in heart failure," *Current Heart Failure Reports*, vol. 13, no. 2, pp. 103–109, 2016.

[10] "Vineyard soil bacterial diversity and composition revealed by 16S rRNA genes: differentiation by geographic features," *Soil Biology & Biochemistry*, vol. 91, pp. 232–247, 2015.

[11] G. Lim, "Gut flora – pathogenic role in chronic heart failure," *Nature Reviews Cardiology*, vol. 13, no. 2, p. 61, 2016.

[12] C. B. Newgard, "Metabolomics and Metabolic Diseases: Where Do We Stand?- Science Direct," *Cell Metabolism*, vol. 25, no. 1, pp. 43–56, 2017.

[13] I. Ryutaro, S. Ippei, and Y. Yohko, "Metabolomic analysis in heart failure," *Circulation Journal*, vol. 82, no. 1, pp. 10–16, 2017.

[14] R. Powers and B. Worley, "Multivariate Analysis in Metabolomics," *Current Metabolomics*, vol. 1, 2013.

[15] F. Desmoulin, M. Galinier, C. Trouillet et al., "Metabonomics analysis of plasma reveals the lactate to cholesterol ratio as an independent prognostic factor of short-term mortality in acute heart failure," *PLoS One*, vol. 8, no. 4, article e60737, 2013.

[16] J. Wang, Z. Li, J. Chen et al., "Metabolomic identification of diagnostic plasma biomarkers in humans with chronic heart failure," *Molecular BioSystems*, vol. 9, no. 11, pp. 2618–2626, 2013.

[17] N. R. Jones, A. K. Roalfe, I. Adoki, F. D. R. Hobbs, and C. J. Taylor, "Survival of patients with chronic heart failure in the community: a systematic review and meta-analysis," *European Journal of Heart Failure*, vol. 21, no. 11, pp. 1306–1325, 2019.

[18] A. Dhariwal, J. Chong, S. Habib, I. L. King, L. B. Agellon, and J. Xia, "MicrobiomeAnalyst: a web-based tool for comprehensive statistical, visual and meta-analysis of microbiome data," *Nucleic Acids Research*, vol. 45, no. W1, pp. W180–w188, 2017.

[19] J. Chong, P. Liu, G. Zhou, and J. Xia, "Using MicrobiomeAnalyst for comprehensive statistical, functional, and meta- analysis of microbiome data," *Nature Protocols*, vol. 15, no. 3, pp. 799–821, 2020.

[20] Z. Pang, J. Chong, G. Zhou et al., "MetaboAnalyst 5.0: narrowing the gap between raw spectra and functional insights," *Nucleic Acids Research*, vol. 49, no. W1, pp. W388–w396, 2021.

[21] M. Kanehisa and S. Goto, "KEGG: Kyoto encyclopedia of genes and genomes," *Nucleic Acids Research*, vol. 28, no. 1, pp. 27–30, 2000.

[22] W. H. W. Tang, W. Tong, K. Shrestha et al., "Differential effects of arginine methylation on diastolic dysfunction and disease progression in patients with chronic systolic heart failure," *European Heart Journal*, vol. 29, no. 20, pp. 2506–2513, 2008.

[23] H. Fukui, "Increased intestinal permeability and decreased barrier function: does it really influence the risk of inflammation?," *Inflammatory Intestinal Diseases*, vol. 1, no. 3, pp. 135–145, 2016.

[24] R. Wenkai, C. Shuai, and Z. Liwen, "Interferon tau affects mouse intestinal microbiota and expression of IL-17," *Mediators of Inflammation*, vol. 2016, 9 pages, 2016.

[25] Z. Jia, X. Zhao, X. Liu et al., "Impacts of the plateau environment on the gut microbiota and blood clinical indexes in Han and Tibetan individuals," *mSystems*, vol. 5, no. 1, 2020.

[26] Y. Sata, F. Z. Marques, and D. M. Kaye, "The emerging role of gut dysbiosis in cardio-metabolic risk factors for heart failure," *Current Hypertension Reports*, vol. 22, no. 5, 2020.

[27] X. Cui, L. Ye, J. Li et al., "Metagenomic and metabolomic analyses unveil dysbiosis of gut microbiota in chronic heart failure patients," *Scientific Reports*, vol. 8, no. 1, p. 635, 2018.

[28] T. Hayashi, T. Yamashita, H. Watanabe et al., "Gut microbiome and plasma microbiome-related metabolites in patients with decompensated and compensated heart failure," *Circulation Journal*, vol. 83, 2018.

[29] J. Yin, S.-. X. Liao, Y. He et al., "Dysbiosis of gut microbiota with reduced trimethylamine-N-oxide level in patients with large-artery atherosclerotic stroke or transient ischemic attack," *Journal of the American Heart Association*, vol. 4, no. 11, 2015.

[30] T. Kamo, H. Akazawa, W. Suda et al., "Dysbiosis and compositional alterations with aging in the gut microbiota of patients with heart failure," *PLoS One*, vol. 12, no. 3, article e0174099, 2017.

[31] X. Li, Z. Cao, Y. Yang et al., "Correlation between jejunal microbial diversity and muscle fatty acids deposition in broilers reared at different ambient temperatures," *Scientific Reports*, vol. 9, no. 1, p. 11022, 2019.

[32] J. Zierer, M. A. Jackson, G. Kastenmüller et al., "The fecal metabolome as a functional readout of the gut microbiome," *Nature Genetics*, vol. 50, no. 6, pp. 790–795, 2018.

[33] J. Zhou, X. Chen, W. Chen, L. Zhong, and M. Cui, "Comprehensive plasma metabolomic and lipidomic analyses reveal potential biomarkers for heart failure," *Molecular and Cellular Biochemistry*, vol. 476, no. 9, pp. 3449–3460, 2021.

[34] U. A. Tahir, D. H. Katz, T. Zhao et al., "Metabolomic profiles and heart failure risk in black adults: insights from the Jackson heart study," *Circulation. Heart Failure*, vol. 14, no. 1, article e007275, 2021.

[35] J. Zhao, S. Yang, R. Jing et al., "Plasma metabolomic profiles differentiate patients with dilated cardiomyopathy and ischemic cardiomyopathy," *Front Cardiovasc Med*, vol. 7, p. 597546, 2020.

[36] S. Nichols, G. McGregor, A. Al-Mohammad, A. N. Ali, G. Tew, and A. F. O'Doherty, "The effect of protein and essential amino acid supplementation on muscle strength and performance in patients with chronic heart failure: a systematic review," *European Journal of Nutrition*, vol. 59, no. 5, pp. 1785–1801, 2020.

Hindawi
Mediators of Inflammation
Volume 2021, Article ID 2752265, 12 pages
https://doi.org/10.1155/2021/2752265

Research Article

Effects of IQW and IRW on Inflammation and Gut Microbiota in ETEC-Induced Diarrhea

Naiyuan Liu, Lingsi Zhou, Jun Fang, Hongmei Jiang, and Gang Liu

College of Bioscience and Biotechnology, Hunan Agricultural University, Hunan Provincial Engineering Research Center of Applied Microbial Resources Development for Livestock and Poultry, Changsha, Hunan 410125, China

Correspondence should be addressed to Jun Fang; fangjun1973@hunau.edu.cn and Gang Liu; gangle.liu@gmail.com

Received 7 July 2021; Revised 26 August 2021; Accepted 30 August 2021; Published 24 September 2021

Academic Editor: Mingliang Jin

Background/Aims. Changing gut microbiota is one of the most common causes of host gut inflammation. The active triple peptides, lle-Gln-Trp (IQW) and lle-Arg-Trp (IRW), cause remarkable changes to gut microbiota. The effects of the triple peptides IQW and IRW in gut-damage treatment were explored in this study via an enterotoxigenic *Escherichia coli*- (ETEC-) induced mouse model. *Methods.* The mice were randomly distributed into four groups: (a) control (CTRL) group, (b) ETEC group, (c) IQW-ETEC group, and (d) IRW-ETEC group. Villus length and crypt depth were measured after hematoxylin and eosin staining. The inflammatory reaction was analyzed via inflammatory cytokines (i.e., TNF-α, IL-1β, IL-6, and IL-10) using the enzyme-linked immunosorbent assay (ELISA). The microbiota in the colon was sequenced using 16S ribosomal RNA. *Results.* The villus length decreased, the crypt depth decreased, and the expression of inflammatory cytokines (i.e., TNF-α, IL-1β, IL-6, and IL-10) increased due to ETEC. In the IRW-ETEC and IQW-ETEC groups, the Shannon index decreased ($P < 0.05$). IQW and IRW increased the abundance of *Firmicutes*, *Proteobacteria*, *Clostridiales*, *Lachnospiraceae*, and *Alloprevotella*; contrastingly, it decreased the abundance of *Epsilonproteobacteria*, *Erysipelotrichales*, *Prevotellaceae*, and *Flavobacteriaceae* compared to the ETEC group ($P < 0.05$). *Conclusion.* This study ascertained that the addition of IQW and IRW could alleviate jejunal inflammation and increase microbiota community diversity.

1. Introduction

According to records, diarrhea kills approximately 800,000 children each year [1]. One in ten children worldwide has died due to diarrhea [2]. The cause of diarrhea is complicated; however, pathogenic bacterial infections are one of the major causes. Pathogenic bacteria were detected in 80% of diarrhea patients in Southeast Asia and 72% of diarrhea patients in South America [3].

The traditional treatment of infectious diarrhea involves antibiotics (and sometimes antiviral or antiparasitic medications), which may increase pathogen resistance to drugs. Simultaneously, antibiotics ruin the intestinal microenvironment of the host. Thus, there is much concern about determining alternatives to antibiotics in diarrhea treatment. Natural products, polypeptides, polysaccharides, probiotics, and other substances can be added to the host diet to treat infectious diarrhea; these have received much attention in recent years [4–6]. For example, one study revealed that adding plant polysaccharides to one's diet can alleviate diarrhea symptoms of mice infected with enterotoxigenic *Escherichia coli* (ETEC) [7].

Ile-Gln-Trp (IQW) and Ile-Arg-Trp (IRW) are two active tripeptides extracted from egg whites. Some studies have proved that IQW and IRW have several functions, including lowering blood pressure and cholesterol and antioxidant and anti-inflammatory properties [8–11]. Studies have shown that IQW and IRW can reduce the TNF-induced inflammatory and oxidative stress responses in endothelial cells; these anti-inflammatory and antioxidative effects of IRW and IQW are regulated through the NF-κB signal pathway [12, 13]. It has been shown that IRW can display anti-inflammatory effects by inhibiting p65 protein activity in NF-κB [14]. Additionally, research has shown that IRW can upregulate the expression of nicotinamide phosphoribosyltransferase (NAMPT) protein in mouse muscle

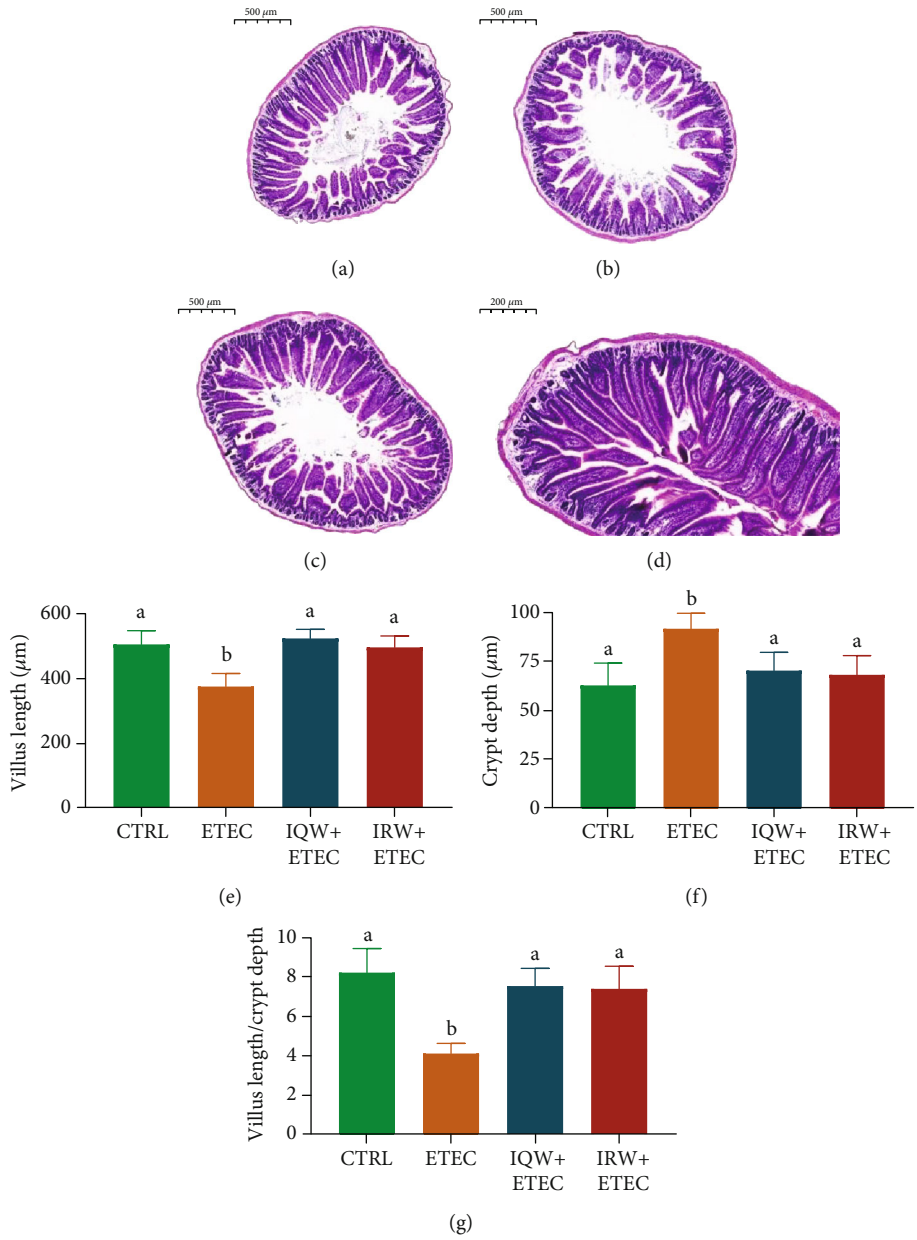

Figure 1: H&E staining results of mouse jejunum ($n = 6$): (a) CTRL, (b) ETEC, (c) IQW+ETEC, and (d) IRW+ETEC. The villus length (e), crypt depth (f), and the ratio of villi length to crypt depth (g); the change in letter denotes a significant difference.

cells, improving metabolic levels and alleviating obesity [15]. Our team focused on adding this active peptide to the host diet, exploring the prevention and treatment of intestinal damage. We explored the impact of colitis by adding IRW and IQW to the diet of a DSS-induced colitis mouse model; research showed that IQW could adjust the amino acid levels in serum and regulate intestinal immune function to relieve inflammation; IQW and IRW could reduce oxidative stress induced by DSS by increasing antioxidant enzyme activity; IQW and IRW achieved this by increasing the diversity of the host's intestinal microorganisms and increasing the probiotic biomass [16, 17]. In view of the IQW and IRW effect in the DSS-induced mouse model, we expect IQW and IRW can perform a similar effect in the ETEC-induced mouse model. In this study, we explore the effects of IQW and IRW on jejunal inflammation in an ETEC-induced mouse model.

2. Materials and Methods

2.1. Experiment Design. The Chinese guidelines for animal welfare were observed for the experimental strategy design. Approval from the Animal Care and Use Committee of Hunan Agricultural University was obtained. In total, 24 male mice (8 weeks, average weight: 23 g) were used in the experiment. All mice were raised at Hunan Agricultural

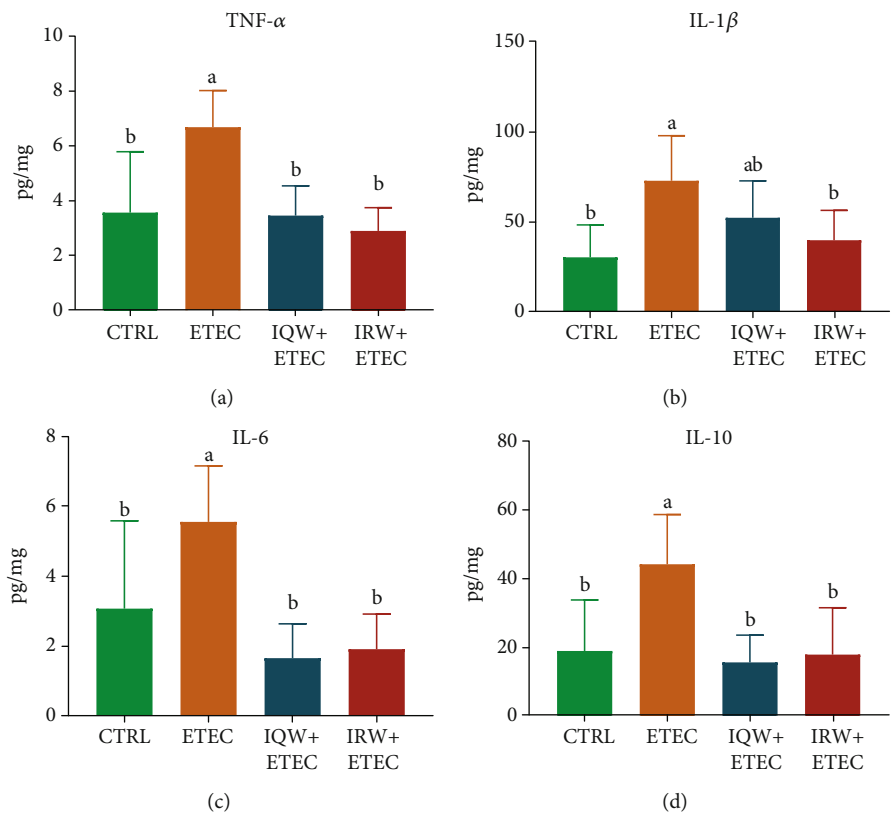

Figure 2: Inflammatory cytokines in the mouse jejunum in each group ($n = 6$): (a) TNF-α, (b) IL-1β, (c) IL-6, and (d) IL-10; the change in letter denotes a significant difference.

University and fed in a comfortable environment (relative humidity: 53%; average temperature: 24 degrees). In order to simulate natural light conditions, the animals were fed under 12 h of light and 12 h without light. In order to alleviate the stress response caused by the environmental change, mice were given a 3-day adaptation period before the experiment. After 3 days, the mice were randomly divided into four groups: (a) control (CTRL) group ($n = 6$), (b) ETEC group ($n = 6$), (c) IQW-ETEC group ($n = 6$), and (d) IRW-ETEC group ($n = 6$). Groups a and b were given basal diet and natural drinking water for the first 7 days. Group a was given 0.1 mL saline in the first 7 days. Group b was given 0.1 mL 5×10^9 CFU/mL ETEC for 7 days. Mice in groups c and d were put on a basal diet of IQW (93.04% purity, 0.03% mass concentration) and 0.03% IRW (87.91% purity; 0.03% mass concentration), respectively. Meanwhile, 0.1 mL ETEC was given to groups c and d 7 days after the first day of the feeding experiment; this lasted for 7 days. At the end of the 15th day of the feeding experiment, all mice fasted for 12 h and were subsequently weighed before being sacrificed. The acute blood loss method is used to collect blood in mice. The jejunal tissues and colon contents were collected after autopsy; all samples were frozen using liquid nitrogen and stored in a -80°C freezer for further experimentation.

2.2. Histological Analysis of the Jejunum. Samples contained different alcohol concentrations (50%, 70%, 80%, 90%, and 95%). For dehydration, a dimethyl benzene ethanol and paraffin (1 : 1) solution was used for the sample embedding processing. The jejunal tissue morphology and tissue damage were analyzed, and the height of intestinal villi and crypt depth were microscope measured using hematoxylin-eosin-stained samples.

2.3. Jejunal Tissue Inflammatory Cytokine Detection. Jejunal TNF-α, IL-1β, IL-6, and IL-10 were detected via enzyme-linked immunosorbent assay (ELISA). Antibodies (anti-TNF-α, IL-1β, IL-6, and IL-10) were added into the polystyrene HRP-plate well after dilution with carbonate-coated buffer (1 : 100) and placed at 4°C for 12 h overnight. The solution was poured out, and the plates were washed with PBS solution three times. The blocking solution was added to each plate well, incubated at 37°C for 1.5 h. After washing the samples three times using PBS solution, they were incubated at 37°C for 1.5 h. Diluted biotinylated antibodies (goat against mice) were added for 30 min at 37°C. TMB (3,3′,5,5′-Tetramethylbenzidine) substrate was added to each reaction well for the color reaction; the reaction lasted 20 min at 37°C. Sulfuric acid was added to each reaction well for the termination reaction. The absorbance of each reaction was measured at 450 nm.

2.4. Microbial Community Analysis. The DNA of colon content samples was extracted, and the purified DNA was used as a template to amplify the variable region of V3+V4 of bacterial 16S rDNA gene by PCR. The PCR products were sent to MicroBio for sequencing analysis. The obtained

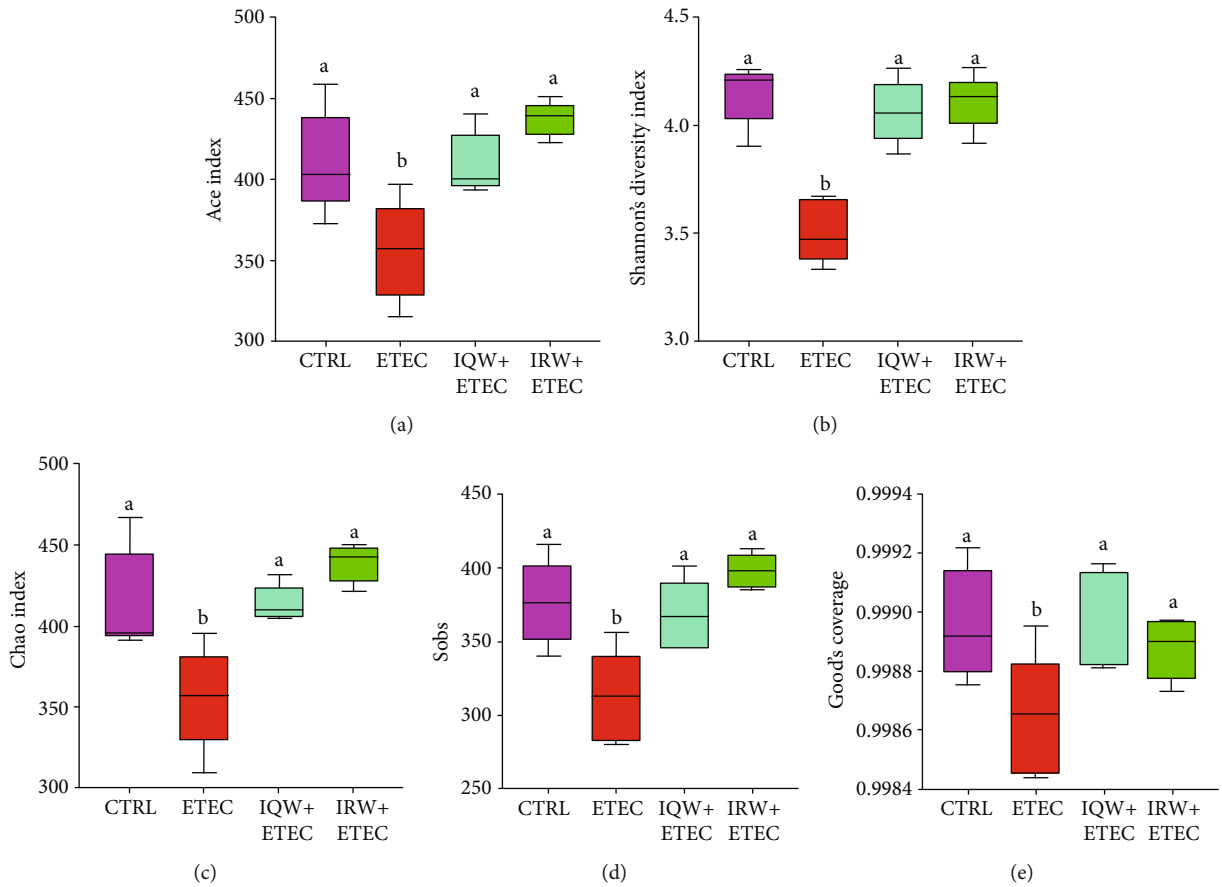

Figure 3: α-Diversity of colon microorganisms of mice in each group ($n = 6$), letter (b) denotes a significant difference: (a) Ace index, (b) Shannon index, (c) Chao index, (d) Sobs index, and (e) coverage index.

sequencing results were optimized for OTU-operational taxonomic unit cluster analysis. Alpha diversity analysis (species richness statistics, such as Chao and Ace, and species diversity statistics, such as Shannon and Simpson) was performed using Mothur (version 1.33.3) software. Microbial Ecology (QIIME) was an open-source tool for analyzing the original sequence. PycGootookit6 software was used to deal with the sequence errors and database redundancy in the original data [18]. The optimal overlapping sequence was found by splicing the original sequence [19]. For each sample, the sequence was analyzed using QIIME and the UPARSE application to determine the operational classification unit (OTUs), and the classification data were assigned to each OTUs using the RDP classifier (version 2.2) [20]. The selected sequence of representatives. RDP classifier and Greengenes database were used for classification. Alpha diversity analysis of the jejunal bacterial community was performed using the abundance-based coverage estimator (ACE), bias-corrected Chao richness estimator, Shannon index, and Good's coverage.

2.5. Data Analysis. The statistical software package (SPSS V16.0) was used for statistical analysis. The one-way ANOVA method was used to analyze significant differences among groups, and the data were represented as mean ± SD. GraphPad Prism 8 was used to make graphs. P values < 0.05 were regarded as significantly different.

3. Results

As shown in Figure 1, compared to the CTRL group, the length of intestinal villi in the ETEC group was significantly decreased ($P < 0.05$), and crypt depth was increased considerably ($P < 0.05$), which indicated that ETEC could cause severe jejunal damage. However, compared to the ETEC group, in the IQW-ETEC and IRW-ETEC groups, the length of intestinal villi increased while the crypt depth decreased ($P < 0.05$), which might indicate that IQW and IRW dramatically improve the status of intestinal injury, improving damage recovery.

As shown in Figure 2, the contents of inflammatory cytokines (TNF-α, IL-1β, IL-6, and IL-10) in the ETEC group were significantly higher than those in the CTRL group. The contents of TNF-α, IL-1β, IL-6, and IL-10 in the IQW-ETEC and IRW-ETEC groups were significantly lower than those in the ETEC group ($P < 0.05$).

Sequencing analysis was from the V3-V4 region of 16S rRNA in collected colon content samples. Figure 3 shows the α-diversity analysis of each group. In the ETEC group, the Ace index, Shannon index, Chao index, Sobs index,

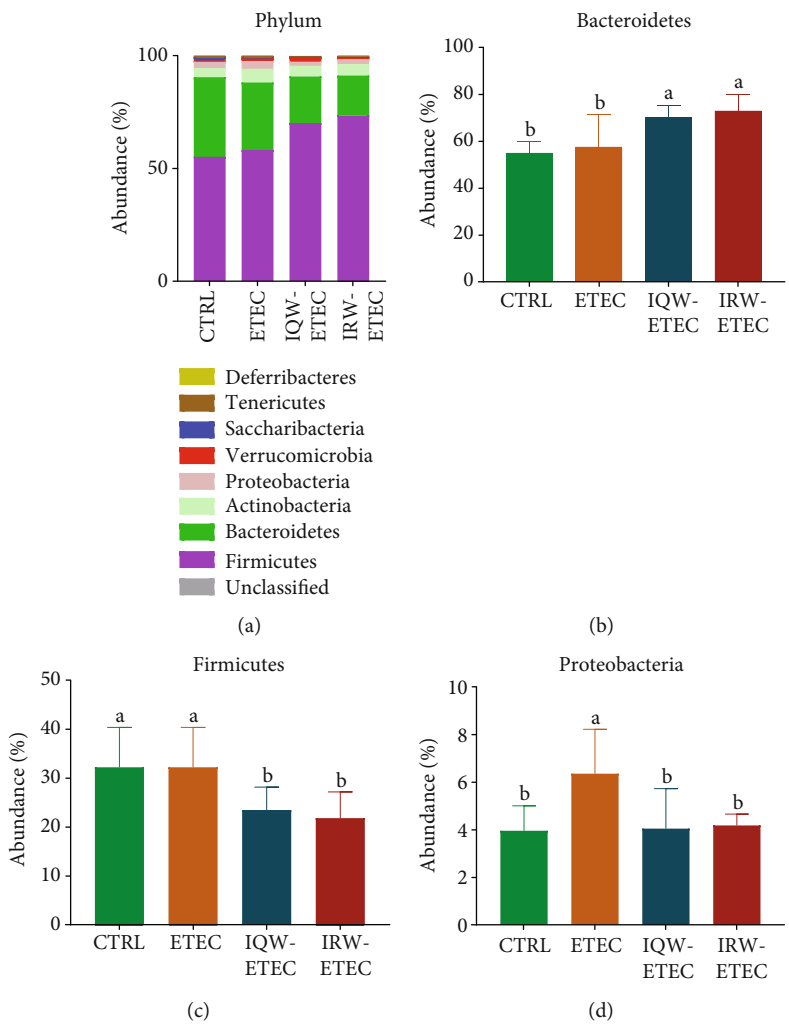

Figure 4: Effect of IQW and IRW treatment on the microorganisms at the phylum level: (a) microbiota of the colon in the four groups at the phylum level ($n = 6$), (b) *Bacteroidetes*, (c) *Firmicutes*, and (d) *Proteobacteria*; the change in letter denotes a significant difference.

and Good's coverage were significantly lower than in the CTRL group. Additionally, compared to the ETEC group, the α-diversity of the IQW-ETEC and IRW-ETEC groups was significantly increased ($P < 0.05$).

Microbiota analysis was conducted on colon content samples; Figure 4(a) shows the relative abundance of collected microorganisms at the phylum level. The abundance of *Bacteroidetes*, *Firmicutes*, and *Proteobacteria* showed advantages in the phylum level. In the CTRL group, the relative abundance of microbiota was *Bacteroidetes* (55.20%), *Firmicutes* (35.33%), and *Proteobacteria* (4.08%). In the IQW-ETEC group, the relative abundance of microbiota was *Bacteroidetes* (58.24%), *Firmicutes* (29.92%), and *Proteobacteria* (6.11%). In the IRW-ETEC group, the relative abundance of microbiota was *Bacteroidetes* (70.21%), *Firmicutes* (20.66%), and *Proteobacteria* (4.77%). In Figure 4(b), IQW and IRW significantly increased the abundance of *Bacteroidetes* compared with the ETEC group ($P < 0.05$). In Figure 4(c), IQW and IRW significantly reduced the abundance of *Firmicutes* in mice compared with the ETEC group ($P < 0.05$). The IRW-ETEC and IQW-ETEC groups were significantly different from the ETEC group ($P < 0.05$), and the proportion of *Firmicutes* in the colon of mice in the IRW-ETEC group also increased to a certain extent. In Figure 4(d), the abundance of *Proteobacteria* in ETEC is significantly higher than in the CTRL group ($P < 0.05$). The abundance of *Proteobacteria* in the IRW-ETEC and IQW-ETEC groups is significantly lower than in the ETEC group ($P < 0.05$).

Figure 5(a) shows the nine classes with the most abundant abundance in colon contents. In the CTRL group, *Bacteroides* (54.95%), *Clostridia* (23.7%), and *Bacilli* (10.7%) were the most abundant. In the ETEC group, *Bacteroidetes* (57.5%), *Clostridium* (12.96%), *Bacillus* (12.99%), and *Erysipelotrichia* (3.95%) were the most abundant groups. In the IQW-ETEC group, *Bacteroidetes* (70.1%), *Clostridium* (11.6%), and *Bacillus* (7.1%) were the largest groups. In the IRW-ETEC group, *Bacteroides* (72.9%), *Clostridium* (9.1%), *Bacillus* (5.4%), and *Erysipelas* (3.0%) were the most abundant groups. The results in Figure 5(b) show that both IQW and IRW treatments increased the abundance of *Bacteroidia* in the intestine of mice, and both groups showed significant differences compared with the ETEC group ($P < 0.05$). At the same time, it can be seen from Figure 5(c) that ETEC treatment significantly

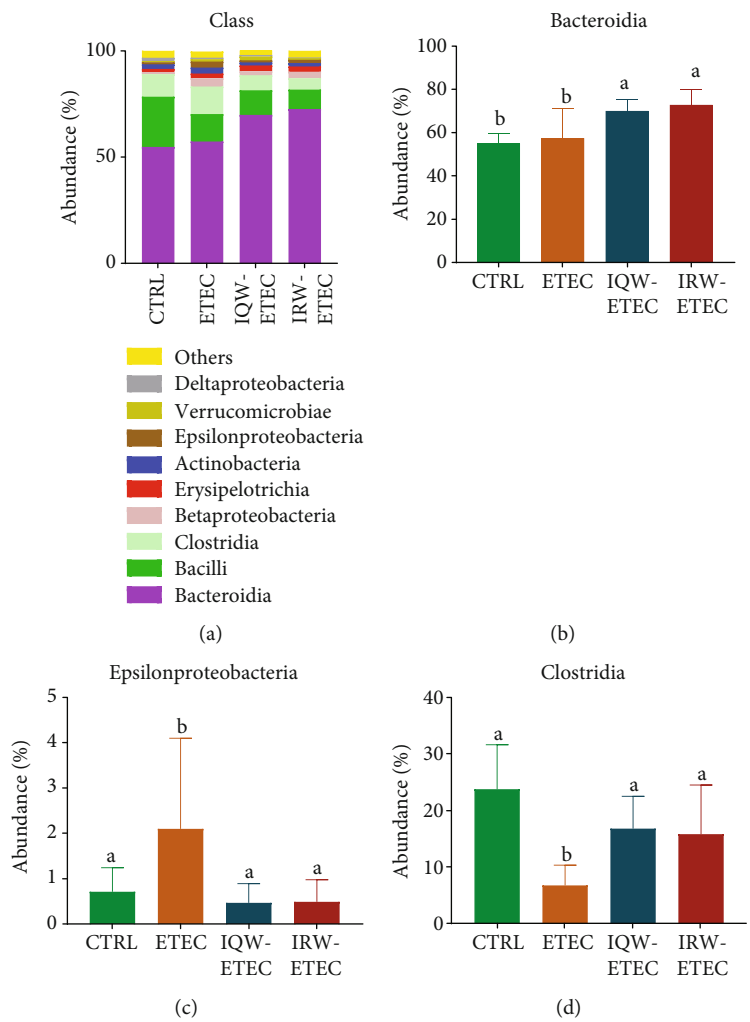

Figure 5: Effect of IQW and IRW treatment on the microorganisms at the class level: (a) microbiota of the colon in the four groups at the class level ($n = 6$), (b) *Bacteroidia*, (c) *Epsilonproteobacteria*, and (d) *Clostridia*; the change in letter denotes a significant difference.

increased the abundance of *Epsilonproteobacteria* ($P < 0.05$). IQW and IRW treatment could significantly reduce the growth of *Epsilonproteobacteria* ($P < 0.05$). In Figure 5(d), the relative abundance of *Clostridia* in the ETEC group is significantly decreased compared to the CTRL group; IQW and IRW significantly increased the abundance of *Clostridia* compared to the ETEC group.

Figure 6 shows the highest abundance of colon contents at the order level (Figure 6(a)). And in the CTRL group, *Bacteroidales* (54.95%), *Clostridiales* (23.7%), *Lactobacillales* (5.78%), and *Bacillales* (4.9%) were the most abundant groups. In the ETEC group, *Bacteroidetes* (57.53%), *Clostridium* (12.96%), *Lactobacillus* (10.3%), and *Erysipelotrichales* (3.95%) were the most abundant groups. In the IQW-ETEC group, *Bacteroidetes* (70.1%), *Clostridium* (11.6%), *Lactobacillus* (3.1%), and *Bacillus* (4.0%) were the most abundant groups. In the IRW-ETEC group, *Bacteroidetes* (72.9%), *Clostridium* (9.12%), and *Lactobacillus* (3.99%) were the largest groups. Figure 6(b) shows that ETEC significantly increases the abundance of *Bacteroidales* ($P < 0.05$). The effects of IQW-ETEC and IRW-ETEC were not significant according to the ETEC group ($P > 0.05$). Figure 6(c) shows the levels of *Clostridiales* in the colon of mice: the group treated with ETEC had significantly decreased amounts compared to the CTRL group ($P < 0.05$); in contrast, the abundance of *Clostridiales* in the IQW-ETEC and IRW-ETEC groups was significantly increased compared to the ETEC group ($P < 0.05$). Thus, the effects of IQW and IRW treatment were effective. Figure 6(d) shows that ETEC can significantly increase the abundance of *Erysipelotrichales* ($P < 0.05$). The addition of IQW and IRW had an obvious trend in reducing the *Erysipelotrichales* content compared with the ETEC group.

At the family level, nine families had the highest abundance (Figure 7(a)). In the CTRL group, *Lachnospiraceae* (12.9%), *Prevotellaceae* (8.1%), and *Bacteroidaceae* (5.6%) were the most abundant microorganisms. *Lactobacillaceae* (5.8%) was the most abundant microorganisms in the ETEC group. *Lachnospiraceae* (6.4%), *Prevotellaceae* (9.1%), *Bacteroidaceae* (8.3%), and *Lactobacillaceae* (7.5%) were the most abundant microorganisms in the IQW-ETEC group. The most abundant microorganisms in the IRW-ETEC group included *Lachnospiraceae* (9.6%), *Prevotellaceae* (6.2%), *Bacteroidaceae* (9.2%), and *Staphylococcaceae*

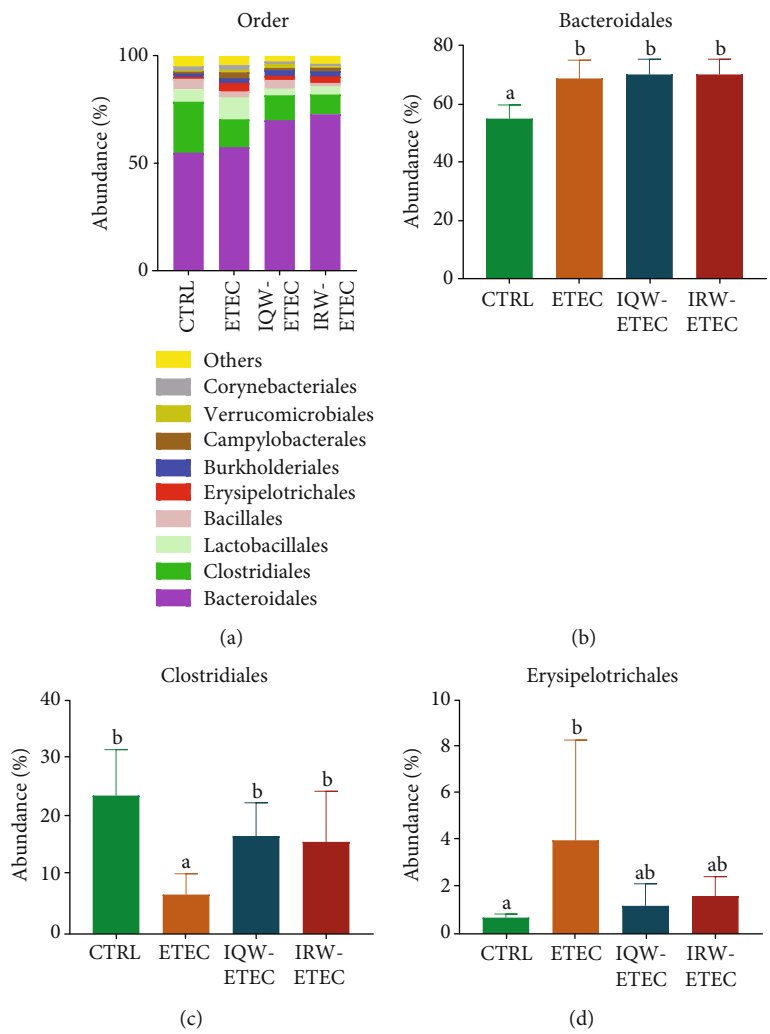

Figure 6: Effect of IQW and IRW treatment on the microorganisms at the order level: (a) microbiota of the colon in the four groups (order level; $n = 6$), (b) *Bacteroidales*, (c) *Clostridiales*, and (d) *Erysipelotrichales*; the change in letter denotes a significant difference.

(3.9%). *Lachnospiraceae* (7.9%), *Prevotellaceae* (7.6%), *Bacteroidaceae* (7.6%), and *Ruminococcaceae* (4.8%) were the most abundant microorganisms in the IQW-ETEC group. It can be concluded from Figure 7(b) that the *Lachnospiraceae* in the ETEC group is significantly lower than in the CTRL and IQW-ETEC groups ($P < 0.05$). However, there was no significant difference between the ETEC and IRW-ETEC groups. There was a clear trend on increasing the abundance of *Lachnospiraceae*. In Figure 7(c), ETEC significantly increases the abundance of *Prevotellaceae* ($P < 0.05$). And the effect of IQW and IRW was effective ($P < 0.05$). In Figure 7(d), the abundance of *Flavobacteriaceae* is significantly increased by ETEC ($P < 0.05$) compared to the CTRL group. There is a significant decrease of *Flavobacteriaceae* in the IQW-ETEC group compared to the ETEC group. However, there is no significant difference between the ETEC group, IRW-ETEC group, and CTRL group, despite the obvious presence of a trend of *Flavobacteriaceae* decrease in the IRW-ETEC group.

At the genus level, nine genera have the highest abundance (Figure 8(a)). In the CTRL group, *Bacteroides* (5.3%), *Alloprevotella* (5.6%), *Lactobacillus* (5.4%), and *Staphylococcus* (4.7%) were the most abundant groups. In the ETEC group, *Bacteroides* (5.3%), *Prevotella* (4.8%), *Lactobacillus* (9.1%), and *Helicobacter* (2.8%) were the most abundant groups. In the IQW-ETEC group, *Bacteroides* (9.96%), *Prevotella* (4.6%), *Lactobacillus* (2.7%), and *Staphylococcus* (3.8%) were the most abundant groups. In the IRW-ETEC group, *Bacteroides* (8.97%), *Prevotella* (6.4%), and *Lactobacillus* (3.4%) were the largest groups. As shown in Figure 8(b), the abundance of *Bacteroides* in intestinal microorganisms was significantly increased by the IQW compared to the ETEC group ($P < 0.05$), and there was still an obvious trend of *Bacteroides* increase in the IRW-ETEC group compared to the ETEC group. Figure 8(c) shows that ETEC significantly increased the abundance of *Helicobacter* compared to the CTRL group ($P < 0.05$), and the IQW and IRW significantly increased the abundance of *Helicobacter* compared to the ETEC group ($P < 0.05$). In Figure 8(d), there is a trend of decreasing abundance of *Alloprevotella* after ETEC treatment; there was also a recovery effect after IQW and IRW treatment.

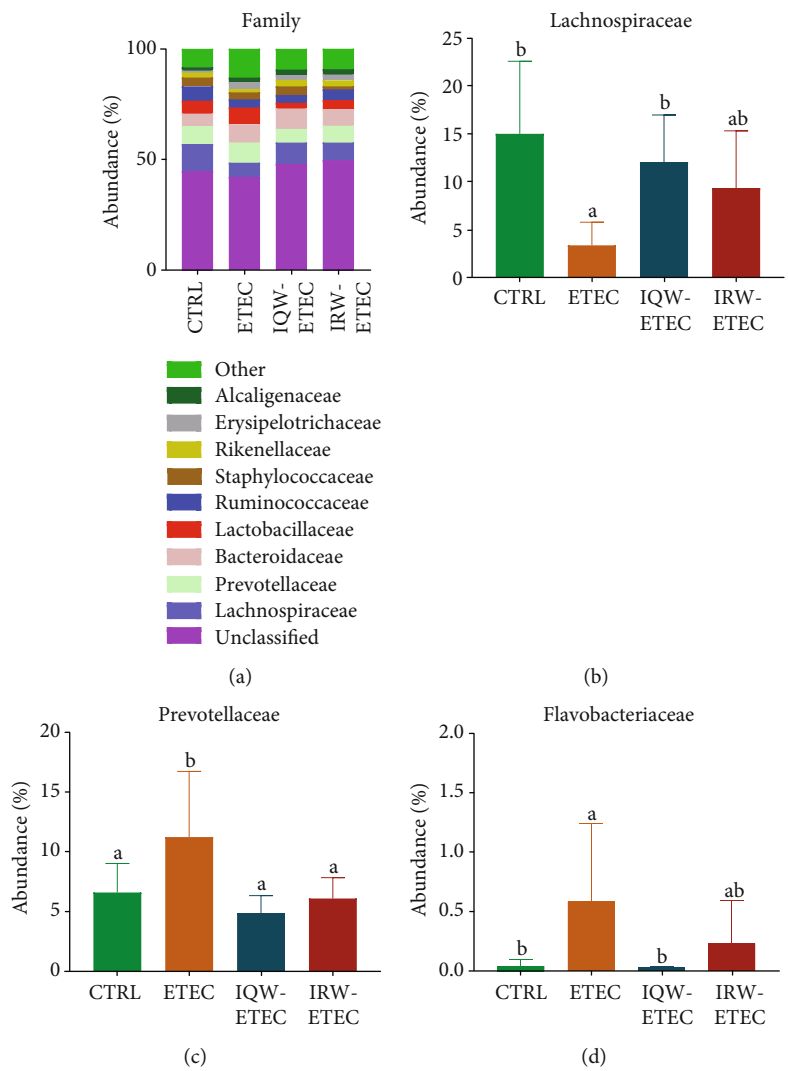

Figure 7: Effect of IQW and IRW treatment on the microorganisms at the family level: (a) microbiota of the colon in the four groups (family level; $n = 6$), (b) content of *Lachnospiraceae*, (c) *Prevotellaceae*, and (d) *Flavobacteriaceae*; the letter change denotes a significant difference.

4. Discussion

The intestinal tract is one of the most important digestive organs in mammals. Equally important, the intestinal tract also plays an important role in immune function [21]. The intestinal tract is a dynamic and complex system; the intestinal microenvironment is the coexistent result of host and microbiota [22, 23]. The intestinal cells have a strong regenerative capability, with damaged cells recovering within 3 days [24]. The intestinal cells are composed of two types of cell lineages: an absorptive (enterocyte) cell lineage and a secretory (exocrine) cell lineage, both of which originate from intestinal stem cells (ISCs) [25]. Active ISCs are the major actuator for damaged intestinal cells; crypts are the storage region of ISCs [26]. Intestinal villus length and crypt depths are the two common evaluation indexes of intestinal inflammation. Studies have shown that intestinal damage can decrease villus height while increasing crypt depth [27]. Our research highlights the ability of ETEC to cause jejunal damage. Notably, IRW and IQW polypeptides can promote jejunal cell recovery.

After infection, ETEC can adhere to intestinal cells and initiate damage via toxins in a short period [28]. Additionally, ETEC, through the MAPK and NF-κB pathways, causes further inflammatory damage [29]. A previous study pointed out that ETEC infection increased the expression of IL-1β, IL-6, TNF-α, IL-17, and IL-18 [30]. Our research also determined that ETEC can significantly increase the expression of TNF-α, IL-1β, IL-6, and IL-10. Moreover, IQW and IRW can significantly alleviate the overexpression of inflammatory cytokines ($P < 0.05$). Accordingly, there is no significant difference between the IQW and IRW groups ($P > 0.05$).

The intestinal microbiota plays an important role in host immunity, digestion, and metabolism and is unique to a specific host body [31]. The mammalian intestinal tract is homeostatically an orderly symbiotic environment; adverse conditions destroy the balance between intestinal microbiota and host [32, 33]. Intestinal inflammation can lead to a

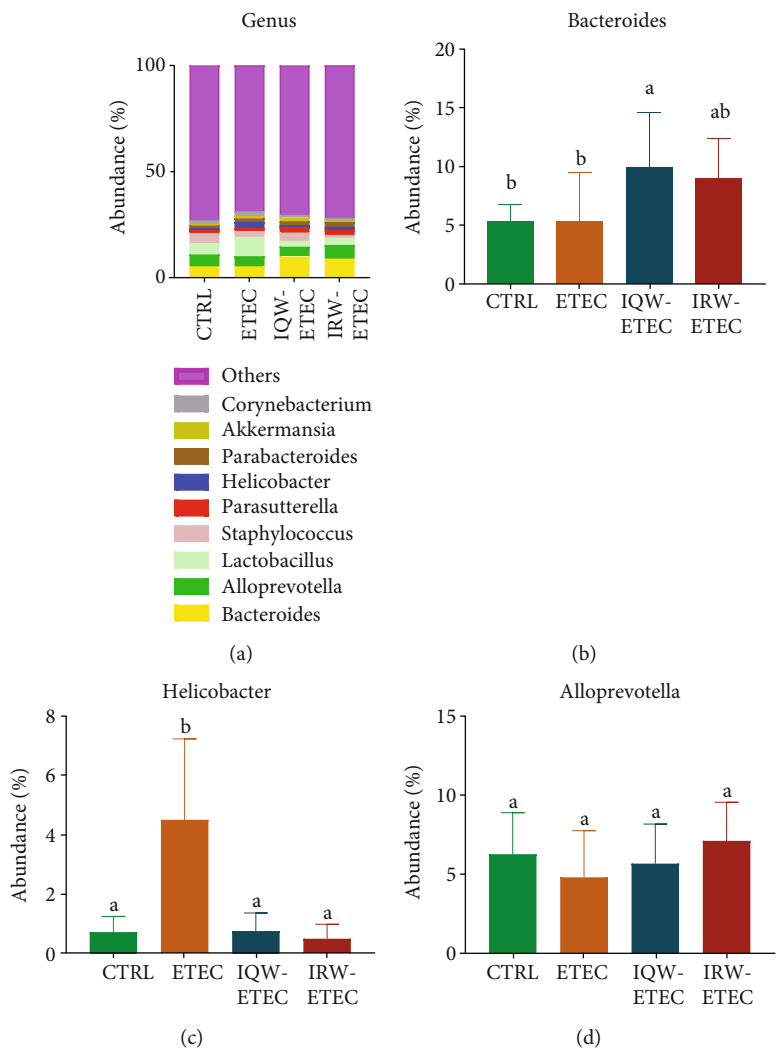

Figure 8: Effect of IQW and IRW treatment on the microorganisms at the genus level: (a) microbiota of the colon in the four groups at the genus level ($n = 6$), (b) *Bacteroides*, (c) *Helicobacter*, and (d) *Alloprevotella*; a letter change denotes a significant difference.

disturbance of host intestinal organisms. A study showed that pathogenic bacterial infections, such as *Salmonella enterica* infection, can cause host intestinal inflammation, reducing intestinal microbiota diversity [34]. Our research points out that in the α-diversity test of the colon intestinal tissue of experimental mice, the microbial community richness in the ETEC group was significantly decreased compared with that in the CTRL group ($P < 0.05$). Figure 4 shows that the microbial abundance in the ETEC group was significantly lower than the CTRL, IQW-ETEC, and IRW-ETEC groups ($P < 0.05$). To a certain extent, IQW and IRW can alleviate the decrease in intestinal microbial microorganisms caused by ETEC.

IQW and IRW are two kinds of polypeptides that possess numerous excellent biological activities. A study revealed that IRW functions by regulating and improving the diversity of the intestinal microbiome of the host [35, 36]; our research confirmed this. IRW and IQW can significantly promote intestinal microbiome recovery. In the IQW-ETEC and IRW-ETEC groups, the Shannon index, Sobs index, Chao index, Ace index, and Good's coverage were significantly higher than in the ETEC group.

ETEC reduced the abundance of *Bacteroidetes*. *Bacteroidetes* are the most common intestinal microbes in the human gut, accounting for roughly 50% of the intestinal microbes in a Western person [37]. Some bacteria in the *Bacteroides* genus, such as *Bacteroides fragilis*, have been shown to prevent and treat intestinal diseases. One study showed that *B. fragilis* could alleviate inflammation in the DSS-induced IBD colitis model in mice and alleviate weight loss caused by IBD and inflammation [38]. Some studies have shown that *Bacteroides* have several probiotic effects, such as promoting the digestion of dietary-fiber polysaccharides and the host immunity [39, 40]. Our experimental results showed that IQW and IRW could facilitate the restoration of the host intestinal microbiome environment, improving the abundance of intestinal probiotics in the host intestinal tract and alleviating the jejunal inflammatory response caused by ETEC. A previous study by our research group revealed that IQW could increase the *Bacteroides*

biomass, and IRW can increase the abundance of *Clostridium* [41]. And our research showed similar results. Another study pointed out that IRW and IQW intake could increase the abundance of *Firmicutes* and *Actinobacteria* and reduce the proportion of *Bacteroidetes* and *Proteobacteria* [42]. ETEC increased the abundance of *Flavobacteriaceae*, e.g., *F. aquatile* and *F. meningosepticum*, which can cause many diseases, including aquatic diseases (shark fin rot and equine back disease) and neonatal meningitis, respectively [43]. *Flavobacteria* infection is also the infectious agent for chronic skin disease and bacterial gill disease in fish [42]. The experimental results demonstrate that the proportion of *Flavobacteriaceae* in the intestines of IQW-treated mice significantly decreased ($P < 0.05$); after IRW treatment, the proportion of intestinal *Flavobacteriaceae* decreased. Studies have pointed out that IQW and IRW can improve the abundance of *Firmicutes*, *Bacteroidetes*, and *Proteobacteria*, increase the *Lactobacillus* and *Bifidobacterium* biomass, and decrease the abundance of *Helicobacter pylori* and *Verrucomicrobia*[43, 44]. Our research shows similar results, with IRW and IQW improving the abundance of probiotics such as *Firmicutes*, *Proteobacteria*, *Clostridiales*, *Lachnospiraceae*, and *Alloprevotella* and decreasing the abundance of pathogenic bacteria such as *Epsilonproteobacteria*, *Erysipelotrichales*, *Prevotellaceae*, and *Flavobacteriaceae*.

5. Conclusions

ETEC can cause jejunal damage, exacerbating the inflammatory reaction. However, IQW and IRW can decrease the expression of inflammatory cytokines, thereby improving the abundance of probiotics such as *Firmicutes*, *Proteobacteria*, *Clostridiales*, *Lachnospiraceae*, and *Alloprevotella* and decreasing the abundance of pathogenic bacteria such as *Epsilonproteobacteria*, *Erysipelotrichales*, *Prevotellaceae*, and *Flavobacteriaceae*.

Data Availability

The data of this study was available at the corresponding author upon reasonable request.

Conflicts of Interest

The authors declare that the research was conducted in the absence of any commercial or financial relationships that could be construed as a potential conflict of interest.

Acknowledgments

This research was supported by the Hunan Provincial Science and Technology Department (2020NK2004, 2019TP2004, 2018WK4025, 2020ZL2004, 2016NK2101, and 2016TP2005), National Natural Science Foundation of China (Nos. 31772642, 31672457, and 41807135), Local Science and Technology Development Project Guided by The Central Government (YDZX20184300002303 and 2018CT5002), China Postdoctoral Science Foundation (2018M632963 and 2019T120705), Scientific Research Fund of Hunan Provincial Education Department (2020JGYB112 and 18B107), Double First-Class Construction Project of Hunan Agricultural University (SYL201802003, YB2018007, and CX20190497), and Natural Science Foundation of Hunan Province, China (No. 2019JJ50220).

References

[1] K. L. Kotloff, J. P. Nataro, W. C. Blackwelder et al., "Burden and aetiology of diarrhoeal disease in infants and young children in developing countries (the Global Enteric Multicenter Study, GEMS): a prospective, case-control study," *Lancet*, vol. 382, no. 9888, pp. 209–222, 2013.

[2] Z. D. Jiang and H. L. DuPont, "Etiology of travellers' diarrhea," *Journal of Travel Medicine*, vol. 24, suppl_1, pp. S13–s16, 2017.

[3] C. Zhang, J. Iqbal, and O. G. Gómez-Duarte, "Murine immunization with CS21 pili or LngA major subunit of enterotoxigenic *Escherichia coli* (ETEC) elicits systemic and mucosal immune responses and inhibits ETEC gut colonization," *Veterinary Microbiology*, vol. 202, pp. 90–100, 2017.

[4] W. Ren, J. Yin, J. Duan et al., "Mouse intestinal innate immune responses altered by enterotoxigenic *Escherichia coli* (ETEC) infection," *Microbes and Infection*, vol. 16, no. 11, pp. 954–961, 2014.

[5] Y. Xu, L. Lahaye, Z. He, J. Zhang, C. Yang, and X. Piao, "Micro-encapsulated essential oils and organic acids combination improves intestinal barrier function, inflammatory responses and microbiota of weaned piglets challenged with enterotoxigenic *Escherichia coli* F4 ($K88^+$)," *Animal Nutrition (Zhongguo xu mu shou yi xue hui)*, vol. 6, no. 3, pp. 269–277, 2020.

[6] C. Wang, X. Chen, Y. Nakamura, C. Yu, and H. Qi, "Fucoxanthin activities motivate its nano/micro-encapsulation for food or nutraceutical application: a review," *Food & Function*, vol. 11, no. 11, pp. 9338–9358, 2020.

[7] X. Y. Dong, M. M. M. Azzam, and X. T. Zou, "Effects of dietary threonine supplementation on intestinal barrier function and gut microbiota of laying hens," *Poultry Science*, vol. 96, no. 10, pp. 3654–3663, 2017.

[8] Y. Liu, W. Liu, Y. Wang et al., "Inhibitory effect of depolymerized sulfated galactans from marine red algae on the growth and adhesion of diarrheagenic Escherichia coli," *Marine Drugs*, vol. 17, no. 12, p. 694, 2019.

[9] W. Liao, S. Chakrabarti, S. T. Davidge, and J. Wu, "Modulatory effects of egg white ovotransferrin-derived tripeptide IRW (Ile-Arg-Trp) on vascular smooth muscle cells against angiotensin II stimulation," *Journal of Agricultural and Food Chemistry*, vol. 64, pp. 7342–7347, 2016.

[10] W. Liao, H. Fan, S. T. Davidge, and J. Wu, "Egg white-derived antihypertensive peptide IRW (Ile-Arg-Trp) reduces blood pressure in spontaneously hypertensive rats via the ACE2/Ang (1-7)/mas receptor axis," *Molecular Nutrition & Food Research*, vol. 63, article e1900063, 2019.

[11] K. Majumder, G. Liang, Y. Chen, L. Guan, S. T. Davidge, and J. Wu, "Egg ovotransferrin-derived ACE inhibitory peptide IRW increases ACE2 but decreases proinflammatory genes expression in mesenteric artery of spontaneously hypertensive rats," *Molecular Nutrition & Food Research*, vol. 59, pp. 1735–1744, 2015.

[12] Q. Xu, H. Fan, W. Yu, H. Hong, and J. Wu, "Transport study of egg-derived antihypertensive peptides (LKP and IQW) using

Caco-2 and HT29 coculture monolayers," *Journal of Agricultural and Food Chemistry*, vol. 65, no. 34, pp. 7406–7414, 2017.

[13] C. Grootaert, B. Matthijs, S. Voorspoels, S. Possemiers, G. Smagghe, and J. Van Camp, "Egg-derived bioactive peptides with ACE-inhibitory properties: a literature update," *Food & Function*, vol. 8, no. 11, pp. 3847–3855, 2017.

[14] M. Son, C. B. Chan, and J. Wu, "Egg white ovotransferrin-derived ACE inhibitory peptide ameliorates angiotensin II-stimulated insulin resistance in skeletal muscle cells," *Molecular Nutrition & Food Research*, vol. 62, no. 4, 2018.

[15] K. Majumder, S. Chakrabarti, S. T. Davidge, and J. Wu, "Structure and activity study of egg protein ovotransferrin derived peptides (IRW and IQW) on endothelial inflammatory response and oxidative stress," *Journal of Agricultural and Food Chemistry*, vol. 61, no. 9, pp. 2120–2129, 2013.

[16] K. S. Bhullar, M. Son, E. Kerek et al., "Tripeptide IRW upregulates NAMPT protein levels in cells and obese C57BL/6J mice," *Journal of Agricultural and Food Chemistry*, vol. 69, no. 5, pp. 1555–1566, 2021.

[17] Y. Ma, H. Jiang, J. Fang, and G. Liu, "IRW and IQW reduce colitis-associated cancer risk by alleviating DSS-induced colonic inflammation," *BioMed Research International*, vol. 2019, Article ID 6429845, 9 pages, 2019.

[18] G. Liu, W. Yan, S. Ding et al., "Effects of IRW and IQW on oxidative stress and gut microbiota in dextran sodium sulfate-induced colitis," *Cellular Physiology and Biochemistry: International Journal of Experimental Cellular Physiology, Biochemistry, and Pharmacology*, vol. 51, no. 1, pp. 441–451, 2018.

[19] J. G. Caporaso, J. Kuczynski, J. Stombaugh et al., "QIIME allows analysis of high-throughput community sequencing data," *Nature Methods*, vol. 7, no. 5, pp. 335-336, 2010.

[20] T. Magoč and S. L. Salzberg, "FLASH: fast length adjustment of short reads to improve genome assemblies," *Bioinformatics (Oxford, England)*, vol. 27, no. 21, pp. 2957–2963, 2011.

[21] S. M. Huse, D. B. Mark Welch, A. Voorhis et al., "VAMPS: a website for visualization and analysis of microbial population structures," *BMC Bioinformatics*, vol. 15, no. 1, 2014.

[22] A. M. O'Hara and F. Shanahan, "The gut flora as a forgotten organ," *EMBO Reports*, vol. 7, no. 7, pp. 688–693, 2006.

[23] C. L. Maynard, C. O. Elson, R. D. Hatton, and C. T. Weaver, "Reciprocal interactions of the intestinal microbiota and immune system," *Nature*, vol. 489, no. 7415, pp. 231–241, 2012.

[24] S. H. Jeurissen, F. Lewis, J. D. van der Klis, Z. Mroz, J. M. Rebel, and A. A. ter Huurne, "Parameters and techniques to determine intestinal health of poultry as constituted by immunity, integrity, and functionality," *Current Issues in Intestinal Microbiology*, vol. 3, no. 1, pp. 1–14, 2002.

[25] L. Weichselbaum and O. D. Klein, "The intestinal epithelial response to damage," *Science China. Life Sciences*, vol. 61, no. 10, pp. 1205–1211, 2018.

[26] L. Lu, W. Li, L. Chen et al., "Radiation-induced intestinal damage: latest molecular and clinical developments," *Future Oncology*, vol. 15, no. 35, pp. 4105–4118, 2019.

[27] S. Ding, Y. Ma, G. Liu, W. Yan, H. Jiang, and J. Fang, "Lactobacillus brevis alleviates DSS-induced colitis by reprogramming intestinal microbiota and influencing serum metabolome in murine model," *Frontiers in Physiology*, vol. 10, p. 1152, 2019.

[28] P. Ondrackova, P. Alexa, J. Matiasovic, J. Volf, and M. Faldyna, "Interaction of porcine neutrophils with different strains of enterotoxigenic *Escherichia coli*," *Veterinary Microbiology*, vol. 160, no. 1-2, pp. 108–116, 2012.

[29] G. Zanello, M. Berri, J. Dupont et al., "Saccharomyces cerevisiae modulates immune gene expressions and inhibits ETEC-mediated ERK1/2 and p38 signaling pathways in intestinal epithelial cells," *PLoS One*, vol. 6, no. 4, article e18573, 2011.

[30] S. Messori, P. Trevisi, A. Simongiovanni, D. Priori, and P. Bosi, "Effect of susceptibility to enterotoxigenic *Escherichia coli* F4 and of dietary tryptophan on gut microbiota diversity observed in healthy young pigs," *Veterinary Microbiology*, vol. 162, no. 1, pp. 173–179, 2013.

[31] R. L. Brown, R. P. Sequeira, and T. B. Clarke, "The microbiota protects against respiratory infection via GM-CSF signaling," *Nature Communications*, vol. 8, no. 1, p. 1512, 2017.

[32] P. Videnska, F. Sisak, H. Havlickova, M. Faldynova, and I. Rychlik, "Influence of Salmonella enterica serovar Enteritidis infection on the composition of chicken cecal microbiota," *BMC Veterinary Research*, vol. 9, no. 1, p. 140, 2013.

[33] H. Jiao, Q. Zhang, Y. Lin, Y. Gao, and P. Zhang, "The ovotransferrin-derived peptide IRW attenuates lipopolysaccharide-induced inflammatory responses," *BioMed Research International*, vol. 2019, Article ID 8676410, 7 pages, 2019.

[34] W. Zhu, L. Ren, L. Zhang, Q. Qiao, M. Z. Farooq, and Q. Xu, "The potential of food protein-derived bioactive peptides against chronic intestinal inflammation," *Mediators of Inflammation*, vol. 2020, Article ID 6817156, 15 pages, 2020.

[35] A. N. Jacobson, B. P. Choudhury, M. A. Fischbach, Y. Tang, and P. Dorrestein, "The biosynthesis of lipooligosaccharide fromBacteroides thetaiotaomicron," *mBio*, vol. 9, no. 2, 2018.

[36] M. Delday, I. Mulder, E. T. Logan, and G. Grant, "Bacteroides thetaiotaomicron ameliorates colon inflammation in preclinical models of Crohn's disease," *Inflammatory Bowel Diseases*, vol. 25, no. 1, pp. 85–96, 2019.

[37] N. T. Porter, A. S. Luis, and E. C. Martens, "_Bacteroides thetaiotaomicron_," *Trends in Microbiology*, vol. 26, no. 11, pp. 966-967, 2018.

[38] D. Ndeh, A. Baslé, H. Strahl et al., "Author Correction: Metabolism of multiple glycosaminoglycans by *Bacteroides thetaiotaomicron* is orchestrated by a versatile core genetic locus," *Nature Communications*, vol. 11, no. 1, p. 4396, 2020.

[39] Y. Ma, S. Ding, G. Liu et al., "Egg protein transferrin-derived peptides IRW and IQW regulate Citrobacter rodentium-induced," *Inflammation-Related Microbial and Metabolomic Profiles. Frontiers in microbiology*, vol. 10, p. 643, 2019.

[40] E. Gómez, J. Méndez, D. Cascales, and J. A. Guijarro, "Flavobacterium psychrophilum vaccine development: a difficult task," *Microbial Biotechnology*, vol. 7, no. 5, pp. 414–423, 2014.

[41] F. A. Sebastião, D. Nomura, R. Sakabe, and F. Pilarski, "Hematology and productive performance of nile tilapia (Oreochromis niloticus) naturally infected with Flavobacterium columnare," *Brazilian Journal of Microbiology: [publication of the Brazilian Society for Microbiology]*, vol. 42, no. 1, pp. 282–289, 2011.

[42] S. S. Jean, W. S. Lee, F. L. Chen, T. Y. Ou, and P. R. Hsueh, "*Elizabethkingia meningoseptica* : an important emerging pathogen causing healthcare-associated infections," *The Journal of Hospital Infection*, vol. 86, no. 4, pp. 244–249, 2014.

[43] G. Liu, Y. Ma, Q. Yang, and S. Deng, "Modulation of inflammatory response and gut microbiota in ankylosing spondylitis mouse model by bioactive peptide IQW," *Journal of Applied Microbiology*, vol. 128, no. 6, pp. 1669–1677, 2020.

[44] Y. Ma, S. Ding, G. Liu et al., "Egg protein transferrin-derived peptides IRW and IQW regulate Citrobacter rodentium-induced, inflammation-related microbial and metabolomic profiles," *Frontiers in Microbiology*, vol. 10, 2019.

Hindawi
Mediators of Inflammation
Volume 2021, Article ID 8698923, 6 pages
https://doi.org/10.1155/2021/8698923

Research Article

The Role of Heart Rate, Body Temperature, and Respiratory Rate in Predicting Anastomotic Leakage following Surgery for Rectal Cancer

Jiajun Luo, Hongxue Wu, Yue Jiang, Yu Yang, Jingwen Yuan, and Qiang Tong

Department of Gastrointestinal Surgery I Section, Renmin Hospital of Wuhan University, Wuhan 430060, China

Correspondence should be addressed to Qiang Tong; qiangtong@whu.edu.cn

Received 28 June 2021; Accepted 6 August 2021; Published 19 August 2021

Academic Editor: Deguang Song

Objective. To explore the value of the heart rate, body temperature, and respiratory rate in the early prediction of anastomotic leakage after rectal cancer surgery. *Methods*. Clinical data from patients with rectal cancer who underwent anterior rectal resection in the Department of Gastroenterology, Renmin Hospital of Wuhan University, from January 2017 to December 2019 were collected and analyzed retrospectively. Based on the occurrence of anastomotic leakage after surgery, the patients were divided into two groups: those with and without anastomotic leakage. The quantitative values of the heart rate, body temperature, and respiration rate at day 7 postsurgery were compared between the two groups. The ROC curve was used to analyze their role in the early prediction of anastomotic leakage. *Results*. Among 441 patients with rectal cancer, 30 (6.81%) had clinical anastomotic leakage and were diagnosed at 7 ± 3 days postsurgery. Within 7 days postsurgery, the heart rate, body temperature, and respiratory rate in the anastomotic leakage group were higher than those in the nonanastomotic leakage group. The differences in heart rate (1-5 d), body temperature (2-7 d), and respiratory rate (1-7 d) were statistically significant ($P < 0.05$). The three ROC curves were drawn, respectively. The predictive value of the heart rate is greatest at days 2-3 postsurgery. The predictive value of the body temperature is greatest at days 4-6 postsurgery. The predictive value of the respiratory rate is best at days 1-4 postsurgery. *Conclusion*. The changes of vital signs (heart rate, body temperature, and respiratory rate) have a certain value in the early prediction of anastomotic leakage after rectal cancer surgery. Observation of postoperative vital signs at 7 days postsurgery is helpful for the early diagnosis of anastomotic leakage.

1. Introduction

Colorectal cancer is the third most common malignant tumor in the world and has the second highest mortality rate [1]. Surgery has long been considered the main treatment for colorectal cancer [2]. Anastomotic leakage is a major postoperative complication following colorectal surgery, and it is often associated with poor surgical outcomes [3]. Rectal cancer accounts for approximately 30% of colorectal cancer cases [4], and rectal surgery has a higher incidence of postoperative anastomotic leakage than colon surgery [5]. Anastomotic leakage after rectal surgery may adversely affect the morbidity, mortality, and prognosis of patients [6, 7]. Even with increased surgical proficiency, meticulous management of patients, and active attempts to avoid the occurrence of anastomotic leakage, the incidence of anastomotic leakage has not changed significantly [8]. Nowadays, due to the popularization of the enhanced recovery after surgery (ERAS) concept [9], the early diagnosis of anastomotic leakage is particularly important. For instance, early diagnosis can be used as a criterion for whether patients can be discharged early, which helps reduce the length of hospitalization and hospitalization costs for low-risk patients. This article is aimed at exploring the correlation of vital signs to the early prediction of

anastomotic leakage following rectal cancer surgery by comparing the heart rate, body temperature, and respiratory rate within 7 days postsurgery.

2. Materials and Methods

This was a retrospective, single-center cohort study. We retrospectively analyzed the clinical data of patients undergoing anterior rectal resection for rectal cancer in the Department of Gastrointestinal Surgery of Renmin Hospital of Wuhan University from January 2017 to December 2019. This study was approved by the Ethics Committee of Renmin Hospital of Wuhan University.

2.1. Inclusion Criteria. All patients met the following requirements: (1) at least 18 years old; (2) the preoperative pathological diagnosis was confirmed to be rectal cancer, and the lower edge of the tumor was judged by colonoscopy or other examinations to be less than 15 cm from the anal margin; (3) the primary anastomosis is performed with anterior rectal resection; and (4) postoperative pathology confirms that the tumor was completely removed.

2.2. Exclusion Criteria. The patients who did not meet the inclusion criteria or meet the following characteristics were excluded: (1) palliative, Hartmann, or Miles surgery; (2) serious infection other than that caused by an anastomotic leak after the operation; (3) use of immunosuppressive drugs before surgery; (4) history of other malignancies; and (5) incomplete patient clinical data.

2.3. Diagnostic Criteria and Classification of Anastomotic Leakage. Diagnostic criteria are as follows: (1) the abdominal drainage tube drains out turbid pus-like or fecal-like matter, (2) the abdominal drainage tube has a sudden increase in drainage fluid or drainage of gas, (3) digital rectal examination reaches the stoma site defect, and (4) persistent fever, peritonitis, and reoperation found anastomotic defect.

The following are according to the 2010 International Study Group of Rectal Cancer (ISREC) definition and classification of anastomotic leakage after anterior rectal resection [10]: (1) grade A: subclinical anastomotic leakage, no clinical symptoms, and required no active therapeutic intervention; (2) grade B: manifested as abdominal pain; fever; purulent or scum-like drainage from the anus, drainage tube, or vagina; and white blood cells and C-reactive protein increased and required active therapeutic intervention but manageable without relaparotomy; and (3) grade C: manifested as peritonitis, sepsis, and other clinical manifestations of grade B anastomotic leakage and required relaparotomy.

2.4. Statistical Analysis. Statistical analyses were performed using SPSS Statistics 22.0 software and GraphPad Prism 8 v8.0.1. Data are presented as means ± standard error and were analyzed using Student's t test. Count data were expressed as percentages and were analyzed using x^2 Fisher's test. The receiver operating curve (ROC) was used to evaluate the predictive effects of the postoperative heart rate, body temperature, and respiratory rate on anastomotic leakage after rectal cancer surgery.

3. Results

3.1. Population. A total of 441 patients with rectal cancer were included in the study according to the inclusion and exclusion criteria. All of them survived rectal surgery and were divided into two groups according to whether or not an anastomotic leakage occurred after the surgery.

Thirty-three patients (7.48%) had postoperative anastomotic leakage, which was diagnosed within 7 ± 3 days after the surgery. Among them, three cases (9.10%) were grade A leakage, fifteen cases were grade B leakage (45.45%), and fifteen cases (45.45%) were grade C leakage. The thirty patients with grade B and C leakage were regarded as the anastomotic leakage group. Characteristics of the patients are shown in Table 1. The postoperative hospital stay in the anastomotic leakage group was significantly longer than that in the nonanastomotic leakage group. Gender, diabetes mellitus, neoadjuvant CRT, albumin, and tumor distance from the anal margin were statistically significant in comparison between the two groups, while differences between the groups in the remaining assessed factors were not statistically significant.

3.2. Postoperative Trend of Heart Rate, Body Temperature, and Respiratory Rate. The heart rate of the patients with anastomotic leakage was higher than those without leakage within 7 days postsurgery, and it was statistically significant within 1 to 5 days. From postsurgery day 2 onwards, the heart rate showed an overall downward trend, as shown in Figure 1(a).

The body temperature of patients with anastomotic leakage within 7 days after surgery was higher than those without anastomotic leakage, and it was statistically significant at days 2-7 postsurgery. The overall postoperative trend was a decrease in the body temperature, as shown in Figure 1(b).

The respiratory rate of patients with anastomotic leakage within 7 days after surgery was higher than those without anastomotic leakage, and it was statistically significant from 1-7 days postsurgery. The overall postoperative trend showed a downward trend in respiratory rate, as shown in Figure 1(c).

3.3. Predictive Effect of Postoperative Heart Rate, Body Temperature, and Respiratory Rate. The postoperative heart rate, body temperature, and respiratory rate were drawn with ROC curves, as shown in Figure 2.

The area under the heart rate curve from 1 to 5 days after surgery was 0.73, 0.81, 0.81, 0.75, and 0.78, respectively, as shown in Figure 2(a). The prediction effect was best on days 2-3 postsurgery. The area under the curve was the largest on postsurgery day 2. When the heart rate was greater than 89 bpm, the sensitivity was 62.5% and the specificity was 89.2%.

The area under the body temperature curve from 2 to 7 days after surgery was 0.71, 0.72, 0.78, 0.77, 0.79, and 0.58, respectively, as shown in Figure 2(b). The prediction effect is best on days 4-6 postsurgery. The area under the curve was the largest on postsurgery day 6. When the body temperature is greater than 37°C, the sensitivity is 62.5% and the specificity is 85.3%.

Table 1: Demographic and clinical data.

Parameter	Leak ($n = 30$)	No leak ($n = 408$)	P value
Gender (M (%))	23 (76.7)	222 (54.4)	0.018
Age (≥60 y, n (%))	24 (80.0)	273 (66.9)	0.139
Diabetes (n (%))	9 (30.0)	24 (5.88)	0.001
Cardiovascular disease (n (%))	8 (26.7)	84 (20.6)	0.430
BMI (≥25 kg/m^2, n (%))	20 (66.6)	255 (62.5)	0.648
ASA score (3~4, n (%))	8 (26.7)	132 (32.4)	0.519
Hb (≤110 g/L, n (%))	5 (16.6)	60 (14.7)	0.770
ALB (≤35 g/L, n (%))	6 (20.0)	30 (7.35)	0.015
Surgical method (laparoscopy, n (%))	28 (93.3)	387 (94.9)	0.719
Prophylactic ileostomy (n (%))	9 (30.0)	118 (28.9)	0.900
Tumor distance from anal verge (≤5 cm, n (%))	13 (43.3)	96 (23.5)	0.015
Neoadjuvant CRT (n (%))	11 (36.6)	42 (10.3)	0.001
TNM stage (III~IV, n (%))	16 (53.3)	186 (45.9)	0.411
Tumor diameter (≥3 cm, n (%))	25 (83.3)	270 (66.2)	0.053
Postoperative hospital stay (days, $x \pm s$)	24.5 ± 5.5	11.2 ± 4.1	0.001

Note: M: male; BMI: body mass index; ASA: American Society of Anesthesiologists; Hb: hemoglobin; ALB: albumin; CRT: chemoradiotherapy; TNM: tumor node metastasis.

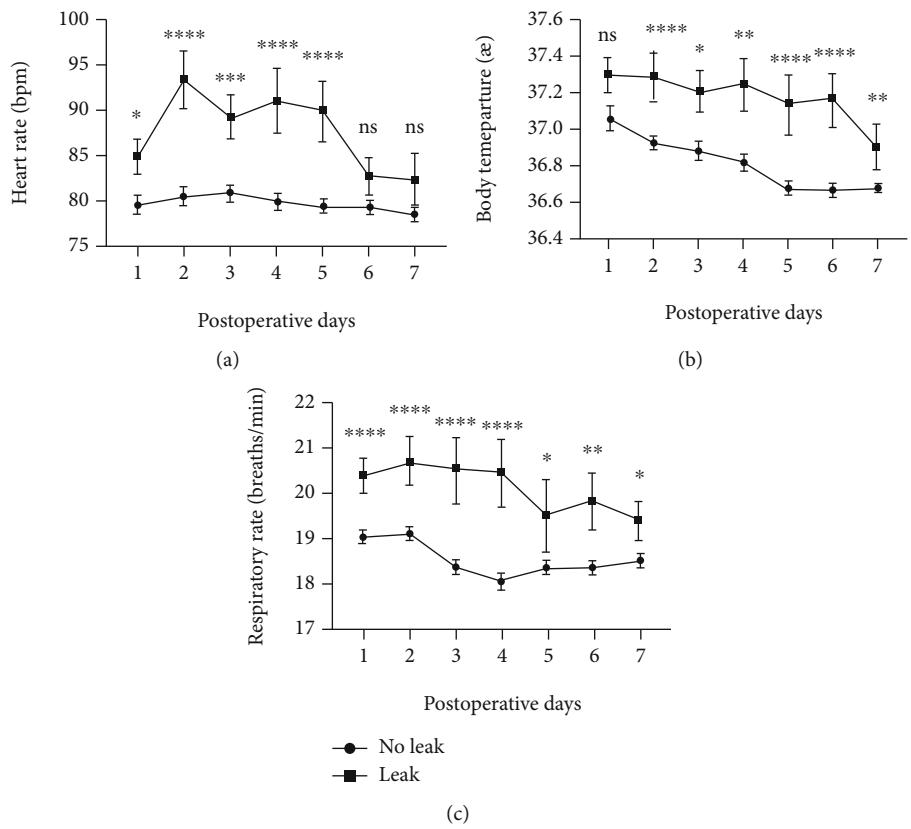

Figure 1: Mean levels of heart rate (a), body temperature (b), and respiratory rate (c) and relative error bars on days 1-7 after surgery.

The area under the respiratory rate curve from 1 to 7 days after surgery was 0.78, 0.78, 0.79, 0.78, 0.59, 0.67, and 0.64, respectively, as shown in Figure 2(c). The prediction effect is best on days 1-4 postsurgery. The area under the curve was the largest on postsurgery day 3. When the respiratory rate is greater than 20 breaths/min, the sensitivity is 62.5% and the specificity is 76.9%.

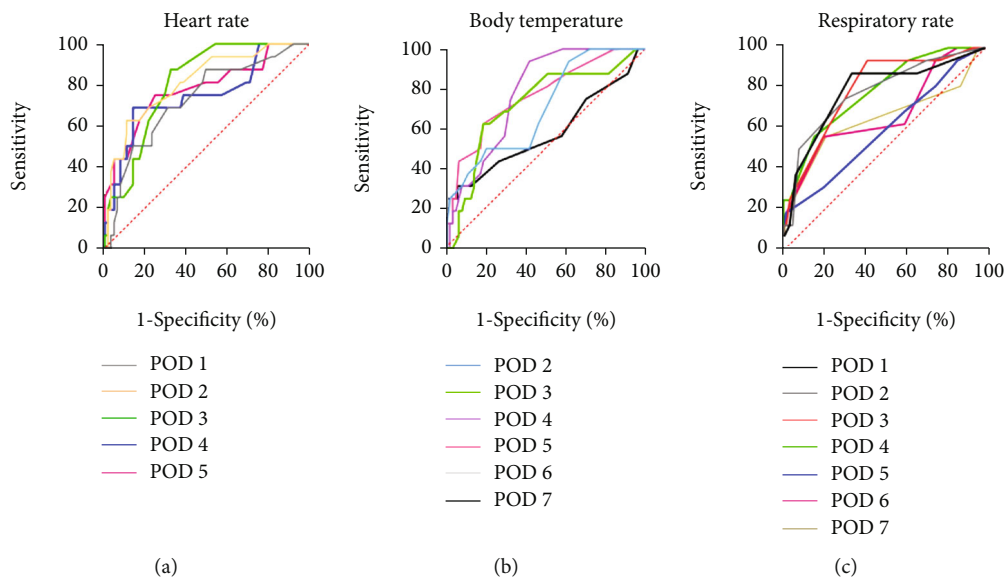

Figure 2: ROC curve analysis for heart rate (a), body temperature (b), and respiratory rate (c).

4. Discussion

Although the surgical techniques for colorectal cancer continue to advance, the incidence of postoperative anastomotic leakage has not been significantly reduced. According to reports in the literature, the incidence of anastomotic leakage after rectal surgery ranges from 3.1% to 13.7% [11]. In our study, the incidence of anastomotic leakage after radical resection of rectal cancer was 7.48%, which was consistent with reports in the literature. The average length of stay for patients with anastomotic leakage in this study was significantly higher than for those without anastomotic leakage. The occurrence of anastomotic leakage prolonged the patient's hospital stay and increased the economic burden on patients. The concept of ERAS has been gradually and steadily implemented in clinical practice, reducing hospitalization time, expenses, and psychological burden for most patients. However, there are also certain risks that may require patients with anastomotic leakage to undergo a second hospitalization or develop serious complications after discharge. Existing studies have reported many risk factors for anastomotic leakage, such as male gender, neoadjuvant CRT, anastomotic position, diabetes, and low albumin [12]. From the clinical data statistically compared in our study, male gender, diabetes, neoadjuvant therapy, low albumin, and distance from the anal margin ≤ 5 cm are all statistically significant risk factors for anastomotic leakage. In some studies, high BMI, low hemoglobin, large tumor diameter, and late pathological stage are also considered risk factors for anastomotic leakage, but in our study, these factors were not statistically significant. Numerous risk factors do not facilitate accurate prediction of the potential for anastomotic leakage after rectal surgery. Therefore, it is extremely urgent to develop diagnostic tools for early screening and the detection of anastomotic leakage in patients following rectal surgery. Diagnostic imaging and digital rectal examination are recognized procedures for the diagnosis of anastomotic leakage, but early diagnosis cannot be achieved. Many other laboratory tests such as C-reactive protein (CPR) [13], procalcitonin (PCT) [14], white blood cell (WBC) counts [15], and ascites cytokine [16] detection methods are currently under extensive research, but all still have their shortcomings. Other methods [17–19] that have been investigated have problems such as insufficient evidence or more complicated implementation. There is still no accepted method for the early diagnosis of anastomotic leakage in clinical practice.

Vital signs are the most accessible and noninvasive indicators, but their value in the early diagnosis of anastomotic leakage is still controversial in the current research [20]. Erb et al. [21] propose that abnormal vital signs such as fever and tachycardia are very common after rectal cancer surgery and are of no value for the early diagnosis of anastomotic leakage. In their study, abnormal vital signs were defined. They compared abnormal vital signs between patients with and without anastomotic leakage and concluded they showed no obvious predictive value. The study by Twohig et al. [22] found that 96.8% of patients had at least one abnormal vital sign after surgery, a common manifestation following surgery. A single vital sign alone cannot independently predict postoperative anastomotic leakage. However, our study found that not all patients exhibit abnormal vital signs following surgery. Patients with postoperative anastomotic leakage may have relatively slight changes in early vital signs compared with patients without anastomotic leakage. Stearns et al. [23] reported that changes in vital signs appeared early after surgery; more specifically, the heart rate, body temperature, and respiratory rate of patients with anastomotic leakage began to change 2 to 3 days after surgery. In our study, the heart rate and respiratory rate of patients with anastomotic leakage began to change from the first day after surgery, which may indicate the hemodynamic changes in the early stage of anastomotic leakage, and the body temperature began to change on day 2 postsurgery, which is consistent with other reports. Postoperative monitoring of vital signs

is commonplace in clinical protocols. Compared with other laboratory and imaging tests, monitoring of vital signs has obvious advantages in the ease of acquisition but lacks diagnostic accuracy. For patients with abnormal vital signs, other relevant laboratory and imaging tests can be performed to confirm the diagnosis, so as to avoid the possibility of anastomotic leakage in patients who were not adequately monitored after early discharge and therefore susceptible to poor postoperative outcomes.

5. Conclusion

In conclusion, changes in postoperative vital signs have value for the early prediction of anastomotic leakage after rectal cancer surgery. Close observation of the patient's vital signs within 7 days after surgery is beneficial for the early diagnosis of anastomotic leakage.

Data Availability

All data used and analyzed during the current study are available from the corresponding authors on reasonable request.

Conflicts of Interest

The authors declare that the research was conducted in the absence of any commercial or financial relationships that could be construed as a potential conflict of interest.

Authors' Contributions

Qiang Tong designed the study, interpreted the results, and wrote the manuscript. Jiajun Luo, Hongxue Wu, Yu Yang, Yue Jiang, and Jingwen Yuan performed the experiments. All authors read and approved the final manuscript. Jiajun Luo and Hongxue Wu contributed equally to this work.

Acknowledgments

This work was supported by the National Natural Science Foundation of China No. 81172186 (QT), by the Natural Science Foundation of Hubei Province No. 2018CFB504 (QT), by the Guidance Foundation of Renmin Hospital of Wuhan University No. RMYD2018M67 (QT), and by the Hubei Province Health and Family Planning Scientific Research Project No. WJ2019M200 (HXW).

References

[1] H. Sung, J. Ferlay, R. L. Siegel et al., "Global cancer statistics 2020: GLOBOCAN estimates of incidence and mortality worldwide for 36 cancers in 185 countries," *CA: a Cancer Journal for Clinicians*, vol. 71, no. 3, pp. 209–249, 2021.

[2] M. Rentsch, T. Schiergens, A. Khandoga, and J. Werner, "Surgery for colorectal cancer - trends, developments, and future perspectives," *Visceral Medicine*, vol. 32, no. 3, pp. 184–191, 2016.

[3] S. U. Yang, E. J. Park, S. H. Baik, K. Y. Lee, and J. Kang, "Modified colon leakage score to predict anastomotic leakage in patients who underwent left-sided colorectal surgery," *Journal of Clinical Medicine*, vol. 8, no. 9, p. 1450, 2019.

[4] J. D. Yin, L. R. Song, H. C. Lu, and X. Zheng, "Prediction of different stages of rectal cancer: texture analysis based on diffusion-weighted images and apparent diffusion coefficient maps," *World Journal of Gastroenterology*, vol. 26, no. 17, pp. 2082–2096, 2020.

[5] N. C. Buchs, P. Gervaz, M. Secic, P. Bucher, B. Mugnier-Konrad, and P. Morel, "Incidence, consequences, and risk factors for anastomotic dehiscence after colorectal surgery: a prospective monocentric study," *International Journal of Colorectal Disease*, vol. 23, no. 3, pp. 265–270, 2008.

[6] Z. R. Lu, N. Rajendran, A. C. Lynch, A. G. Heriot, and S. K. Warrier, "Anastomotic leaks after restorative resections for rectal cancer compromise cancer outcomes and survival," *Diseases of the Colon & Rectum*, vol. 59, no. 3, pp. 236–244, 2016.

[7] F. E. Turrentine, C. E. Denlinger, V. B. Simpson et al., "Morbidity, mortality, cost, and survival estimates of gastrointestinal anastomotic leaks," *Journal of the American College of Surgeons*, vol. 220, no. 2, pp. 195–206, 2015.

[8] J. Meyer, S. Naiken, N. Christou et al., "Reducing anastomotic leak in colorectal surgery: the old dogmas and the new challenges," *World Journal of Gastroenterology*, vol. 25, no. 34, pp. 5017–5025, 2019.

[9] M. K. Kim, J. G. Kim, G. Lee et al., "Comparison of the effects of an ERAS program and a single-port laparoscopic surgery on postoperative outcomes of colon cancer patients," *Scientific Reports*, vol. 9, no. 1, p. 11998, 2019.

[10] N. N. Rahbari, J. Weitz, W. Hohenberger et al., "Definition and grading of anastomotic leakage following anterior resection of the rectum: a proposal by the International Study Group of Rectal Cancer," *Surgery*, vol. 147, no. 3, pp. 339–351, 2010.

[11] C. Y. Kang, W. J. Halabi, O. O. Chaudhry et al., "Risk factors for anastomotic leakage after anterior resection for rectal cancer," *JAMA Surgery*, vol. 148, no. 1, pp. 65–71, 2013.

[12] A. Vallance, S. Wexner, M. Berho et al., "A collaborative review of the current concepts and challenges of anastomotic leaks in colorectal surgery," *Colorectal Disease*, vol. 19, no. 1, pp. O1–o12, 2017.

[13] P. P. Singh, I. S. Zeng, S. Srinivasa, D. P. Lemanu, A. B. Connolly, and A. G. Hill, "Systematic review and meta-analysis of use of serum C-reactive protein levels to predict anastomotic leak after colorectal surgery," *The British Journal of Surgery*, vol. 101, pp. 339–346, 2014.

[14] U. Zielinska-Borkowska, N. Dib, W. Tarnowski, and T. Skirecki, "Monitoring of procalcitonin but not interleukin-6 is useful for the early prediction of anastomotic leakage after colorectal surgery," *Clinical Chemistry and Laboratory Medicine*, vol. 55, no. 7, pp. 1053–1059, 2017.

[15] E. Asti, G. Bonitta, M. Melloni et al., "Utility of C-reactive protein as predictive biomarker of anastomotic leak after minimally invasive esophagectomy," *Langenbeck's Archives of Surgery*, vol. 403, no. 2, pp. 235–244, 2018.

[16] M. Zawadzki, M. Krzystek-Korpacka, A. Gamian, and W. Witkiewicz, "Serum cytokines in early prediction of anastomotic leakage following low anterior resection," *Videosurgery and Other Miniinvasive Techniques*, vol. 13, pp. 33–43, 2018.

[17] P. A. Neumann, V. Twardy, F. Becker et al., "Assessment of MMP-2/-9 expression by fluorescence endoscopy for

evaluation of anastomotic healing in a murine model of anastomotic leakage," *PLoS One*, vol. 13, no. 3, article e0194249, 2018.

[18] Z. Wu, G. S. Boersema, D. Taha et al., "Postoperative hemodynamic index measurement with miniaturized dynamic light scattering predicts colorectal anastomotic healing," *Surgical Innovation*, vol. 23, no. 2, pp. 115–123, 2016.

[19] S. Hayami, K. Matsuda, H. Iwamoto et al., "Visualization and quantification of anastomotic perfusion in colorectal surgery using near-infrared fluorescence," *Techniques in Coloproctology*, vol. 23, no. 10, pp. 973–980, 2019.

[20] M. Fukada, N. Matsuhashi, T. Takahashi et al., "Risk and early predictive factors of anastomotic leakage in laparoscopic low anterior resection for rectal cancer," *World Journal of Surgical Oncology*, vol. 17, no. 1, p. 178, 2019.

[21] L. Erb, N. H. Hyman, and T. Osler, "Abnormal vital signs are common after bowel resection and do not predict anastomotic leak," *Journal of the American College of Surgeons*, vol. 218, no. 6, pp. 1195–1199, 2014.

[22] K. Twohig, A. Ajith, A. Mayampurath, N. Hyman, and B. D. Shogan, "Abnormal vital signs after laparoscopic colorectal surgery: more common than you think," *American Journal of Surgery*, vol. 221, 2021.

[23] A. T. Stearns, F. Liccardo, K. N. Tan et al., "Physiological changes after colorectal surgery suggest that anastomotic leakage is an early event: a retrospective cohort study," *Colorectal Disease*, vol. 21, no. 3, pp. 297–306, 2019.